THE UNIVERSITY
of ADELAIDE

Development of continuous-wave Tm:$YAlO_3$ lasers for high power applications

by

Ka Shun Wu

A thesis submitted for degree of

Doctor of Philosophy

in

The University of Adelaide

School of Physical Sciences

October 2015

Statement of Originality

This work contains no material which has been accepted for the award of any other degree or diploma in any university or other tertiary institution and, to the best of my knowledge and belief, contains no material previously published or written by another person, except where due reference has been made in the text;

I give consent to this copy of my thesis, when deposited in the University Library, being made available for loan and photocopying, subject to the provisions of the Copyright Act 1968;

The author acknowledges that copyright of published works contained within this thesis (as listed below) resides with the copyright holder(s) of those works;

I also give permission for the digital version of my thesis to be made available on the web, via the University's digital research repository, the Library catalogue, the Australasian Digital Theses Program (ADTP) and also through web search engines, unless permission has been granted by the University to restrict access for a period of time.

Signed: ……

Date: ……

Supervisors: Prof. Jesper Munch, Dr. David J. Ottaway, A/Prof. David Lancaster

Abstract

Thulium and holmium lasers operating near 2 μm are required for applications in various industries, such as remote sensing and detection, spectroscopy, surgery and optical countermeasures. High power lasers with high brightness are necessary for many of these applications, with fibre lasers often preferred due to their various advantages. However, a major drawback of fibre lasers is the brightness requirement on the pump source, which needs to have moderate to high brightness in order to couple light into the fibres efficiently. Such pump sources are often prohibitively expensive.

A possible solution is the use of brightness converters. Brightness converters are lasers that are designed such that the output brightness is significantly greater than that of its pump source, and is sufficiently bright to pump fibre lasers efficiently. For example, by using a thulium-doped solid-state laser as a brightness converter, holmium-doped fibre lasers can be pumped efficiently by cheap, high power but low brightness diode stacks.

Thulium-doped $YAlO_3$ lasers are ideal for this purpose: their emission wavelength corresponds to the peak absorption of holmium in silica, high power diode stacks are readily available at its absorption wavelength, and it is a crystal with a high damage threshold. However, Tm:$YAlO_3$ lasers suffer from significant self-pulsing, which can lead to unstable gain-switching of the holmium-doped fibre laser as well as risking damage due to the high peak power.

In this thesis, I describe the investigation and development of Tm:$YAlO_3$ lasers as high power brightness converters and pump sources. A detailed analysis of the self-pulsing is conducted using a 6.5 W Tm:$YAlO_3$ laser. The self-pulsing is shown initially to be consistent with an unstable relaxation oscillation in the gain medium. A model based on significant excited-state absorption at the lasing wavelength is shown to reproduce the experimental results. The assumed cross-section required for this

process is tested in a further experiment, which rules out this theory. The Tm:$YAlO_3$ laser is then analysed as a chaotic system, with results from time delay embedding and the 0–1 test for chaos indicating strongly that the laser system is chaotic. To the best of my knowledge, this is the first analysis and evidence of Tm:$YAlO_3$ lasers as a chaotic system.

I describe the suppression of the self-pulsing using a method applicable to high power. Using this feedback system, the Tm:$YAlO_3$ laser is shown to produce a stable, continuous-wave output. To the best of my knowledge, this is the first demonstration of the suppression of such strong self-pulsing.

This thesis also describes the design and development of a high power Tm:$YAlO_3$ laser using a novel geometry, which in principle is capable of several hundred watts of output power. This design aims to combine the superior thermal handling of disk lasers with the ease of pumping and laser design of the slab laser. A comprehensive model of such a laser is described, and the development of the laser up to the construction stage is presented.

Acknowledgements

First and foremost, I would like to thank my supervisors Jesper Munch, David Ottaway and David Lancaster for all of the support and guidance they have provided me through the course of my PhD. In the same vein, I would like to thank Peter Veitch, who has essentially been an additional supervisor for me.

To David Hosken: words cannot express my gratitude for all of your help and advice throughout my PhD. Without it, I would have been so lost.

To the members of the Optics group: Eleanor, Keiron, Matt, Miftar, Murray, Myles, Nick, Ori, Sophie, and the rest of the group: thank you for all the discussions and help in the lab. To those that have graduated, thank you for showing me that it is in fact possible!

To Blair, Neville and Trevor: I am very grateful for all the excellent technical assistance and advice you have provided.

To the staff at the school, Carol, Jeanette, Katie, Mary, Ramona, Sharon, Wayne, and the front office staff: thank you for the all the administrative support.

I would like to thank those in the OSA/SPIE student chapter, for making my PhD journey so enjoyable and giving me much needed morale boosts. Hosting the KOALA conference was one of the highlights of my PhD experience, and thank you for making it so successful with me! I will miss organising and attending the events.

Finally, I am eternally grateful to my parents, Georgia, and my close friends for being there for me through my journey. Without the love and support from all of you, I would not have made it to the finish line.

Contents

List of Symbols

α_p	Pump absorption
γ	Ratio of ESA cross-section to GSA cross-section
ζ	Damping constant
η_q	Quantum efficiency
η_{red}	Density-reduction scaling parameter
η_{slope}	Slope efficiency
θ	Far-field divergence angle
θ_B	Brewster's angle
θ_{inc}	Angle of incidence
λ	Wavelength
σ	Laser emission cross-section
σ_{ESA}	ESA cross-section at the lasing wavelength
σ_p	Pump absorption cross-section
τ_{CR}	Cross-relaxation time constant
τ_{delay}	Transport delay time
τ_{in}	Time constant of the input high-pass filter
τ_{out}	Time constant of the output low-pass filter
τ_{RT}	Round-trip time constant
ϕ	Intra-cavity laser photon density
ω	Beam size (radius)
ω_0	Waist size (radius)
ω_v	Natural frequency (angular) of relaxation oscillation
ω_{CR}	Frequency (angular) for cross-relaxation
ω_{FB}	Frequency (angular) of the high-pass filter

ω_{pump}	Beam size (pump)
Ω	Solid angle
a_{ijkl}	Cross-relaxation and co-operative up-conversion rates from level i, k to j, l
A_{laser}	Laser mode area
A_{pump}	Pump mode area
c	Speed of light
d	Dimension
$D_c(n)$	Modified mean square displacement
E_{pump}	Pump photon energy
f	Focal length
f_l	Boltzmann thermal occupation factor for lower lasing level
f_u	Boltzmann thermal occupation factor for upper lasing level
g	Gain coefficient
G_{amp}	Amplifier gain
G_{DC}	DC gain
$G_{feedback}$	Feedback gain
K	Median linear correlation coefficient with time for 0–1 test
l	Length of the laser gain medium
l_{air}	Length of the air within the cavity
$L_{Interface}$	Loss due to scatter at the interface
L_{RT}	Total round-trip loss
$L_{Scatter}$	Loss due to bulk scatter
M	Molar mass
n	Refractive index
N	Population density of Tm:$YAlO_3$
N_{Av}	Avagadro's number
N_i	Population density of energy level i
P_{losses}	Pump power required to overcome losses
P_{max}	Maximum attainable output power
P_{out}	Output power
P_{pump}	Pump power
P_{th}	Threshold pump power
P_{trans}	Pump power required to achieve transparency

R	Reflectivity
R_d	Euclidean distance between two points in dimension d
R_p	Pump rate
r_c	Cavity photon decay rate
r_{ij}	Natural decay rate from i to j (j omitted if to ground state)
r_s	Reflection coefficient for an incident s-polarisation beam
r_{sp}	Spontaneous radiative decay rate
T	Temperature
T_{eq}	Equilibrium transmission
T_{ns}	Nanosecond time scale transmission
$T_{\mu s}$	Microsecond time scale transmission
T_{OC}	Transmission of the output coupler
z_0	Distance of the beam waist
AoI	Angle of incidence
AOM	Acouto-optic modulator
AR	Anti-reflective
ASE	Amplified spontaneous emission
CAD	Computer-aided design
CW	Continuous-wave
DI	Deionised
ESA	Excited-state absorption
FEA	Finite element analysis
FFT	Fast Fourier transform
FWHM	Full-width half maximum
GRIN	Gradient-index
GSA	Ground-state absorption
HeNe	Helium-neon
HT	High transmission
HR	High reflectivity
N.A.	Numerical aperture
ODE	Ordinary differential equation
OPO	Optical parametric oscillator
OSA	Optical spectrum analyser

PD	Photodetector
PRF	Pulse repetition frequency
RMS	Root mean square
ThOR	Thin outer-region-doped
TIR	Total internal reflection
YAG	Yttrium aluminum garnet ($Y_3Al_5O_{12}$)
YAP	Yttrium aluminum perovskite ($YAlO_3$)
YLF	Yttrium lithium fluoride

List of Figures

List of Tables

1 Introduction

1.1 Mid-infrared lasers

Lasers have revolutionised an ever-growing number of fields and industries since their invention in 1960 [1]. Recently, there has been significant advances in the development of lasers that operate in the mid-infrared region of the spectrum, which is nominally between 1.9 μm and 5 μm [2]. This spectral region hosts several atmospheric transmission windows [3], [4], allowing low-loss propagation of light through the atmosphere. Light at this wavelength range is considered eye-safe, as it is absorbed by the anterior segments of the eye well before being focused on the retina [5]. This makes it ideal for applications such as range finding [6] and laser radar (LiDAR) [7], [8]. Active threats to aircrafts typically operate in the 3–5 μm range, making this region very important for optical countermeasures in defence [9], [10].

Many molecules have strong rotational and vibrational absorption lines in the mid-infrared region [11], and hence this region is used extensively in spectroscopy [12]–[14]. Coupled with a high atmospheric transmission, applications for mid-infrared lasers extend to atmospheric sensing and remote pollutant and gas detection [7], [15]–[17].

Light in the mid-infrared region is used for many medical applications because strong absorption lines of water are present in this region [18], as well as the ability to target specific molecules in cells. These include surgical scalpels [19]–[21], biomedical spectroscopy, biosensors and bio-imaging [10].

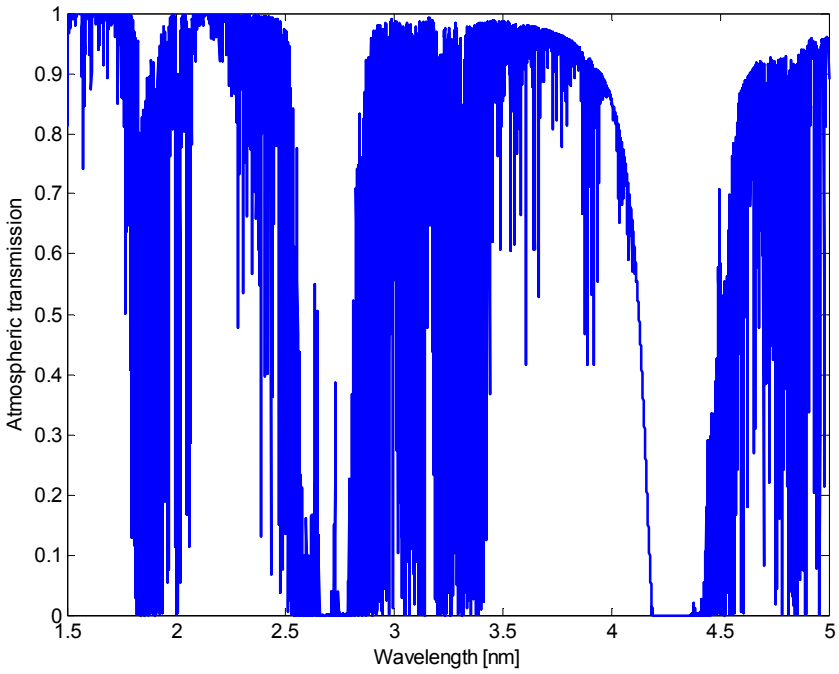

Figure 1.1: Atmospheric transmission in the mid-infrared wavelength region [4].

1.1.1 Thulium and holmium lasers

First demonstrated shortly after the invention of the laser, thulium- [22] and holmium-doped [23] lasers are two important rare-earth dopants for mid-infrared light generation. Operating near 2 μm, they are used extensively in many of the listed applications due to their relatively high efficiency and ease of use. They also make excellent pump sources for non-linear light conversion to the 3–5 μm range via optical parametric oscillators using Zinc Germanium Phosphide ($ZnGeP_2$) [24], [25] and Orientation-Patterned Gallium Arsenide (OPGaAs) [26], [27].

Thulium-doped lasers operate within a broad wavelength range of 1.85 – 2.05 μm. They can be pumped efficiently either in-band at 1.55 μm by erbium-doped pump sources [28] or at 790 nm by highly efficient AlGaAs laser diodes [29], both of which are readily available at high powers. A cross-relaxation process in thulium allows for very high efficiencies, despite the significant quantum defect when pumping at 790 nm [30]. During cross-relaxation, ions that are excited to the $^3H_4$ manifold by 790 nm photons can interact with and transfer energy to a neighbouring ground-state ion. This results in two ions in the $^3F_4$ upper lasing manifold for every 790 nm photon absorbed, potentially doubling the quantum efficiency. The energy level diagram and the cross-

relaxation process for thulium are shown in Figure 1.2. Efficient operation of thulium lasers utilising cross-relaxation have been demonstrated in many hosts including crystals [31], [32] and glasses [30], [33]–[35], with slope efficiencies up to 80% [36]. High powers have been achieved, including over 200 W from solid-state lasers [37], [38] and almost 900 W [39] from a fibre laser.

Holmium-doped lasers emit at a wavelength around 2.1 μm, and are typically pumped in-band at 1.95 μm [40], as shown in Figure 1.2. The resulting low quantum defect of 92% allows for extremely high efficiencies, with demonstrated slope efficiencies in holmium-doped lasers exceeding 70% [41], [42]. The pump wavelength lies within the emission wavelength of thulium-doped lasers, and hence holmium lasers are often pumped by thulium-doped lasers [43]–[46]. This also allows for co-doping [47], [48], where thulium ions act as sensitisers to absorb 790 nm pump light. Energy is then transferred directly from an excited thulium ion in the $^3F_4$ manifold to a neighbouring holmium ion. Over 400 W of output power have been demonstrated for singly-doped holmium lasers [49], while over 80 W have been achieved from thulium, holmium co-doped lasers [50].

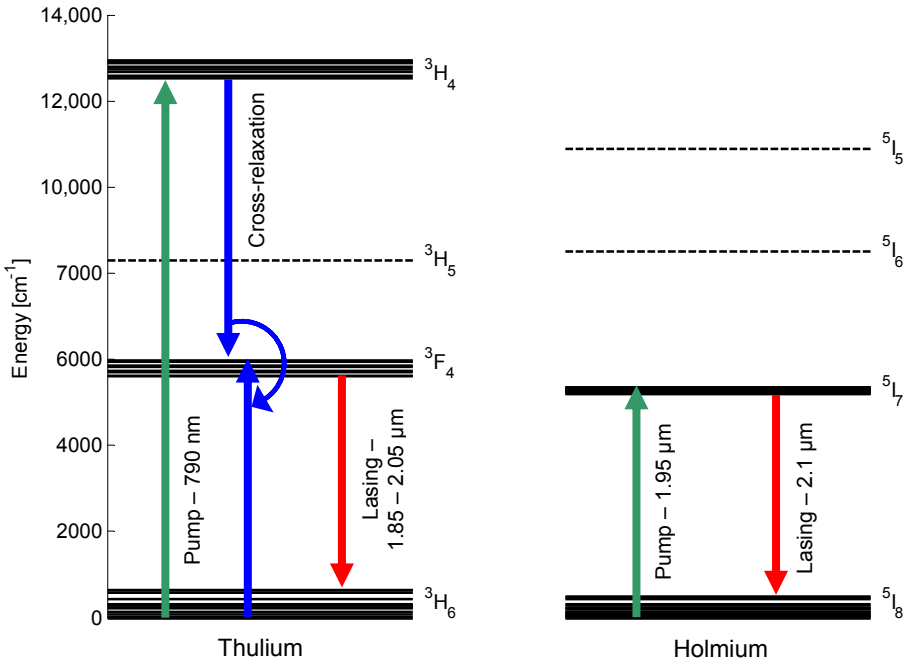

Figure 1.2: Energy level diagram for thulium and holmium, including the transitions involved in lasing.

1.2 Beam quality and brightness

Many of the applications mentioned previously require the delivery of optical power at a large distance or focused tightly at a precise location. In these cases, it is necessary to use high power lasers with near diffraction-limited beam quality.

Fundamentally, the beam quality is quantified in reference to a Gaussian near-field intensity pattern by the Beam Parameter Product, which is defined as the product of beam radius at the waist ω_0 and the far-field beam divergence half-angle θ. Often, the beam quality is given in terms of the M^2 of the beam, which is defined as the ratio of the beam parameter product to that of a perfect Gaussian beam at the beam wavelength λ. This is given by:

$$M^2 = \frac{\omega_0 \theta \pi}{\lambda}. \tag{1.1}$$

For a perfect TEM_{00} Gaussian beam, $\theta = \theta_0 = \lambda / \pi\omega_0$ and thus $M^2 = 1$.

The beam quality of a laser is defined by the laser resonator, and cannot be improved using standard optics external to the cavity, regardless of the optics used. For example, focusing a laser beam with an ideal lens will reduce the spot size and hence reduce the spot size of the beam, but the divergence will increase at the same rate.

The term "brightness" is often used when describing high power laser sources and beams. It is often a non-quantitative concept that combines the power and beam quality of the laser. Lasers with relatively high power and good beam quality, such as many high power fibre lasers, are often described as "high brightness" sources. High power lasers with poor beam quality, such as laser diode stacks, are often described as having "low brightness".

Like beam quality, the brightness of a beam is predetermined by the source and cannot be improved using standard optics. For example, spatial filtering of a beam can be used to improve the beam quality; however, some of the power of the beam is sacrificed in the process, and the brightness of the resultant beam remains the same or is lower than the original beam.

1.2.1 Fibre lasers as high-brightness sources

High-brightness laser beams can be generated by both solid-state and fibre lasers; however recent developments in fibre lasers have seen them become the preferred high-brightness laser source for an increasing number of industries and applications. This is due to the various advantages of fibre lasers over conventional solid-state lasers.

The guiding property of fibres allows the gain medium to be any desired length. A longer gain length can increase pumping efficiencies and improve gain distribution through the gain medium, as well as allow for better cooling due to a large surface to volume ratio. Efficient cooling of the fibre not only raises the power limitation from thermal damage [51], but also limits the temperature of the gain medium. This is particularly important for quasi-three-level lasers, where a high temperature results in lower laser efficiencies due to unfavourable population distributions of the Stark sublevels of the upper and lower lasing manifolds [52]. Guidance also allows for limited bending of the fibre gain medium without introducing loss [53], leading to compact devices.

The size of the core and the numerical aperture of the fibre determine the number of spatial modes that are confined to the core [54], which defines the beam quality of the fibre laser. If single-mode fibre is used to construct a fibre laser, the resultant laser beam will have diffraction-limited beam quality. This makes the fibre laser more rugged than solid-state lasers, where a misalignment of the cavity mirrors will result in reduced power and potentially a poorer beam quality. The invention and development of fibre-Bragg gratings [55] further enhances the ruggedness of the fibre laser, with all-fibre lasers insensitive to movement and vibrations.

One major drawback of high power fibre lasers is the brightness requirement on the pump source. The pump light must be coupled into and guided along the fibre for efficient pumping, and hence the beam quality of the pump source must be sufficiently high. For a standard step-index fibre, the beam quality of the pump source must therefore be almost the same as that of the laser. The development of the double-clad fibre [56], [57] relaxed the beam quality requirement to a certain extent, allowing excellent coupling of pump sources with moderate beam quality. However, this is still limiting as increasing the cladding size reduces the pump absorption per unit length, thermal handling, and flexibility of the fibre.

1.2.2 Brightness converters

Pump sources for direct pumping of fibre lasers ($M^2 \sim 10$), such as fibre-coupled diodes, can be elusive and prohibitively expensive at high power, thus limiting the applications. High power, low beam quality pump sources such as diode stacks, however, can provide ample power and are substantially cheaper, but cannot be used to pump fibre lasers directly due to their low beam quality ($M^2 \sim 100$).

It is not possible to improve the brightness of these pump sources directly, but one possible solution is to use a "brightness converter". A brightness converter is essentially a laser that has an output beam with brightness higher than that of the pump source [58]. Brightness converters do not violate the conservation of brightness, as the original pump beam is absorbed and the energy is used to produce a new beam. By the use of brightness converters, cheap, high power pump sources with low brightness can be used to pump near diffraction-limited fibre lasers efficiently.

The most effective brightness converters are solid-state lasers, which have much larger dimensions and unlike fibre lasers, do not require confinement of the pump light. They can therefore accept pump light with much larger spot size and divergence, and were traditionally even pumped by non-directional pump sources such as flash-lamps and arc-lamps [59]. These solid-state lasers can be made to operate with excellent beam quality, and hence provide a major increase in brightness.

Efficient brightness conversion can be achieved conveniently and efficiently in the mid-infrared region using thulium and holmium-doped lasers. A thulium-doped solid-state laser can be used to pump indirectly a diffraction-limited holmium-doped fibre laser, as illustrated in Figure 1.3. This allows the use of high power, low-brightness, inexpensive AlGaAs laser diodes. Assuming efficient cross-relaxation process in the thulium-doped laser, the quantum efficiency from 790 nm to 2.1 μm can be as high as 75%. This is potentially a much cheaper solution to obtaining high power, high brightness laser light in the mid-infrared region. This thesis will focus on the development of the thulium-doped solid-state laser as a brightness converter.

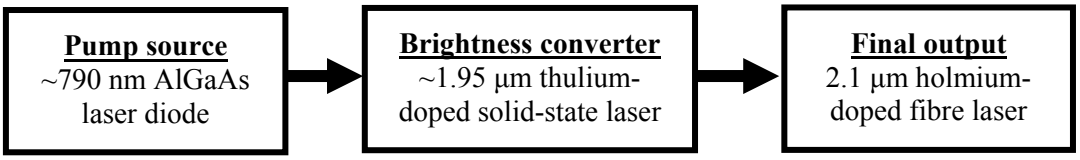

Figure 1.3: Summary of the pumping sequence.

1.3 Thulium-doped brightness converter

1.3.1 Crystal host

The three most common crystal hosts, YAG, $YAlO_3$ (YAP) and YLF, were considered for the thulium-doped brightness converter. The main points of consideration were power handling, availability of inexpensive, high power pump sources, and the holmium absorption cross-section at the thulium lasing wavelength. A number of crystal properties and the energy level diagrams of thulium in the three crystal hosts are shown in Table 1.1 and Figure 1.4 respectively.

The absorption spectrum of holmium-doped silica [40], shown in Figure 1.5, shows a strong absorption peak centred at 1.95 μm. The absorption at the Tm:$YAlO_3$ emission wavelength of 1.94 μm is almost 120 dB/m, nearly 60 dB/m higher than that at both Tm:YAG and Tm:YLF emission wavelengths. A stronger absorption allows for a shorter fibre or a larger inner cladding, relaxing the coupling conditions.

AlGaAs laser diodes typically operate at a wavelength beyond 800 nm [60], and the addition of Al to the active region, or tensile straining, is required to obtain shorter wavelengths [61]. However, this reduces the internal power density and limits the reliability, making high power laser diodes at shorter wavelengths difficult to manufacture [62]. AlGaAs laser diodes operating at 795 nm for pumping Tm:$YAlO_3$

	Tm:YAG	Tm:$YAlO_3$	Tm:YLF
Pump wavelength [nm]	786	**795**	792
Pump absorption cross-section [10^{-21} cm^2]	**8.7**	7.5	6.0
Peak emission wavelength [μm]	2.01	**1.945**; 1.99	1.91
Emission cross-section [10^{-21} cm^2]	1.5	**5.0**	4.0
Emission/Reabsorption ratio	**25.8**	22.3	9.05
Refractive index	1.8	1.9	1.5
Thermal conductivity [$W \cdot cm^{-1} \cdot K^{-1}$]	0.13	0.11	0.06
Stress fracture limit [MPa]	175-200	160	40

Table 1.1: Selected properties of three crystal hosts for thulium [63]–[66]. Preferential properties are shown in bold.

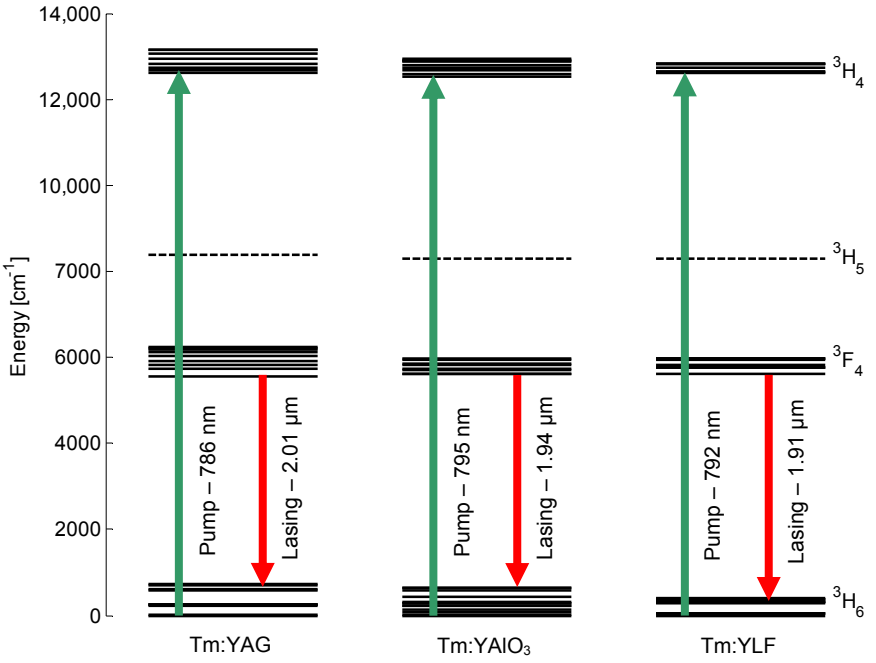

Figure 1.4: Energy level diagram Tm:YAG, Tm:$YAlO_3$ and Tm:YLF, including Stark-splitting of the levels [63], [67].

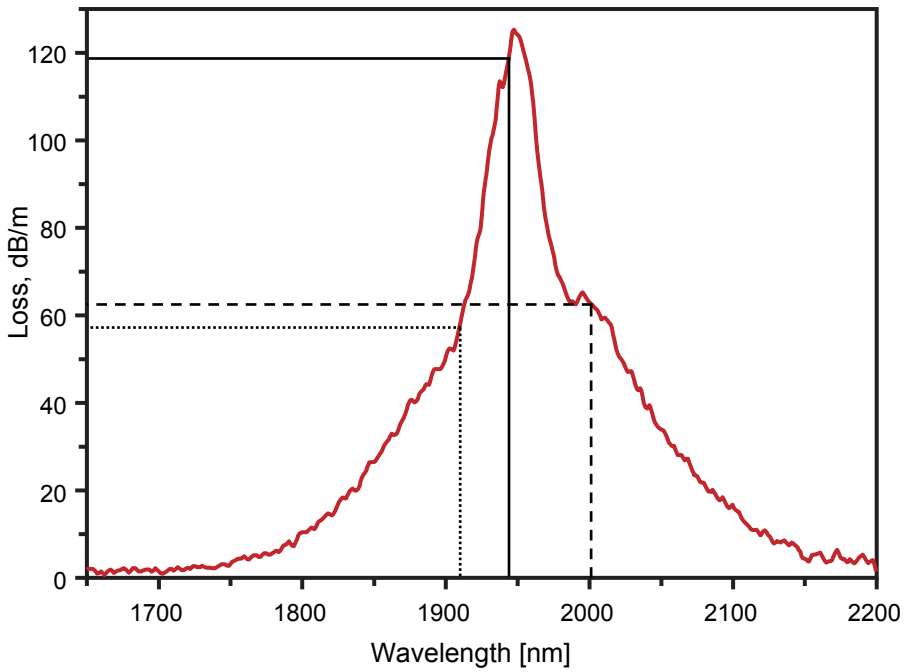

Figure 1.5: Absorption spectrum of holmium-doped silica, and the emission wavelength of Tm:YAG (dashed), Tm:$YAlO_3$ (solid) and Tm:YLF (dotted). Reproduced from [40]

are readily available cheaply at high powers up to 1 kW, but the additional tensile straining required results in higher costs for diminishing maximum output powers for pumping Tm:YLF and in particular Tm:YAG due to the shorter absorption wavelength.

Tm:$YAlO_3$ lasers are more efficient compared to Tm:YAG [68], [69] due to a significantly higher emission cross-section. $YAlO_3$ is biaxial and hence naturally birefringent [70], which dominates any thermally-induced birefringence and depolarisation at high power. Compared to Tm:YLF, Tm:$YAlO_3$ has superior thermal handling capabilities; with almost twice the thermal conductivity and four times the stress fracture limit, Tm:$YAlO_3$ lasers are capable of significantly higher powers before thermal fracture. Tm:$YAlO_3$ has a greater absorption and emission cross-section, as well as a significantly greater emission to reabsorption ratio at the emission wavelength.

$YAlO_3$ was therefore chosen as the best host based on a number of properties that make it superior for use as a brightness converter for holmium-doped fibre lasers.

1.3.2 Tm:$YAlO_3$ laser properties

Yttrium aluminium perovskite ($YAlO_3$, or YAP) is one of the phases of the yttrium-aluminium composite, along with YAG ($Y_3Al_5O_{12}$). It has many similar physical properties to YAG, such as hardness, thermal conductivity, etc. However, while YAG has a cubic crystal structure and hence isotropic [64], $YAlO_3$ has an orthorhombic crystal structure with space group D_{2h}^{16} [71], making it biaxial. As such, it has three distinct axes with different physical as well as spectroscopic properties. When doped with thulium ions, Tm^{3+} displaces yttrium in the crystal lattice. A number of properties of thulium-doped $YAlO_3$ are tabulated in Table 1.2, including axis-specific parameters.

The preferred axis for lasing is the *c*-axis due to its peak emission at 1.94 μm. The *a*-axis also has an emission peak at 1.94 μm, but reabsorption losses at this wavelength cause preferential lasing at longer wavelengths around 1.99μm [72]. The *b*-axis has a very low emission cross-section for wavelengths beyond 1.9μm. The *b*-axis is preferential for pump absorption due to the broad dual peak at 793 nm and 795 nm, with a combined full width half maximum (FWHM) of 4 nm.

		a-axis	*b*-axis	*c*-axis
Orthorhombic crystal lattice	(Pbnm)	5.176	5.307	7.355
cell parameters [Å]	(Pnma)	5.330	7.375	5.180
Thermal Expansion [10^{-6} K^{-1}]		9.5	4.3	10.8
dn/dT [10^{-6} K^{-1}]		9.7	-5.48	14.5
Refractive Indices	(λ = 800 nm)	1.916	1.930	1.939
	(λ = 1.94 µm)	1.905	1.919	1.927
790 nm absorption peak [nm]		795	793, 795	793
Free-running lasing wavelength [µm]		1.99	1.87	1.94
Density [g·cm^{-1}]			5.36	
Mohs hardness			8.5	
Thermal Conductivity [W·cm^{-1}·K^{-1}]			0.11	
Young's Modulus [GPa]			220	
Poisson's Ratio			0.268	
Fracture Stress [MPa]			160	

Table 1.2: Selected properties of Tm:$YAlO_3$ [65], [69], [71]–[76].

1.3.2.1 Sellmeier's Equation

The refractive index of $YAlO_3$ at different wavelengths was calculated using the Sellmeier's Equation:

$$n(\lambda)^2 = 1 + \frac{B\lambda^2}{\lambda^2 - C}, \tag{1.2}$$

where λ is the wavelength in µm, and B and C are the Sellmeier coefficients for $YAlO_3$. A plot of the refractive index along each axis for different wavelengths is shown in Figure 1.6 for $YAlO_3$. The Sellmeier coefficients are tabulated in Table 1.3.

	B	*C*
a-axis	2.6196	0.012338
b-axis	2.67171	0.012605
c-axis	2.70381	0.012903

Table 1.3: Sellmeier coefficients for the different axes of $YAlO_3$ [77]

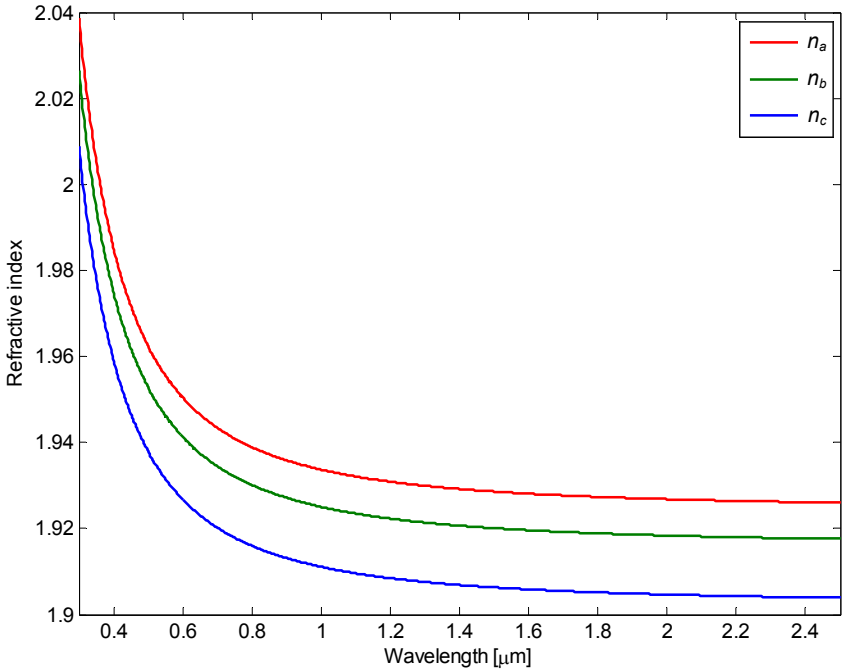

Figure 1.6: Refractive index along each axis of $YAlO_3$ as a function of wavelength.

1.3.3 Self-pulsing in Tm:$YAlO_3$ lasers

A major drawback of Tm:$YAlO_3$ lasers is their tendency to self-pulse, even under continuous-wave (CW) pumping [78]–[81]. Self-pulsing results in a laser output consisting of unstable, high-amplitude oscillations with modulation depth up to 100%. Such strong self-pulsing severely limits the usefulness of the laser, particularly when used as a high-power pump source for a fibre laser. High peak power can risk damaging the fibre laser due to the strong instantaneous electric field, particularly at the input end surface, where the field is strongest and the fibre is exposed. The fibre laser may also be forced to operate in a pulsed regime, as the pulsed pump source could induce gain-switching. Depending on the pump pulse energy, the output pulses from the fibre laser could also be erratic. In particular, pulse stacking could occur if the energy of some of the pump pulses was insufficient for the fibre laser to reach threshold [28], leading to an irregular pulse repetition rate. Therefore, it is extremely desirable to eliminate the oscillations and achieve CW operation.

A number of mechanisms have been proposed to explain the self-pulsing behaviour in Tm:$YAlO_3$ lasers. These include pump power fluctuations and acoustic or mechanical perturbations [79], [81], [82]. Saturable absorption within the resonator can also explain self-pulsing [83] and could be due to absorption by the air or within the gain medium caused by up-conversion or excited state absorption [84]–[86]. This is feasible in Tm:$YAlO_3$ operating around 1.94 μm, as there is an absorption line of water at this wavelength.

Very little work on modelling or experimental verification of the mechanisms for self-pulsing in Tm:$YAlO_3$ have been reported to date. The most detailed analysis was done by Razdobreev and Shestakov in their investigation of a monolithic Tm:$YAlO_3$ laser [85]. They observed a stable CW output from the laser at low normalized pump rates, which changed to a regular self-pulsing regime at higher pump powers. A rate equation model based on a phonon-assisted excited state absorption (ESA) was reported and was shown to reproduce the experimental results qualitatively. However, this model relies on a large ESA cross-section, the value of which has never been measured prior to the work in this thesis.

An alternative mechanism that results in strong self-pulsing in lasers is nonlinear dynamical chaos [87]–[89]. No work prior to this thesis involving the analysis of Tm:$YAlO_3$ lasers as a chaotic system has been reported. The presence of two distinct regimes observed by Razdobreev and Shestakov [85] is also consistent with chaos in lasers. Lasers that exhibit chaotic behaviour have a second threshold above the laser threshold for the onset of chaotic behaviour [90]; the laser is stable below the second threshold, and chaotic above.

1.3.3.1 Pulse suppression techniques

Self-pulsing must be suppressed in order for a Tm:$YAlO_3$ laser to be useable as a pump source for holmium fibre lasers. While a monolithic laser design has been shown to result in stable CW operation at low power levels, it does not remain stable for higher power levels [85]. Furthermore, the beam quality of a monolithic laser is very difficult to control, as the design does not allow for the intra-cavity components such as lenses for thermal distortion compensation. This usually results in a deteriorating beam quality with increasing output power [81].

Stable output can be achieved by active suppression of the self-pulsing via feedback. A fast detector is used to measure the change in the output power of the laser.

The signal from the detector is then passed to an actuator, which attempts to suppress the observed fluctuations. Active suppression has been demonstrated using intra-cavity acousto-optic modulators (AOMs) to modulate the cavity loss [80], [91]. This works because, as the laser power builds to form the leading edge of a pulse, the intra-cavity loss increases and limits the peak of the pulse. The reverse occurs for the trailing edge of the pulse, reducing the loss as the laser signal reduces. This repeats until the oscillations are fully damped out. The disadvantage of this method is that it introduces additional cavity losses and complexity. Further, AOMs typically have small apertures and a low damage threshold, which limit the power attainable from an actively stabilised Tm:$YAlO_3$ laser.

An alternative method of pulse suppression is via current feedback to the pump source. Instead of loss modulation within the cavity, the signal from the detector is used to modulate the available gain via the power of the pump laser diodes [92]–[95]. This method operates outside the laser cavity and hence does not require additional intra-cavity components. It can be applied to any diode-pumped laser without imposing additional limitations. This method has been used to eliminate intensity noise with low modulation depth in lasers of other dopants and hosts such as Nd:YAG [92], [96] and co-doped Tm–Ho:YAG [97] lasers. However, the self-pulsing in Tm:$YAlO_3$ lasers can result in modulation depths of up to 100% of the output power, which is far greater than that for these lasers [68]. Previously, pulse suppression via gain modulation for a laser with such strong modulation has been demonstrated only in a four-level Nd-doped fibre laser at very low powers (pump power < 10 mW) [98].

1.3.4 Tm:$YAlO_3$ laser systems

To date, there has been very little work published on high power Tm:$YAlO_3$ lasers or their use as brightness converters. In the majority of the papers published, the Tm:$YAlO_3$ lasers are limited to below 10 W of output power, with a typical slope efficiency around 40%. Most are pumped by fibre-coupled diode lasers with moderate to high beam quality, and hence do not act as significant brightness converters. A number of notable Tm:$YAlO_3$ lasers with high output power or slope efficiency are tabulated in Table 1.4.

Type	Pump diode	P_{out}	P_{pump}	η_{slope}	M^2	Year	Ref.
Slab	Fast-axis collimated	72 W	220 W	37.9%	--	2011	[99]
Rod	Fibre-coupled	50 W	115 W	56%	4.7	2004	[80]
Slab	Fibre-coupled	48.1 W	140 W	43.6%	4.2	2014	[100]
Slab	Fast-axis collimated	15 W	45 W	40%	--	2009	[101]
Rod	Fibre-coupled	14 W	54 W	38%	2.65	2003	[24]
Slab	Fibre-coupled	11 W	24 W	52%	--	2009	[102]
Rod	Fibre-coupled	4.8 W	10.1 W	57%	1.5	2006	[103]

Table 1.4: Selected published Tm:$YAlO_3$ systems with high output power and/or slope efficiencies.

1.3.5 Laser geometry

The primary factors limiting the output power and beam quality of Tm:$YAlO_3$ lasers are thermal effects at high power. $YAlO_3$ has a high temperature coefficient of refractive index (dn/dT). This can result in strong detrimental thermal- and stress-induced effects such as lensing and depolarisation, especially in rod lasers [104], [105]. Slab lasers suffer the same effects [106], but good beam quality ($M^2 \sim 10$ or better) can still be obtained by careful analysis and compensation of the thermal lens [107], [108]. The effects on the laser mode can also be reduced by the use of a zigzag laser mode to average out refractive index variations across one plane of the slab [109], [110] or active temperature control of the surfaces [111]. While this minimises the impact on the laser mode, the stress in the slab remains and the power of the laser is ultimately limited by the fracture limit of the crystal.

Alternatively, the disk geometry has superior thermal handling capabilities and hence is attractive for high power operation [112]–[114]. The gain medium is made very thin and mounted directly onto the heat sink. Heat generated from optical pumping is in close proximity to the heat sink and is removed readily, resulting in a minimal temperature gradient. Additionally, this temperature gradient is typically parallel to the beam path and thus has limited detrimental effect on the laser mode. However, its thinness also makes the disk laser difficult to pump uniformly due to the short interaction length, leading to complex multi-pass pumping systems [115]. Disk lasers also suffer from significant amplified spontaneous emission (ASE) at high powers [116].

With significant shortfalls in each of the standard laser geometries for high power operation, a novel laser design that will allow for simple high power, high brightness operation is highly desirable. One such design would be a slab/disk hybrid geometry, where the laser crystal is split into three regions: a large, undoped region in the centre sandwiched by two thin, doped regions on the outer edges. These doped layers would be in direct contact with heat sinks, similar to that of disk lasers, for excellent heat dissipation. The undoped region provide a large aperture for the pump light, allowing it to be end-pumped similar to a standard slab.

1.4 Thesis overview

This thesis describes the investigation and development of Tm:$YAlO_3$ lasers as high power brightness converters and pump sources. There are three primary aims for this work:

- To conduct a detailed analysis into the cause of the self-pulsing behaviour of Tm:$YAlO_3$ lasers;
- To demonstrate suppression of the self-pulsing using current feedback to the pump source; and
- Design and develop a high power Tm:$YAlO_3$ laser with a novel geometry for the gain medium.

The design and construction of a low power Tm:$YAlO_3$ laser to investigate self-pulsing is described in Chapter 2. The self-pulsing behaviour of the laser is characterised. This chapter also describes the construction and testing of a feedback system based on current feedback to the pump source for pulse suppression.

A comprehensive model of the laser dynamics based on ESA at the lasing wavelength is presented in Chapter 3. This model describes the lasing behaviour in both time and frequency domain, and includes the addition of a feedback system.

Chapter 4 describes the measurement of the ESA cross-section at the lasing wavelength of Tm:$YAlO_3$, an assumed parameter that is critical in the laser dynamics model. The value obtained is introduced into the model to investigate its impact on the accuracy of the model. The laser output is also analysed as a chaotic system, using time delay embedding and the 0–1 test for chaos.

Chapter 5 describes the design and development of a moderate-power, side-pumped, straight-through Tm:$YAlO_3$ slab laser for initial power scaling. The self-pulsing behaviour of Tm:$YAlO_3$ at higher output powers is also investigated.

Chapter 6 describes the design and modelling of a high power Tm:$YAlO_3$ laser based on a hybrid slab/disk laser geometry. Development of the laser up to the construction stage is presented.

Finally, the work presented is summarised in Chapter 7, and potential future developments are discussed.

2 Low-power Tm:$YAlO_3$ cuboid laser

2.1 Introduction

Thulium-doped $YAlO_3$ is a promising solid-state gain medium for generating light at 2 μm. It is highly efficient, naturally polarised, has excellent mechanical properties and high-power pump sources are readily available. However, it suffers from significant self-pulsing, which limits the usefulness of the laser. This chapter describes the investigation of the self-pulsing and the successful demonstration of a new approach to suppress it.

The absorption spectroscopy of our Tm:$YAlO_3$ cuboid sample is described in Section 2.2. The first cuboid laser is described in Section 2.3, which is a short-cavity laser that produces up to 4.5 W and shows significant self-pulsing. Section 2.4 describes the cuboid laser Mk-II, a 6.5 W laser with an extended cavity to slow the pulsing dynamics as well as improve the beam quality. Section 2.5 describes the design, modelling and successful implementation of a feedback circuit to suppress the self-pulsing. The chapter is concluded in Section 2.6.

Some of the results reported in this chapter have been published in Applied Physics B [117]. A copy of that paper is included in Appendix A.

2.2 Absorption spectroscopy of Tm:$YAlO_3$

A sample of 4 at.% thulium-doped $YAlO_3$ was obtained from Scientific Materials Corp. for absorption spectroscopy. As the thulium-doped $YAlO_3$ crystals for all lasers in this thesis are sourced from Scientific Materials Corp, it is important to verify that the spectral properties of the crystal match that published in the literature [72].

The sample was a small cuboid with dimensions 4.55 mm × 5.02 mm × 5.54 mm along the crystal axes of *a*-, *b*- and *c*-axis respectively, as shown in Figure 2.1. Collimated light from a super-continuum source (Koheras SuperK Compact) was passed through the sample at normal incidence and directed onto the entrance slit of a spectrometer (Acton SP2500). To obtain the absorption curves for each crystal axes individually, a polarising beam-splitter cube was used to polarise the light, followed by a half-wave plate to adjust the polarisation. A slit-width of 50 μm and a 600 lines/mm grating blazed at 1 μm was used for the spectrometer, which corresponds to a resolution of 0.2 nm. The averaging time was set to 200 ms.

The spectra with and without the sample was obtained for each axis for calibration. The data obtained was then corrected for the Fresnel reflections off of each surface, and normalised with respect to the length of the crystal dimension along which light propagated.

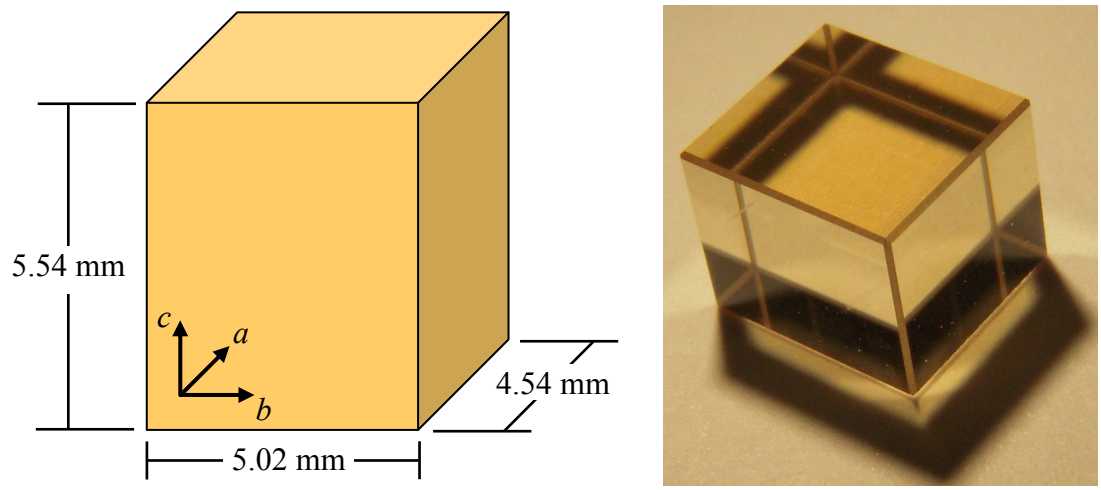

Figure 2.1: Tm:$YAlO_3$ cuboid geometry and crystal axes alignment.

The absorption spectrum for each axis is shown in Figure 2.2 (top), next to the spectrum found in literature Figure 2.2 (bottom) [72]. Comparing the two spectra, it can be observed that the locations and widths of the peaks are very similar, indicating good agreement with literature. Our spectra show a slightly weaker absorption, which may be attributed to slight differences in dopant concentration.

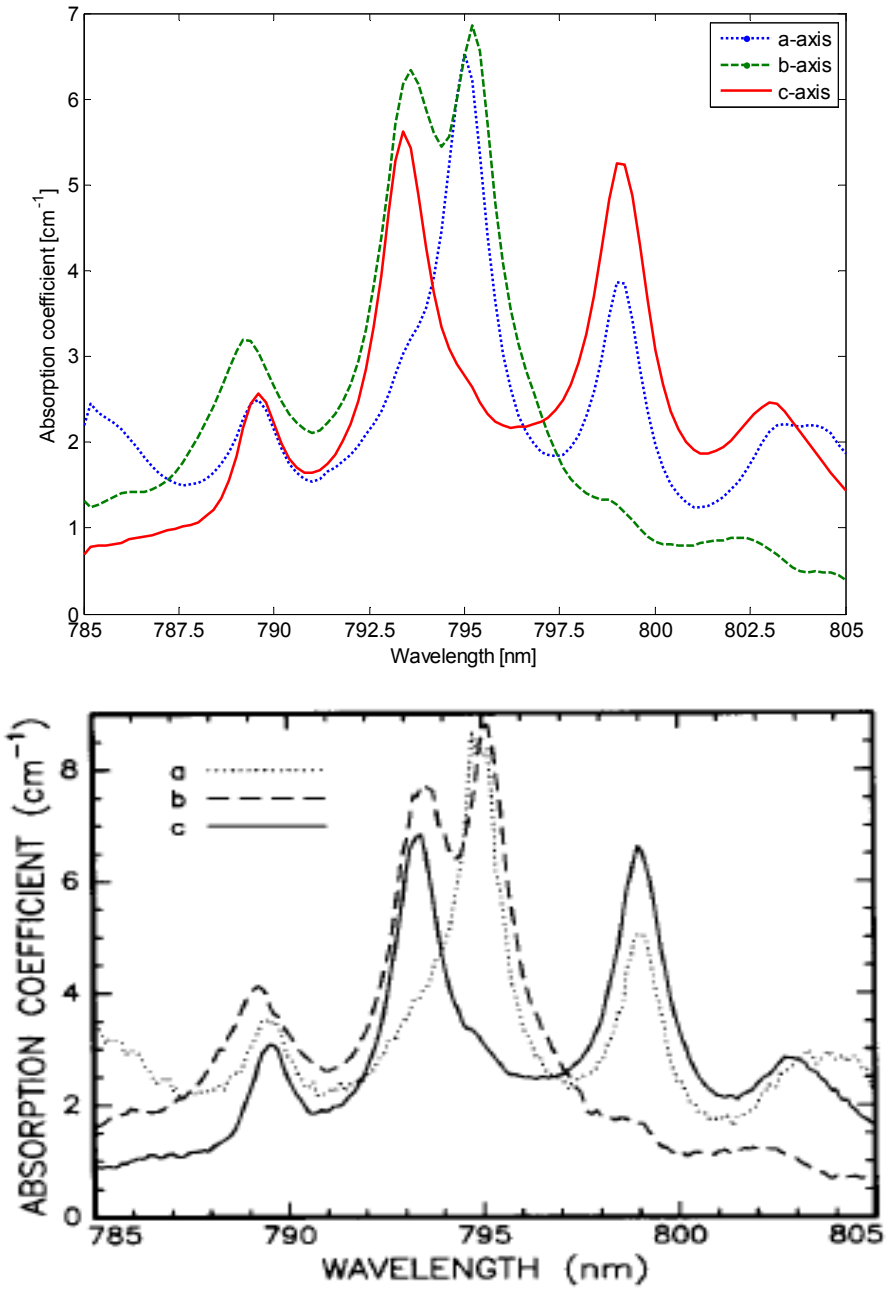

Figure 2.2: Measured absorption spectra for each axis from Tm:$YAlO_3$ sample (top), and absorption spectra from literature (bottom). Reprinted, with permission, from [72] © 1995 IEEE.

2.3 Initial cuboid laser

2.3.1 Laser design

The thulium-doped $YAlO_3$ cuboid was used as the gain medium for a simple end-pumped laser, as shown in Figure 2.3. The crystal was oriented such that the pump and laser beam propagated along the *a*-axis. Two water-cooled copper blocks were used to mount the crystal. A 125-μm layer of indium was sandwiched between the copper and the crystal to maximise thermal contact.

The cuboid was uncoated when it was used in the absorption measurements; however, the intra-cavity losses due to Fresnel reflections would equal approximately 10% per interface or 34.6% per round-trip, which would prevent lasing. The two surfaces on which the beams were incident were anti-reflective (AR) coated by Altechna Co. Ltd for both 790 nm and 1.94 μm, reducing the losses to 2% and < 0.5% for the two wavelengths respectively.

The pump source used was a fibre-coupled diode laser (LIMO35-F100-DL790), with an output fibre diameter of 100 μm and a numerical aperture (N.A.) of 0.22. The output was imaged into the centre of the Tm:$YAlO_3$ crystal to a 200 μm spot size within the crystal using 2× magnification coupling optics. The laser cavity consisted of a flat, high reflectivity (HR) back mirror (measured reflectivity > 99.5% at 1.94 μm and AR, reflectivity ~ 10% at 790 nm) and a flat, partially reflecting output coupler (measured reflectivity ~ 95% at 1.94 μm). The mirrors were placed as close to the crystal as possible to maximise the chance of lasing. The estimated separation between the mirrors and the crystal was 3 mm, giving a total cavity length of 10 mm. Since both mirrors were flat, the stability of the laser was achieved using thermal lensing, as explained below.

The laser output and the transmitted pump light were separated via a set of two dichroic mirrors, identical to that of the HR mirror described above. Two thermal power meters were used to measure the power of each beam.

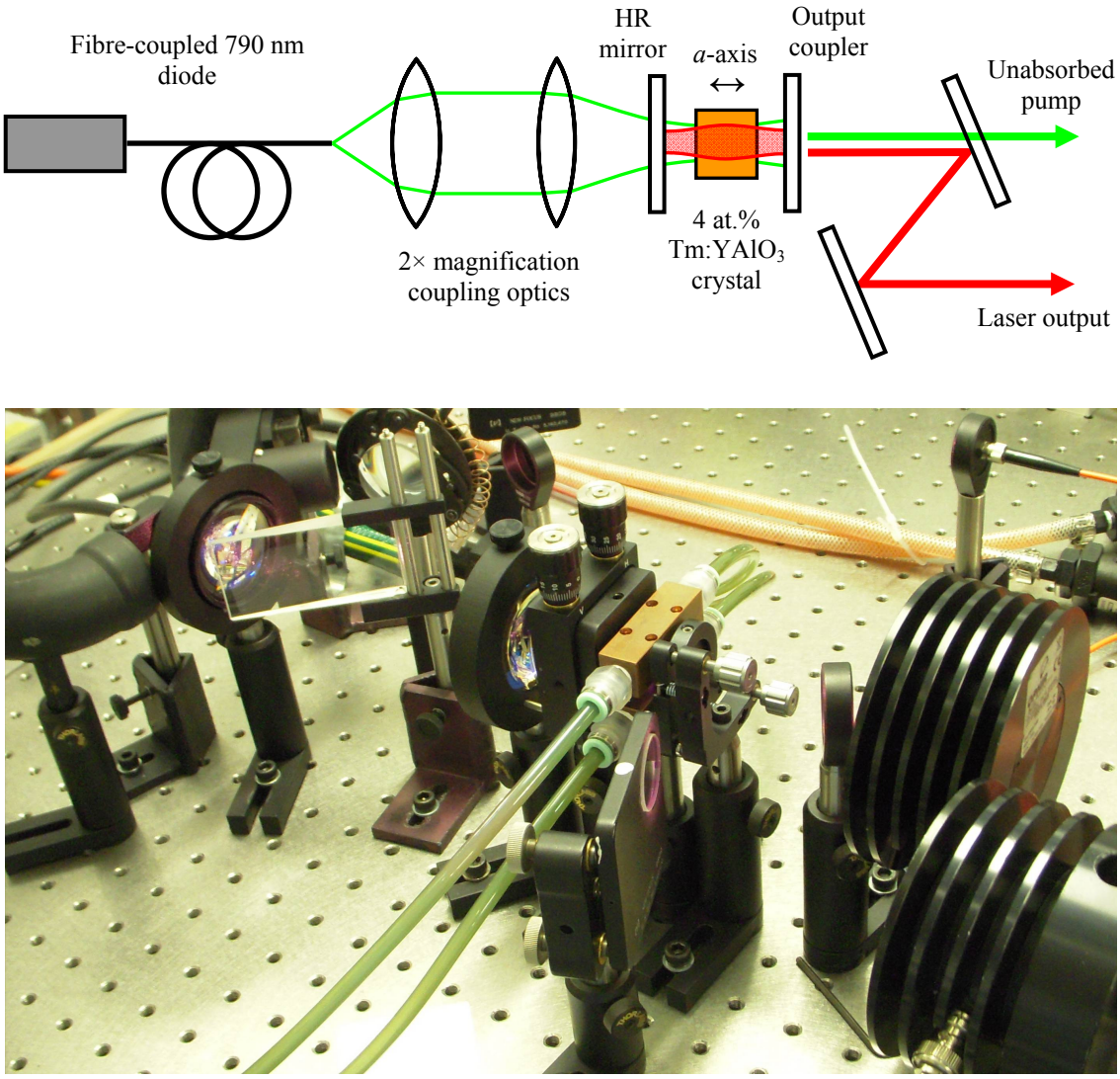

Figure 2.3: Schematic (top) and photo (bottom) of the initial Tm:$YAlO_3$ laser. The laser crystal is held within the copper cooling blocks.

2.3.1.1 Thermal lensing

When energy is deposited into a medium, such as from optical pumping, a portion of that energy is converted into heat. This localised heat is conducted through the medium and is eventually dissipated at interfaces, such as on the surfaces or into cooling blocks. The finite conduction rate causes temperature gradients to form throughout the medium. Temperature gradients lead to several changes in the properties of the medium. The most direct effect is to the refractive index of the medium, which is temperature-dependent. This is governed by the thermal coefficient of refractive index (dn/dT) of the material. A thermal gradient therefore translates directly into a refractive index gradient, altering the optical path length and potentially the direction of a ray passing

through the medium. Thermal gradients also induce mechanical stress in the medium due to differential expansion. Stress can induce a number of effects, which could include refractive index change [64], birefringence [118], depolarisation [119], and surface distortions such as bulging. Thermal effects can severely reduce the efficiency of a laser [118] and can ultimately lead to catastrophic failure (fracture) of the medium [75]. Thermal effects can be significant at even modest power levels, and it is therefore important to model the effects and design the laser accordingly to minimise detrimental effects.

The thermal effects on the cuboid due to pump absorption were modelled using finite element analysis (FEA) in COMSOL. In FEA modelling, the object is divided into triangular segments to form a 3-dimensional mesh. Thermomechanical equations, such as that for heat transfer and mechanical stress and strain, are solved for each segment based on boundary conditions and the nearest neighbours.

The pump source was approximated as a 200-μm diameter collimated beam with a top-hat transverse profile due to the highly multimode nature of the beam. For simplicity, the heat deposition was approximated to be uniform along the beam path within the crystal. Thus, heat deposition in the crystal was modelled as a uniform cylinder of 200 μm diameter and length 4.55 mm, situated in the middle of the crystal. The temperature was clamped to a reference point T = 0 K on the two surfaces perpendicular to the *z*-axis (*b*-axis of the crystal) to simulate water cooling via copper cooling blocks.

The resultant temperature distribution for 10 W of absorbed heat is shown in Figure 2.4. The temperature is highest at the centre, and decreases with increasing distance from the beam centre. Light that is polarised along the *c*-axis has a positive $\frac{dn}{dT}$, and hence this temperature profile results in a positive lens. This provides the focusing power needed to overcome diffraction, resulting in a stable laser cavity.

A gradient-index (GRIN) lens can be used to approximate the thermal lens, with a refractive index profile in the form $n(r) = n_0 - \frac{n_2}{2} r^2$. The temperature profile along the *z*-axis of the crystal was exported into Matlab, and a quadratic fit to the central 200-μm pumped region was made. The temperature profile in this region is approximated to be $T(r) = 128.5 - 1.423 \times 10^{-9} r^2$ as shown in Figure 2.5, corresponding to a radially-dependent refractive index coefficient of $n_2 = 41267$.

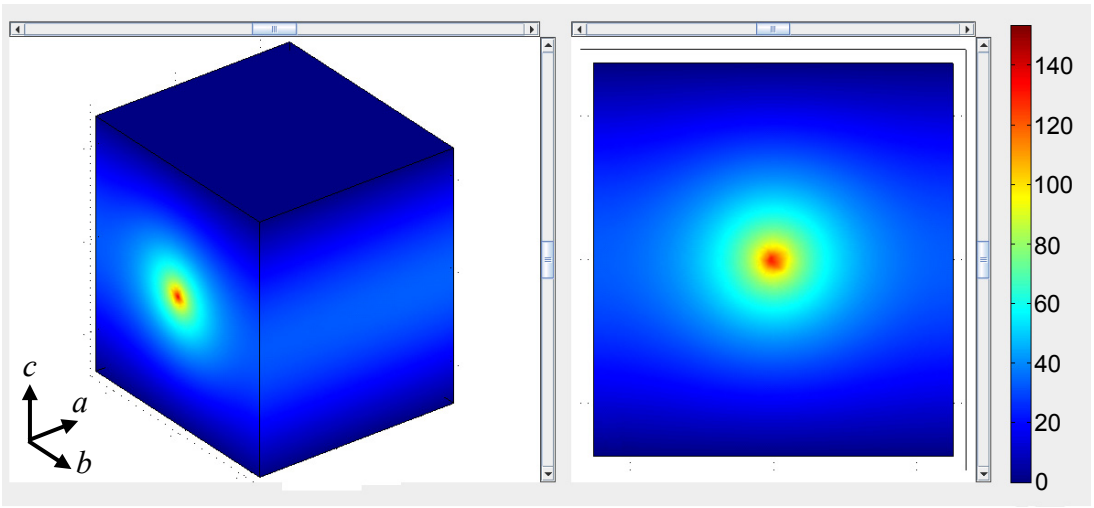

Figure 2.4: Temperature distribution for 10 W of total absorbed heat. Cooling is through the top and bottom surfaces.

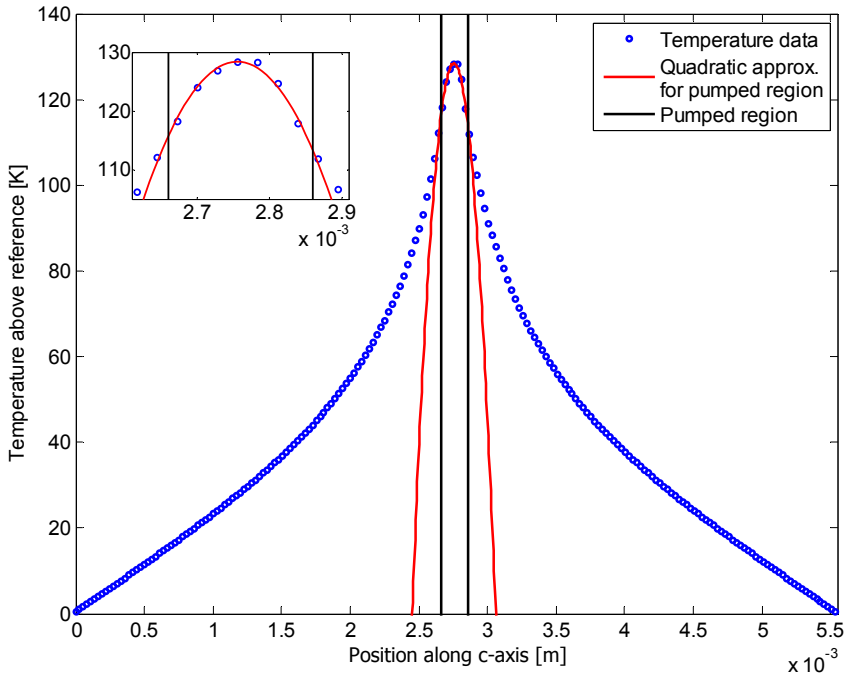

Figure 2.5: Calculated temperature profile in the vertical direction (z-axis) along the centre of the beam path (blue) and quadratic fit to the central pumped region (red).

2.3.1.2 Cavity mode modelling

A Gaussian beam propagation model, which can be found in Appendix C.1.3, was written from scratch using Matlab to work out the fundamental mode of the laser resonator. The matrices corresponding to each component [120] were multiplied together to form the overall matrix representing the system, and the eigenmode solution representing the self-consistent cavity mode was obtained.

A model of the fundamental laser mode within the cavity at two different heat depositions is shown in Figure 2.6. A GRIN lens was used to approximate the thermal lensing, as mentioned previously. A greater heat deposition results in a stronger thermal lens and hence a smaller fundamental mode. This will result in poorer laser beam quality due to the mode mismatch between the pump and the laser, which is discussed later in Section 2.3.3. Note that not all of the absorbed pump power results in heat, as much of the energy is radiated out as the laser output or fluorescence.

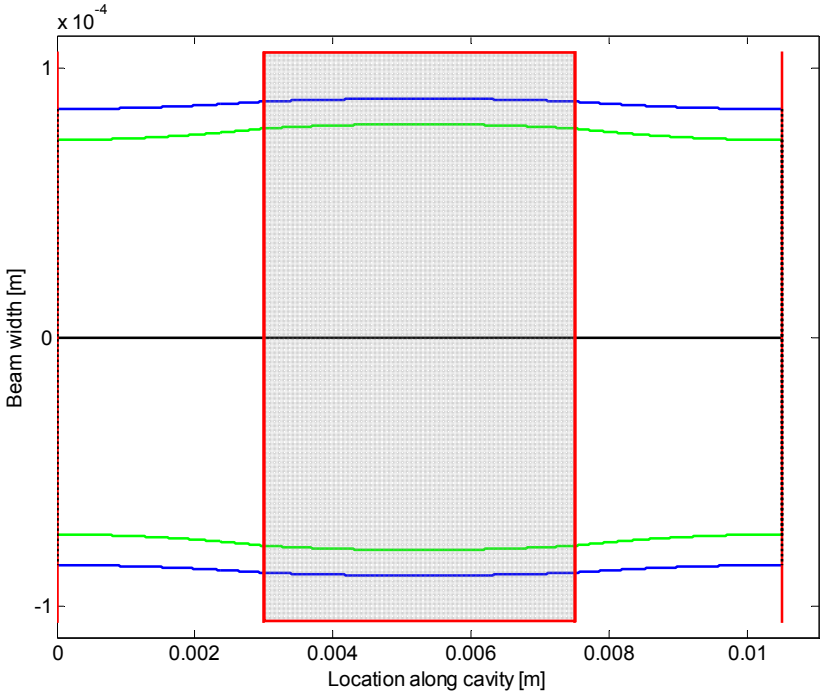

Figure 2.6: Fundamental cavity mode for 3 W (blue) and 5 W (green) total absorbed heat. The shaded area represents the crystal.

2.3.2 Laser operation

2.3.2.1 Output power

The laser output power was measured for different incident pump powers. A significant fraction of the pump power was not absorbed, leading to a low efficiency with incident pump power. This is due to the wavelength of the pump diode being too short, with a measured wavelength shorter than 788 nm when operated at the recommended temperature of 20ºC. At these wavelengths, total single-pass absorption was estimated to be 27%. Higher powers caused a red-shift in the emission wavelength, which increased the absorption up to 46% for 17 W of incident pump power. The chiller used to cool the pump diode fluctuated in temperature by ±3ºC. This corresponded to a wavelength variation of ±1 nm, resulting in significant variations in total absorption.

The red-shifting at higher powers and temperature fluctuations can be calibrated out by quantifying the absorbed power. The amount of transmitted pump light through the crystal was measured and used to calculate the single-pass absorption. The total double-passed pump absorption was then calculated using the measured reflectivity of

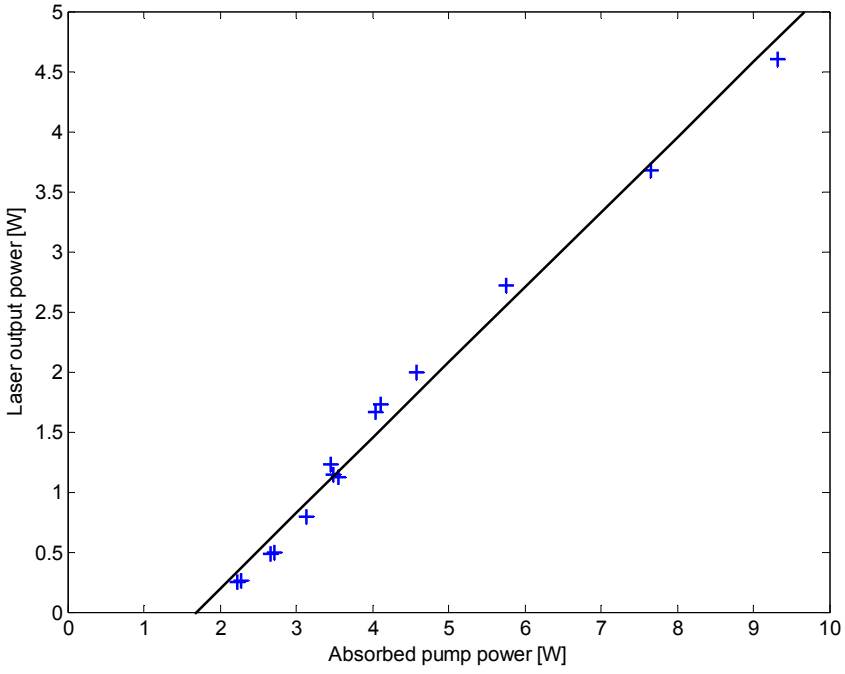

Figure 2.7: Laser output power versus total absorbed pump power, with 1.7 W threshold of and 62.5% slope efficiency.

the output coupler at the pump wavelength and the calculated absorption coefficient from the single-pass absorption.

The laser output power against absorbed power is plotted in Figure 2.7. The line of best fit for this plot gave a threshold of 1.7 W and a slope efficiency against absorbed power of 62.5%; both are comparable or better than the best published results [80], [102], [103].

2.3.2.2 Output spectrum

The output spectrum of the laser was measured using a 500-mm focal length spectrometer (Acton SP2500). A broad scan over the typical emission range of Tm:$YAlO_3$ lasers from 1.85 to 2 µm was first taken. Signal was observed only around 1.94 µm. A narrower sample output spectrum centred at 1.94 µm was obtained, as shown in Figure 2.8. A slit-width of 100 µm and a 600 lines/mm grating blazed at 1.6 µm was used in the spectrometer, which corresponds to a resolution of 0.2 nm at the 2 µm range. Averaging time was set to only 30 ms due to the strong signal. 10-point averaging was used, and the spectrum was averaged over 5 sweeps.

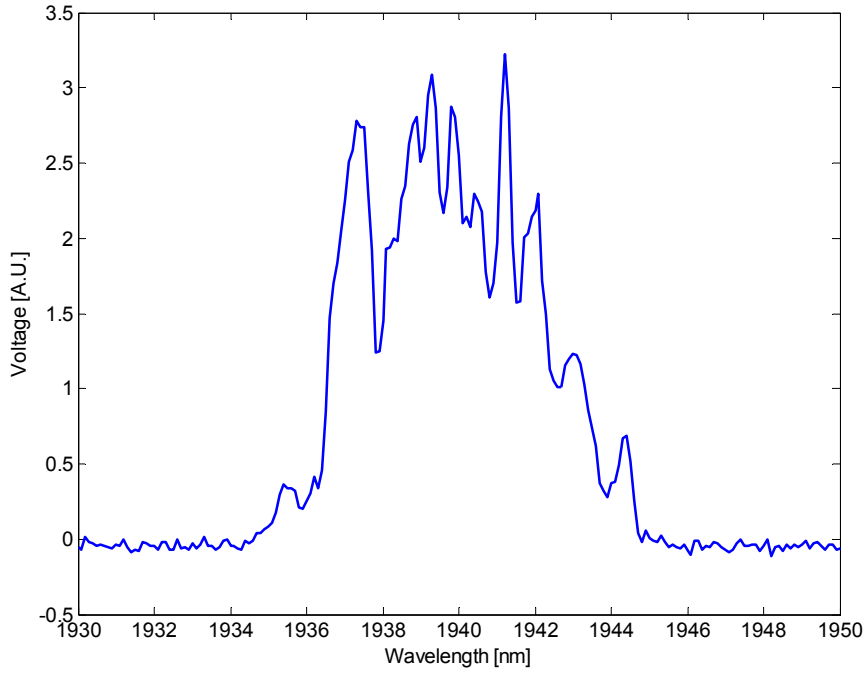

Figure 2.8: Output spectrum of the Tm:$YAlO_3$ laser averaged over several sweeps.

Emission solely at 1.94 μm indicates that lasing occurred only along the *c*-axis [72], as discussed in Section 1.3.2. The biaxial nature of Tm:$YAlO_3$ leads to a distinct gain profile for each axis. The laser was free-running, and therefore the output wavelength was determined by the peaks of the gain spectra. The propagation direction of the pump and laser beams was parallel to the *a*-axis and thus lasing was only possible for light polarised parallel to the *b*- and *c*-axes, which have gain peaks at 1.88 μm and 1.94 μm respectively [72]. The absence of any emission at 1.88 μm indicates lasing along the *c*-axis was preferred over the *b*-axis. This is not surprising, since there is a lower emission cross-section and higher reabsorption loss at 1.88 μm [72]. Thermal lensing also results in higher losses for light polarised along the *b*-axis, and is explained in the next section.

2.3.2.3 Polarisation

A wire-grid polariser with an extinction ratio of >1500 was used to verify the Tm:$YAlO_3$ cuboid laser was linearly polarised. The output was observed to have minimal loss when the polariser was aligned along the *c*-axis of the crystal. The output was extinguished to within noise level when the polariser was aligned along the *b*-axis. This is consistent with the output spectrum of the laser.

As mentioned earlier, this inherent polarisation along the *c*-axis is primarily due to its higher emission cross-section and lower reabsorption. In addition, lasing along the *b*-axis is unstable due to the thermal lensing. For light polarised along the *c*-axis, $\frac{dn}{dT}$ is positive [71] and hence a positive thermal lens is formed for light travelling through the centre of the crystal. The light is focused by the thermal lens and a stable mode is established within the flat-flat cavity. On the other hand, $\frac{dn}{dT}$ is negative for light polarised along the *b*-axis [74] and thus forms a negative thermal lens. This diverges the light and the mode within the cavity is unstable. This results in higher losses and thus the laser preferentially operates in the polarisation parallel to the *c*-axis. Note that this type of discrimination between the *a*- and *c*-axes does not occur as $\frac{dn}{dT}$ is also positive for the *a*-axis.

2.3.3 Beam quality

The beam quality of the output beam was determined by measuring the beam parameter product. This was then used to calculate the M^2 of the beam, defined in Section 1.2 as the ratio of the beam parameter product to that of a perfect Gaussian beam:

$$M^2 = \frac{\omega_0 \theta \pi}{\lambda}, \tag{2.1}$$

where ω_0 is the beam waist of an ideal Gaussian beam and θ is the far-field divergence angle. For a perfect TEM_{00} Gaussian beam, $M^2 = 1$. The equation for the radius of a Gaussian beam, $\omega^2(z) = \omega_0{}^2\left(1 + z/z_R\right)^2$ [120], can be rearranged to be a function of ω_0 and θ:

$$\omega^2(z) = \omega_0{}^2 + \theta^2 (z - z_0)^2, \tag{2.2}$$

where z_0 is the distance of the beam waist from an arbitrary zero point. The beam waist and far-field divergence angles can be obtained by fitting a curve to the beam widths sampled at different points along the beam, giving the beam parameter product.

To measure the beam quality, the output beam was allowed to diverge and then focused using an f = 100 mm lens. The beam profiles were measured at various distances from the lens using a pyroelectric array camera (Spiracon Pyrocam III). The beam profiles were analysed using Matlab. The analysis code, written from scratch, can be found in Appendix C.1.4 and works as follows:

1. Comma-delimited files containing the beam profiles at each of the sample locations are read;
2. The centre of each beam profile is located;
3. Gaussian functions are fitted to each beam profile using the curve fitting tool, either as two Gaussian functions along the x- and y- axes, or a 2-dimensional Gaussian;
4. The beam widths along each axis are obtained for each sample location, and;
5. The beam widths are fitted to Equation 2.2 using the curve fitting tool to obtain the waist size and θ, and hence M^2.

The M^2 was measured at different output powers, with the results shown in Figure 2.9. A sample near-field beam profile at 2 W output power shown in Figure 2.10. At 2 W of output power, the laser operates with an M^2 of 6–7. The beam quality degrades with higher power, with the M^2 increasing to up to 9 for 4 watts of output power.

The poorer beam quality at higher powers is likely due to the size difference between the fundamental Gaussian mode and the pumped region. The fundamental mode, which is defined by the cavity optics, extracts maximum gain from the gain medium; however, pumped regions of the gain medium outside that of the fundamental mode result in residual gain for higher order modes, which reduces the beam quality. Although the pumped region is unchanged at higher powers, the size of the fundamental mode changes due to the thermal lensing in the crystal. Thermal lensing

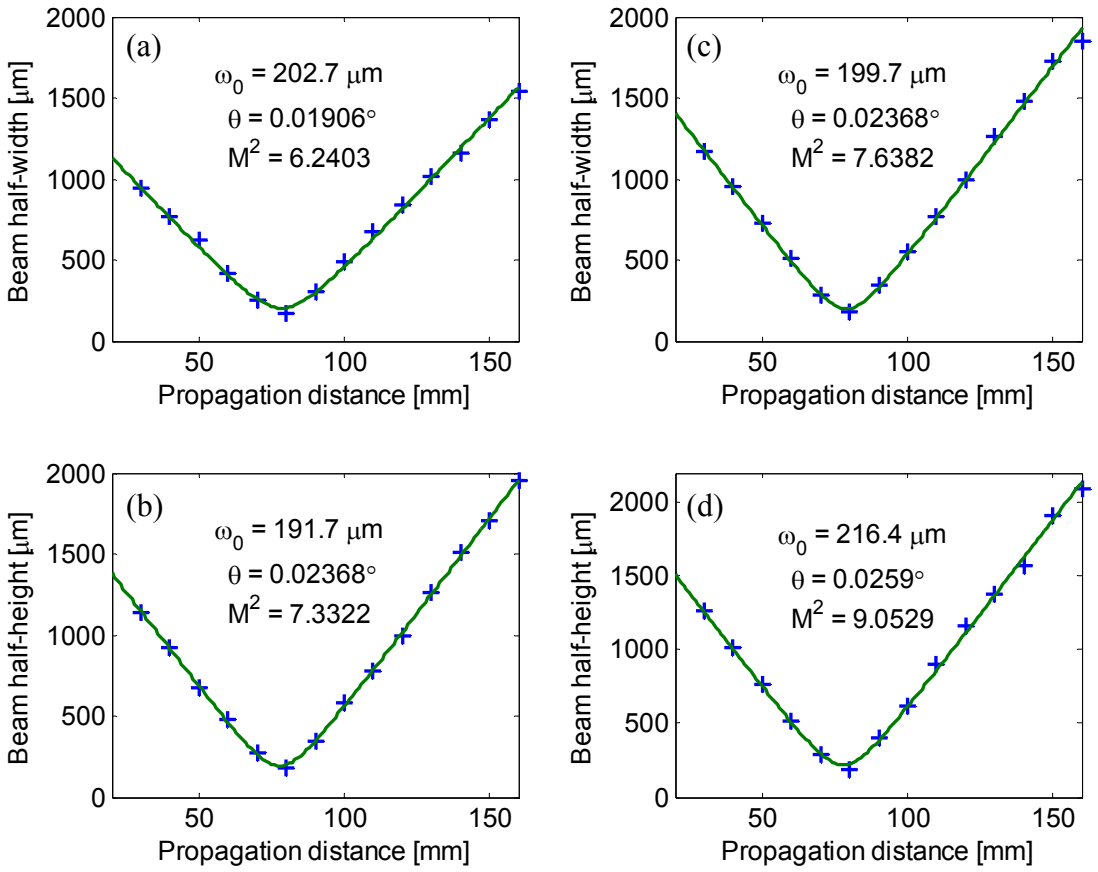

Figure 2.9: Beam quality measurement in the horizontal (a,c) and vertical (b,d) directions for the laser operating at an output power of 2 W (a,b) and 4 W(c,d).

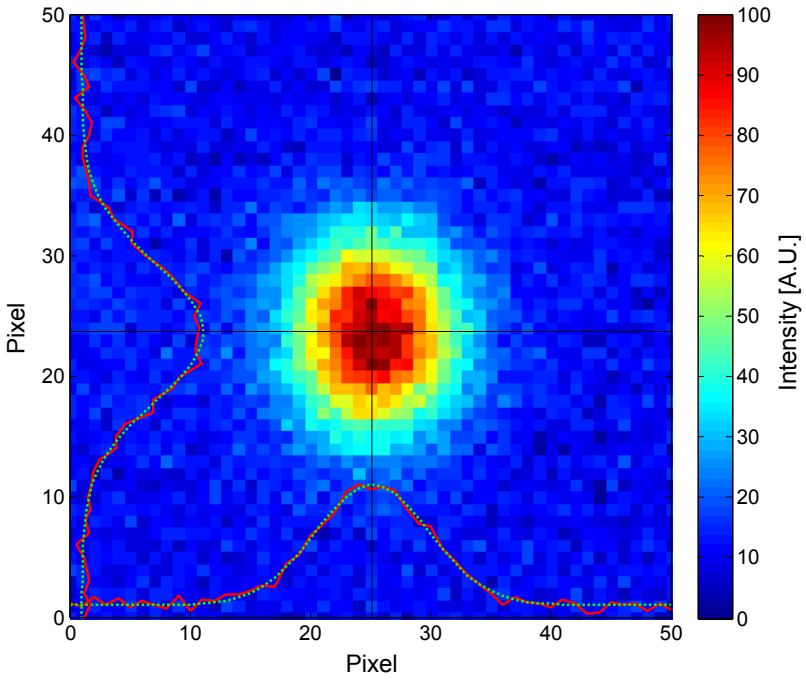

Figure 2.10: Sample near-field beam profile at 2 W output power.

acts to focus the beam (for $\frac{dn}{dT} > 0$), and thus a stronger thermal lens will focus the light harder and reduce the fundamental mode size, as shown in Figure 2.6. The mode size mismatch subsequently reduces the beam quality. The effect can be quite significant when the laser mode is defined primarily by the thermal lens, as evident in the 25% increase in M^2 for the two power levels.

A possible explanation for the slightly poorer beam quality in the vertical direction is the thermal gradient from cooling. As the cooling is applied on the top and bottom surfaces, the thermal gradient along the vertical direction is slightly stronger. This causes a smaller mode size, and hence a greater mismatch between the pump beam and the laser mode and thus a slightly poorer beam quality. The temperature distribution of the crystal at 10 W absorbed heat can be seen in Figure 2.4.

2.3.4 Temporal properties

The temporal output of the Tm:$YAlO_3$ laser was measured using an extended InGaAs detector (Thorlabs DET10D), and is shown in Figure 2.11. Strong self-pulsing dominated the laser output, to the point where no lasing occurred between pulses, and CW operation never occurred.

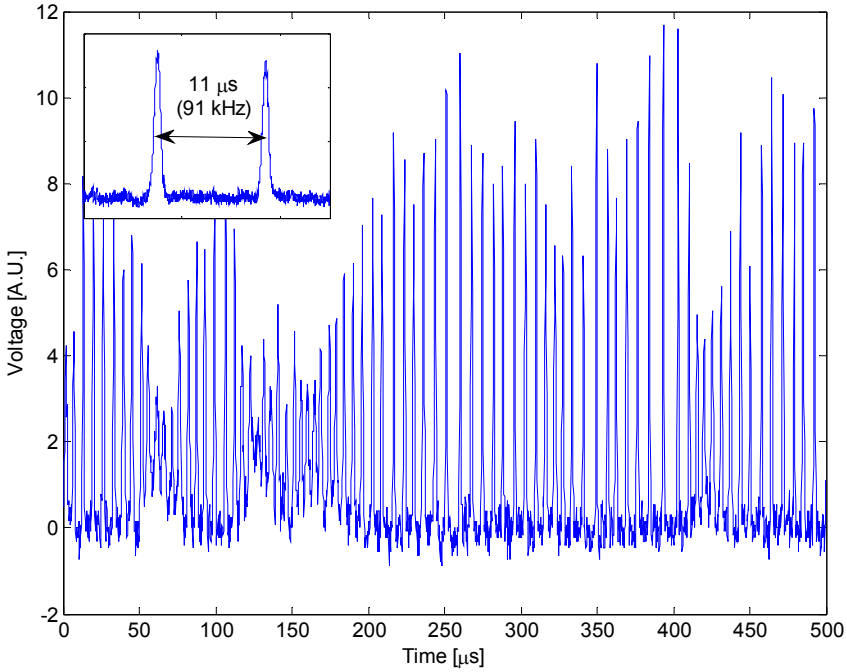

Figure 2.11: Temporal output of the Tm:$YAlO_3$ laser at 500 mW output power, and a high-resolution trace showing the typical pulse separation (inset).

Such strong and erratic pulsing is undesirable for CW pumping, as it could cause unstable gain-switching of the holmium-doped fibre laser, as well as risking damage due to the high peak power.

Pulse suppression using current feedback to the pump diode was attempted to suppress the self-pulsing. Due to the significant modulation depth, fast, high-current electronics (current output up to ±1 A, corresponding to a change in pump power of > 1 W) was used. The bandwidth of the electronics was limited to 140 kHz as a result. However, the pulse repetition frequency (PRF) of the laser at even modest powers rapidly exceeded the bandwidth of the electronics. To achieve suppression at all operating powers, the laser cavity needed to be lengthened to increase the photon cavity lifetime, thus slowing the laser dynamics and reducing the self-pulsing oscillation frequency. The extension of the cavity length is described later in Section 2.4.

2.3.4.1 Water Vapour as a Saturable Absorber

J. Šulc *et al.* [81] have suggested that the self-pulsing may be caused by intra-cavity saturable absorption by water vapour, absorbing at the lasing wavelength [83]. This possibility was investigated by examining the pulsing dynamics at different pump powers and atmospheric water vapour content.

The concentration of water vapour, either trapped within the crystal or in the air within the resonator, is fixed, assuming a stable ambient environment over the observed period. Subsequently, the energy required for it to saturate is also fixed. This means that transparency of the saturable absorber occurs when a fixed amount of intra-cavity laser energy is absorbed, which is proportional to the gain of the system. A laser pulse occurs whenever the intra-cavity gain reaches this fixed level, independent the gain build-up time (i.e. pump power). This sets the laser photon build-up time, which in turn defines the pulse width. Thus, in order for the oscillations to be due to a saturable absorber, the pulse widths must be independent of pump power for a given laser configuration.

When the output power was varied, both the typical pulse width and the time between pulses were found to decrease with increasing pump power at approximately the same rate, as shown in Figure 2.12. This observation is contrary to that predicted by passive Q-switching of a saturable absorber.

The water vapour content within the resonator was varied by enclosing the entire laser in a large box, then filling the box with dry nitrogen gas to expel water vapour. By lowering the number of water molecules within the cavity, the amount of saturable

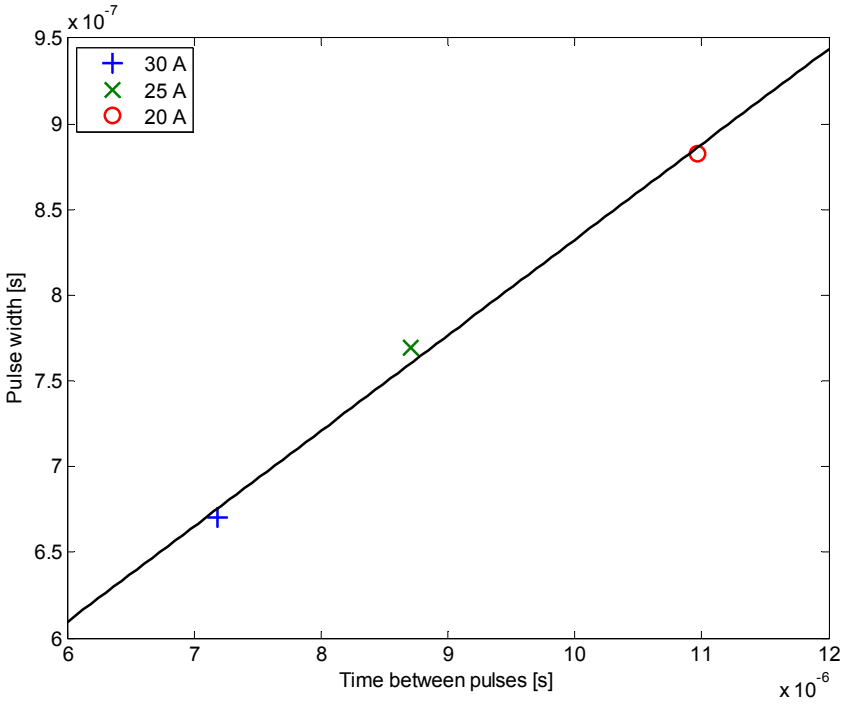

Figure 2.12: Typical laser pulse width and pulse separation for different pump diode input currents.

absorption and hence energy required for transparency should decrease. This lowers the required gain per pulse, and should both increase the PRF as well as reduce the laser pulse build-up time. The result should be more frequent but weaker pulses with lower peak power.

This was quantified by measuring the root mean square (RMS) of the detector signal with AC coupling. The humidity level within the box was monitored using an off-the-shelf humidity sensor. As the humidity decreased from 49% to 22%, the RMS of the signal did not decrease as predicted, again contradicting this theory.

Based on these observations, it was concluded that water vapour acting as a saturable absorber was not the cause of the self-pulsation.

2.4 Cuboid laser Mk-II

2.4.1 Laser design

The cavity length was extended using an $f = 43$ mm lens, as shown in Figure 2.13. This lens also acted as a thermal lens compensator and ensured stability. The laser resonator was extended to 210 mm. To increase the absorption by the crystal, the pump diode was red-shifted by operating at 30ºC. This increased the total absorption to 60%. The remaining laser components were unchanged. A photodetector (PD) was used to observe pulsing and as the sensor for pulse suppression, which is mentioned later.

As the pumping configuration was unchanged, the spatial distribution of the heat deposition into the crystal for this laser is the same as that of the initial cuboid laser. Thus, the same thermal modelling can be used to estimate the thermal effects in this laser.

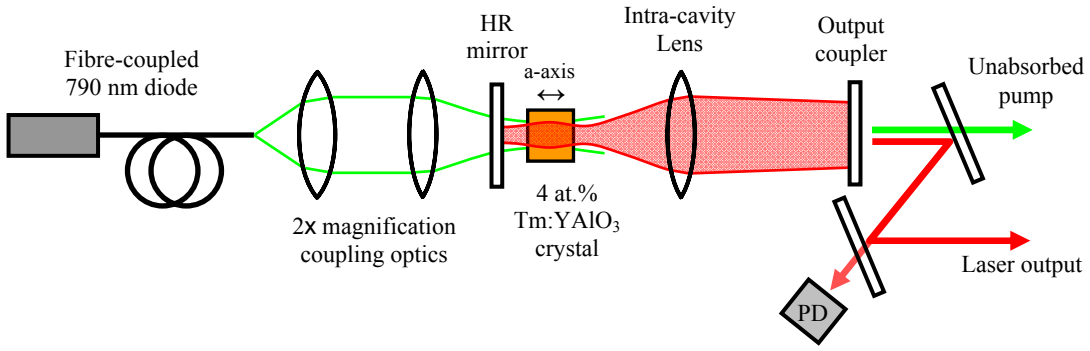

Figure 2.13: Schematic of the modified Tm:$YAlO_3$ laser Mk-II.

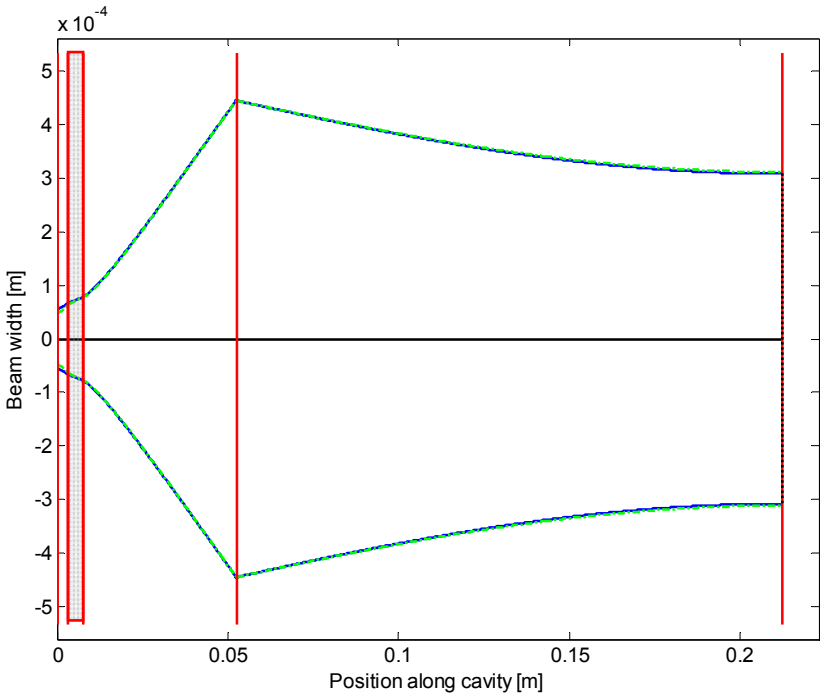

Figure 2.14: Fundamental cavity mode for 3 W (blue) and 5 W (green) total absorbed heat. The shaded area represents the crystal.

A model of the fundamental laser mode within the resonator, again at 3 W and 5 W of absorbed heat, is shown in Figure 2.14. In contrast to the fundamental laser mode in the initial cuboid laser, the mode is almost unchanged for the two thermal lenses. This is due to the intra-cavity lens being the dominant focusing element in the cavity, and thus is the major factor determining the fundamental mode.

2.4.2 Laser operation

The output power, spectrum and beam quality of the Tm:$YAlO_3$ cuboid laser Mk-II were measured using the same method as used for the initial cuboid laser.

The plot of laser output power against the absorbed power is shown in Figure 2.15. The power absorbed was calculated using the same method as described in Section 2.3.2.1. The line of best fit for this plot gave a threshold of 1.8 W and a slope efficiency of 56% for absorbed power (31% for incident power).

The output spectrum of the laser was measured using an optical spectrum analyser (OSA) (Yokogawa AQ6375). This Tm:$YAlO_3$ laser also only emitted light at 1.94 μm. The laser emission spectrum is shown in Figure 2.16.

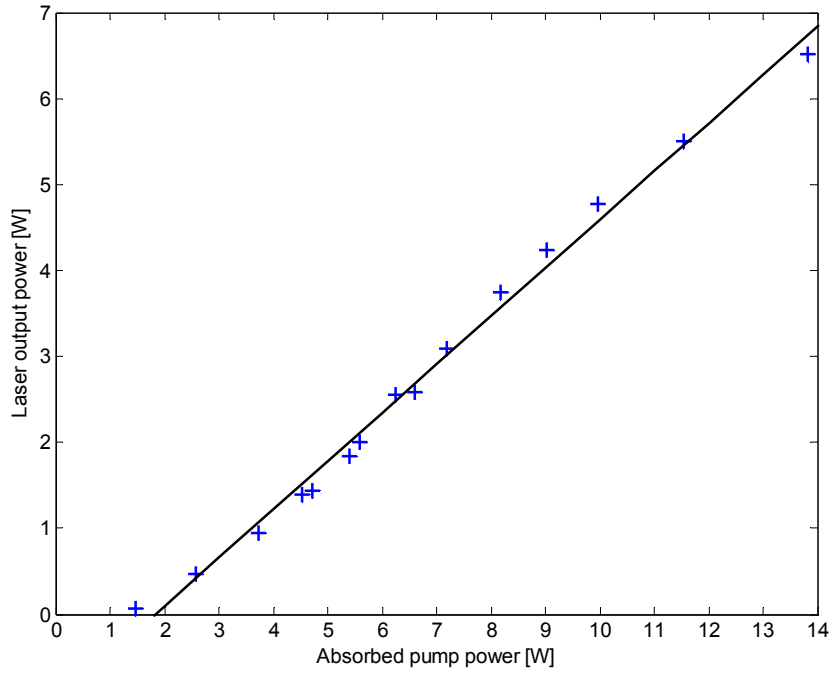

Figure 2.15: Laser output power versus total absorbed pump power, with 1.8 W threshold of and 56% slope efficiency.

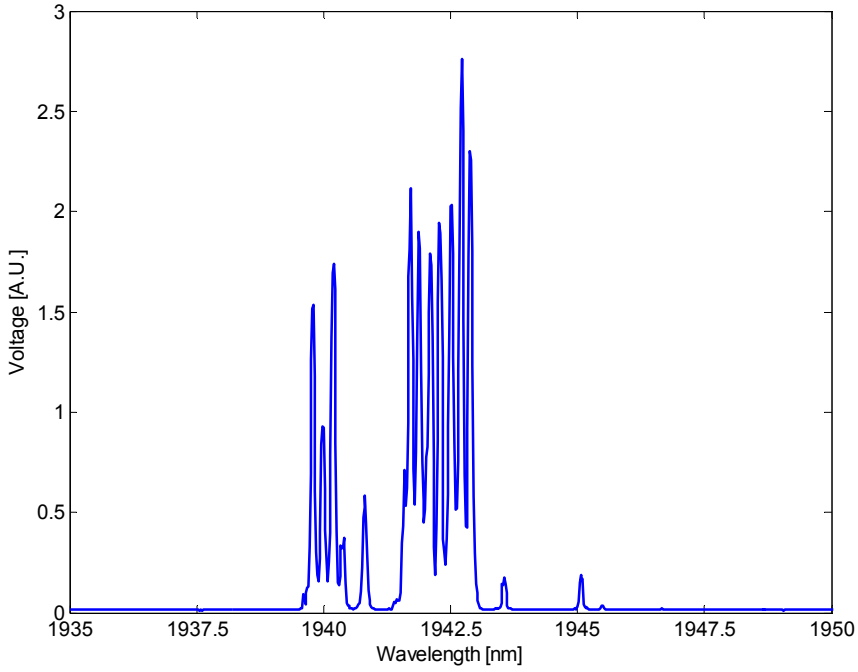

Figure 2.16: A sample output spectrum of the Tm:$YAlO_3$ laser Mk-II.

2.4.3 Beam quality

The M^2 was measured at different output powers, with the results shown in Figure 2.17, with a sample near-field beam profile at 4 W output power shown in Figure 2.18. The beam quality of the laser is significantly better than that for the initial laser. The beam quality also remains approximately constant, with an $M^2 \sim 4$ to 4.5 for both 2 W and 4 W output. This is most likely due to the intra-cavity lens dominating the thermal lens and acting as the cavity-defining element.

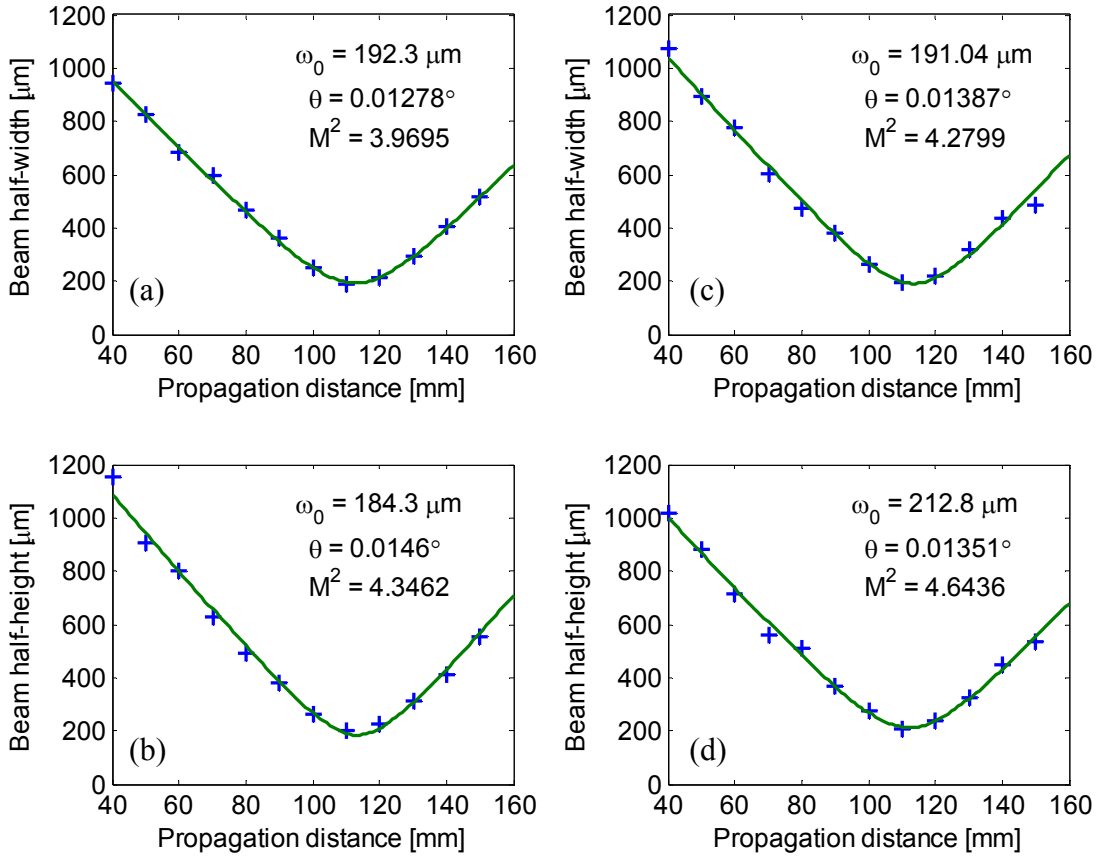

Figure 2.17: Beam quality measurement for the Tm:$YAlO_3$ laser Mk-II operating at an output power of 2 W (a)-(b) and 4 W(c)-(d).

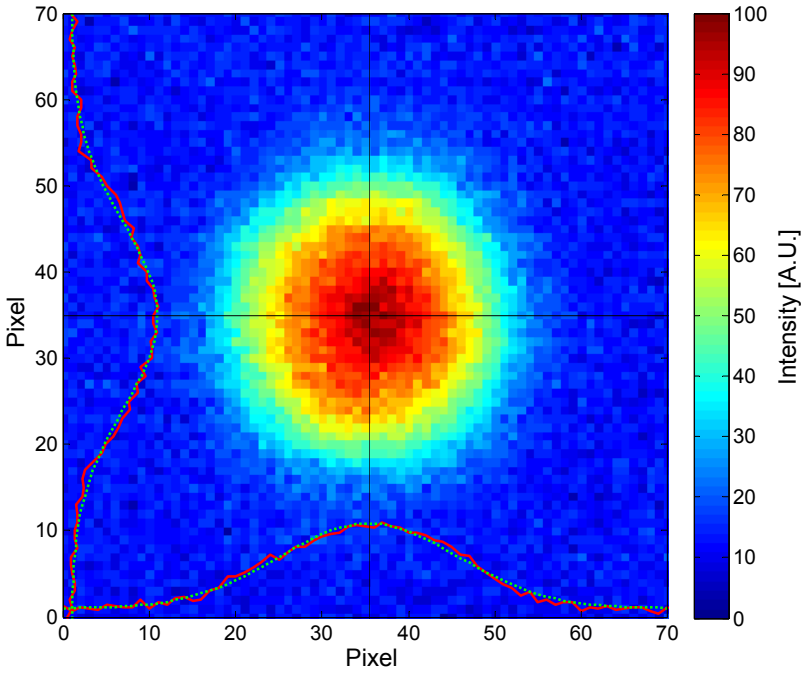

Figure 2.18: Sample near-field beam profile at 4 W output power.

2.4.4 Temporal properties

The temporal output of the cuboid laser Mk-II was observed using the same InGaAs detector as before. Significant self-pulsing of the laser output was observed, but with a lower oscillation frequency as expected, due to the longer cavity length. At low power, an exponentially increasing envelope of the oscillations can be observed, as shown in Figure 2.19 and in higher resolution in Figure 2.20, where an exponential fit to the envelope is also included. This behaviour was also observed for the initial cuboid laser in Figure 2.11, but it is much more obvious for this laser resonator. This may be due to gain competition between more transverse modes in the initial cuboid laser leading to a greater level of instability. However further investigation is required to confirm this.

The pulsing behaviour may also be the result of chaos within the laser, as the exponential increase in amplitude with time is very similar to the output from a NH_3 laser, well-known for its Lorenz-type chaos behaviour [87], [88]. An analysis of the laser as a chaotic system is described in Chapter 4.

The cause of the erratic termination of the oscillations is unknown; however external perturbations and vibrational noise, such as from the water cooled crystal holder, or optical noise from the pump diode may be contributing factors.

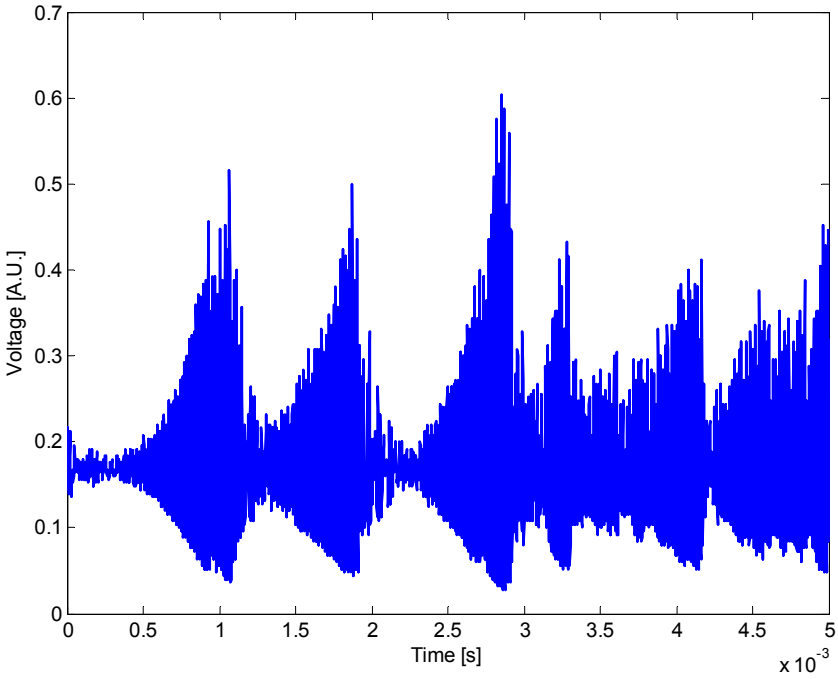

Figure 2.19: Temporal output of the Tm:$YAlO_3$ laser Mk-II at 1 W output power.

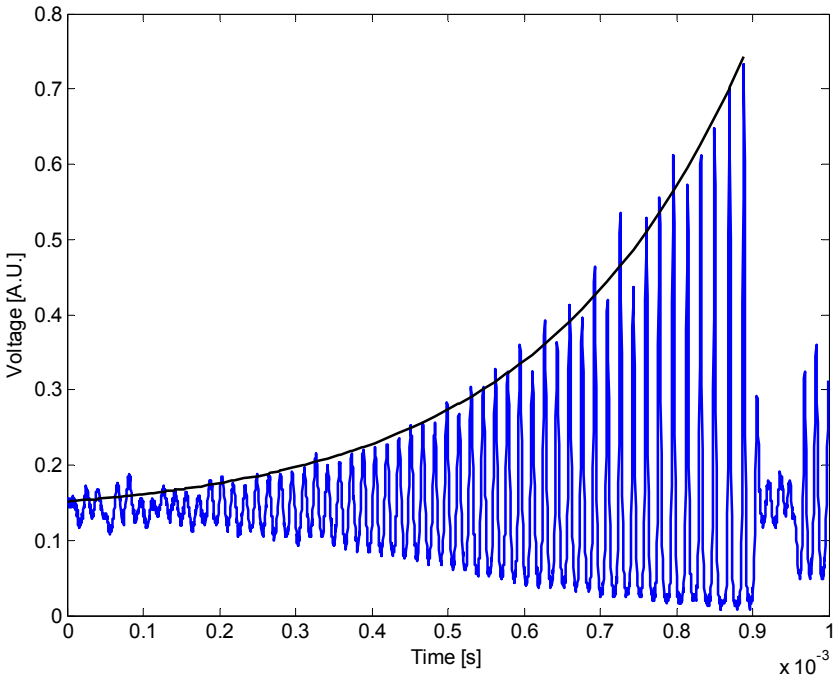

Figure 2.20: High temporal resolution trace of one output 'burst' with an exponential fit to the pulse peaks.

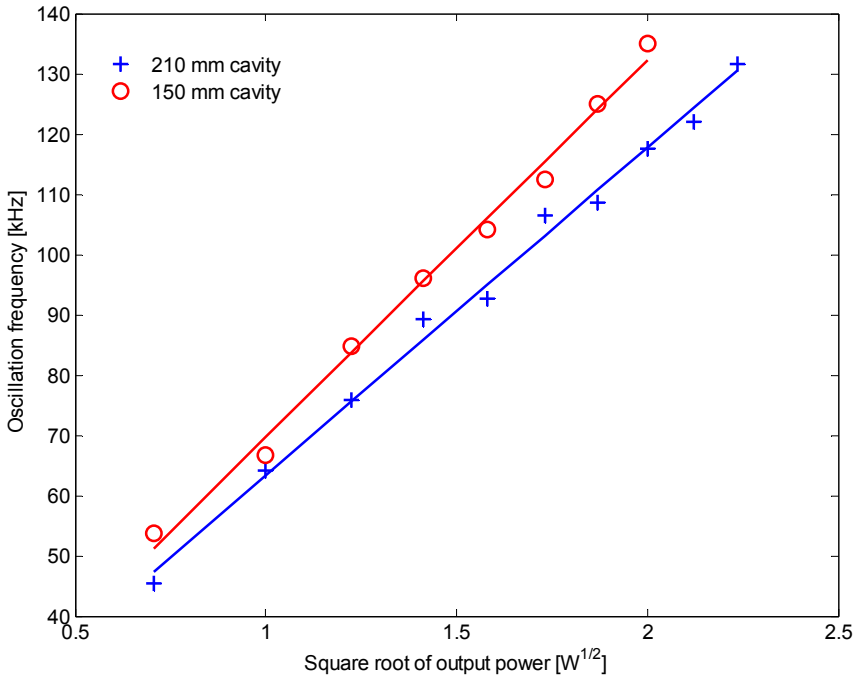

Figure 2.21: Dependence of oscillation frequency on output power for two different cavity lengths.

The exponential nature of the envelope suggests a possible explanation for the oscillations is a negatively damped relaxation oscillation in the laser gain medium. To test this hypothesis, the oscillation frequency of the laser was measured at different output powers for the two different laser cavity lengths. A linear relation between the oscillation frequency and the square root of the output power could be observed in both cases, as shown in Figure 2.21. This is consistent with the oscillations being relaxation oscillations [54]. This oscillatory behaviour will be explored in more detail in the following chapters.

2.5 Feedback control system

Feedback via gain modulation was chosen in an attempt to suppress the self-pulsing of the Tm:$YAlO_3$ laser. To accomplish this, a small fraction of the laser output was directed onto a photodetector (shown in Figure 2.13). The signal from the photodetector was amplified electronically, and then used to control the laser system by varying the current that drives the pump diode.

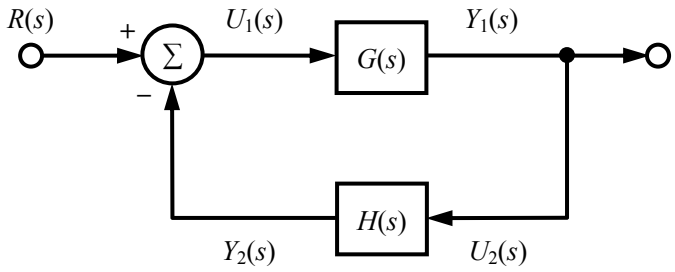

Figure 2.22: Block diagram of a system with negative feedback.

The laser system was modelled as a dynamic system using standard control theory [121]. Each component of the system was represented in a block diagram by its transfer function, and the dynamic response of the system was analysed in the frequency domain. Figure 2.22 shows the block diagram of a system with negative feedback [121]. The transfer functions $G(s)$ and $H(s)$ represent the laser and the feedback system respectively, while $R(s)$ and $Y_1(s)$ are the input (DC pump signal with noise) and laser output respectively.

By rearranging and reducing the equations of the system, $Y_1(s)$ relates to $R(s)$ by:

$$Y_1(s) = \frac{G(s)}{1 + G(s)H(s)} R(s) . \tag{2.3}$$

This equation gives the overall transfer function of the system, allowing for the analysis of the laser system under a closed-loop condition. The temporal output of the laser can be obtained by taking the inverse Laplace transform of $Y_1(s)$.

2.5.1 Simple model of the laser transfer function

The laser was modelled as a series of transfer functions to investigate the effectiveness of a feedback system for self-pulsing suppression. In the model, the operation of the laser was represented by three main processes:

1. Conversion of electrical current into optical power by the pump diode;
2. Excitation of Tm^{3+} ions to the upper lasing level in the gain medium, via the absorption of pump photons and subsequent cross-relaxation; and,
3. The lasing process.

Assuming the pump diode is operating above threshold, the output power of the diode is related to the input current by the slope efficiency of the pump diode. This occurs on a time scale much shorter than the feedback system and hence the transfer function of this process can be approximated to be a constant:

$$G_1(s) = A_1 . \tag{2.4}$$

Similarly, the absorption of pump photons by the gain medium is also a near-instantaneous process dependent on the absorption efficiency, and hence also has a transfer function independent of frequency.

The decay of a pumped ion to the upper lasing level is not instantaneous and in the case of thulium, corresponds to the cross-relaxation rate into the upper lasing level ($^3H_4 + {}^3H_6 \rightarrow {}^3F_4 + {}^3F_4$). While gradual changes in the pump power will translate directly to a proportional change in upper state ions, fast changes on the order of or faster than the cross-relaxation time constant will result in a smaller change in the upper state ion population as well as a time (phase) delay. This is analogous to a low-pass filter in electronics, and thus this process can be modelled using the same transfer function:

$$G_2(s) = \frac{A_2 \omega_{CR}}{s + \omega_{CR}} , \tag{2.5}$$

where A_2 is a constant corresponding to the absorption efficiency, and $\omega_{CR} = 2\pi / \tau_{CR}$ and τ_{CR} is the cross relaxation time constant.

The self-pulsing behaviour in the Tm:$YAlO_3$ output can be modelled as a relaxation oscillation due to its regular pulsing frequency and exponential envelope. The transfer function for a relaxation oscillation has the form:

$$G_3(s) = \frac{{\omega_v}^2}{s^2 + 2\zeta\omega_v s + {\omega_v}^2} , \tag{2.6}$$

where ω_v and ζ are the natural angular frequency and damping constant of the relaxation oscillation respectively.

The transfer function of the laser is thus the product of the three transfer functions:

$$G(s) = G_{DC} \cdot \frac{\omega_{CR}}{s + \omega_{CR}} \cdot \frac{{\omega_v}^2}{s^2 + 2\zeta\omega_v s + {\omega_v}^2}, \tag{2.7}$$

where $G_{DC} = A_1 A_2$ is the DC (low frequency) gain of the laser.

2.5.2 Modelling of a proportional feedback system

The laser system was modelled in Matlab with Simulink. Simple proportional feedback was tried on the laser system to suppress the self-pulsing, as shown in Figure 2.23.

The laser transfer function, $G(s)$, is that from Equation 2.7, while the transfer function of the feedback loop, $H(s)$, consists of a transport delay, a high-pass filter to eliminate DC feedback, and a gain factor:

$$H(s) = G_{feedback} \cdot \frac{s}{s + \omega_{FB}} \cdot e^{-s\tau_{delay}}. \tag{2.8}$$

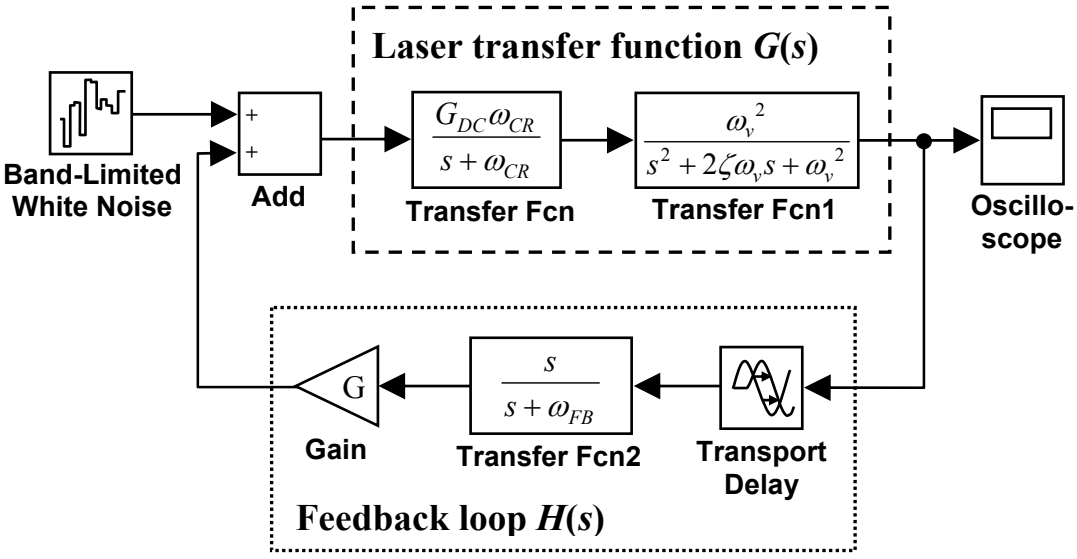

Figure 2.23: Schematic of the laser system with proportional feedback used in Simulink.

Parameter	Description	Value
G_{DC}	DC gain	1
τ_{CR}	Cross-relaxation lifetime [122]	3 μs
ω_v	Angular frequency of the relaxation oscillation	$2\pi \cdot 100$ kHz
ζ	Damping constant of the relaxation oscillation	–0.01
τ_{delay}	Measured transport delay	1 μs
ω_{FB}	Angular frequency of the high-pass filter	$2\pi \cdot 3$ kHz
$G_{feedback}$	Feedback gain (open loop)	0
	(closed loop)	–0.1

Table 2.1: Parameters for the proportional feedback modelling.

Bandwidth-limited white noise is used to introduce noise into the system as a seed. Values for the modelling parameters, taken from experimental observations and literature, and are tabulated in Table 2.1. The transport delay was obtained by comparing the lag between an injected signal and the output of the feedback loop.

Under open loop operation, the small signal at the resonance frequency from the white noise is amplified exponentially with time, as shown in Figure 2.24. The exponentially growing signal is the result of the negative damping constant, ζ, which is characteristic of an unstable oscillator [123]. A bode plot of the open loop transfer function is shown in Figure 2.25. The phase lead of approximately 180º accompanying the relaxation oscillation resonance peak, rather than a phase lag, is a characteristic of oscillations with a negative damping constant. This is because the sign of the phase shift in the frequency domain is opposite that of the damping constant.

Disregarding the unphysical negative values from the simulated output in Figure 2.24, the exponential growth of the modelled laser output is comparable to that of a single "burst" in the laser output, such as those shown in Figure 2.20.

For closed loop operation, this simulation shows that the output no longer grows exponentially, but instead decays to a steady state as shown in Figure 2.26. A greater values of $G_{feedback}$ results in a more rapid decay rate, and vice versa. A phase lag across the resonance peak can be observed in the bode plot of the closed loop transfer function, shown in Figure 2.27, which is characteristic of a damped second-order oscillator. For completeness, the bode plot of the feedback section $H(s)$ and the loop transfer function $G(s)H(s)$ for this simulation are also shown in Figure 2.28 and Figure 2.29 respectively.

Thus, the model predicts that simple proportional feedback would be sufficient to suppress the self-pulsing, assuming a feedback gain greater than some threshold value.

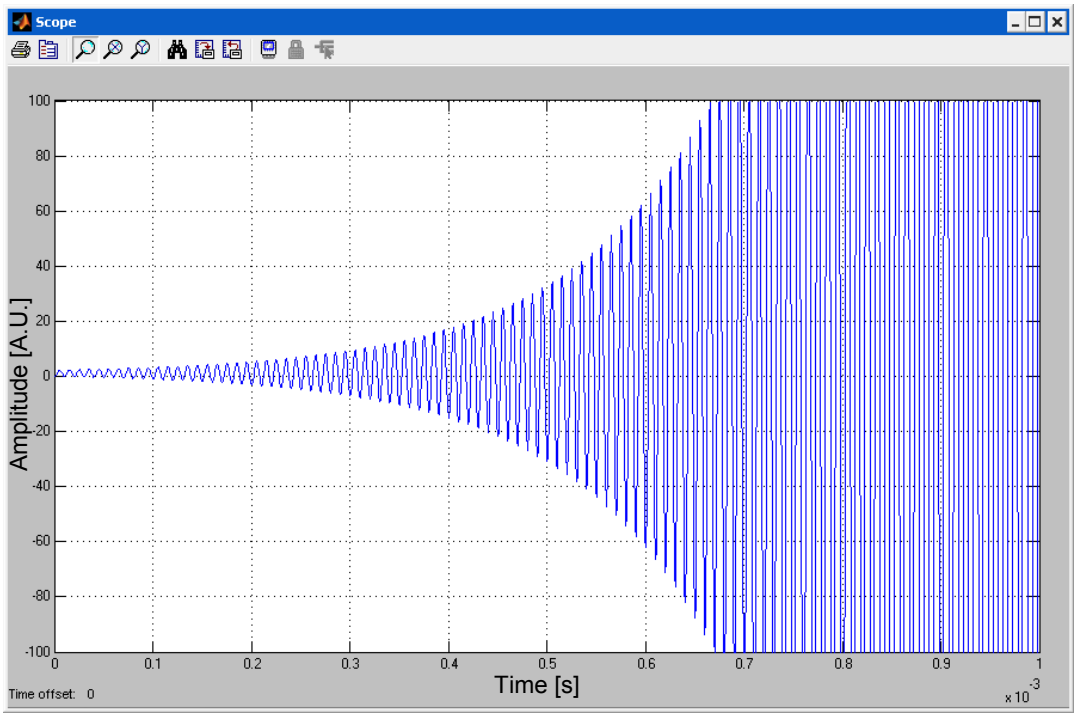

Figure 2.24: Simulated output of the laser in Simulink for open loop operation.

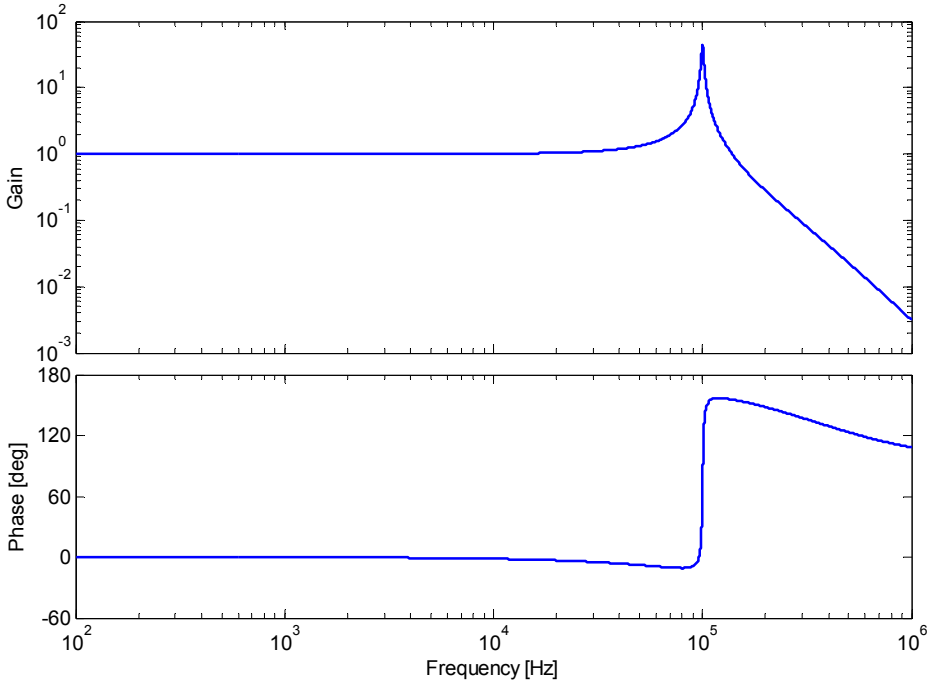

Figure 2.25: Bode plot of the open loop transfer function, $G(s)$, from simulation.

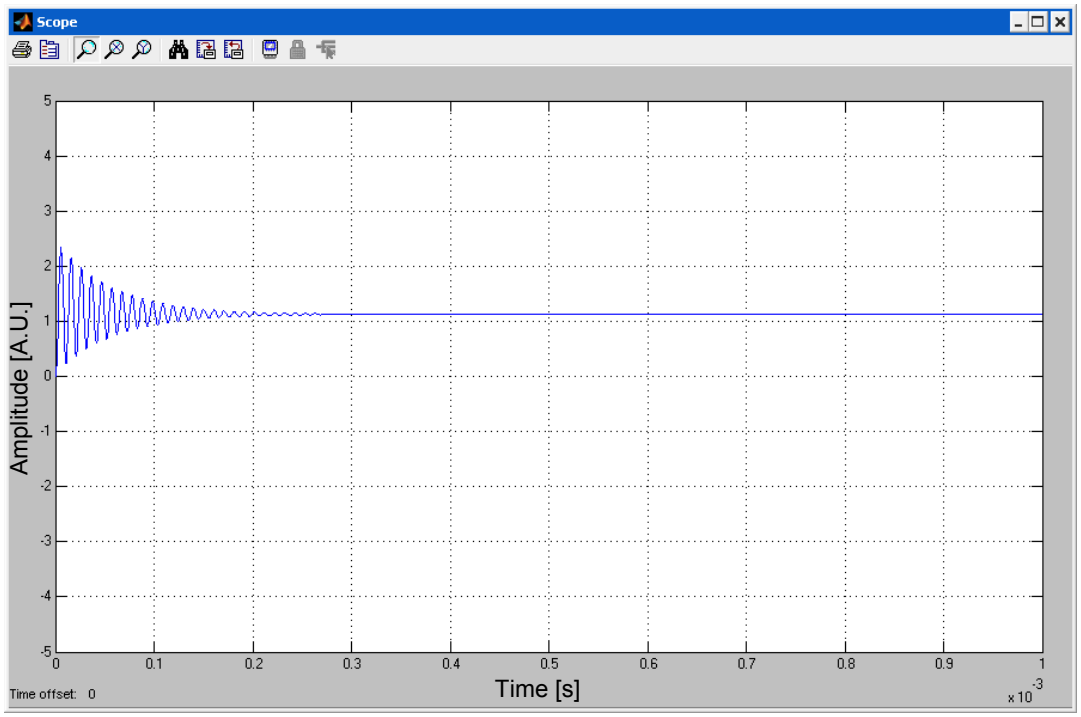

Figure 2.26: Simulated output of the laser in Simulink for closed loop operation.

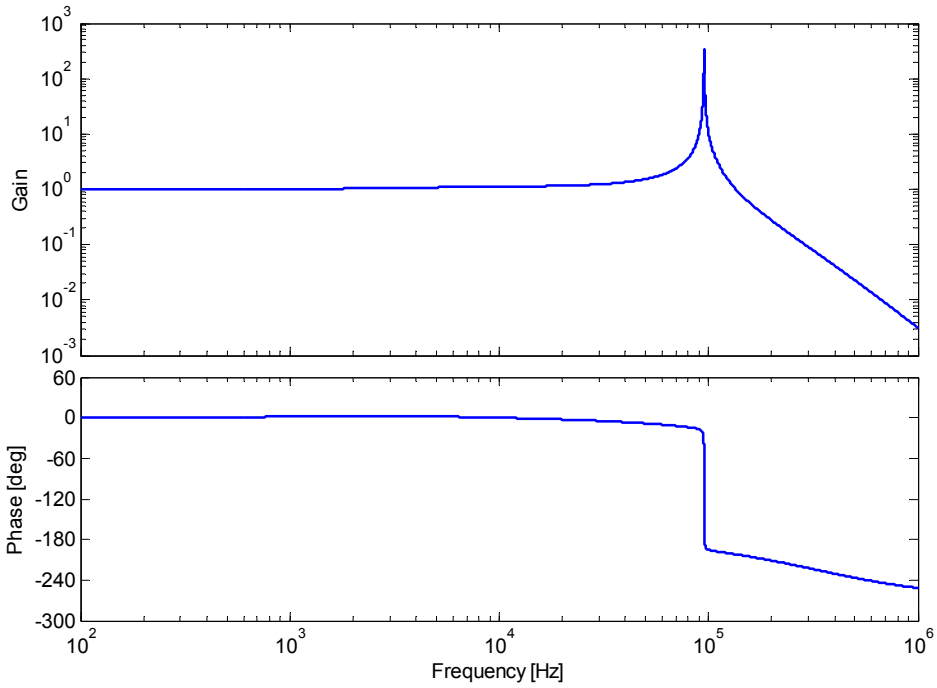

Figure 2.27: Bode plot of the closed loop transfer function, $G(s) / (1 + G(s)H(s))$, from simulation.

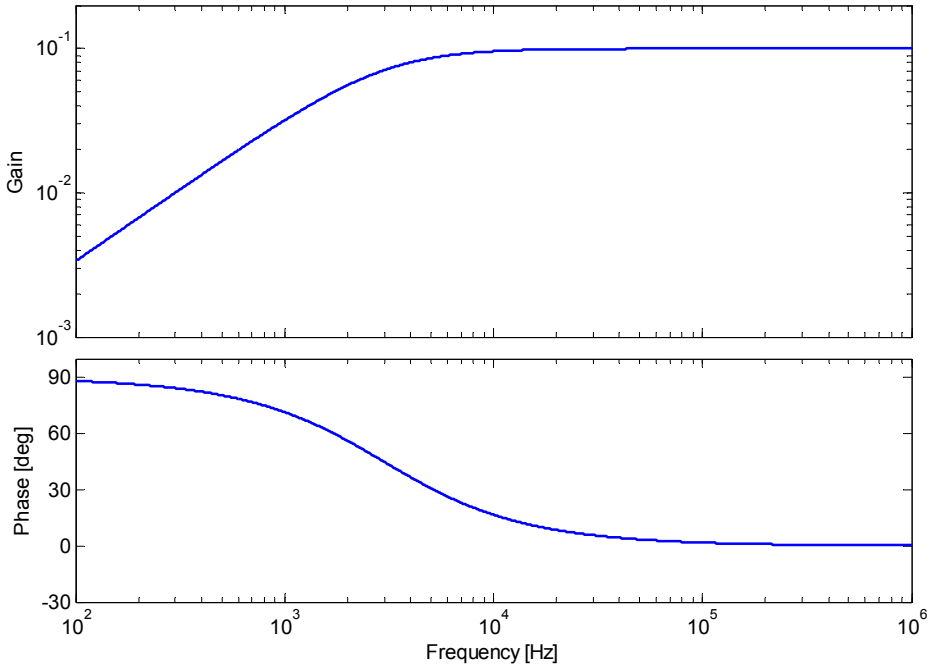

Figure 2.28: Bode plot of the transfer function of the feedback section, $H(s)$, from simulation.

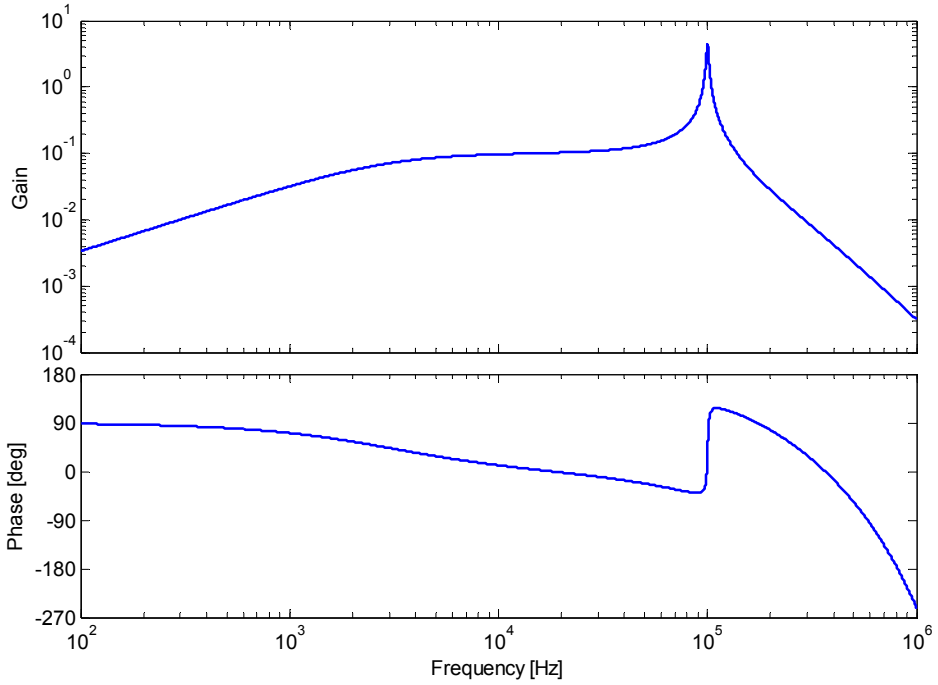

Figure 2.29: Bode plot of the loop transfer function, $G(s)H(s)$, from simulation.

2.5.2.1 Poles analysis

To understand better the mechanism by which the feedback system could suppress the oscillations, the pole locations of the closed-loop transfer function (corresponding to Figure 2.27) were plotted on the *s*-plane. In the *s*-plane, the imaginary part of a pole transforms to an oscillation in the time domain, while the real part corresponds to an exponential envelope in the signal. Poles that lie in the left-hand side of the *s*-plane correspond to an exponentially decaying signal with time, and conversely, poles in the right-hand side correspond to an unstable, exponentially growing signal.

Figure 2.30 shows the poles corresponding to the relaxation oscillation, at various DC feedback gains. The pole locations for a near-zero cross-relaxation lifetime and that of an additional low-pass filter at 200 kHz are also shown. At low gain, the poles

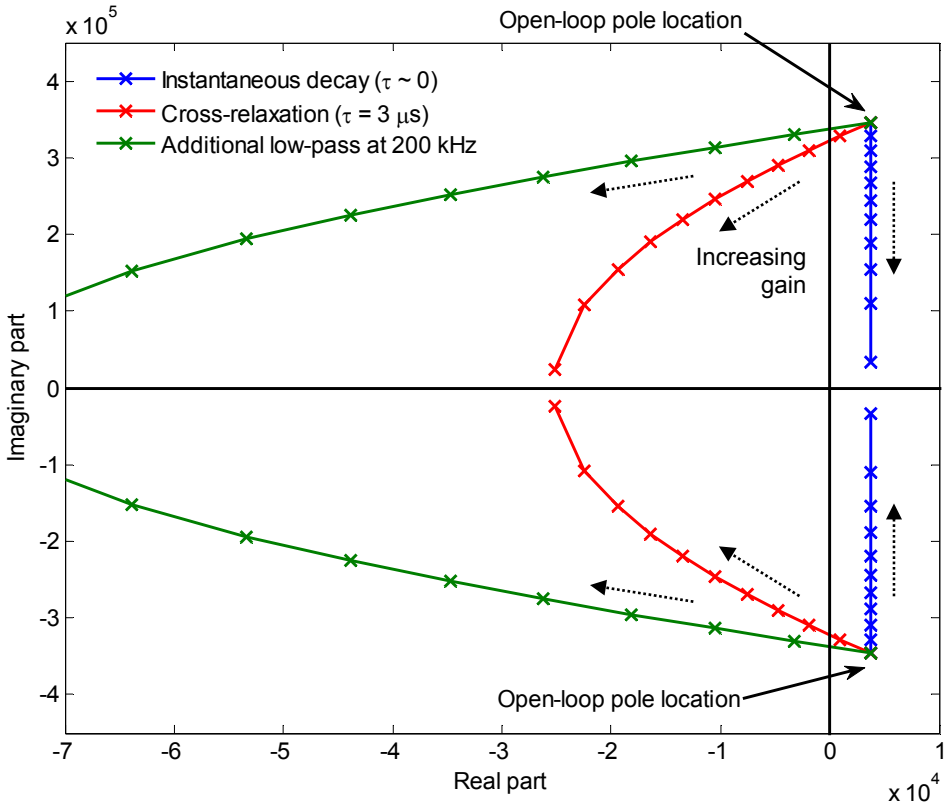

Figure 2.30: *s*-plane plot of the poles of the closed-loop transfer function for different feedback gains for three different cases: a near-zero cross-relaxation lifetime, a 3 μs cross-relaxation lifetime [122], and a 3 μs cross-relaxation lifetime plus an additional low-pass filter at 200 kHz. The values of gain used to calculate the locations of the poles ranged from 0 at the open-loop pole location through 0.1, 0.2… to 0.99. The movement of the poles with increasing gain is denoted by the dotted arrow.

are approximately those of the open-loop transfer function, which lies on the right-hand side of the *s*-plane due to the negative damping constant. If the cross-relaxation is near-instantaneous, the poles remain on the right-hand side and the system remains unstable irrespective of the feedback gain.

However, for a 3-μs cross-relaxation lifetime [122], increasing the gain results in the poles moving into the left-hand half of the *s*-plane. This corresponds to a positive damping coefficient. Hence the cross-relaxation lifetime ensures that simple proportional feedback can be used to damp the relaxation oscillation. As shown in Figure 2.30, introducing an additional low-pass filter into the feedback loop would result in further improvement to the damping of the oscillation. This prediction that suppression can be achieved by simply adjusting the gain of the proportional feedback is consistent with the experimental observations, described below.

2.5.3 Implementation

The feedback was provided in the form of an electrical current to the pump diode, and was proportional to the Tm:$YAlO_3$ laser output. A schematic of the implementation is shown in Figure 2.31, while the circuit diagram of the feedback electronics is shown in Appendix D.

An extended InGaAs photodetector (Thorlabs Det 10D) with a 100 Ω terminator instead of the standard 50 Ω was used to increase the gain. The signal from the photodetector was first amplified by a pre-amplifier stage with variable gain, and then passed through a 3-kHz high-pass filter into a voltage to current converter with unity gain. The current was then fed directly to the pump diode, in parallel with the current from the diode driver. Both the pump diode and the feedback loop drivers are current

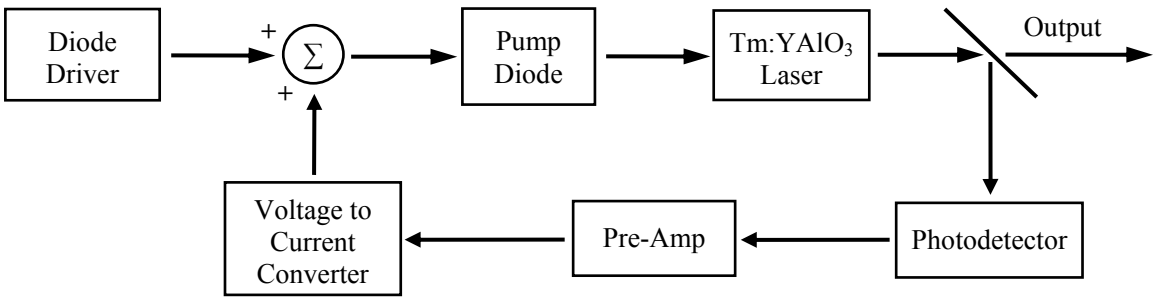

Figure 2.31: Schematic of the implementation of proportional feedback.

sources with high output impedance, thus isolation was not required. Grounding of the negative terminal of the normally-floating diode driver had no perceivable effect on the operation of the diode driver. Note that the electronic feedback loop was non-inverting due to the additional phase delay resultant from the cross-relaxation lifetime in Tm:$YAlO_3$.

2.5.4 Demonstration of pulse suppression

A comparison between the open-loop (free-running) and closed-loop operation of the laser is shown in Figure 2.32. Under closed-loop operation, the fluctuations in the output power were indistinguishable from the photodetector noise floor.

The laser stability was sensitive to environmental variations, with vibrations inducing bursts of oscillations before the feedback circuit reengaged and returned the system back to stability. This is due to the unstable nature of the laser as well as the limited bandwidth of the feedback electronics. This sensitivity increased with higher output power as the natural oscillation frequency of the laser approaches the bandwidth of the electronics. However, stable CW output was achieved for all operating powers

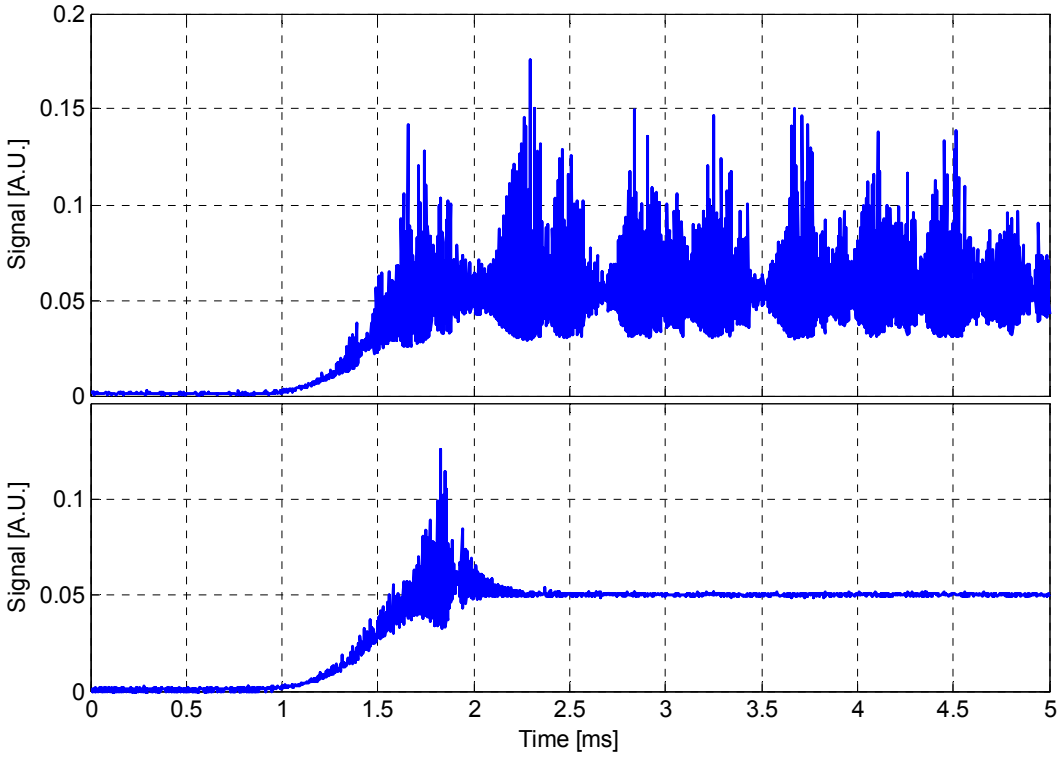

Figure 2.32: Output power for open-loop (top) and closed-loop (bottom) operation.

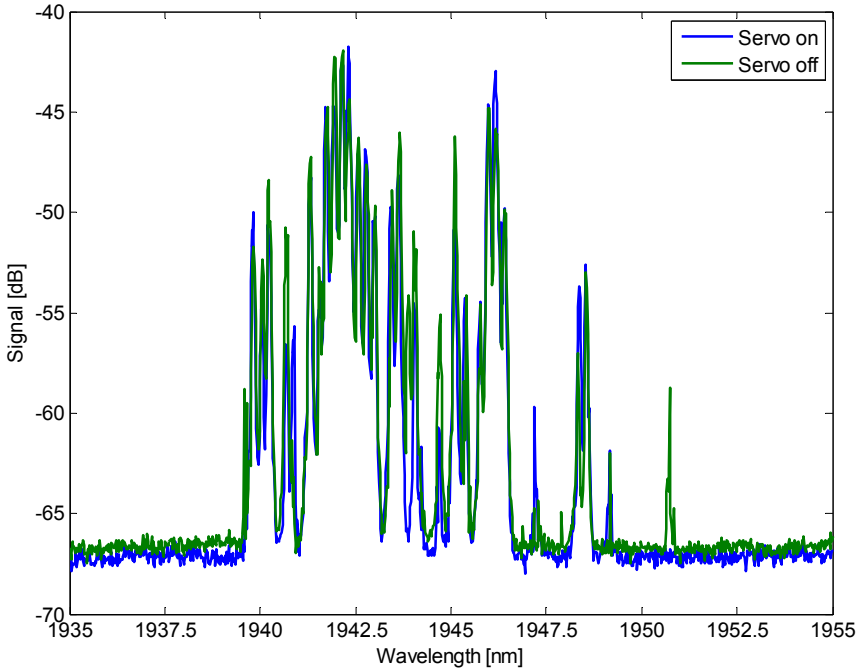

Figure 2.33: The output spectrum of the Tm:$YAlO_3$ laser Mk-II at 4 W output power with feedback (blue) and when free-running (green).

of this laser (up to 6 W) by adjusting the gain of the feedback loop.

The average output power of the laser was unchanged by the feedback. Similarly, the wavelength spectrum was also unchanged, as shown in Figure 2.33.

While the feedback loop was closed prior to lasing in the traces in Figure 2.32, it was not necessary for the feedback to be engaged at low power first. Even when the laser was running unstably at the maximum power level, the feedback circuit could be switched on at any time to obtain a stable output, making this a rugged system.

2.5.5 Measuring the open-loop laser transfer function

To verify the phenomenological model used, the transfer function of the Tm:$YAlO_3$ laser was measured by injecting a small electrical AC signal into the pump diode while the self-pulsing was suppressed. Suppression ensures a good signal-to-noise for the probe AC signal, which would have otherwise been obscured by other frequency components. By comparing the optical outputs of the pump diode and the laser, the gain and phase change at that frequency can be determined. The measured Bode plot of the laser is shown in Figure 2.34, along with a fitted transfer function in the form of

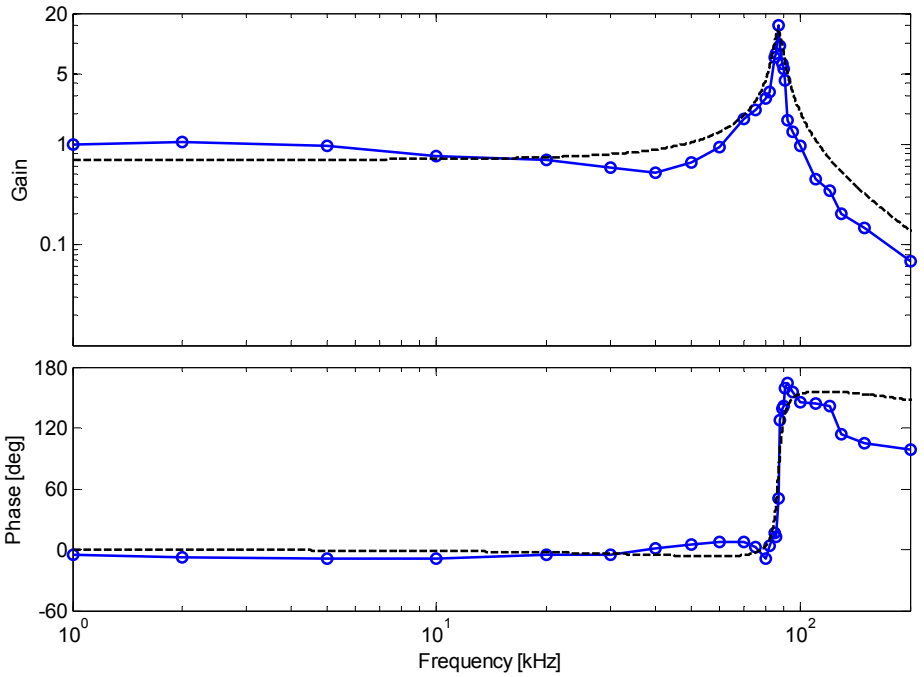

Figure 2.34: Measured (solid blue line) and modelled (dashed black line, best-fit using Equation 2.7 with $G = 0.7$, $\omega_v = 2\pi \cdot (87{,}000\ \text{Hz})$, and $\zeta = 0.025$) transfer functions of the Tm:$YAlO_3$ laser.

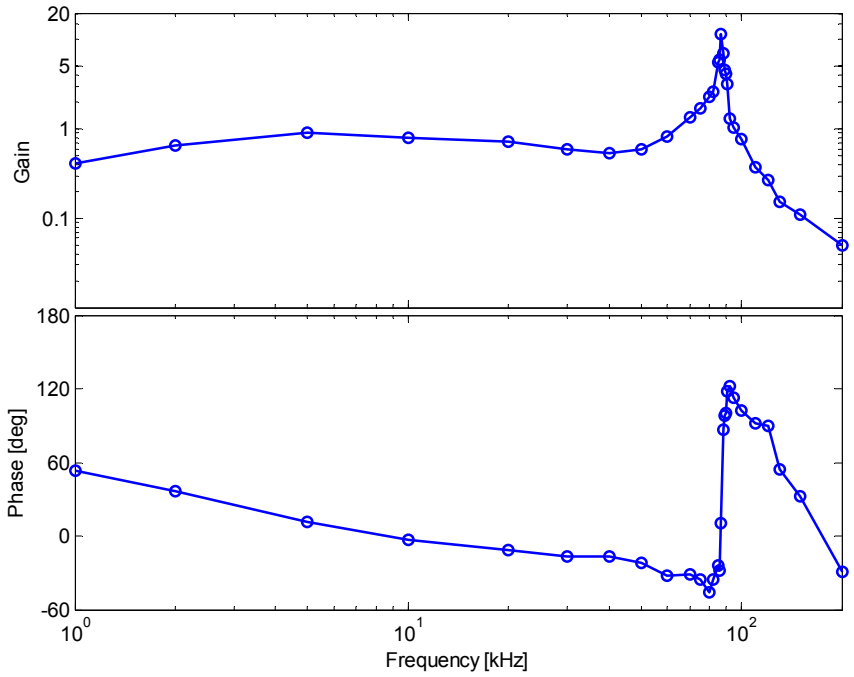

Figure 2.35: Bode plot of the loop transfer function.

Equation 2.7. The measured transfer function was combined with that of the rest of the loop to produce the loop transfer function, which is shown in Figure 2.35.

There is good agreement in terms of shape and phase change between the measured and modelled transfer functions for the laser, thus verifying the model developed and confirming the understanding of the laser.

2.6 Chapter summary

A small sample cuboid of 4 at.% thulium-doped $YAlO_3$ was used to verify the absorption spectra of the crystal around 795 nm. The sample was then used as the gain medium for an efficient end-pumped Tm:$YAlO_3$ laser, which operated with a threshold of 1.5 W and a slope efficiency of 56%. The beam quality of the laser was measured to have an $M^2 \sim 4 - 4.5$. The output of the laser was observed to suffer from significant large-amplitude self-pulsing. This was shown to be due to an unstable relaxation oscillation in the gain medium rather than saturable absorption by water vapour in the laser resonator. The laser was modelled as an unstable relaxation oscillator with a low-pass filter. The model showed that simple proportional feedback could be used to suppress the self-pulsing. This was demonstrated experimentally, and the measured transfer function of the laser was shown to agree with a phenomenological model.

A pulse suppression method based on current feedback to the pump diode was developed. Pulse suppression was successfully demonstrated on the Tm:$YAlO_3$ laser, resulting in a detector-noise-limited output.

3 Model of the laser dynamics

3.1 Introduction

To develop a further understanding of self-pulsing in Tm:$YAlO_3$ lasers, it is important to understand the dynamics within the laser gain medium. This chapter describes the modelling of the laser dynamics in Matlab, assuming that significant ESA at the lasing wavelength occurs as proposed by I. Razdobreev and A. Shestakov [85]. The model, which is based on that described by I. Razdobreev and A. Shestakov but developed further, investigates the laser dynamics in both the time and frequency domains, using the parameters of the cuboid laser Mk-II described in Chapter 2. The model also extends to consider the effect of the feedback system on the laser output.

Section 3.2 outlines the energy levels and the transitions of interest in Tm:$YAlO_3$. The rate equations and parameters associated with these transitions are described in Section 3.3. The results of the model in the time domain are presented in Section 3.4. Section 3.5 describes the linearization of the rate equations in order to solve them in the frequency domain. These linearized rate equations are solved in Section 3.6, with the results also presented. For comparison, Section 3.7 describes the modelled laser output in the absence of excited-state absorption (ESA) at the lasing wavelength to demonstrate its importance in this model. Section 3.8 describes the addition of the feedback loop into the model and presents the modelled laser output under closed-loop operation. The chapter is concluded in Section 3.9.

3.2 Tm:$YAlO_3$ energy levels

The temporal dynamics of the Tm:$YAlO_3$ laser was modelled by considering the transitions between the first four energy levels, namely $^3H_6$, $^3F_4$, $^3H_5$ and $^3H_4$, as shown in Figure 3.1 [124]. Ions are excited to the $^3H_4$ energy level from the ground state ($^3H_6$) by the pump source, denoted as R_p. The excited ions then transfer to the other energy levels via various transitions, with the main transitions that were considered by the model shown. The cross-relaxation-based transitions are denoted with the letter *a*, while natural decay rates denoted with the letter *r*. Finally, stimulated emission occurs between the $^3F_4$ and $^3H_6$ energy levels to produce laser photons.

The rate equation model using only these transitions does not result in the observed self-pulsing behaviour [124], which is demonstrated later in Section 3.6. Thus, some additional processes must be considered in order to reproduce the self-pulsation, such as an intra-cavity saturable absorber or ESA. While intra-cavity water vapour acting as a saturable absorber has already been ruled out (see Section 2.3.4.1), it has been shown in a model that ESA at the lasing wavelength can reproduce the observed self-pulsing behaviour in a laser [125]. Thus, an ESA transition in Tm:$YAlO_3$ between the $^3H_5$ and $^3H_4$ energy levels was also included in the model [85].

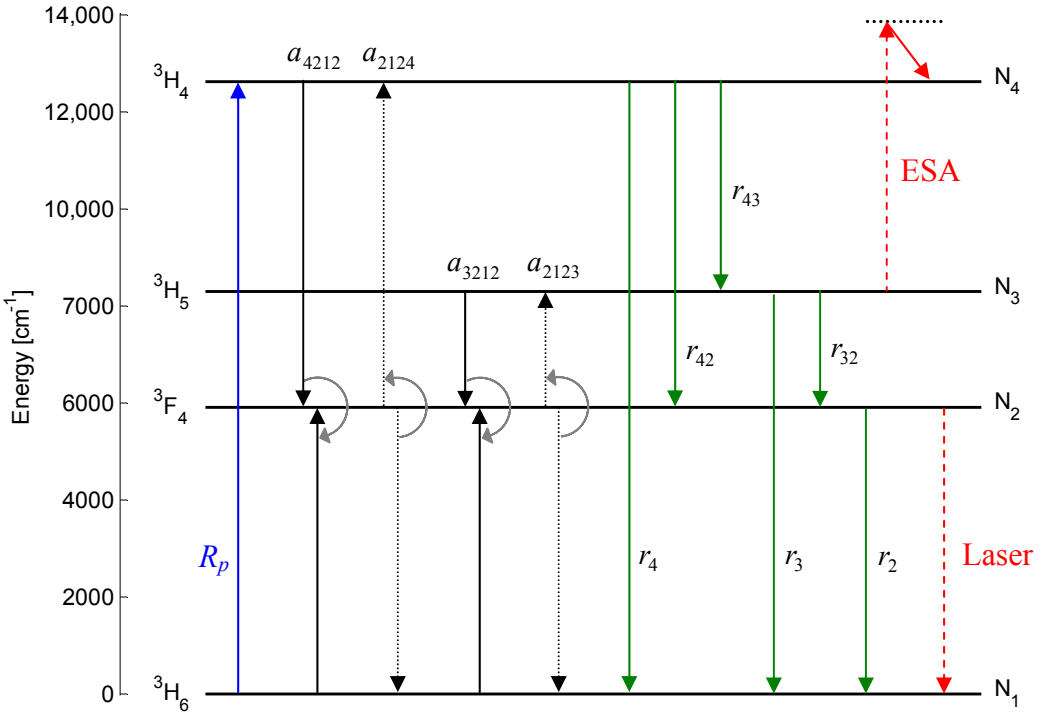

Figure 3.1: The first four energy levels of Tm:$YAlO_3$ with corresponding transitions.

The energy gap of the transition between the $^3H_5$ and $^3H_4$ energy levels ranges from 4400 to 4800 cm^{-1}, depending on the specific Stark sublevel of the $^3H_4$ manifold [63]. This is lower than the energy of a laser photon (5150 cm^{-1}), and hence the transition must be assisted by a phonon emission of energy between 350 cm^{-1} and 750 cm^{-1}. Phonon energy in $YAlO_3$ can range up to 750 cm^{-1} with the highest density in the 550-600 cm^{-1} range [126]. Thus, a phonon-assisted ESA transition between the $^3H_5$ and $^3H_4$ energy levels may require only a single phonon, and hence is entirely feasible. Other possible ESA transitions, such as $^3F_4$ to $^3H_4$ and $^3H_5$ to an even higher energy level $^3F_3$, are improbable, as total phonon energies in excess of 1000 cm^{-1} are required, corresponding to two or more phonons.

3.3 Rate equations

The rate equations corresponding to the transitions shown in Figure 3.1 and laser photon emission/absorption are given by:

$$\begin{aligned}
\frac{dN_2}{dt} &= 2a_{4212}\,N_1\,N_4 - 2\left(a_{2124}+a_{2123}\right)N_2{}^2 + 2a_{3212}\,N_1\,N_3 \\
&\quad -2\sigma\,c\left(f_u N_2 - f_l N_1\right)\phi + r_{42}N_4 + r_{32}N_3 - \left(r_2 + r_{sp}\right)N_2 \\
\frac{dN_3}{dt} &= a_{2123}N_2{}^2 - a_{3212}N_1N_3 + 2\sigma_{\mathrm{ESA}}\,c\left(N_4 - N_3\right)\phi + r_{43}N_4 - r_3N_3 \\
\frac{dN_4}{dt} &= R_p\left(N_1 - N_4\right) + 2a_{2124}\,N_2{}^2 - 2\sigma_{ESA}\,c\left(N_4 - N_3\right)\phi - a_{4212}\,N_1\,N_4 - r_4N_4 \\
\frac{d\phi}{dt} &= \left(\sigma\,c\left[f_u N_2 - f_l N_1\right] + \sigma_{\mathrm{ESA}}\,c\left[N_4 - N_3\right]\right)\phi\cdot\eta_{red} - r_c\phi + r_{sp}N_2\,,
\end{aligned} \tag{3.1}$$

where the parameters are defined in Table 3.1.

To conserve the ion population in the gain medium, the population density of the ground state is defined as $N_1 = N - N_2 - N_3 - N_4$, where N is the total ion density, and its variation with respect to time is given by:

$$\frac{dN_1}{dt} = -\left(\frac{dN_2}{dt} + \frac{dN_3}{dt} + \frac{dN_4}{dt}\right). \tag{3.2}$$

Parameter	Description
N_i	Population density of energy level i
ϕ	Intra-cavity laser photon density
σ	Laser emission cross-section
σ_{ESA}	ESA cross-section
a_{ijkl}	Cross-relaxation and co-operative up-conversion rates from level i, k to j, l
r_{mn}	Non-radiative decay rates from level m to n
r_o	Total non-radiative decay rates from level o
r_c	Cavity photon decay rate
r_{sp}	Spontaneous radiative decay rate
f_u	Boltzmann thermal occupation factor for upper lasing level
f_l	Boltzmann thermal occupation factor for lower lasing level
R_p	Pump rate
c	Speed of light
η_{red}	Density-reduction scaling parameter

Table 3.1: Definition of terms in Equation 3.1.

3.3.1 Physical parameters

The values used for each parameter were calculated based on our laser system, estimated to an appropriate value, or obtained from literature. The value for the emission cross-section is the measured value from Chapter 4. The physical parameters of the laser system are listed in Table 3.2, Table 3.3 and Table 3.4 below.

Parameter	**Description**	**Value**
N	Population density of Tm:$YAlO_3$	7.87×10^{20} cm^{-3}
σ	Laser emission cross-section	7.8×10^{-21} cm^2
γ	Ratio of σ_{ESA} to σ	0.65
σ_{ESA}	ESA cross-section	$\gamma\cdot\sigma$
f_u	Boltzmann thermal occupation factor for upper lasing level	0.263
f_l	Boltzmann thermal occupation factor for lower lasing level	0.03
Ω	Solid angle for which spontaneously emitted photons contribute to the photon count	1×10^{-6} sr

Table 3.2: Tm:$YAlO_3$ physical parameters [63], [85], [127].

Coefficient	Value	Coefficient	Value
a_{4212}	1.5×10^{-14} s^{-1}	r_{42}	130 s^{-1}
a_{3212}	0	r_4	1590 s^{-1}
a_{2123}	2.8×10^{-18} s^{-1}	r_3 , r_{32}	1.8×10^{5} s^{-1}
a_{2124}	8×10^{-19} s^{-1}	r_2	210 s^{-1}
r_{43}	1460 s^{-1}	r_{sp}	$r_2 \cdot \Omega$

Table 3.3: Transition rates between energy levels [63], [85], [128].

Parameter	Description	Value
α_p	Absorption at the pump wavelength	3 cm^{-1}
P_{pump}	Incident pump power	4 W
ω_{pump}	Radius of the pump beam	100 μm
l	Length of the laser gain medium	4.545 mm
l_{air}	Length of the air within the cavity	205 mm
T_{OC}	Transmission of the output coupler	10%

Table 3.4: Measured parameters from the Tm:$YAlO_3$ cuboid laser.

3.3.2 Calculated parameters

In addition to the parameters listed above, a number of parameters were calculated.

Pump rate R_p: defined as the number of ions excited by the pump photons per unit volume, the pump rate was calculated from the absorption of the pump light, and is given by:

$$R_p = \frac{\sigma_p (N_1 - N_4)}{E_{pump}\ A_{pump}} \left(P_{pump} \frac{A_{laser}}{A_{pump}} \right), \tag{3.3}$$

where $\sigma_p = \alpha_p / N$ is the absorption cross-section at the pump wavelength, E_{pump} is the pump photon energy, A_{pump} and A_{laser} are the pump and laser mode areas respectively, and the other parameters as defined previously. This equation is obtained as follows: Firstly, the pump power density is defined as the total pump power absorbed, given by the Beer-Lambert law, divided by the pump volume. Pump power that lies outside of the laser mode cannot be accessed by the laser. This unused pump power can be

accounted for by multiplying the pump power density by the ratio of the laser area to pump area. The useful pump power density is therefore given by:

$$I = \frac{(1 - \exp[\sigma_p (N_1 - N_4)\, l])}{l A_{pump}} \left(P_{pump} \frac{A_{laser}}{A_{pump}} \right). \tag{3.4}$$

The exponential can be simplified to the first two terms of its binomial expansion, $e^x \approx 1 + x$:

$$I = \frac{\sigma_p (N_1 - N_4)}{A_{pump}} \left(P_{pump} \frac{A_{laser}}{A_{pump}} \right). \tag{3.5}$$

The pump rate R_p can then be obtained by dividing the useful pump power density by the pump photon energy E_{pump} to give the number of ions excited by the pump photons per unit volume, resulting in Equation 3.3.

Cavity photon decay rate r_c: some of the photons in the cavity are extracted from the cavity via the output coupler for every round trip. The cavity photon decay rate is given by the output coupling fraction for each round trip divided by the cavity round-trip time $\tau_{RT} = 2(n_{YAlO_3} l_{cryst} + n_{air} l_{air})/c$:

$$r_c = \frac{-\log(1 - T_{OC})}{\tau_{RT}}. \tag{3.6}$$

Density-reduction scaling parameter η_{red}: the scaling parameter in Equation 3.1 arises because the rate equations assume uniform photon emission throughout the cavity, rather than only from the crystal. This can be resolved by considering an identical system where the same total number of ions is distributed uniformly along the cavity. Thus, the scaling parameter is given by:

$$\eta_{red} = \frac{2 n_{YAlO_3} l_{cryst}}{n_{YAlO_3} l_{cryst} + n_{air} l_{air}}. \tag{3.7}$$

3.3.3 Solving the differential equations

The rate equations in Equation 3.1 were solved in the time domain as a series of coupled differential equations. The rate equations were solved using the ordinary differential equations (ODEs) solver in Matlab, *ode45*, a one-step solver based on an explicit fifth-order Runge-Kutta method. The Matlab code, originally written by Dr. David Ottaway and developed in conjunction with him, can be found in Appendix C.1.1.

There are two different time scales associated with solving the laser dynamics problem. The first deals with the initial pumping of the laser prior to lasing, where the different energy levels are populated and no net laser photons are generated. The time scale for this process is on the order of milliseconds. Once the gain medium is above threshold, a much shorter, microsecond-time scale is required for the lasing dynamics.

Because of this significant difference in time scale before and after threshold is reached, two separate ODE solvers were used. The first solver used a long time scale to find the onset of lasing, and obtained the population densities of each state at the point where the gain is greater than unity. All laser photon interactions were ignored by this solver. The population densities at the onset of lasing were passed to the second ODE solver. Using these values as the initial values, the full rate equations including laser photon interactions were solved by this ODE solver. Due to the much faster dynamics, this solver operated on a much shorter time scale.

3.4 Temporal dynamics

The output of the Matlab model is shown in Figure 3.2, showing the photon emission (top) and population densities with time. At time $t = 0$, gain exceeds unity and photon emission begins. The system initially shows a transient behaviour typical of most systems at start-up; however, instead of relaxing to a stable CW operation, the system continues to self-pulse strongly. This behaviour continues indefinitely with a stable pulse shape, and is consistent with I. Razdobreev and A. Shestakov [85] with their monolithic Tm:$YAlO_3$ laser system. The output is also consistent with the hypothesis that the laser is an inherently unstable oscillator.

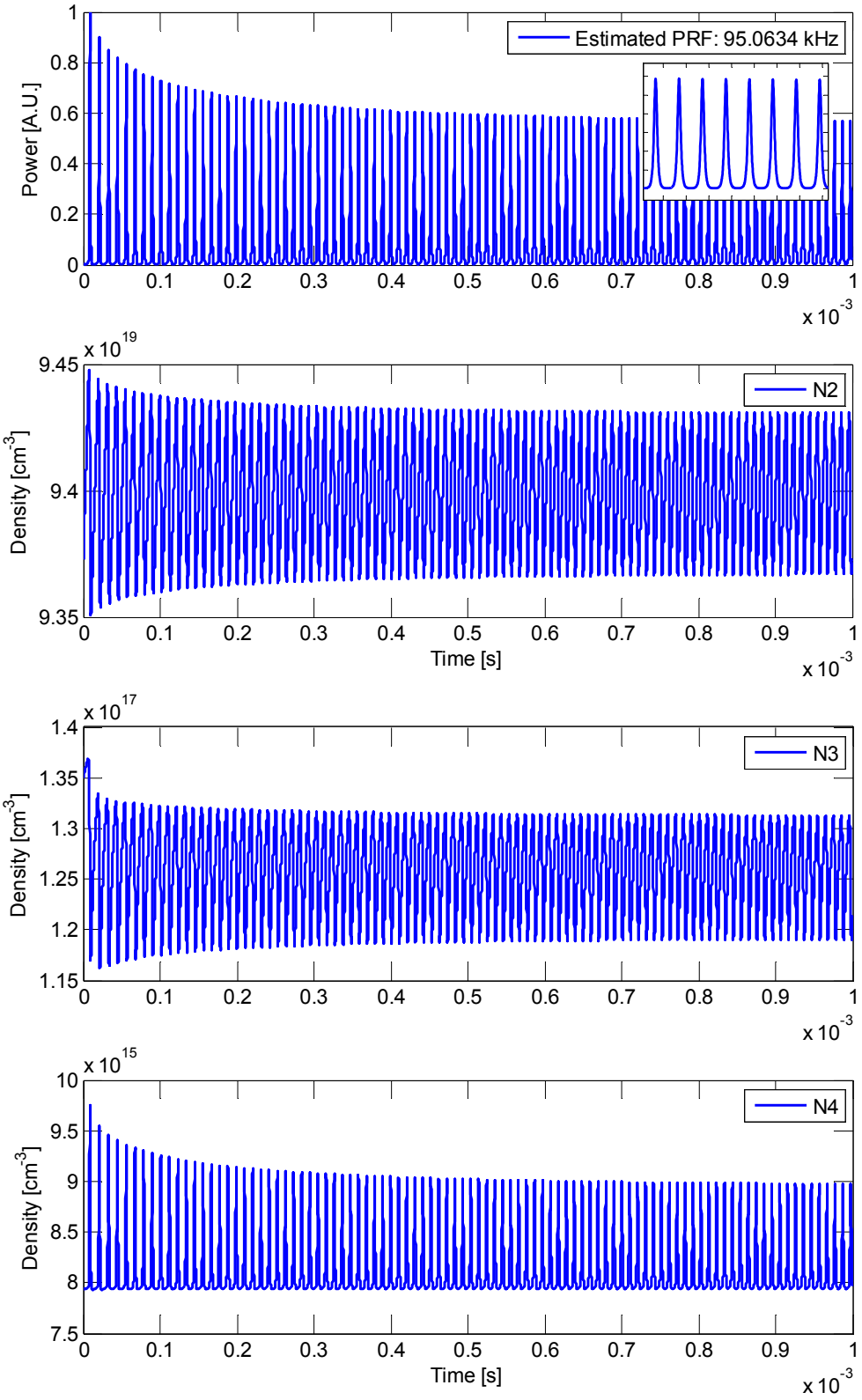

Figure 3.2: The output of the laser model, showing the photon emission (top) and population densities with time. Significant oscillatory behaviour can be observed in all cases, which do not damp out with time.

The PRF is estimated to be approximately 95 kHz based on the mean separation of the pulses, and is in approximate agreement with experiment described in Chapter 2.

3.5 Linearized rate equations

To study the dynamics of the Tm:$YAlO_3$ laser system in the frequency domain, it is necessary to linearize the rate equations. This is required to determine the frequency response of the model laser, in the form of its transfer function.

All frequency components are assumed initially to be zero, and hence the system is in an equilibrium state. Linearization is then achieved by considering the changes to the population densities, photon density and pump rate induced by a probe frequency signal as small perturbations from this equilibrium state, i.e.:

$$\begin{aligned} N_i(t) &= \overline{N_i} + \Delta N_i(t) \\ \phi(t) &= \bar{\phi} + \Delta\phi(t) \\ R_p(t) &= \overline{R_p} + \Delta R_p(t)\,. \end{aligned} \tag{3.8}$$

The mean values of the population and photon densities are assumed to be time independent, i.e. $\frac{d\overline{N_i}}{dt} = 0$ and $\frac{d\bar{\phi}}{dt} = 0$, and all time-dependent behaviour is encapsulated in the perturbation term. With this assumption, it follows from Equation 3.2 that the sum of all mean population densities $\sum_{i=1}^{4} \overline{N_i} = N$ and the sum of the time-dependent variations $\sum_{i=1}^{4} \Delta N_i = 0$.

Substituting Equation 3.8 into the rate equations in Equation 3.1 gives:

$$
\begin{aligned}
\frac{d\Delta N_2}{dt} = & -\left[2a_{4212}\overline{N_4} + 2a_{3212}\overline{N_3} + 4\left(a_{2124}+a_{2123}\right)\overline{N_2} + 2\sigma\, c\left(f_u + f_l\right)\overline{\phi} + \left(r_2 + r_{sp}\right)\right]\cdot \Delta N_2 \\
& -\left[2a_{4212}\overline{N_4} + 2a_{3212}\left(\overline{N_3} - \overline{N_1}\right) + 2\sigma\, cf_l\overline{\phi} - r_{32}\right]\cdot \Delta N_3 \\
& -\left[2a_{4212}\left(\overline{N_4} - \overline{N_1}\right) + 2a_{3212}\overline{N_3} + 2\sigma\, cf_l\overline{\phi} - r_{42}\right]\cdot \Delta N_4 - 2\sigma\, c\left(f_u\overline{N_2} + f_l\overline{N_1}\right)\cdot \Delta\phi \\
& + 2a_{4212}\Delta N_1\Delta N_4 - 2\left(a_{2124}+a_{2123}\right)\Delta N_2{}^2 + 2a_{3212}\Delta N_1\Delta N_3 - 2\sigma\, c\left(f_u\Delta N_2 - f_l\Delta N_1\right)\Delta\phi \\
& + 2a_{4212}\overline{N_1}\,\overline{N_4} - 2\left(a_{2124}+a_{2123}\right)\overline{N_2}^2 + 2a_{3212}\overline{N_1}\,\overline{N_3} - 2\sigma\, c\left(f_u\overline{N_2} - f_l\overline{N_1}\right)\overline{\phi} + r_{42}\overline{N_4} \\
& + r_{32}\overline{N_3} - \left(r_2 + r_{sp}\right)\overline{N_2}
\end{aligned}
$$

$$
\begin{aligned}
\frac{d\Delta N_3}{dt} = & \left[a_{3212}\overline{N_3} + 2a_{2123}\overline{N_2}\right]\cdot \Delta N_2 + \left[a_{3212}\left(\overline{N_3} - \overline{N_1}\right) - 2\sigma_{\mathrm{ESA}}c\overline{\phi} - r_3\right]\cdot \Delta N_3 \\
& + \left[-2\overline{R_p} + a_{4212}\left(\overline{N_4} - \overline{N_1}\right) - 2\sigma_{\mathrm{ESA}}c\overline{\phi} - r_4\right]\cdot \Delta N_4 + 2\sigma_{\mathrm{ESA}}c\left(\overline{N_4} - \overline{N_3}\right)\cdot \Delta\phi \\
& + a_{2123}\Delta N_2{}^2 - a_{3212}\Delta N_1\Delta N_3 + 2\sigma_{\mathrm{ESA}}c\left(\Delta N_4 - \Delta N_3\right)\Delta\phi \\
& + a_{2123}\overline{N_2}^2 - a_{3212}\overline{N_1}\,\overline{N_3} + 2\sigma_{\mathrm{ESA}}c\left(\overline{N_4} - \overline{N_3}\right)\overline{\phi} + r_{43}\overline{N_4} + r_3\overline{N_3}
\end{aligned}
$$

$$
\begin{aligned}
\frac{d\Delta N_4}{dt} = & \left[-\overline{R_p} + a_{4212}\overline{N_4} + 2a_{2124}\overline{N_2}\right]\cdot \Delta N_2 + \left[-\overline{R_p} + a_{4212}\overline{N_4} + +2\sigma_{\mathrm{ESA}}c\overline{\phi}\right]\cdot \Delta N_3 \\
& + \left[-2a_{4212}\left(\overline{N_4} - \overline{N_1}\right) - 2a_{3212}\overline{N_3} - 2\sigma\, cf_l\overline{\phi} + r_{42}\right]\cdot \Delta N_4 - 2\sigma_{\mathrm{ESA}}c\left(\overline{N_4} - \overline{N_3}\right)\cdot \Delta\phi \\
& + \left(\overline{N_1} - \overline{N_4}\right)\cdot \Delta R_p \\
& - \Delta R_p\left(\Delta N_4 - \Delta N_1\right) + 2a_{2124}\Delta N_2{}^2 - 2\sigma_{\mathrm{ESA}}c\left(\Delta N_4 - \Delta N_3\right)\Delta\phi - a_{4212}\Delta N_1\Delta N_4 \\
& + \overline{R_p}\left(\overline{N_1} - \overline{N_4}\right) + 2a_{2124}\overline{N_2}^2 - 2\sigma_{\mathrm{ESA}}c\left(\overline{N_4} - \overline{N_3}\right)\overline{\phi} - a_{4212}\overline{N_1}\,\overline{N_4} - r_4\overline{N_4}
\end{aligned}
$$

$$
\begin{aligned}
\frac{d\Delta\phi}{dt} = & \left(\sigma\, c\left[f_u + f_l\right]\overline{\phi}\cdot\rho_{red} + r_{sp}\right)\cdot \Delta N_2 + \left(\sigma\, cf_l - \sigma_{\mathrm{ESA}}c\right)\overline{\phi}\cdot\rho_{red}\cdot \Delta N_3 \\
& + \left(\sigma\, cf_l - \sigma_{\mathrm{ESA}}c\right)\overline{\phi}\cdot\rho_{red}\cdot \Delta N_4 \\
& + \left[\left(\sigma\, c\left[f_u\overline{N_2} - f_l\overline{N_1}\right] + \sigma_{\mathrm{ESA}}c\left[\overline{N_4} - \overline{N_3}\right]\right)\cdot\rho_{red} - r_c\right]\cdot \Delta\phi \\
& + \left(\sigma\, c\left[f_u\Delta N_2 - f_l\Delta N_1\right] + \sigma_{\mathrm{ESA}}c\left[\Delta N_4 - \Delta N_3\right]\right)\Delta\phi\cdot\rho_{red} \\
& + \left(\sigma\, c\left[f_u\overline{N_2} - f_l\overline{N_1}\right] + \sigma_{\mathrm{ESA}}c\left[\overline{N_4} - \overline{N_3}\right]\right)\overline{\phi}\cdot\rho_{red} - r_c\overline{\phi} + r_{sp}\overline{N_2}
\end{aligned}
\tag{3.9}
$$

which can be condensed to the following:

$$
\begin{aligned}
\frac{d\Delta N_2}{dt} &= A_{22}\Delta N_2 + A_{23}\Delta N_3 + A_{24}\Delta N_4 + A_{2\phi}\Delta\phi + X_2 + C_2 \\
\frac{d\Delta N_3}{dt} &= A_{32}\Delta N_2 + A_{33}\Delta N_3 + A_{34}\Delta N_4 + A_{3\phi}\Delta\phi + X_3 + C_3 \\
\frac{d\Delta N_4}{dt} &= A_{42}\Delta N_2 + A_{43}\Delta N_3 + A_{44}\Delta N_4 + A_{4\phi}\Delta\phi + \left(\overline{N_1} - \overline{N_4}\right)\cdot\Delta R_p + X_4 + C_4 \\
\frac{d\Delta\phi}{dt} &= A_{\phi 2}\Delta N_2 + A_{\phi 3}\Delta N_3 + A_{\phi 4}\Delta N_4 + A_{\phi\phi}\Delta\phi + X_\phi + C_\phi,
\end{aligned}
\tag{3.10}
$$

where A_{ij} are the first-order coefficients from Equation 3.9, X_i are the second-order terms and C_i are the constant terms.

As the variations are considered to be small perturbations, the second-order terms are small. In addition, these second-order terms result in features in the frequency domain beyond the range of interest. Thus, the second-order terms, X_i, are assumed to be negligible for this investigation. The constant terms, which relate to the mean value, should equate to zero as the system is assumed to be in equilibrium.

Without the second-order terms and equating the constant terms to zero, the equations in Equation 3.10 can be written in matrix form:

$$\begin{bmatrix} \frac{d\Delta N_2}{dt} \\ \frac{d\Delta N_3}{dt} \\ \frac{d\Delta N_4}{dt} \\ \frac{d\Delta \phi}{dt} \end{bmatrix} = \begin{bmatrix} A_{22} & A_{23} & A_{24} & A_{2\phi} \\ A_{32} & A_{33} & A_{34} & A_{3\phi} \\ A_{42} & A_{43} & A_{44} & A_{4\phi} \\ A_{\phi 2} & A_{\phi 3} & A_{\phi 4} & A_{\phi\phi} \end{bmatrix} \begin{bmatrix} \Delta N_2 \\ \Delta N_3 \\ \Delta N_4 \\ \Delta \phi \end{bmatrix} + \begin{bmatrix} 0 \\ 0 \\ \left(\overline{N_1} - \overline{N_4}\right) \cdot \Delta R_p \\ 0 \end{bmatrix} \tag{3.11}$$

Taking the Laplace transform of Equation 3.11 gives:

$$\begin{bmatrix} s\Delta \mathrm{N}_2 \\ s\Delta \mathrm{N}_3 \\ s\Delta \mathrm{N}_4 \\ s\Delta \Phi \end{bmatrix} = \begin{bmatrix} A_{22} & A_{23} & A_{24} & A_{2\phi} \\ A_{32} & A_{33} & A_{34} & A_{3\phi} \\ A_{42} & A_{43} & A_{44} & A_{4\phi} \\ A_{\phi 2} & A_{\phi 3} & A_{\phi 4} & A_{\phi\phi} \end{bmatrix} \begin{bmatrix} \Delta \mathrm{N}_2 \\ \Delta \mathrm{N}_3 \\ \Delta \mathrm{N}_4 \\ \Delta \Phi \end{bmatrix} + \begin{bmatrix} 0 \\ 0 \\ \left(\overline{N_1} - \overline{N_4}\right) \cdot \Delta \Re_p \\ 0 \end{bmatrix} \tag{3.12}$$

where $\Delta \mathrm{N}_i$, $\Delta\Phi$ and $\Delta\Re_p$ are the Laplace transforms of ΔN_i, $\Delta\phi$ and ΔR_p respectively. The population densities and photon density can now be found by rearranging Equation 2.1, and solving for different values of $s = i\omega$:

$$\begin{bmatrix} \Delta \mathrm{N}_2 \\ \Delta \mathrm{N}_3 \\ \Delta \mathrm{N}_4 \\ \Delta \Phi \end{bmatrix} = \begin{bmatrix} s - A_{22} & A_{23} & A_{24} & A_{2\phi} \\ A_{32} & s - A_{33} & A_{34} & A_{3\phi} \\ A_{42} & A_{43} & s - A_{44} & A_{4\phi} \\ A_{\phi 2} & A_{\phi 3} & A_{\phi 4} & s - A_{\phi\phi} \end{bmatrix}^{-1} \begin{bmatrix} 0 \\ 0 \\ \left(\overline{N_1} - \overline{N_4}\right) \cdot \Delta \Re_p \\ 0 \end{bmatrix} \tag{3.13}$$

with $\Delta\Re_p = 1$ for a flat input spectrum, corresponding to $\delta(t)$ input in the time domain.

3.6 Laser transfer function

The linearized rate equations in Equation 3.13 were solved in Matlab using a separate function, the code of which can be found in Appendix C.1.1.6. The mean values of the population and photon densities from the temporal dynamics model were used as the mean values, i.e. $\overline{N_i}$. The matrices were then solved for each value of s. Bode plots of the modelled laser transfer function and that of the various population densities are shown in Figure 3.3 and Figure 3.4 respectively.

The transfer function of the modelled laser is qualitatively very similar to that of the simple model in Section 2.5.2, as well as that of the experiment in Section 2.5.5, with a phase lead of 180º accompanying the relaxation oscillation resonance peak. The oscillation frequency is also roughly in agreement with the PRF in the time domain.

These results indicate that self-pulsing in the free-running Tm:$YAlO_3$ laser could be explained by ESA at the lasing wavelength, resulting in a negatively damped relaxation oscillation.

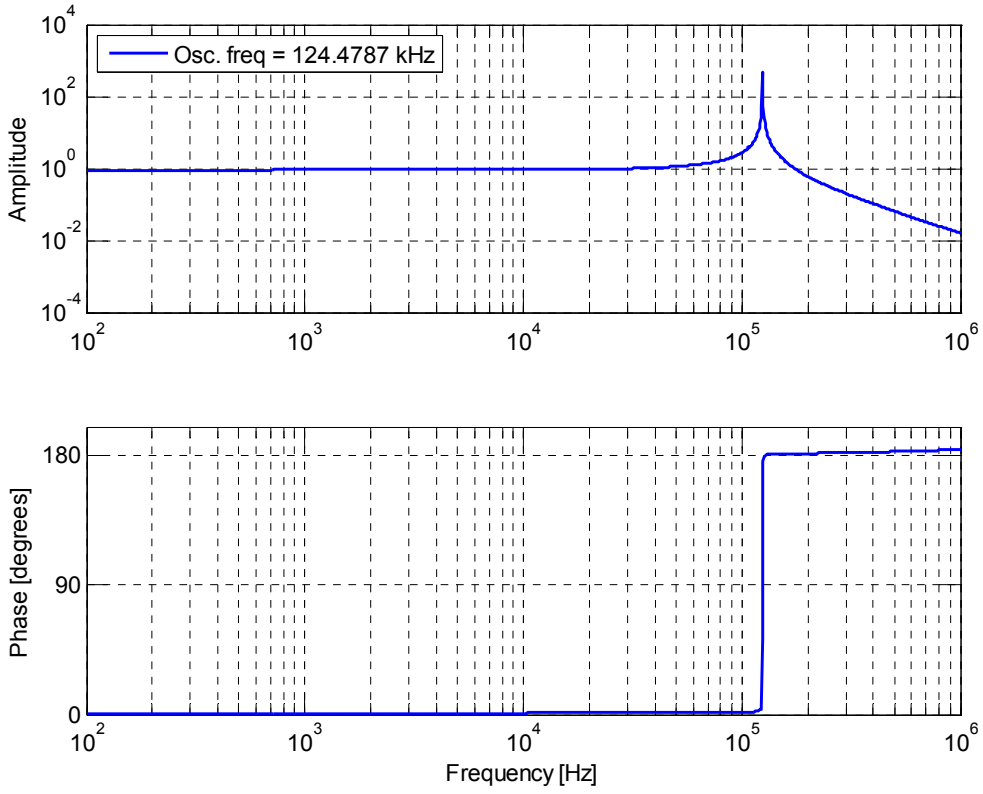

Figure 3.3 Bode plot of the modelled laser transfer function.

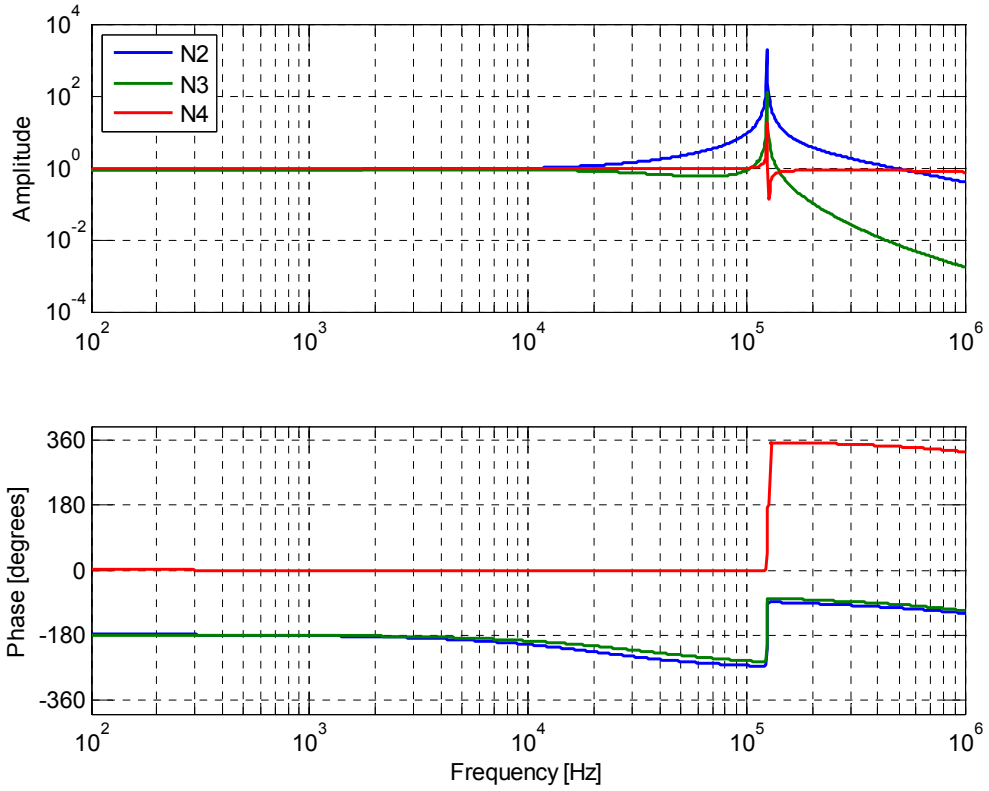

Figure 3.4: Bode plot of the transfer functions of the population densities.

3.7 Without excited-state absorption

To demonstrate the importance of ESA in this model, the ESA at the lasing wavelength was removed. This was achieved by setting the value of γ to zero, and hence $\sigma_{ESA} = 0$.

The output of the Matlab model is shown in Figure 3.5, showing the photon emission (top) and population densities with time. The initial oscillations are due to the modelled laser transitioning to equilibrium from an initial zero state. Bode plots of the modelled laser transfer function and that of the different population densities are shown in Figure 3.6 and Figure 3.7 respectively. Again, the system begins with strong transience; however, these oscillations decay exponentially, resulting in an oscillation-free steady state. This is also reflected in the transfer functions, with the relaxation oscillation resonance peak accompanied by the standard -180° phase lag, or a positively damped oscillator.

Thus, the presence of ESA at the lasing wavelength is crucial in reproducing the observed unstable oscillations in this model.

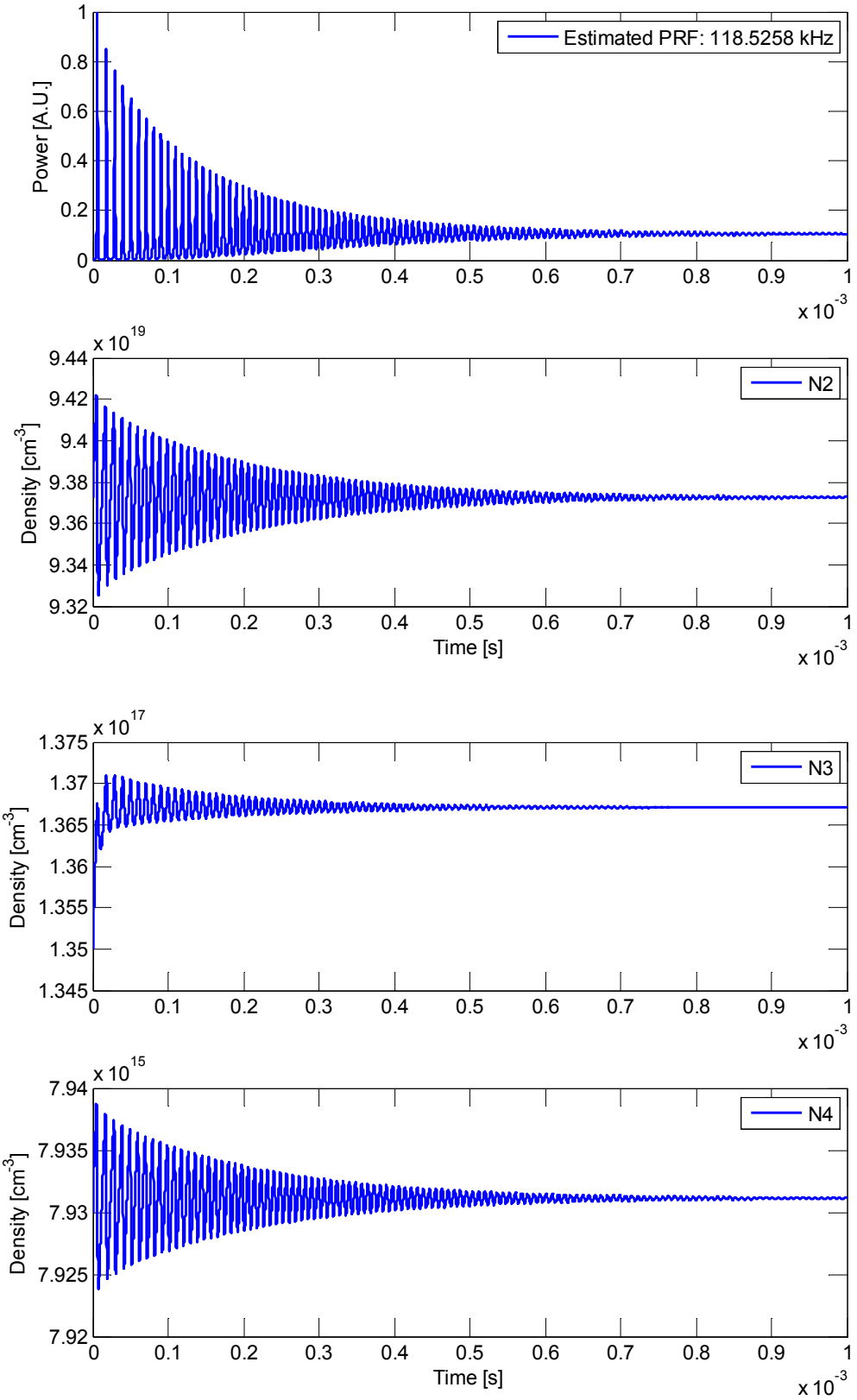

Figure 3.5: The output of the laser model in the absence of ESA, showing the photon emission (top) and population densities with time.

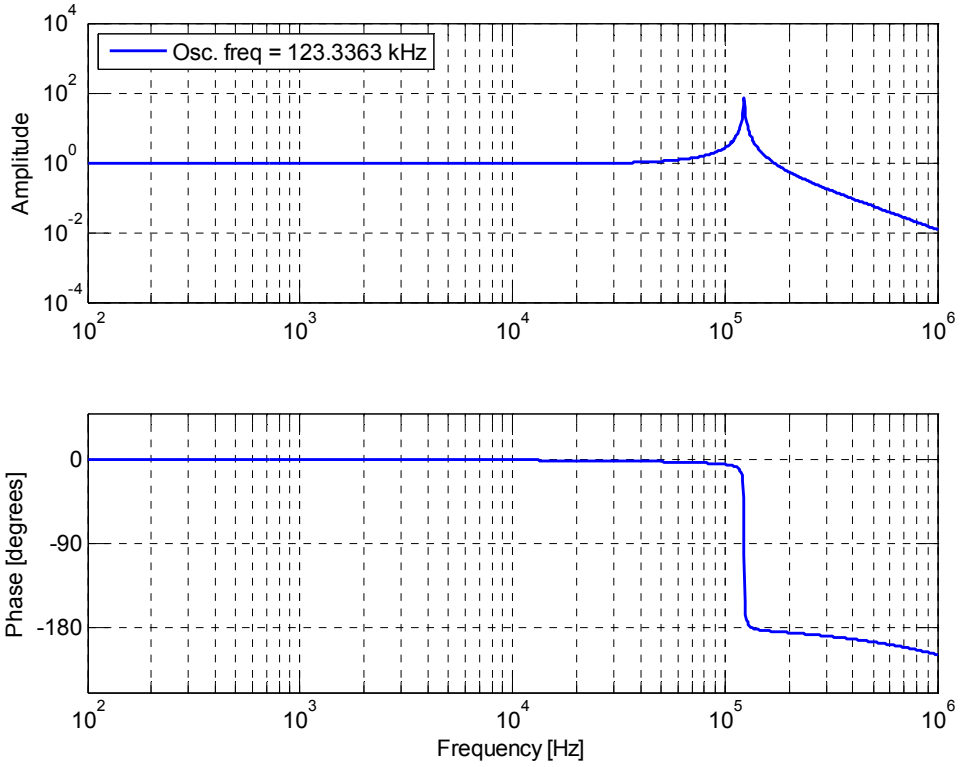

Figure 3.6: Bode plot of the modelled laser transfer function, without ESA.

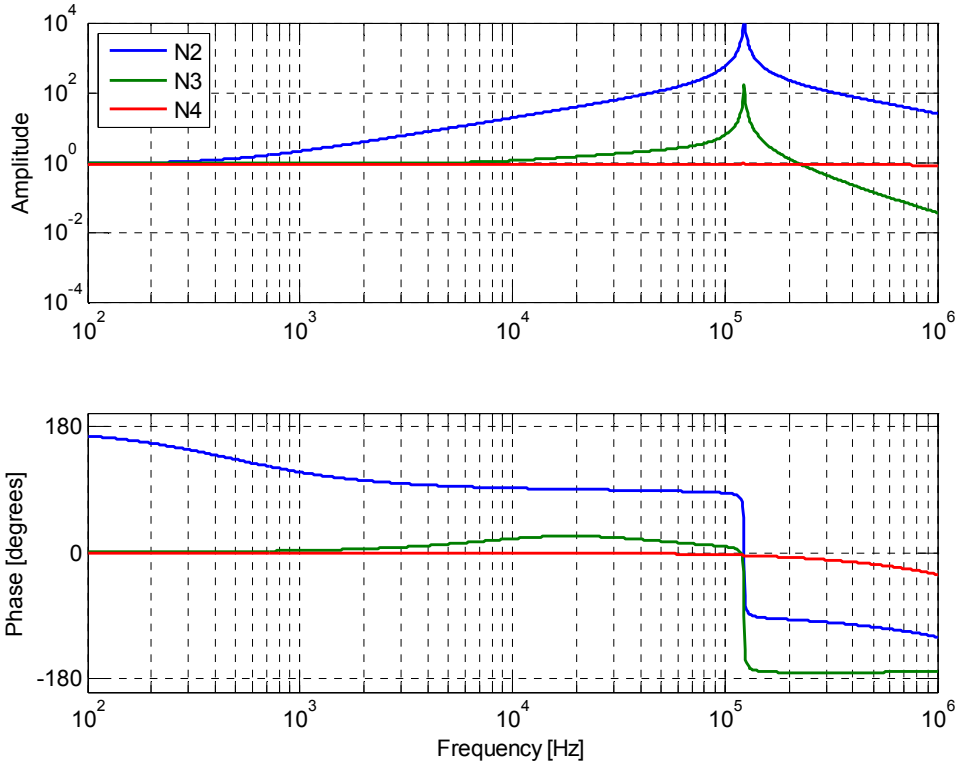

Figure 3.7: Bode plot of the transfer functions of the population densities.

3.8 Feedback modelling

The rate equations were modified to include the effect from feedback. The feedback is directly into the pump diode, and thus affects the pump rate, R_p. This is taken into account by making the substitution $R_p \rightarrow R_p + \Delta R_p$ in the rate equations Equation 3.1, where ΔR_p is the net change in pump rate due to the feedback loop.

In order to determine ΔR_p, the feedback loop was analysed as an AC-coupled non-inverting amplifier, followed by a high-frequency roll-off due to the bandwidth of the electronics, as represented in the circuit diagram shown in Figure 3.8.

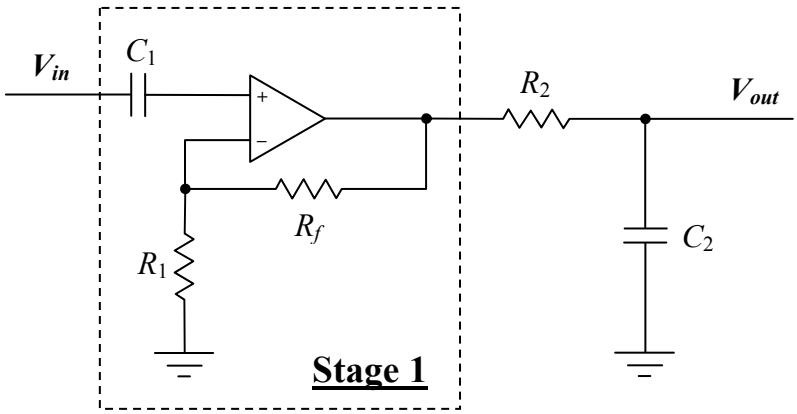

Figure 3.8: Circuit diagram representing the feedback loop.

Recall that the amplifier was non-inverting due to the phase delay resultant from the cross-relaxation lifetime in Tm:$YAlO_3$, as mentioned in Section 2.5.3.

The first stage, the AC-coupled non-inverting amplifier, is described by the equations:

$$V_{in} - \int \frac{I_1(t)dt}{C_1} = I_1 R_1, \tag{3.14}$$

$$V_1 = I\left(R_1 + R_f\right). \tag{3.15}$$

Equation 3.14 can be rewritten in the differential form:

$$\frac{dV_{in}}{dt} - \frac{I_1(t)}{C_1} = \frac{dI_1}{dt} R_1. \tag{3.16}$$

Substituting Equation 3.15 into Equation 3.16 results in an equation for dV_1/dt:

$$\frac{dV_1}{dt} = G_{amp}\frac{dV_{in}}{dt} - \frac{V_1}{\tau_{in}}, \tag{3.17}$$

where $G_{amp} = 1 + R_f / R_1$ is the amplifier gain and $\tau_{in} = R_1 C_1$ is the time constant of the input high-pass filter. The second stage, the low-pass filter, is described by:

$$V_1 = \int \frac{I_2(t)dt}{C_2} + I_2 R_2, \tag{3.18}$$

$$V_{out} = V_1 - I_2 R_2. \tag{3.19}$$

Substituting Equation 3.19 into the differential form of Equation 3.18 and rearranging results in an equation for dV_{out}/dt:

$$\frac{dV_{out}}{dt} = \frac{V_1 - V_{out}}{\tau_{out}}, \tag{3.20}$$

where $\tau_{out} = R_2 C_2$ is the time constant of the output low-pass filter.

For simplicity and due to proportionality, all of the gain and efficiency factors are all encompassed by the gain factor G. These include the fraction of laser photon density incident on the photodetector, the voltage amplifier, the current converter and the change in R_p. With this simplification, the parameters V_{in} and V_{out} equate to the laser photon density, ϕ, and the change in pump rate, ΔR_p, respectively.

Feedback was introduced into the system by considering the following equations in addition to the original rate equations of the system in Equation 3.1, along with the substitution $R_p \rightarrow R_p + \Delta R_p$:

$$\frac{dV_1}{dt} = G_{amp}\frac{d\phi}{dt} - \frac{V_1}{\tau_{in}}, \tag{3.21}$$

$$\frac{d(\Delta R_p)}{dt} = \frac{V_1 - \Delta R_p}{\tau_{out}}. \tag{3.22}$$

The output of the laser model with feedback and the bode plot of the associated transfer function are shown in Figure 3.9 and Figure 3.10 respectively.

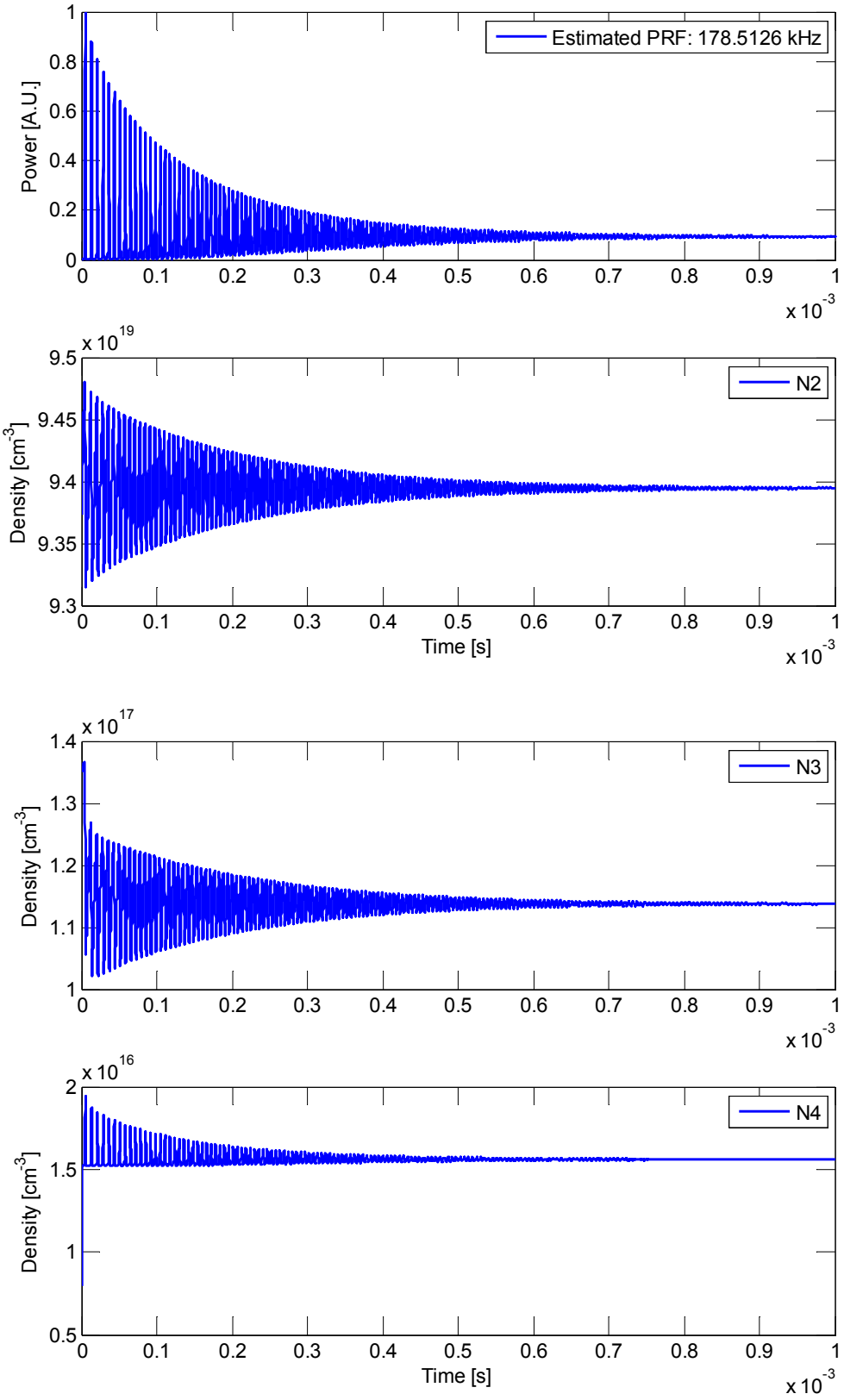

Figure 3.9: The output of the laser model with feedback, showing the photon emission (top) and population densities with time.

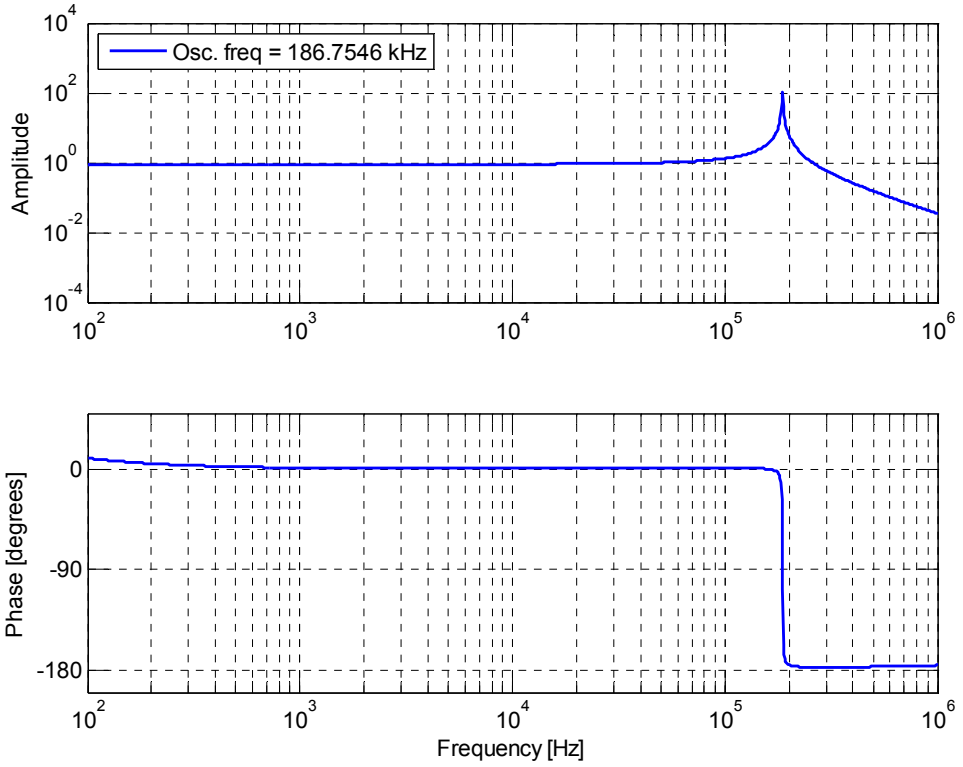

Figure 3.10 Bode plot of the modelled laser transfer function with feedback.

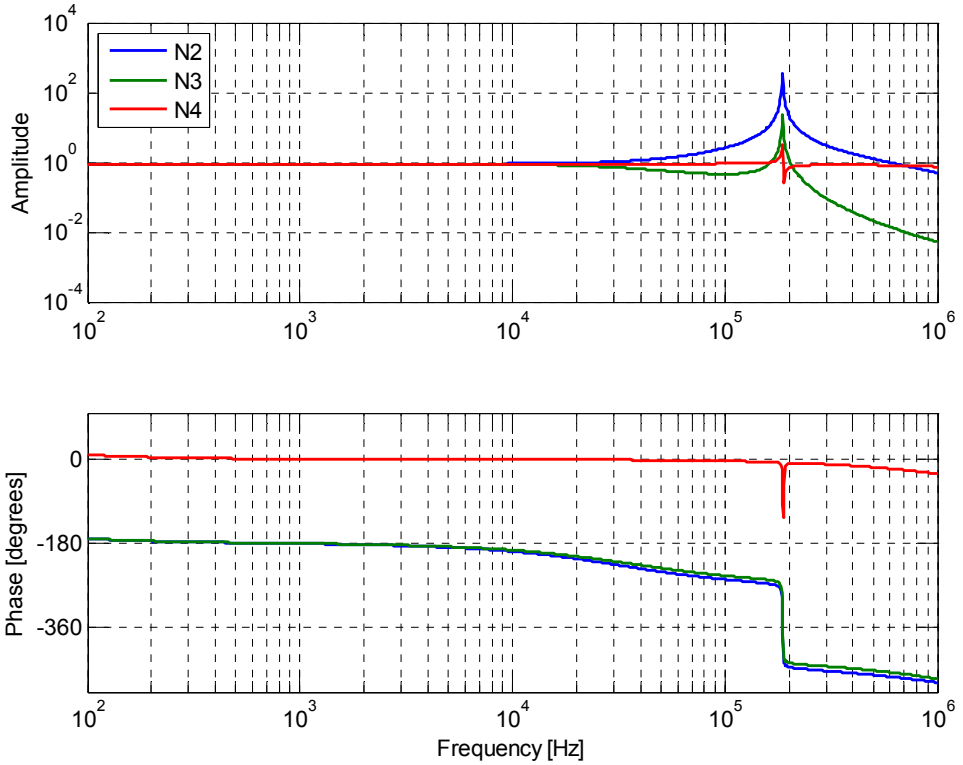

Figure 3.11: Bode plot of the transfer functions of the population densities.

The output of the model with feedback in both the time and frequency domains both demonstrate successful suppression of the self-pulsing, with the initial transient behaviour decaying to a stable CW output. This result is consistent with both the simple model in Section 2.5.2 and experiments.

3.9 Chapter summary

To understand the cause of the self-pulsing in Tm:$YAlO_3$ lasers, the dynamics within the laser gain medium was investigated. A model of the laser was written in Matlab, using the rate equations associated with the first four energy levels and ESA at the lasing wavelength. This model successfully reproduced the self-pulsing behaviour of the Tm:$YAlO_3$ laser. The model was extended to the frequency domain by linearising the rate equations, and the transfer function of the model laser was obtained. The transfer function was that of a negatively damped relaxation oscillation, consistent with the simple model and experiments, described in Section 2.5.5. ESA at the lasing wavelength was demonstrated to be critical for the model to reproduce experimental results. The model was further extended to include the feedback loop, which showed full suppression of the self-pulsing due to ESA.

The model presented has successfully reproduced the behaviours of our Tm:$YAlO_3$ laser experiments for different conditions, including pulse suppression by feedback. Further exploration of the various parameters would likely improve the accuracy of the model in predicting experimental results. However, the validity of these results depend crucially on the value of the ESA cross-section at the lasing wavelength, which is measured in the following chapter.

4 Excited-state absorption

4.1 Introduction

While the model of the laser dynamics described in the Chapter 3 reproduces qualitatively the behaviour of the Tm:$YAlO_3$ cuboid laser, it relies on a significant ESA at the lasing wavelength to occur between the $^3H_5$ level and $^3H_4$ level. The ESA cross-section assumed by the model is half that of the emission cross-section or greater, with $\sigma_{ESA} \sim 0.5 - 0.65\ \sigma$. The value of σ_{ESA} was shown to be critical to the behaviour of the modelled laser, with stable output predicted instead of the experimentally-observed unstable self-pulsing in the absence of ESA at the lasing wavelength. The meareuement of the value of σ_{ESA} has not been reported prior to this work.

An alternative mechanism that can result in strong self-pulsing in lasers is nonlinear dynamical chaos [87]–[89]. The output of the Tm:$YAlO_3$ laser resembles that of NH_3 lasers, which is well-known for exhibiting Lorenz-type chaotic pulsations. No work involving the analysis of Tm:$YAlO_3$ lasers as a chaotic system has been reported prior to this work.

This chapter describes the measurement of the ESA cross-section at the lasing wavelength σ_{ESA} and the ratio of ESA to ground-state absorption (GSA) cross-sections, $\gamma = \sigma_{ESA}/\sigma$. This chapter also describes the chaos analysis of the output of a Tm:$YAlO_3$ laser using two independent methods, and the conclusions regarding the likely cause of self-pulsing is presented.

The theory and experimental design for the direct measurement of the ESA at the lasing wavelength is described in Section 4.2 and Section 4.3, which includes the

predicted result. The two laser sources used are characterised in Section 4.4. The results at different time scales of the probe beam experiment is described in Section 4.5, which is then analysed in Section 4.6 to give the ESA cross-section. Section 4.7 describes the remodelling of the laser dynamics using the experimentally obtained value for γ. The chaos analysis of the laser output intensity is described in Section 4.8. The chapter is concluded in Section 4.9.

The results reported in this chapter have been accepted for publication in Physical Review A [129]. A copy of that paper is included in Appendix A.

4.2 Direct measurement of ESA – theory

4.2.1 Ion transitions

ESA at the lasing wavelength can be observed by using a short, high energy pump pulse to excite ions in the Tm:$YAlO_3$ crystal to the $^3H_5$ level in the presence of a CW probe beam at the lasing wavelength. The excited ions no longer contribute to GSA of the probe beam, but instead causes ESA. By monitoring the transmission of the probe beam during the decay process after the pump pulse, the ESA cross-section and lifetimes of the energy levels can be obtained.

After the short pump pulse, Tm^{3+} ions in the $^3H_5$ level undergo de-excitation to the $^3F_4$ manifold via two primary avenues, as shown in Figure 4.1. If an excited ion in the $^3H_5$ level absorbs a photon from the probe beam, the ion is further excited to the $^3H_4$ level (i.e. ESA); approximately 98% of these ions then undergo cross-relaxation to the $^3F_4$ manifold ($^3H_4 + {}^3H_6 \rightarrow 2\ {}^3F_4$) [130]. For the ions that do not undergo ESA, almost all will decay non-radiatively to the $^3F_4$ level [128]. The probability of the ion undergoing ESA or not is dependent on the power of the probe beam.

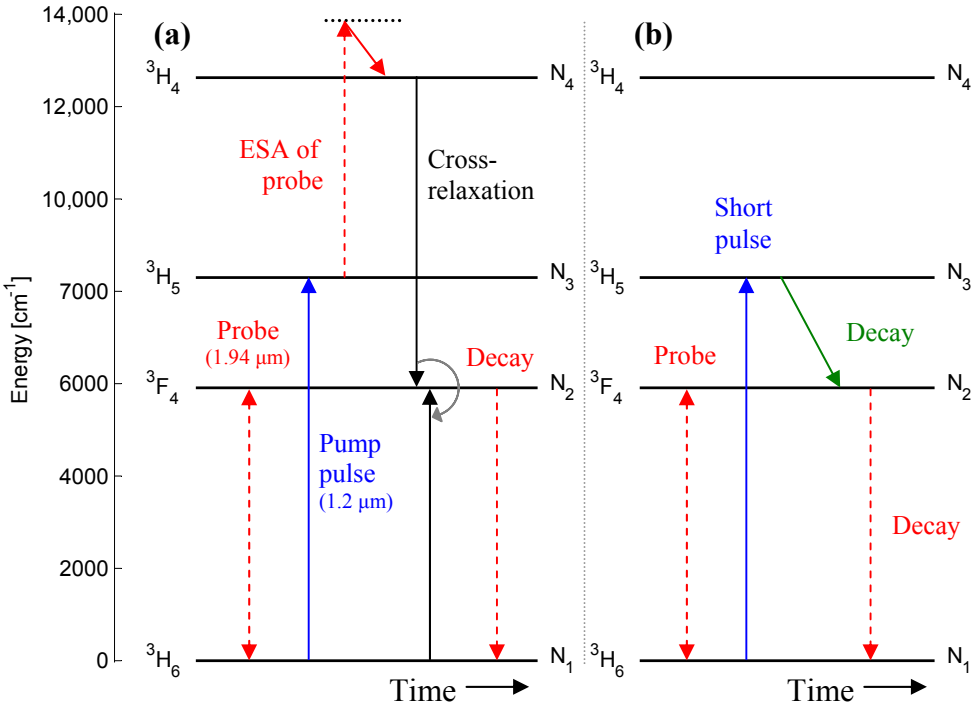

Figure 4.1: Two primary avenues for de-excitation of Tm^{3+} ions after excitation by a short pump pulse at 1.2 µm, via (a) ESA, and (b) no ESA.

4.2.2 Expected probe beam transmission profile

The ions in the Tm:$YAlO_3$ crystal undergo several transitions during and after the short pump pulse, before returning to the ground state, as was shown previously in Figure 4.1. Each of these transitions occurs at different time scales, and hence can be distinguished. They are thus expected to translate into changes in the transmission of the probe beam, as illustrated in Figure 4.2. The stable probe transmission level after each transition can be used to determine the ESA cross-section at the lasing wavelength.

The equilibrium transmission of the probe beam through the crystal prior to the short pulse is given simply by Beer-Lambert's law:

$$\begin{aligned} T_{eq} &= \exp(-\sigma\,[f_u N_2 - f_l (N - N_2)]\,l) \\ &\approx \exp(-\sigma\, f_l N l) \quad \text{for } N_2 << N\,, \end{aligned} \tag{4.1}$$

where σ is the cross-section for transitions at the probe wavelength between the ground state and the $^3F_4$ level, f_u and f_l are the Boltzmann factors for the upper and lower

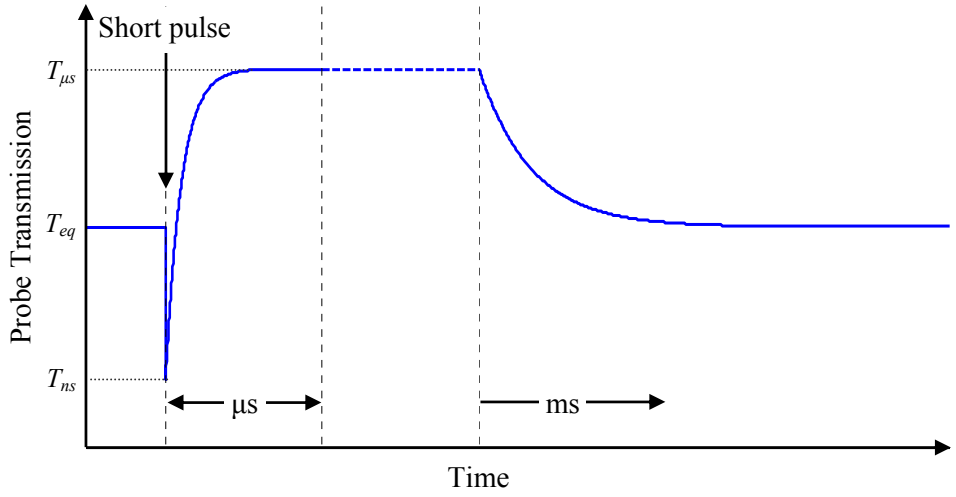

Figure 4.2: Expected probe transmission trace during and after the short pulse.

lasing manifolds respectively, N is the total Tm^{3+} ion density, N_2 is the equilibrium ion density of the $^3F_4$ level, and l_{cryst} is the length of the crystal.

Tm^{3+} ions are excited from the ground state, $^3H_6$, to the $^3H_5$ level during the short pump pulse. The absorption at the lasing wavelength changes due to this excitation, as these ions no longer contribute to the ground-state absorption of the probe beam, but instead contribute to ESA. The transmission of the probe beam immediately after the short pump pulse is given by:

$$T_{ns} = T_{eq} \exp\left([\sigma f_l - \sigma_{ESA}] \Delta N \, l \right), \tag{4.2}$$

where ΔN is the number of ions excited by the pump pulse and σ_{ESA} is the effective cross-section for the absorption of a probe photon by an ion in the $^3H_5$ level.

Ions in the $^3H_5$ level readily decay non-radiatively to the upper lasing level $^3F_4$, as the energy difference between $^3H_5$ and $^3F_4$ levels is readily bridged by phonons. Only one or two phonons are required [126], and hence the decay process between these two states has a lifetime in the order of microseconds [128].

Some of the ions will absorb a probe photon and be excited to the $^3H_4$ level. The majority of these ions will then cross-relax to the $^3F_4$ level, as discussed previously. Cross-relaxation results in additional ions being excited to the $^3F_4$ level from the ground state. This is undesirable, as it introduces uncertainty in the population density of the

$^3F_4$ level. To ensure non-radiative decay is the dominant process, the probe beam needs to be sufficiently weak to minimise the number of ions that undergo ESA.

Assuming negligible ESA, the transmission of the probe beam following the decay is given by:

$$T_{\mu s} \approx T_{eq} \exp\left(\sigma [f_u + f_l] \Delta N \, l\right). \tag{4.3}$$

The ions excited by the pump pulse gradually decay back to the ground state and the system relaxes back to its equilibrium state, with the transmission of the probe beam given by Equation 4.1.

4.2.3 Calculation of the excited-state absorption cross-section

The ratio between the ESA and laser emission cross-section $\gamma = \sigma_{ESA}/\sigma$ can be determined from the measurement of the changes in probe transmission. Assuming that the exponents in Equation 4.2 and Equation 4.3 are much smaller than unity, i.e. if $\Delta N << \left|([\sigma f_l - \sigma_{ESA}] l)^{-1}\right|$ and $\Delta N << \left|(\sigma [f_u + f_l] l)^{-1}\right|$, then the approximation $e^x \approx 1 + x$ can be applied to Equation 4.2 and Equation 4.3. The number of ions excited by the pump pulse is given by:

$$\Delta N = \frac{1}{\sigma (f_u + f_l) l} \left(\frac{T_{\mu s} - T_{eq}}{T_{eq}} \right). \tag{4.4}$$

The ratio of cross-sections $\gamma = \sigma_{ESA}/\sigma$ is then given by:

$$\begin{aligned} \gamma &\approx f_l - \frac{1}{\sigma \Delta N l} \left(\frac{T_{ns} - T_{eq}}{T_{eq}} \right) \\ &= f_l - (f_u + f_l) \left(\frac{T_{ns} - T_{eq}}{T_{\mu s} - T_{eq}} \right). \end{aligned} \tag{4.5}$$

Assuming linearity in the photodetector, the ratio of the transmission change equals that of the voltage change, further simplifying Equation 4.5:

$$\gamma = f_l - (f_u + f_l)\frac{\Delta V_{ns}}{\Delta V_{\mu s}}, \tag{4.6}$$

where $\Delta V_{ns} = K(T_{ns} - T_{eq})P_{probe}$ and $\Delta V_{\mu s} = K(T_{\mu s} - T_{eq})P_{probe}$. K is the detector constant and P_{probe} is the probe power incident on the crystal. Equation 4.1 can be used to determine the cross-section σ, and hence the ESA cross-section σ_{ESA} can also be determined.

4.3 Direct measurement of ESA – experimental design

The schematic of the experiment is shown in Figure 4.3. The 4 at.% Tm:$YAlO_3$ crystal from the laser in Chapter 2 was used. The CW probe beam was generated by fibre-Bragg-grating-stabilised Tm^{3+}-doped fibre laser operating at 1.944 µm. Although this fibre laser operated at a slightly longer wavelength than the peak emission wavelength of 1.940 µm, the energy difference of 10.6 cm^{-1} is negligible when compared to the energy differences between Stark sublevels in $^3H_4$ and the phonon energies in $YAlO_3$, which are both in the order of 100 cm^{-1} [63], [126]. A wire-grid polariser with extinction ratio of >1500 was used to ensure the incident probe light was polarised along the *c*-axis of the Tm:$YAlO_3$ crystal to measure the excited-state.

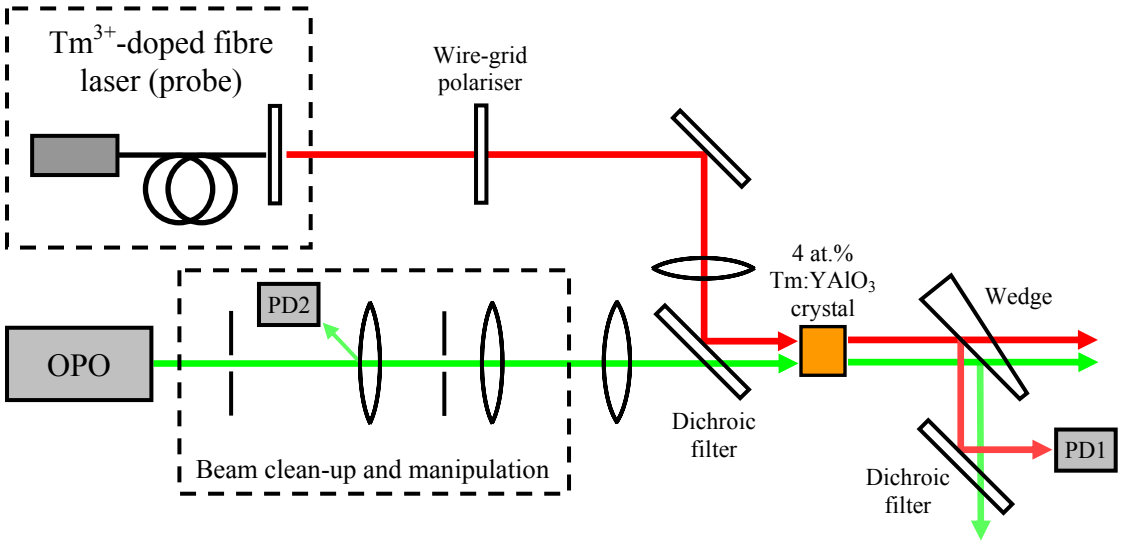

Figure 4.3: Simplified schematic of the ESA measurement experiment.

The fibre laser was operated at an output power of approximately 300 mW, which corresponds to 0.1% of ions in the $^3F_4$ level at steady state. This satisfies the assumption in Equation 4.1. Furthermore, it was calculated that negligible amounts of the ions in the $^3H_5$ level after the pump pulse would undergo ESA due to the short microsecond-scale lifetime of this level. This ensures non-radiative decay is the dominant decay process for ions in the $^3H_5$ level.

A broadband tunable optical parametric oscillator (OPO) (versScan) was used to generate the short pulses at 1.2 μm for excitation into the $^3H_5$ level. The OPO was pumped by a frequency-tripled, Q-switched Nd:YAG laser, which generated 5-ns pulses at 10 Hz with pulse energies up to 80 mJ at 355 nm. These pulses are converted to a wavelength of 1.2 μm by the OPO, the absorption wavelength for the $^3H_6 \rightarrow {}^3H_5$ transition. The output wavelength was then fine-tuned to the absorption peak of Tm:$YAlO_3$ by minimising the transmission through the crystal. The pulse energy at this wavelength was approximately 7 mJ at the output of the OPO. However, the output beam was astigmatic and of very poor beam quality. Apertures were used to clean up the mode in order to focus the beam down to a sufficiently small spot size, while cylindrical lenses were used to correct for the astigmatism. This resulted in only 0.8 mJ of energy incident on the crystal. For a beam diameter of 250 μm measured below in Section 4.4.1, this corresponds to an estimated 2.2×10^{19} cm^{-1} or 2.8% of Tm^{3+} ions excited in the pumped volume.

The two beams were combined using a dichroic mirror, which was HR at 1.94 μm and AR at 1.2 μm. The two beams were focused independently such that both beams focused at the same point with the same beam diameter. This was verified using a pyroelectric camera as described in the following section. The Tm:$YAlO_3$ crystal was placed at the focus of the two beams.

A fast extended-InGaAs photodetector (PD1) with < 25 ns rise time (Thorlabs DET10D) was used to measure the transmission of the probe beam. Some of the bandwidth of the detector was sacrificed for a higher gain from the photodetector by using a 500-Ω terminator instead of a 50-Ω terminator. This boosted the output voltage but also increased the rise time by an order of magnitude. However, it is shown in Figure 4.11 that the rise time was still on the order of nanoseconds, which is more than adequate for this experiment. A dichroic mirror and long-pass filters (wavelength cut-off at 1400 – 1500 nm) were used to further attenuate the transmitted 1.2 μm pump pulse.

An InGaAs photodetector (PD2) with < 10 ns rise time (Thorlabs DET10C) was used to detect the 1.2-μm pulse from the OPO, to be used as the trigger for the oscilloscope. The pulses are highly energetic, and hence scattered light from the optics was sufficient to obtain a strong signal from the detector.

4.3.1 Predicted transmission change

To predict the values for T_{ns} and $T_{\mu s}$ required for $\gamma = \sigma_{ESA}/\sigma = 0.65$ that is necessary for self-pulsation, the GSA cross-section of the probe beam is required. This was calculated by rearranging Equation 4.1:

$$\sigma = \frac{-\ln(T_{eq})}{f_l \, N \, l}. \tag{4.7}$$

The transmission of the probe beam through the Tm:$YAlO_3$ crystal was measured using a thermal power meter to be $T_{eq} = 0.920 \pm 0.003$. With $l = 4.545 \pm 0.005$ mm and $N_{conc} = 7.8 \times 10^{20}$ cm^{-3}, the cross-section σ was calculated to be $(7.8 \pm 0.3) \times 10^{-21}$ cm^2.

The predicted transmissions T_{ns} and $T_{\mu s}$ was calculated using Equation 4.2 and Equation 4.3 respectively, using the values $\Delta N = 0.028\ N$ and $\sigma_{ESA} = 0.65\sigma$. These were calculated to be $T_{ns} = 0.877$ and $T_{\mu s} = 0.941$, which should be readily observable.

Note also that the exponents for Equation 4.2 and Equation 4.3 were calculated to be -0.048 and 0.0227 respectively, which satisfy the approximation conditions for Equation 4.4 and Equation 4.5.

4.4 Characterisation of laser sources

4.4.1 Beam profile at the crystal

A pyroelectric camera (Pyrocam III) was placed at the focal point of the two beams in order to ensure both beams focus at the same point with the same beam diameter. Sample beam profiles of the probe beam and OPO beam are shown in Figure 4.4. The pixel size for the pyroelectric camera is 100 × 100 μm. From these beam profiles, the

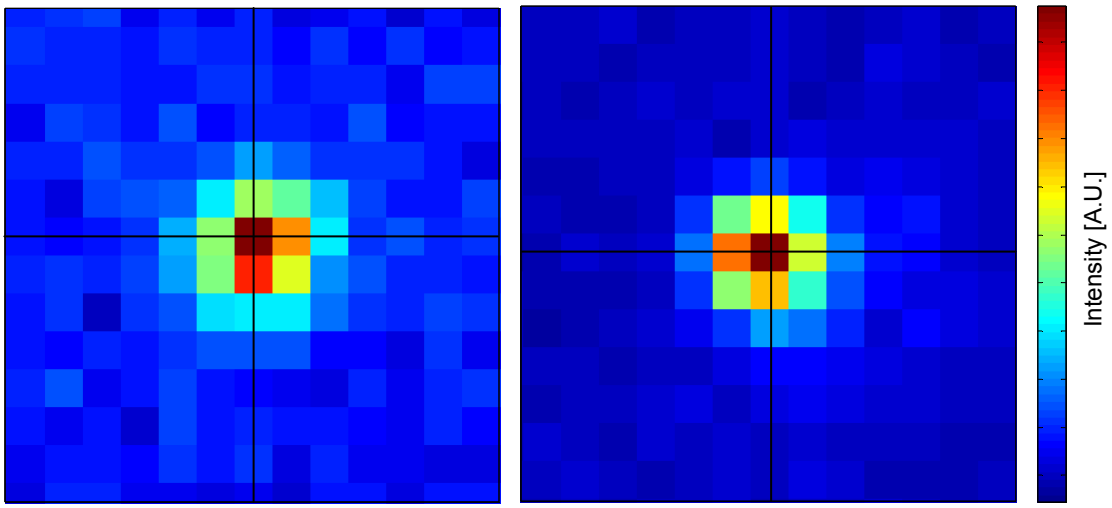

Figure 4.4: Beam profile of the probe beam (left) and OPO pulse (right) at the focal point (pixel size: 100 × 100 μm).

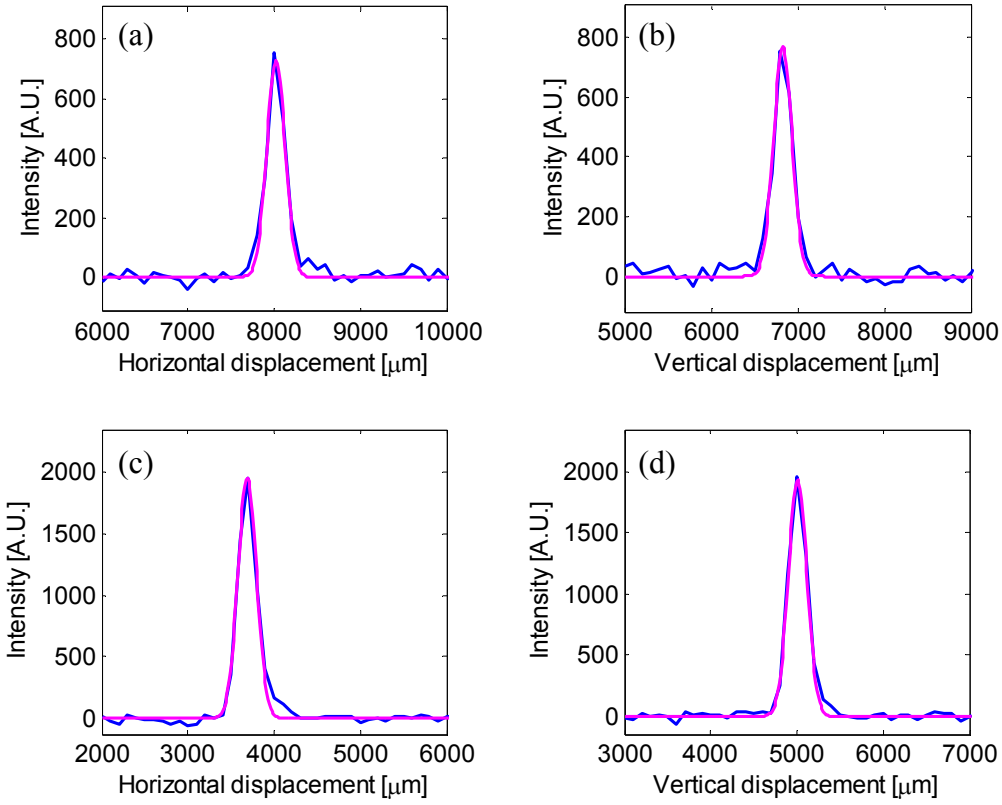

Figure 4.5: Gaussian fits for the two axes of the probe beam (a) – (b) and of the OPO beam (c) – (d).

beam widths for the horizontal and vertical directions were determined using two one-dimension Gaussian fits of the intensity, as shown in Figure 4.5. The beam size for both the probe beam and the OPO beam were found to be well-matched, with a FWHM of approximately 250 μm.

4.4.2 Laser output spectra

The output spectrum of the fibre laser (probe) was measured using an OSA (Yokogawa AQ6375) with a resolution of 0.05 nm, and is shown in Figure 4.6. The doped fibre of the fibre laser was a polarisation-maintaining fibre, and hence the fibre laser operated at two wavelengths corresponding to the two polarisations. The energy difference between the two wavelengths is small compared to the energy differences between Stark sublevels and the phonon energies in $YAlO_3$, which are both in the order of 100 cm^{-1} [63], [126].

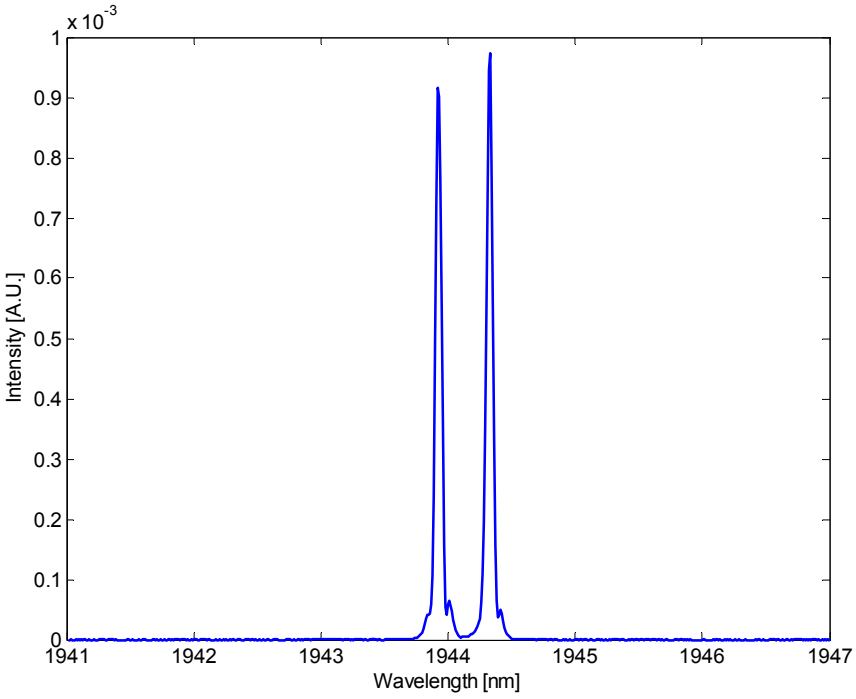

Figure 4.6: Spectrum of the probe beam from the Tm^{3+}-doped fibre laser.

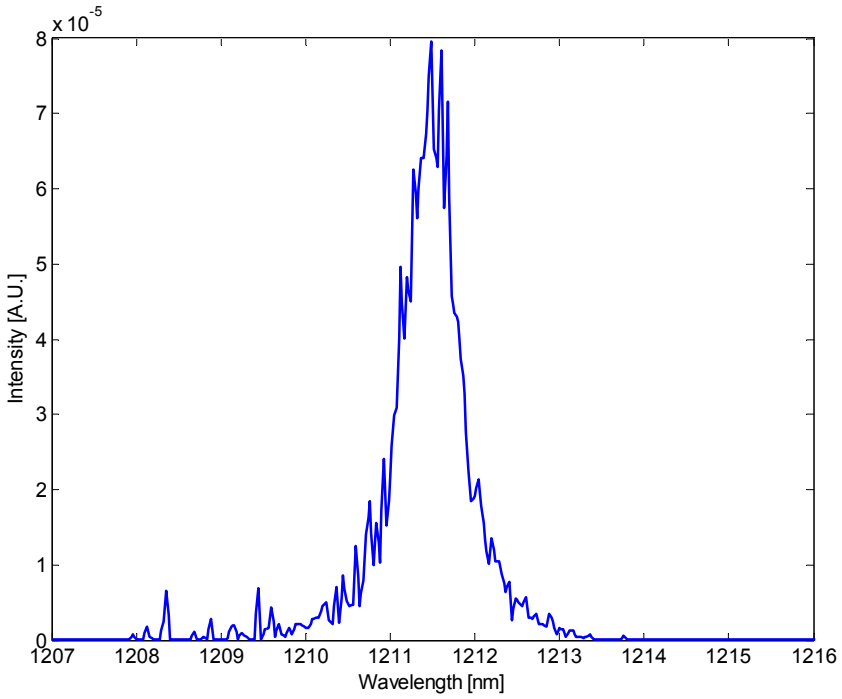

Figure 4.7: Spectrum of the OPO beam, averaged over many pulses.

The output wavelength of the OPO was set to 1.2 μm to excite ions to the $^3H_5$ energy level. The wavelength was fine-tuned to the absorption peak of Tm:$YAlO_3$ by minimising the transmission through the crystal. The output spectrum of the OPO beam, corresponding to maximal absorption in the Tm:$YAlO_3$ crystal, was measured using another OSA (Ando AQ6315E) with a resolution of 0.5 nm, and is shown in Figure 4.7.

4.5 Probe beam transmission

The time dependence of the transmissions of the probe beam at the different time scales are shown in Figure 4.8 and Figure 4.9. The laser noise on the probe beam was on the order of 1% of the DC level, or ±3 mV. As the observed signal was of the same order, the signal was only barely observable above the noise. To improve the signal to noise of the measurement, the traces shown are averaged over 128 pulses. As predicted in Section 4.2.2, the transmission has an exponential increase in the microsecond time scale after the short pump pulse, followed by a gradual exponential decrease on the millisecond time scale.

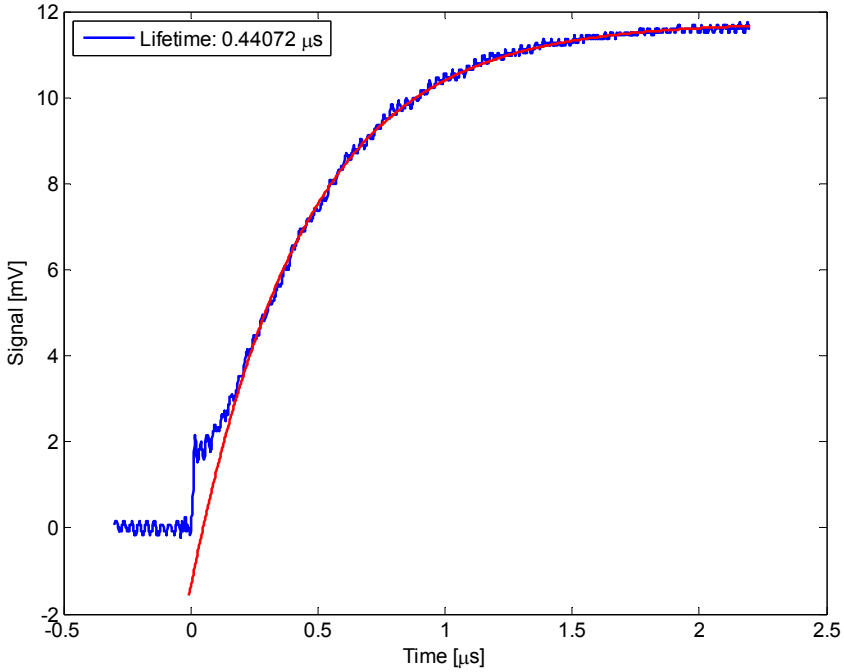

Figure 4.8: AC-coupled probe beam signal in the microsecond range, with an exponential fit.

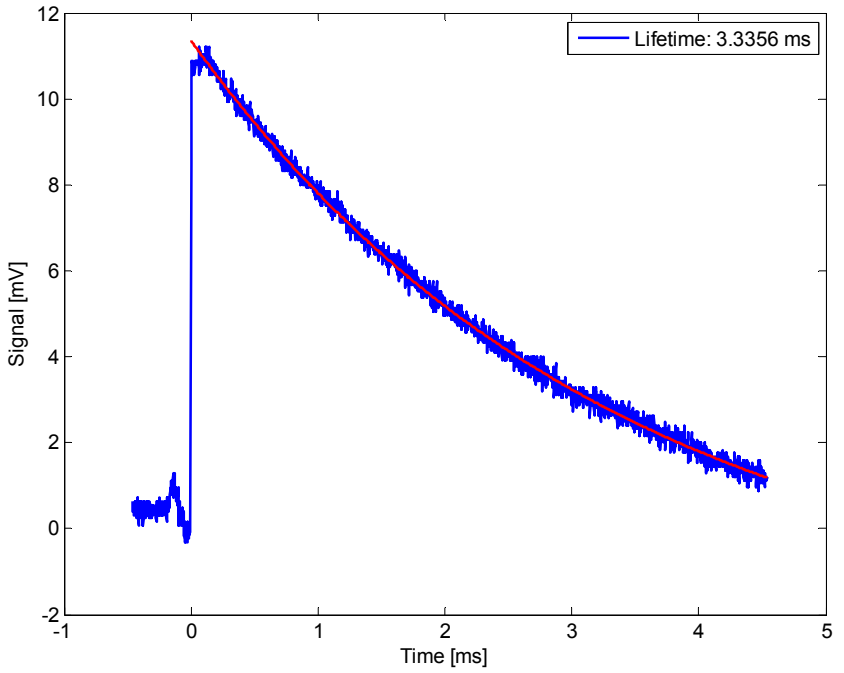

Figure 4.9: AC-coupled probe beam signal in the millisecond range, with an exponential fit.

The transmission on the microsecond timescale corresponds to the decay from the $^3H_5$ level to the $^3F_4$ level. It is the only mechanism in which the transmission of the probe beam increases. The decay rate for the exponential of best fit, fitted using the curve-fitting toolbox in MATLAB, was $(2.27 \pm 0.01) \times 10^6$ s^{-1}, corresponding to a lifetime of 0.440 ± 0.005 μs. The initial 0.25 μs of the data was omitted from the fit due to electronic ringing, which is responsible for the sudden increase in initial transmission, and is discussed below. ESA of the probe beam is negligible due to the low power of the probe beam, and hence this lifetime is the non-radiative lifetime of the $^3H_5$ level. To the best of our knowledge, this is the first measurement of this decay time constant. It is shorter than the 5.6 μs calculated in literature [128].

The transmission on the millisecond timescale corresponds to the decay from the $^3F_4$ level to the ground state. The decay rate for the exponential of best fit was 300 ± 5 s^{-1}, corresponding to a time constant of 3.34 ± 0.05 ms. This time constant is shorter than the spontaneous lifetime from literature [68] due to stimulated emission induced by the incident probe beam. The stimulated emission rate was calculated to be approximately 17% of the total decay rate, using the emission cross-section, Boltzmann distribution factors and probe power. When the stimulated emission rate was subtracted from the total decay rate, the spontaneous decay rate was calculated to be 4.0 ± 0.1 ms, approximately consistent with that in the literature of 4.4 ± 0.1 ms [68].

The expected instantaneous decrease in the transmission of the probe following the pump pulse was obscured by residual pump power from the OPO pulse. Some of the light from the OPO beam could still be observed despite the long-pass filter directly in front of the photodiode. The temporal profile of this leakage was quantified by blocking the probe beam and observing the OPO beam only, as shown in Figure 4.10, along with the original trace and the background noise.

The extended exponentially-decaying tail of the OPO pulse was due to the impedance mismatch between the photodetector output and the oscilloscope due to using to a 500-Ω terminator instead of the normal 50-Ω terminator. A trace with better resolution of the OPO pulse as observed by the photodetector is shown in Figure 4.11, which shows significant ringing. The trace using a 50-Ω terminator is also shown for

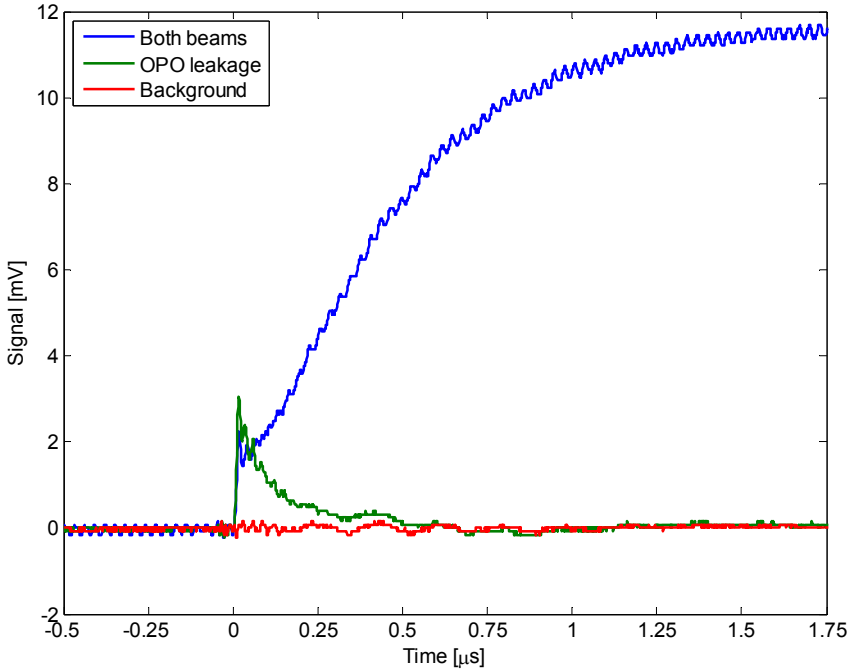

Figure 4.10: Photodetector output during and after a short pulse with both beams (blue), probe beam blocked, i.e. OPO leakage (green) and electrical background when both beams were blocked (red).

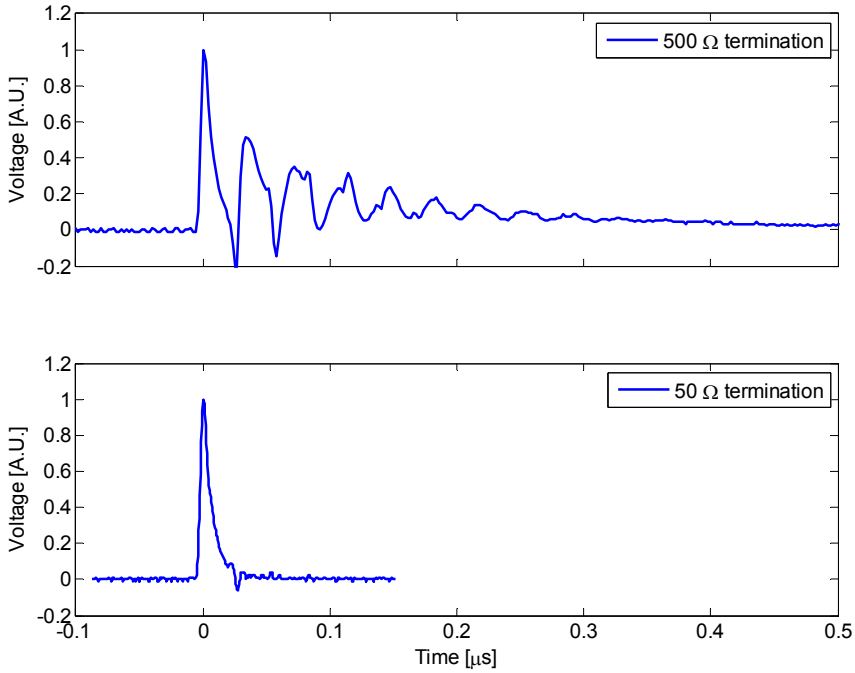

Figure 4.11: The OPO pulse as observed by the extended InGaAs photodetector with 500- Ω termination (top) and 50-Ω termination (bottom).

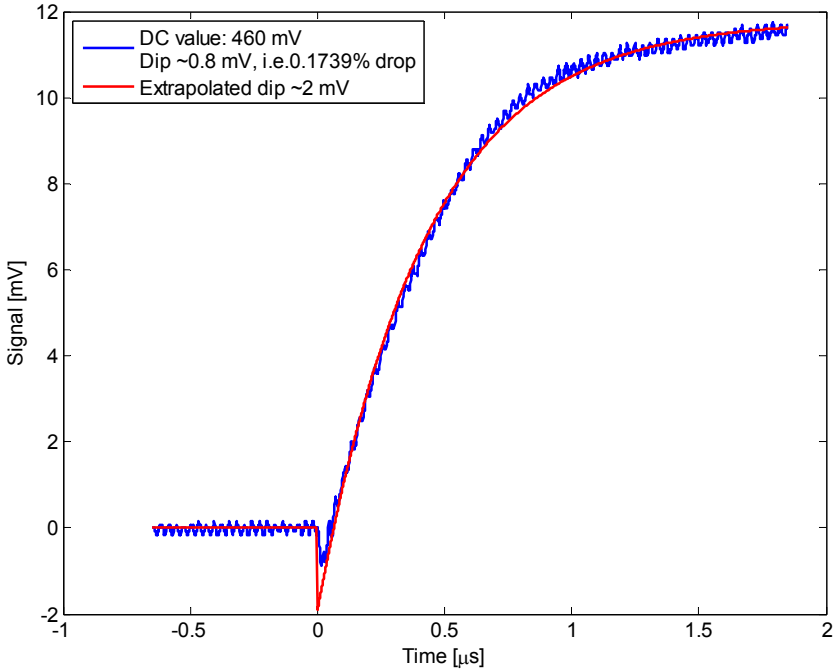

Figure 4.12: Signal from the photodetector with background and OPO leakage removed, with an exponential fit to the latter part of the curve.

comparison, showing no ring-down decay as seen with the 500-Ω terminator. The higher termination resistance was used to boost the signal from the photodetector in order to achieve the required sensitivity, and hence was unavoidable without an additional pre-amplifier that could not be obtained in the timeframe of the experiment.

The instantaneous decrease can be obtained by extrapolating the exponential fit of the decay curve to time $t = 0$ due to the quality of the fit, giving a voltage drop of 2.0 ± 0.25 mV. This result was verified by measuring the leakage signal, measured in the absence of the probe beam, and subtracting it from the photodetector signal to obtain signal from the probe beam only. The resultant corrected trace is shown in Figure 4.12, showing a small drop in probe transmission of 1 mV. Note that the full decrease was not observed, likely due to the limited bandwidth of the photodetector.

4.6 Calculation of the ESA cross-section

The voltage changes from the steady state were measured to be $\Delta V_{\mu s} = 11.75 \pm 0.25$ mV and $\Delta V_{ns} = 2.0 \pm 0.25$ mV. With the equilibrium DC voltage of 460 mV corresponding

to T_{eq} = 0.92, these values correspond to probe transmissions of $T_{\mu s}$ = 0.9435 ± 0.002 and T_{ns} = 0.916 ± 0.002 respectively.

The number of ions initially excited by the OPO pulse was calculated using Equation 4.4. Using the values $f_u = 0.263, f_l = 0.03$, $\sigma = (7.8 \pm 0.3) \times 10^{-21}$ calculated in Section 4.3.1, and l = 4.55 ± 0.01 mm, the number of ions excited by the OPO pulse was calculated to be $(2.4 \pm 0.3) \times 10^{19}$ cm^{-3}. Using $N = 7.8 \times 10^{20}$ cm^{-3}, this corresponds to 3.1 ± 0.3% of the total number of ions. This value is comparable to that calculated in Section 4.3.1, confirming good overlap of the two beams.

The ratio of ESA to GSA cross-sections was calculated using Equation 4.6 to be $\gamma = 0.08 \pm 0.01$. The ESA cross-section was calculated using the value of σ to be $\sigma_{ESA} = \gamma\sigma = (6.3 \pm 0.7) \times 10^{-22}$ cm^2

This value of γ is an order of magnitude lower than that suggested by Razdobreev and Shestakov [85]. The model assumed a ratio of γ = 0.65, corresponding to an instantaneous voltage drop of 25 mV. For comparison, a voltage drop of this range with the same decay constant is plotted also in Figure 4.13. It is clear that the two

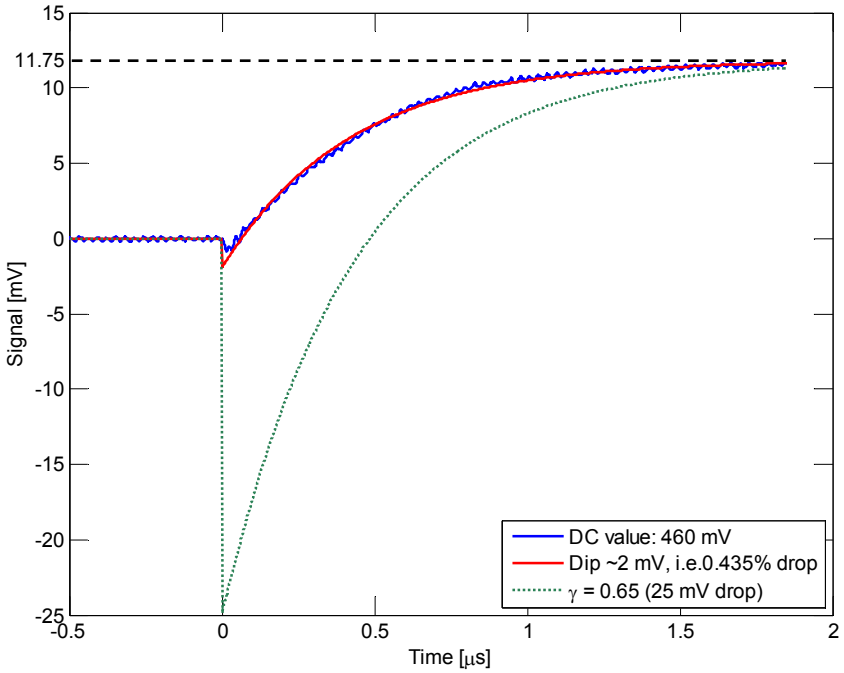

Figure 4.13: Experimental trace (blue) and fit (red), compared to the expected curves for a voltage drop corresponding to γ = 0.65 (green).

traces do not overlap for the entirety of the decay curve. As illustrated by Razdobreev and Shestakov in their modelling results, the lower value of γ would result in CW operation of their Tm:$YAlO_3$ laser for all pump rates.

4.7 Remodelling of the laser dynamics

The Tm:$YAlO_3$ laser dynamics was remodelled in MATLAB using the experimentally obtained value of $\gamma = 0.08$. The results are shown in Figure 4.14. The bode plots of the transfer functions for the laser and population densities are shown in Figure 4.15 and Figure 4.16 respectively.

The system begins with a strong transient, but the resulting oscillations decay exponentially, much like the output predicted in Section 3.7 where $\gamma = 0$. The oscillations damped to zero after a short period of time and the laser operates in CW. This is also consistent with the transfer function of the system, showing a -180° phase lag at the resonance peak, corresponding to a positively damped oscillator.

The laser dynamics model in both the time domain and frequency domain shows that the value of γ obtained from experiments does not result in the unstable self-pulsing behaviour that was observed from the Tm:$YAlO_3$ cuboid laser from Chapter 2. The value of γ was increased to identify the point at which the modelled laser switches from stable CW operation to self-pulsing operation. This threshold value was found to be approximately $\gamma = 0.5$, above which the phase change at the resonance peak switched from a -180° phase lag to a +180° phase lead.

From these results, it can be concluded that ESA at the lasing wavelength is too low, and is insufficient to be solely responsible for the unstable self-pulsing behaviour as observed in the Tm:$YAlO_3$ cuboid lasers. While the model shown in Chapter 3 appears to agree with observed laser behaviour, it is insufficient to explain the self-pulsing behaviour as it requires a value of σ_{ESA} that is much greater than that measured. Thus, alternative mechanisms must be explored to explain the self-pulsing behaviour, such as nonlinear dynamical chaos [87], [88], and an expanded model of the laser system developed.

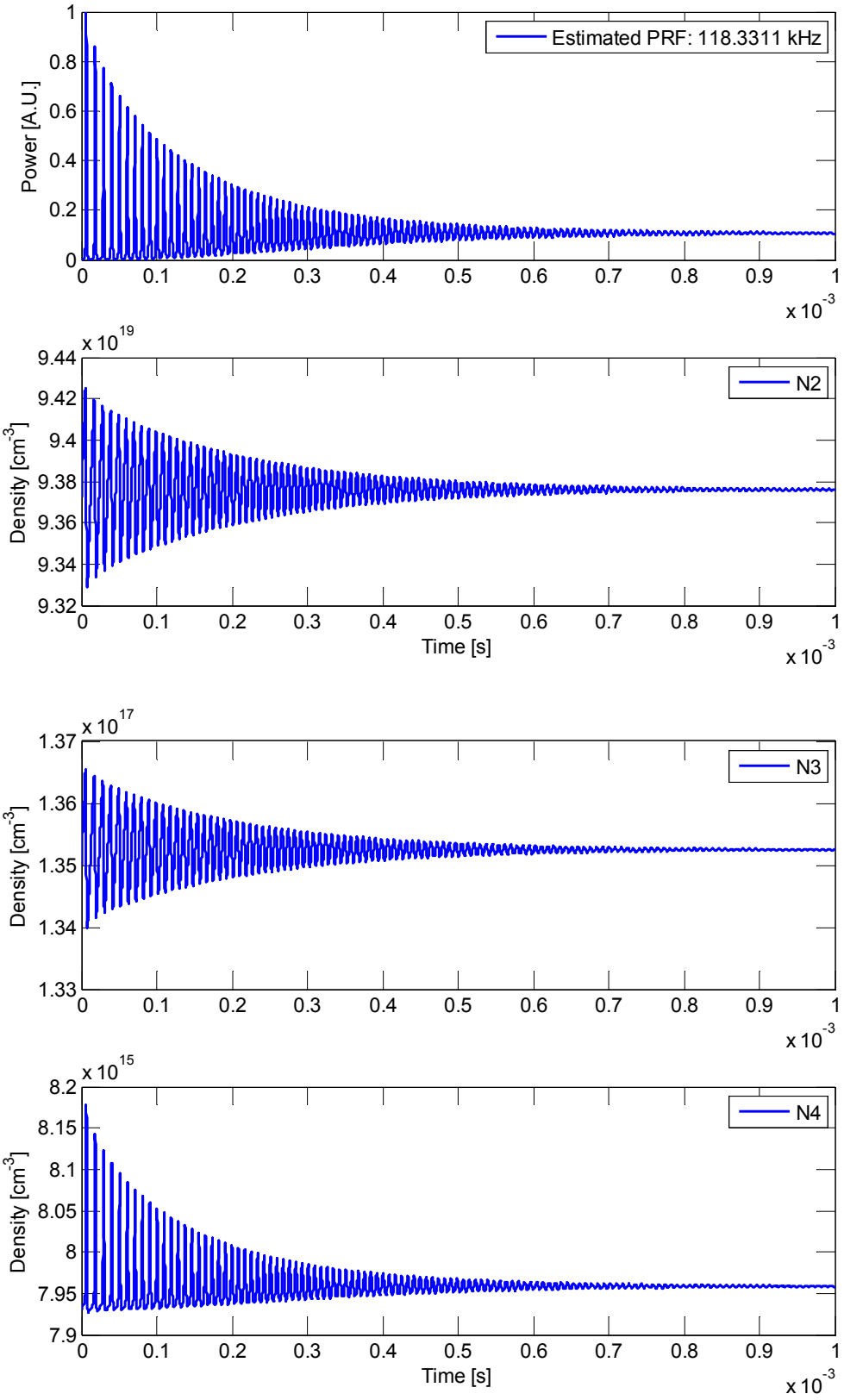

Figure 4.14: The output of the laser model with γ = 0.08, showing the photon emission (top) and population densities with time.

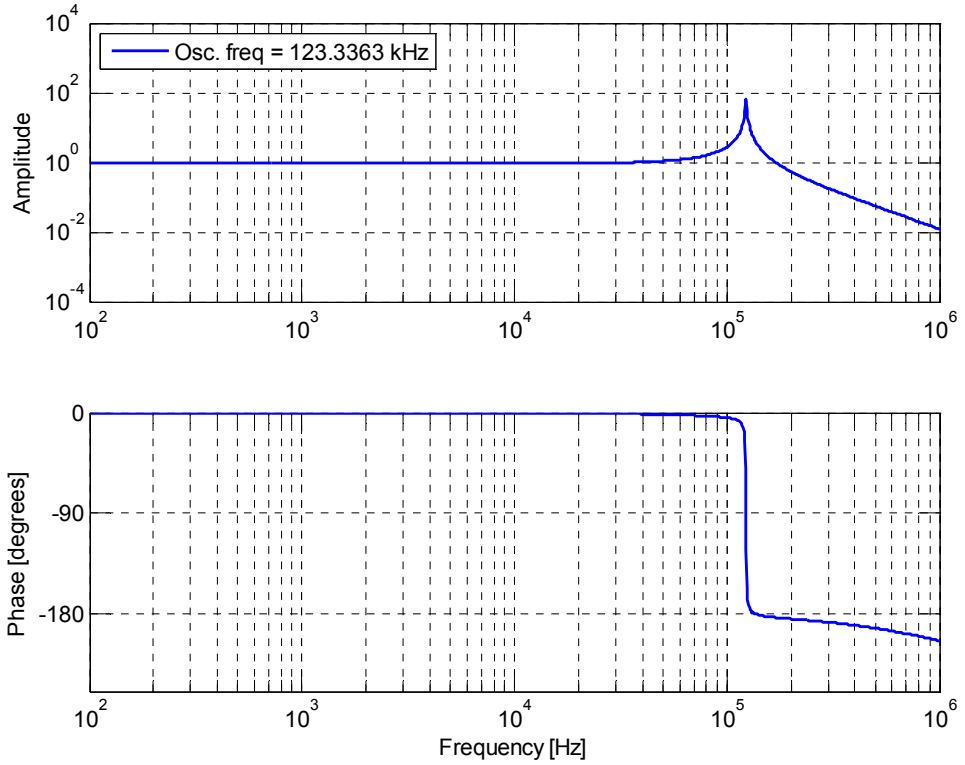

Figure 4.15 Bode plot of the modelled laser transfer function for $\gamma = 0.08$.

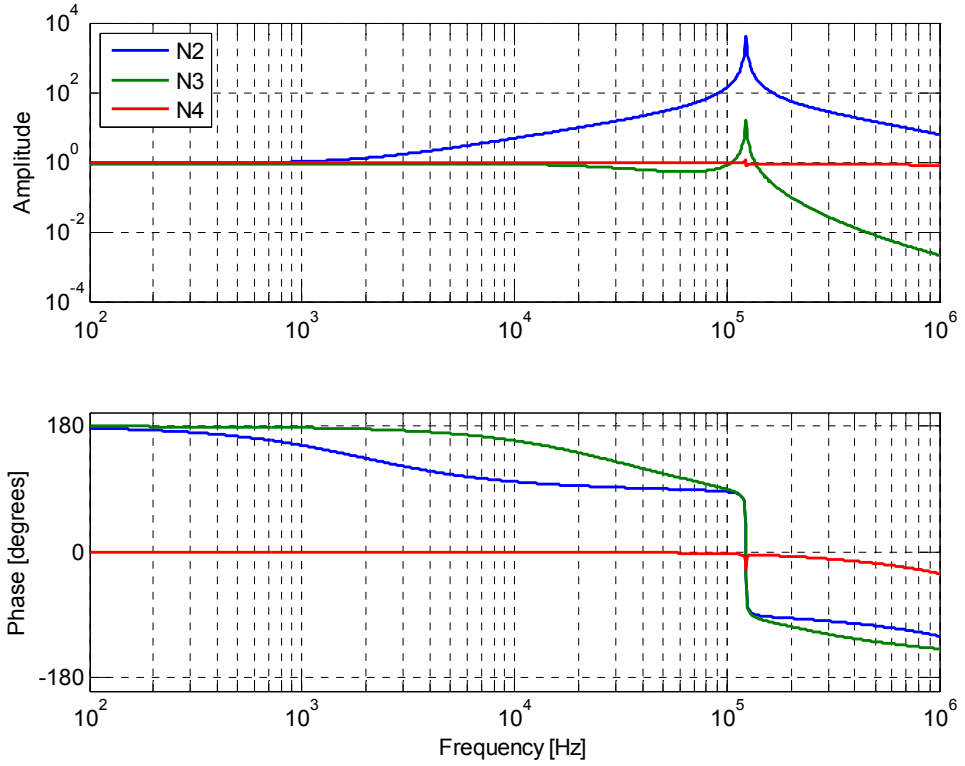

Figure 4.16: Bode plot of the transfer functions of the population densities for $\gamma = 0.08$.

4.8 Evidence of chaos

A possible alternative mechanism to explain the self-pulsing behaviour in Tm:$YAlO_3$ is chaotic dynamics. A chaotic system is defined as a non-linear, dynamical system that is highly sensitive to initial conditions, such that any small differences in initial conditions lead to results that diverge significantly. A key consequence is that it is impossible to predict time domain behaviour over long periods due to limitations in measurement accuracy and calculation precision, despite being deterministic.

A primary reason for suspecting chaotic behaviour in the laser is the similarity between the observed output from our laser, shown in Figure 2.19, and that of an NH_3 laser, which is well-known for exhibiting Lorenz-type chaotic pulsations [87]–[89]. Example outputs of NH_3 lasers, reproduced from the literature [89], are shown in Figure 4.17. The Tm:$YAlO_3$ and NH_3 lasers both exhibit oscillations with exponentially growing amplitudes. These oscillations eventually terminate abruptly.

In chaotic lasers, there is a second threshold beyond the standard lasing threshold [90], above which the laser transitions from a stable to a chaotic regime. Thus, the existence of two distinct regimes, as observed by Razdobreev and Shestakov in their Tm:$YAlO_3$ laser [85] may also be consistent with chaos.

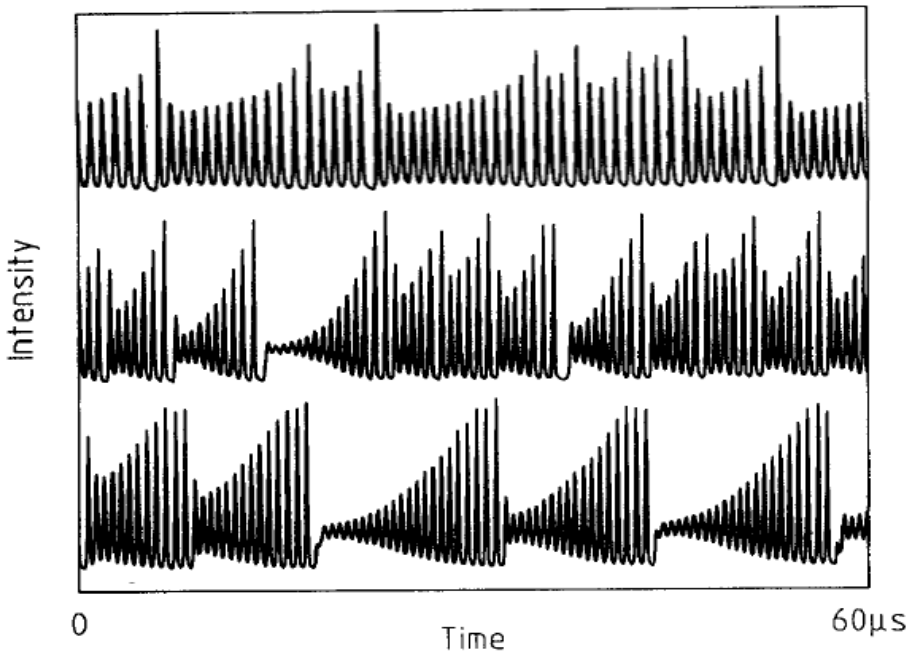

Figure 4.17: Lorenz-like pulsation of the laser intensity in far-infrared NH_3 lasers. Reprinted from [89], with permission from Elsevier.

Generally, only one of the degrees of freedom of a dynamic system is measured at one time, such as the output power of a laser. However, the structure and dynamics of the originating system extends into multiple dimensions, represented as a phase space that is the collection of all possible system states; each dimension corresponds to a degree of freedom of the system. The measured quantity is the projection of these higher dimensions onto this observable variable.

The phase space of dynamic systems can contain attractors, which are sets of states toward which a system tend to evolve. Attractors can be located by examining the time evolution of the system in phase space and identifying orbits in the trajectory. Systems that are chaotic have fractal attractors, where the trajectory forms dense, unstable non-periodic orbits. Any small perturbation can cause a shift of the system state onto a different orbit in the trajectory, resulting in vastly different states with time. This gives rise to the divergent property of chaotic systems.

While the original phase space and dynamical equations are often unknown, it is possible to construct a Euclidean space that is topologically equivalent to the original phase space. This is called phase space reconstruction [131]. One such method that is commonly used for chaotic systems is time delay embedding [132], [133].

4.8.1 Time delay embedding

Time delay embedding is the application of Takens Embedding Theorem [133], which proves that a generic signal (e.g. the output power of a laser over time) and its time-delayed versions can be used to construct a Euclidean space that is a unique map of the original phase space of the system. Assuming sufficient dimensions, trajectories in this reconstructed phase space are topologically equivalent to that of the original system. The properties of the dynamic system are preserved, and the trajectories are fully contained, or "embedded", in this reconstruction of the phase space.

To illustrate this concept, consider a pure sine wave signal. The oscillatory behaviour of a sine wave can be thought of as the one-dimensional projection of an ellipse that exists in a two-dimensional space. By constructing a second dimension using a time-delayed $y(n)$, in this case delayed arbitrarily by $\Delta n = 10$, the one-dimensional data "unfolds" into an ellipse, as shown in Figure 4.18. The data points shown denote the mapping of the sine wave onto the ellipse in phase space, moving

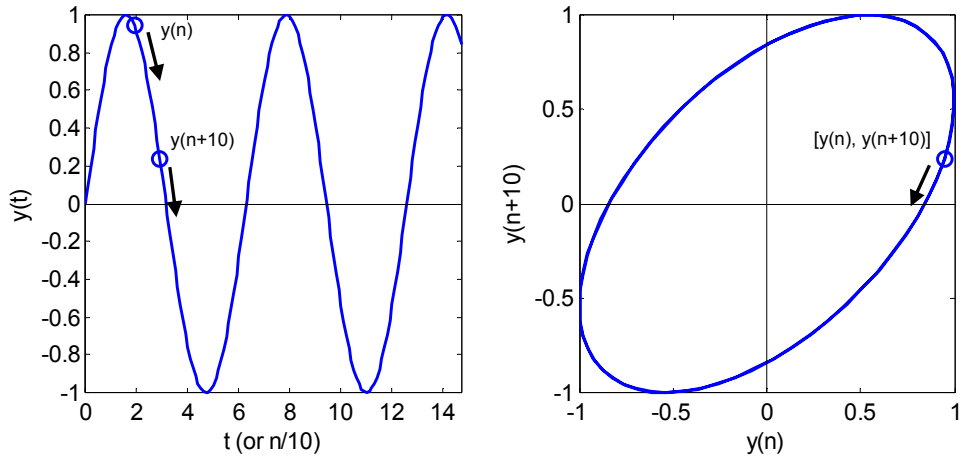

Figure 4.18: Plot of $y = \sin(t)$ sampled at $\Delta t = 0.1$ (left) and its phase space structure in two dimensions $[y(n), y(n + 10)]$ (right).

along the trajectory with time. In this case, no additional information is obtained by further unfolding the signal into a higher dimension, as the trajectory remains an ellipse.

There are two key parameters that need to be determined in time delay embedding – the optimum delay Δn for each dimension, and the minimum number of dimensions required to reconstruct the phase space. The optimum delay Δn is obtained from the "average mutual information" of the signal, while the number of dimensions required is determined by the "false nearest neighbours" analysis. Both of these concepts will be explained in the following sections.

4.8.2 Average mutual information

The ellipse in phase space in Figure 4.18 was constructed using a delay of $\Delta n = 10$. However, a different ellipse would be constructed using a different delay. The data points are more correlated for shorter delays, and hence would result in a narrower ellipse with a smaller area. Similarly, a longer delay (e.g. $\Delta t \approx \pi$) can result in anti-correlated data points, also producing a narrower ellipse. While topologically identical, this could result in trajectories that are difficult to distinguish for more complex phase space structures. Thus, the optimum delay is that which expands the phase space structure maximally.

The optimum delay can be obtained from the average mutual information of the data. The mutual information is analogous to the correlation function, but is sensitive

to nonlinear relationships. The mutual information, $I(X;Y)$, between two data sets X and Y is a measure of the reduction in uncertainty in predicting one data set when observing another, and is defined as:

$$I(X;Y) = \sum_{t} p(x,y) \log_2 \left[\frac{p(x,y)}{p(x) \cdot p(y)} \right], \tag{4.8}$$

where $p(x,y)$ is the joint probability of observing x in X and y in Y respectively, and $p(x)$ and $p(y)$ are the marginal probabilities of x in data sets X and y in data sets Y respectively. In the case of time delay embedding, the data sets are time-shifted versions of the same data set and X and Y become $y(t)$ and $y(t + \Delta t)$ respectively.

The optimum time delay is given by the first minimum of the average mutual information [134]. A minimum means that points in the time series, spaced by Δt, are as statistically independent as possible. When data spaced by this delay are used as coordinate values in the phase space reconstruction, the coordinate axes are as close to orthogonal as possible. This results in a trajectory that is expanded maximally. Using the first minimum minimises the number of data points discarded by the process. Further, real signals are affected by noise and perturbations, and using a smaller time delay minimises any potential impact these have on the phase space structure.

In practice, the probability distributions are generally unknown and must be estimated from the data set to obtain the average mutual information. Time-delay embedding only requires the delay corresponding to the first minimum, and thus an approximation of the mutual information is sufficient. One method to approximate the average mutual information is to separate the data into bins of equal width $\{b\}$. The marginal probability is the probability $p(b_i)$ of the data set values falling into each bin b_i, and the joint probability $p(b_i, b_j) = \Pr[\, y(t) \in b_i \,, y(t + \Delta t) \in b_j \,]$. These probabilities can then be used to calculate $I(X;Y)$.

4.8.3 False nearest neighbours

The reconstructed phase space must have sufficient dimensions in order to preserve the topology of the original phase space. If the reconstructed phase space has insufficient dimensions, points in the original phase space are projected incorrectly into the neighbourhood of points and the mapping is not unique. This is illustrated in the

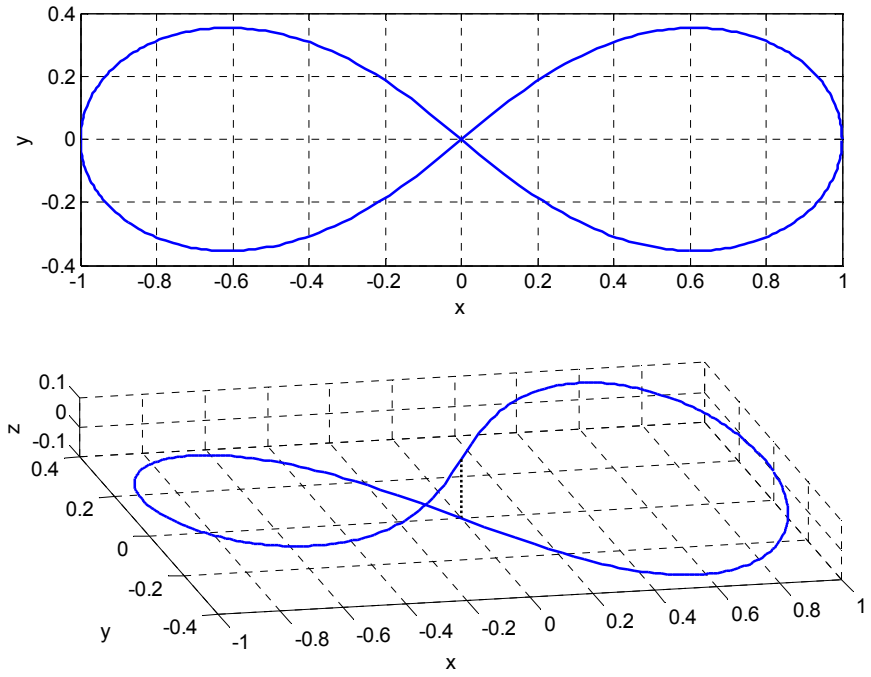

Figure 4.19: An illustration of the concept of false nearest neighbours. The two-dimensional structure (top) contains false neighbours near [0, 0] due to it being a projection from a three-dimensional structure (bottom)

example shown in Figure 4.19. The figure-eight structure in two dimensions indicates multiple neighbours near [0, 0]. However, upon unfolding into the third dimension, it can be seen that the neighbours are not real; the close proximity is an artifact of the projection.

The minimum number of dimensions required can be determined using the false nearest neighbours method [135]. This method analyses each point in a *d*-dimensional phase space to determine if neighbouring points are in close proximity because of a similar dynamical state or if it is a result of a projection of a higher-dimensional phase space into a lower dimension. The minimum dimension required to preserve the topology is therefore the dimension in which the number of false neighbours reaches zero. Note that the percentage of false nearest neighbours does not reach zero in the presence of noise [136].

The process used to calculate the percentage of false nearest neighbours [131] is summarised here. In dimension *d*, the location of each point is defined by a vector:

$$\boldsymbol{y}_d(k) = [y(k), y(k+\Delta n), \ldots y(k+(d-1)\Delta n)]. \qquad (4.9)$$

The proximity of this point to other points in dimension d is quantified using the Euclidean distance R_d. The distance between two points located at $\mathbf{y}_d(k)$ and $\mathbf{y}_d(k')$ is given by:

$$R_d(k,k') = \sum_{l=0}^{d-1} [y(k+l\Delta n) - y(k'+l\Delta n)]^2 \,. \tag{4.10}$$

The nearest neighbour, $\mathbf{y}_d(k_{NN})$, is therefore the point with the smallest R_d. In order to determine whether $\mathbf{y}_d(k)$ and $\mathbf{y}_d(k_{NN})$ are nearest neighbours due to a projection from higher dimensions, the Euclidean distance between the two points are calculated in dimension $d + 1$:

$$R_{d+1}(k,k_{NN})^2 = R_d(k,k_{NN})^2 + [y(k+d\Delta n) - y(k'+d\Delta n)]^2 \,. \tag{4.11}$$

The two points are considered false neighbours if the distance in dimension d and $d + 1$ differ beyond some threshold value R_T:

$$\frac{\left|y(k+d\Delta n) - y(k_{NN}+d\Delta n)\right|}{R_d(k,k_{NN})} > R_T \,. \tag{4.12}$$

The value of R_T is robust, with $10 \leq R_T \leq 50$ yielding similar results for the number of false nearest neighbours [131].

This process is repeated for all points to determine the percentage of points with false nearest neighbours in dimension d. The entire procedure is then repeated for incrementing dimensions, beginning at $d = 1$.

4.8.4 Surrogate data testing

A complementary test to identify non-linearity in a data set is the "surrogate data test" [137]–[140]. Surrogate data sets are used to perform various null hypothesis tests to determine if the system can be represented by a simpler model. The two main null hypotheses to be considered are: 1) the system contains no dynamical processes and the data points are independent (white noise); and 2) the dynamics can be described by a linear stochastic system. Each of these null hypotheses is tested by generating and

analysing surrogate data with the described characteristics and comparing them with identical analyses of the original data set. The method used to generate the surrogate data is described below. Any statistically significant differences that arise between the original and surrogate data sets can then be used to reject the null hypothesis.

Ideally, surrogate data sets should preserve as many properties of the original data set as possible, except for those being tested. This is achieved by modifying the original data set to generate the surrogates. To obtain a data set equivalent of white noise, i.e. with a constant power spectral density across the spectrum, the ordering of the data points is shuffled randomly. This destroys any time dependence in the data while preserving the mean and standard deviation. To simulate the output of a linear stochastic system, the spectral content and linear correlation of the data need to be preserved. This was achieved by first taking the FFT of the original data set, phase-shifting each frequency component randomly, then taking the inverse FFT to obtain a set of "polished" surrogate data [140].

4.8.5 Chaos analysis of a Tm:$YAlO_3$ laser

The output power time series of the lasers in Chapter 2 were not of sufficient length to conduct the chaos analysis. The Tm:$YAlO_3$ laser Mk-II from Chapter 2 was therefore reconstructed and new time series of the output power with significantly more data points were obtained. The laser was operated at a lower power of 188 mW, resulting in oscillations of a lower frequency. This is due to a lower gain and thus build-up time for the oscillations. However, the laser behaviour, namely oscillations with an exponentially growing envelope, was consistent with the previous lasers.

A subset of the output power time series is shown in Figure 4.20. This subset, referred to as the measured data set and used in the chaos analysis, contains 32,000 data points sampled at 2 MS/s using an extended InGaAs detector. The power spectral density of the data set used is shown in Figure 4.21. This data set was modified to produce surrogate data sets that simulated a system with no dynamical processes, i.e. white noise, and a system that was linear and stochastic. These surrogate data sets were generated using the methods explained in the previous section. The surrogate data sets are shown in Figure 4.22, along with the corresponding power spectral densities for each. Time delay embedding was performed also on the original and the surrogate data sets.

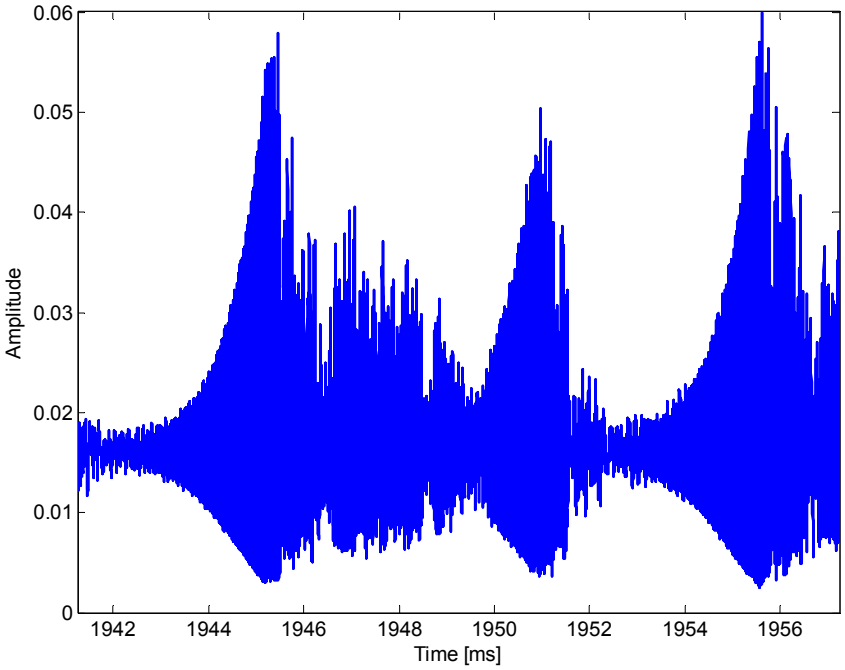

Figure 4.20: Temporal output from the reconstructed Tm:$YAlO_3$ laser Mk-II.

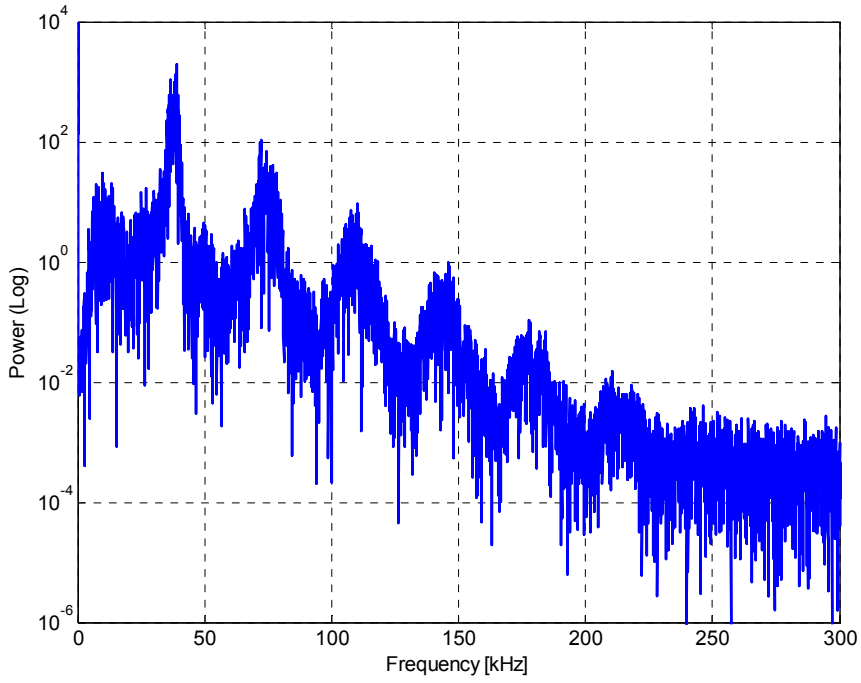

Figure 4.21: Power spectral density of the output signal.

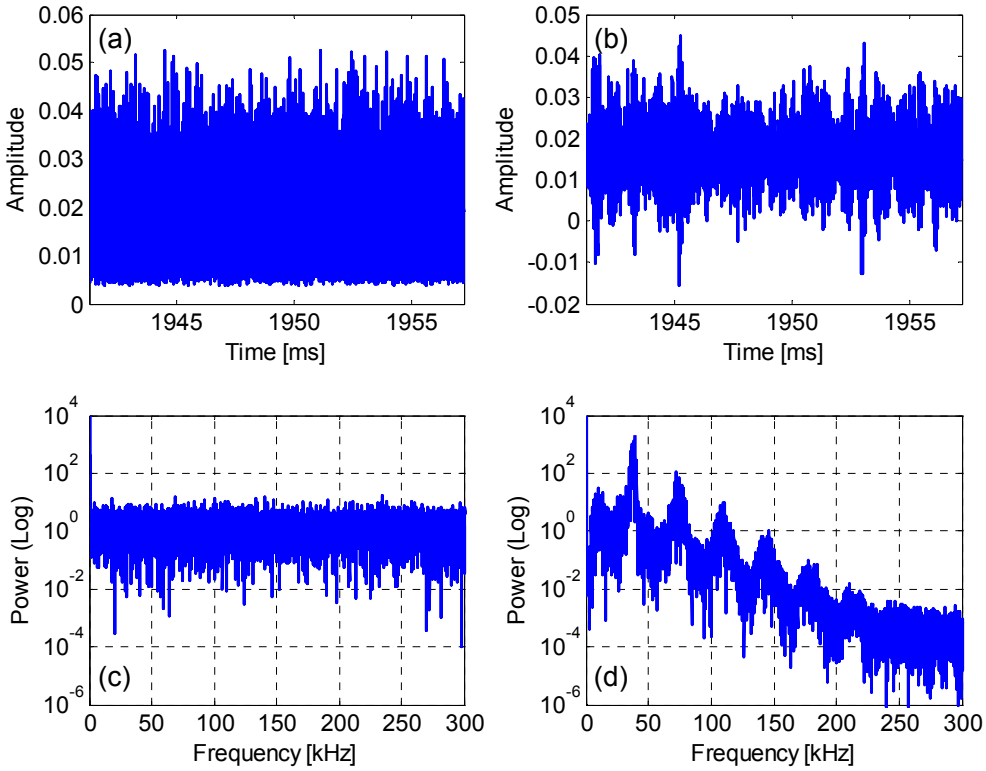

Figure 4.22: Surrogate data sets for no dynamical processes (a) and a linear stochastic system (b), and their corresponding power spectral densities (c) and (d) respectively.

The average mutual information for the measured and surrogate data sets were calculated for delays up to 60 data points (30 μs), and the results are shown in Figure 4.23. Multiple surrogate data sets for the linear stochastic case were generated and analysed to give an indication of what differences in values can be considered statistically significant, and therefore used to reject the null hypothesis of a linear stochastic system.

The average mutual information plots for both measured data and that of the linear surrogates show maxima and minima in mutual information, due to periodicity in the data. Note that the average mutual information plots for each linear surrogate overlap almost entirely. There is negligible mutual information for all non-zero delays in the case of no dynamical process, as expected for white noise.

The first minimum in the average mutual information from each data set was used as the optimum delay, which was $\Delta n = 13$ for the measured data set and $\Delta n = 12$ or 13 for the linear surrogates. The location of the minimum was insensitive to the bin size, with the number of bins ranging from 10 to 150 yielding the same results. The first minimum for the particular white noise surrogate generated was $\Delta n = 5$.

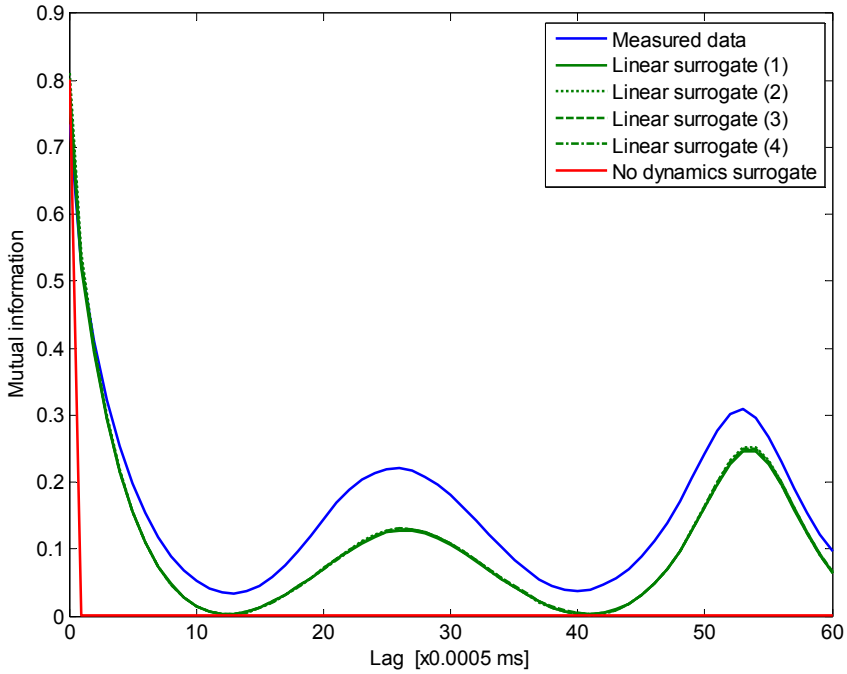

Figure 4.23: Average mutual information for the measured laser intensity (blue) and surrogate data sets for a linear stochastic system (green) and one with no dynamical processes (red).

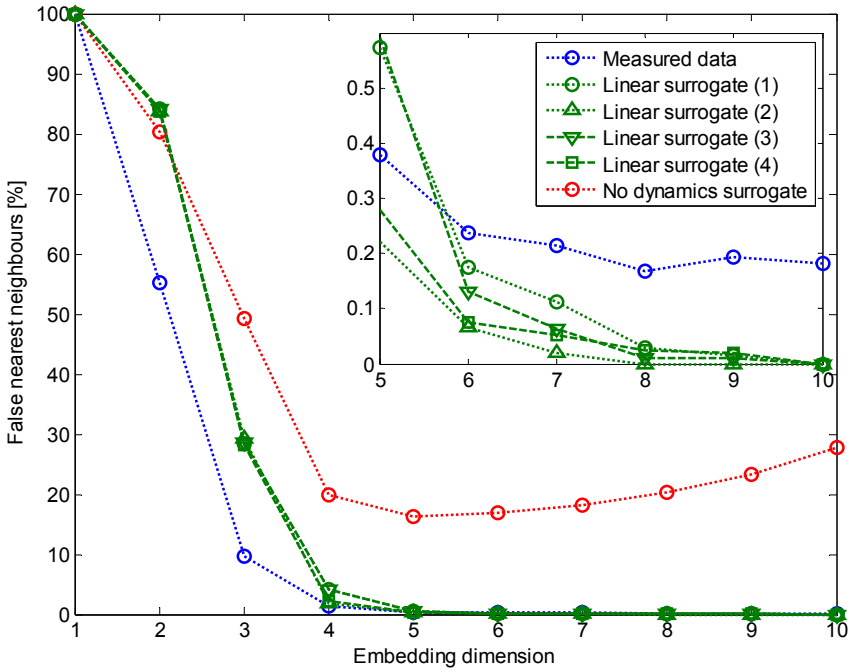

Figure 4.24: False nearest neighbours for the measured laser intensity (blue) and surrogate data sets for a linear stochastic system (green) and one with no dynamical processes (red), with an expanded plot of higher embedding dimensions (inset).

The values for Δn were used to calculate the false nearest neighbours for each data set to determine the embedding dimension, the minimum number of dimensions to preserve the structure. The false nearest neighbours plot is shown in Figure 4.24.

The number of false nearest neighbours for both the measured data set and the linear stochastic data sets reduced significantly with embedding dimension, with 0.4% for a 5-dimensional embedding, and remained at approximately 0.2% for higher dimensions due to noise. As with the average mutual information plots, each of the linear surrogates yielded approximately the same result, with some minor discrepancy for 4- and 5-dimensional embeddings. This is likely to be due to the randomisation of phase resulting in some points being closer or further from each other when unfolded. The white noise surrogate data set clearly behaved differently from the other data sets, with a high level of false nearest neighbours that was well above zero for all embedding dimensions. The increase in false neighbours for higher embedding dimensions after the minimum is consistent with noise [136].

The phase space structures of up to 5 dimensions for each case were generated using time delay embedding. The 3-dimensional projections of these structures are shown in Figure 4.25, Figure 4.26 and Figure 4.27 for the measured data set, one of the linear stochastic surrogate data sets and the white noise surrogate data set respectively. Note the colour variations are for ease of viewing purposes only.

The trajectory for the measured laser intensity data lies in a manifold of limited dimensionality in the reconstructed phase space. A limited dimensionality implies dynamics with a limited number of physical variables, or degrees of freedom, and because the trajectory appears non-periodic and is dense in the manifold, chaos is implied. On the other hand, the phase space structures for the two types of surrogates show a cloud of scattered points with little to no structure.

Coupled with the differences in the average mutual information and false nearest neighbours plots, it can be concluded that the laser system exhibits behaviour that can not be represented by a model system containing no dynamical processes, nor one that is linear and stochastic. Thus, both null hypotheses regarding simpler, stochastic models were rejected and the originating system is deemed to be deterministic and likely to be chaotic.

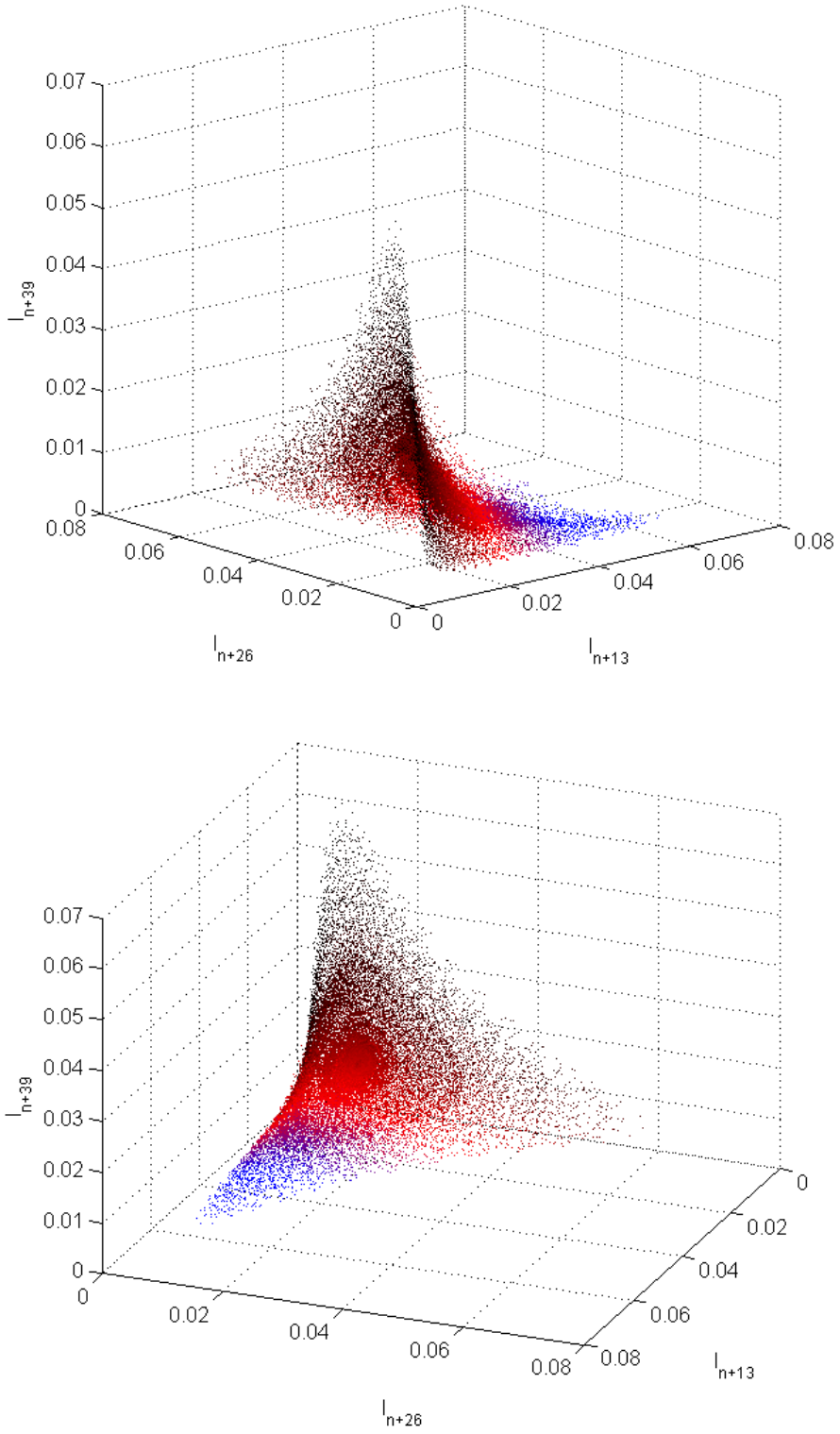

Figure 4.25: Phase space structure of the measured data from opposing viewing angles, showing a clear surface-like structure with an attractor at the centre. The colour variations are for ease of viewing purposes only.

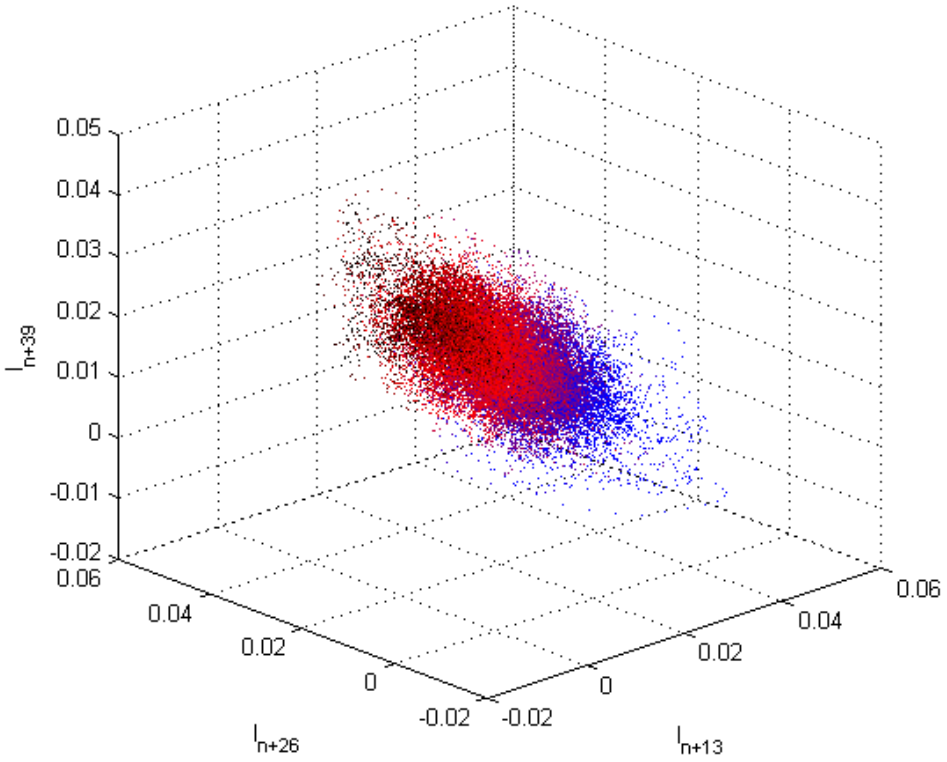

Figure 4.26: Phase space structure of the linear stochastic surrogate data, showing little to no structure. The colour variations are for ease of viewing purposes only.

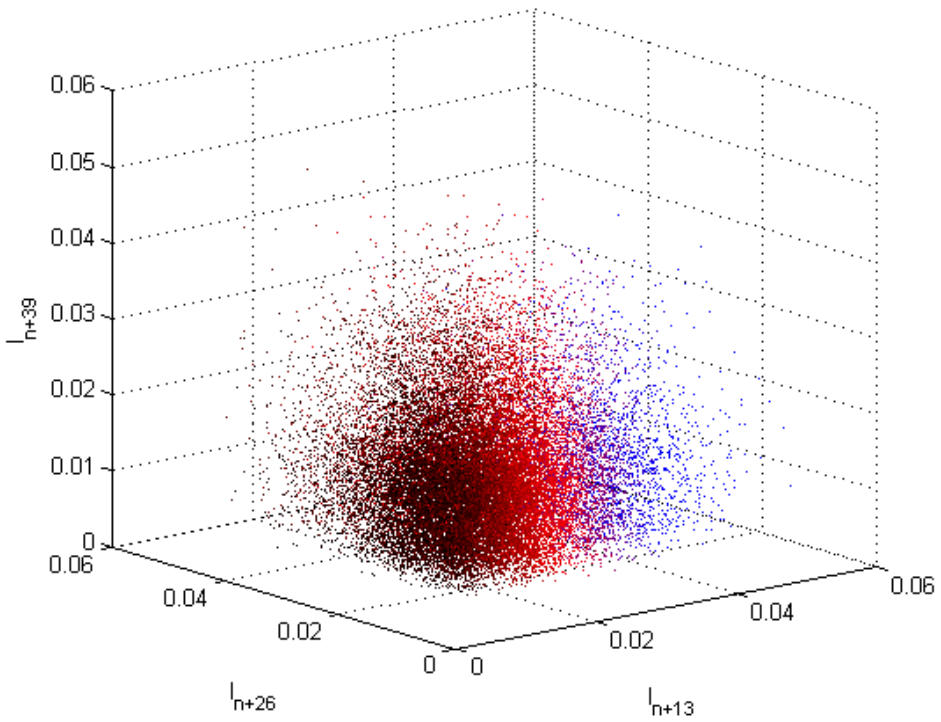

Figure 4.27: Phase space structure of the white noise surrogate, showing no structure. The colour variations are for ease of viewing purposes only.

4.8.6 "0-1" test for chaos

The dynamics of the time series were also investigated using the "0-1" test for chaos developed by Gottwald and Melbourne [141]–[143]. This test is used to distinguish between regular dynamics and chaos in deterministic systems, even in the presence of moderate levels of noise. The methodology and its implementation is explained in detail by Gottwald and Melbourne [143] and will be summarised here.

The 0–1 test for chaos essentially involves constructing random trajectories on a two-dimensional plane based on the input data set. The evolution of these trajectories with time is analysed for diffusive or bound behaviour. Diffusive behaviour indicates chaos, while bound behaviour indicates regular dynamics. The final metric is a binary value K, with $K \approx 1$ indicating chaotic dynamics and $K \approx 0$ indicating regular dynamics.

Firstly translation variables $p_c(n)$ and $q_c(n)$ are computed from the data set y:

$$p_c(n) = \sum_{j=1}^{n} y(j)\cos(jc),\ q_c(n) = \sum_{j=1}^{n} y(j)\sin(jc), \tag{4.13}$$

where c is a randomly-generated constant in the interval $(\pi/5, 4\pi/5)$.

The diffusive behaviour of the translation variables is quantified by a modified mean square displacement $D_c(n)$ from the trajectories (p, q) , and is defined as:

$$D_c(n) = M_c(n) - V_{osc}(c,n), \tag{4.14}$$

where:

$$M_c(n) = \frac{1}{N}\sum_{j=1}^{N}[p_c(j+n) - p_c(j)]^2 + [q_c(j+n) - q_c(j)]^2, \tag{4.15}$$

and

$$V_{osc}(c,n) = \left[\frac{1}{N}\sum_{j=1}^{N} y(j)\right]^2 \frac{1-\cos nc}{1-\cos c}. \tag{4.16}$$

The value of $D_c(n)$ scales linearly with time for chaotic dynamics, and this dependence is quantified by calculating its linear correlation coefficient with time

$$K_c = \mathrm{corr}(n, D_c(n)) . \tag{4.17}$$

This procedure is repeated for 100 or more different randomly generated values of c, and the median value $K = \mathrm{median}(K_c)$ is used to determine whether the system is regular ($K \approx 0$) or chaotic ($K \approx 1$).

The laser output intensity data was analysed using the 0–1 test. This gave a result of $K = 0.99$, which strongly indicates a chaotic system. A sample of the trajectory with $c = 1.9206$ is shown in Figure 4.28, showing diffusive behaviour that is consistent with examples of chaotic systems [143]. Note that this test applies only to deterministic systems and therefore does not apply to the surrogate data sets, which are stochastic.

Based on the result of the 0–1 test and the presence of a chaotic attractor in the reconstructed phase space of the laser system, it can be concluded that the Tm:$YAlO_3$ laser system exhibits deterministic chaotic behaviour, and the self-pulsing is likely to be the result of nonlinear dynamical chaos in the laser system.

While the experimental results are consistent with chaotic dynamics, it is unclear which of the physical parameters are responsible. In order for a laser system to exhibit natural chaotic behaviour, there must exist at least three coupled nonlinear equations

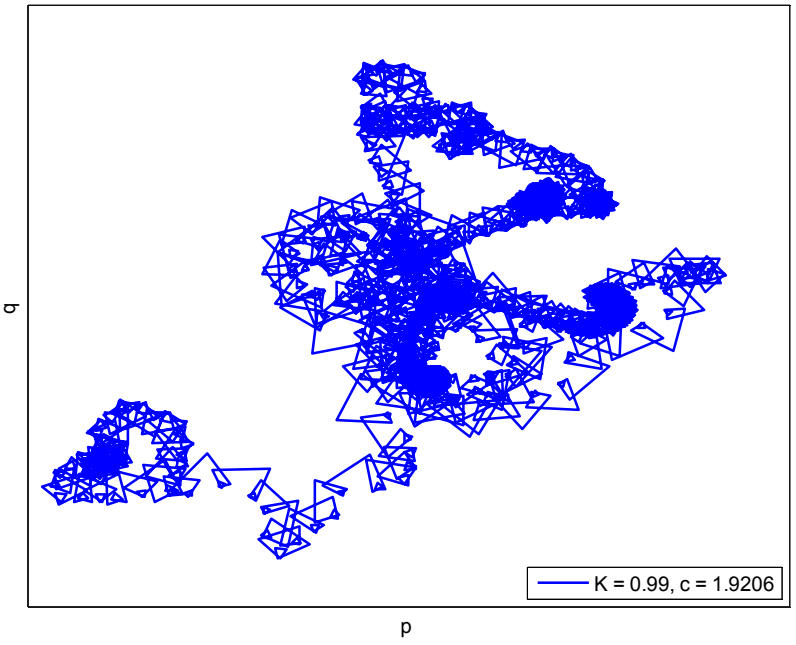

Figure 4.28: Plot of p versus q for the laser intensity data, with $c = 1.9206$.

with variables that have time constants of the same order [90]. Such lasers are called class C lasers [144]. The variables typically associated with class C lasers are the relaxation oscillation for the field (cavity lifetime), polarisation of the gain medium, and the population inversion (upper-state lifetime).

For the Tm:$YAlO_3$ laser, the upper-state lifetime is of the order of milliseconds. However, the photon lifetime is of the order of nanoseconds for the cuboid laser and that presented by Razdobreev and Shestakov. Thus, a parameter of a similar time scale beyond that typically associated with class C lasers must be present in the laser. Additionally, the measurement of the polarisation time constant for Tm:$YAlO_3$ has yet to be reported. The measurement of the polarisation time constant in Tm:$YAlO_3$ and the identification of responsible parameters are beyond the scope of this thesis.

4.9 Conclusion

A tunable OPO operating at 1.2 μm and a Tm-doped fibre laser operating at 1.944 μm were used to determine if significant ESA at the lasing wavelength occurs in Tm:$YAlO_3$. Nanosecond pulses from the OPO excites Tm^{3+} ions to the $^3H_5$ level, which then absorb photons from the probe beam and are further excited to the $^3H_4$ level.

The predicted ion transitions were observed, and the ratio of ESA to GSA cross-sections was calculated from the experimental results to be $\gamma = \sigma_{ESA}/\sigma = 0.08 \pm 0.01$, corresponding to an ESA cross-section of $\sigma_{ESA} = (6.3 \pm 0.7) \times 10^{-22}$ cm^2. This is significantly lower than that required by a model proposed previously. The laser dynamics model predicted a stable CW output when using this experimentally obtained value for γ. This is inconsistent with experimentally observed laser behaviour. Based on these observations, it can be concluded that the ESA cross-section for the laser wavelength is too low to cause the unstable self-pulsing behaviour as seen in the Tm:$YAlO_3$ lasers. Thus, the model described by I. Razdobreev and A. Shestakov does not accurately describe the laser dynamics of Tm:$YAlO_3$ lasers and their proposed mechanism for self-pulsing involving a strong ESA at the lasing wavelength is incorrect.

The Tm:$YAlO_3$ laser behaviour was then analysed for chaos. Time delay embedding using the laser output intensity was used to construct the phase space structure of the laser system. The trajectories were found to be bounded within a

manifold of limited dimensionality with dense, non-period orbits. In contrast, the phase space structure of a model system of white noise and a linear stochastic system show little to no structure and no attractors. The 0–1 test for chaos was applied to the laser output intensity data, giving a K value of 0.99 where a value of 1 indicates chaos. Thus, the self-pulsing in Tm:$YAlO_3$ lasers can be explained by nonlinear dynamical chaos in the laser system.

5 Moderate-power Tm:$YAlO_3$ slab laser

5.1 Introduction

For Tm:$YAlO_3$ lasers to be suitable pump sources for high power holmium-doped lasers, investigation of the self-pulsing at higher output powers is required. The Tm:$YAlO_3$ cuboid laser described in Chapter 2 has poor thermal handling due to its dimensions and is limited to low power. A laser geometry with better thermal handling is needed for higher powers. This chapter describes the design and construction of a Tm:$YAlO_3$ slab laser for investigating self-pulsing at moderate power levels (tens of watts).

The design and modelling of the Tm:$YAlO_3$ slab laser, including the resonator design, thermal modelling, pump geometry, and final laser head design and assembly are described in Section 5.2. The pump source characterisation is described in Section 5.3. Section 5.4 d the laser operation, with the temporal properties described in Section 5.5. The optical wedging induced by pumping is invesitgated in Section 5.6. The chapter is concluded in Section 5.7.

5.2 Laser design and modelling

For moderate power operation, the slab geometry was chosen. The slab geometry is superior to both rod and disk geometries in several ways. It is an excellent middle ground between the rod and disk geometry in terms of power handling. It is easier to achieve uniform side pumping in a slab geometry when diode stacks are used as the

pump source. It is straightforward to mount and conduction-cool the crystal with parallel flat surfaces.

A schematic of the Tm:YAlO$_3$ slab laser is shown in Figure 5.1. Pump light from each pump diode was focused in the vertical direction into the side of the slab by a cylindrical lens of f = 60 mm. The pump beam was allowed to diverge freely in the horizontal direction to fill the slab. The resonator consisted of a curved mirror with a 200-mm radius of curvature as the HR mirror (reflectivity > 99.5% at 1.94 μm), and a flat partially reflecting output coupler. A flat output coupler allowed for easy interchange of output couplers with different reflectivities. Lasing was achieved for three output couplers with reflectivities R = 65%, R = 75% and R = 88%, with the best performance achieved with the R = 65% output coupler. The mirrors were placed as close as possible, 5 mm, to the ends of the slab. The details of the laser design will be described in the following sections.

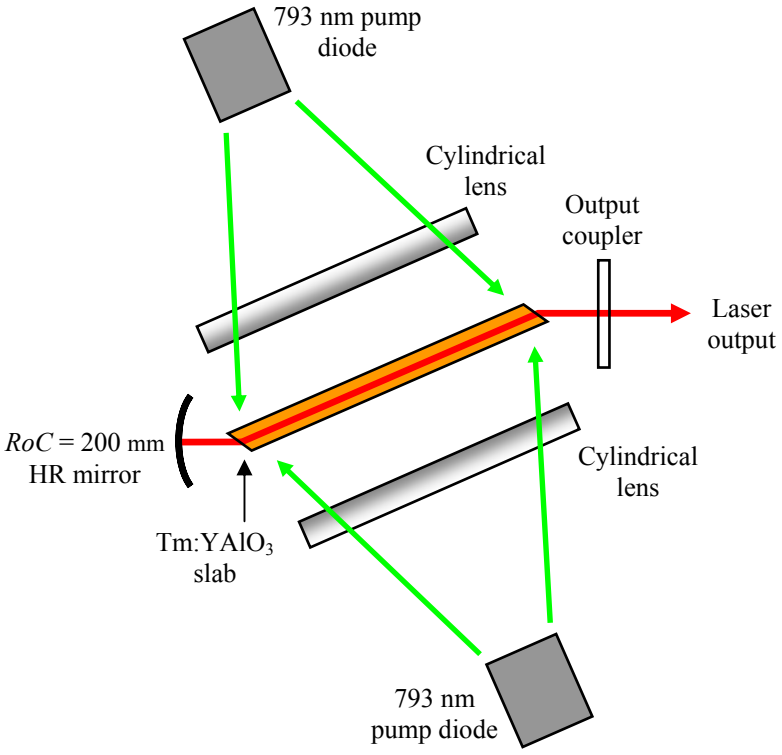

Figure 5.1: Schematic of Tm:YAlO$_3$ slab laser

5.2.1 Slab geometry

A zigzag laser path is common for slab lasers, as it averages out thermally-induced refractive index variations across one plane of the slab, resulting in reduced thermal distortions in the crystal [109], [110]. However, the biaxial nature of $YAlO_3$ makes utilising a zigzag laser path difficult. Polarised light within the crystal must be polarised along the same crystal axis to maximise gain, and thus all reflections within the slab must be *s*-polarised. Brewster's angle end faces cannot be used to minimise Fresnel losses at the entrance and exit faces, as it requires *p*-polarised light. As a result, either the laser mode must enter and exit the crystal out-of-plane for Brewster's angle, or a dielectric coating must be applied to the end faces, both of which complicates the design significantly. Thus, a simpler straight-through laser path was chosen.

The gain medium for the moderate-power laser was a side-pumped, straight-through (non-zigzag) slab with Brewster-angled end faces, as shown by the schematic in Figure 5.2. The Thulium-doped $YAlO_3$ slab had a concentration of 4 at.% and was obtained from and polished by Scientific Materials Corp. The two ends were cut to the Brewster angle $\theta_B = 62.75°$, thereby eliminating the need for dielectric coatings, which are difficult to apply to small surfaces and are susceptible to damage at high power. The full dimensions of the slab were 35.0 mm × 1.0 mm × 3.0 mm along the *a*-, *b*- and *c*-axes of the crystal respectively.

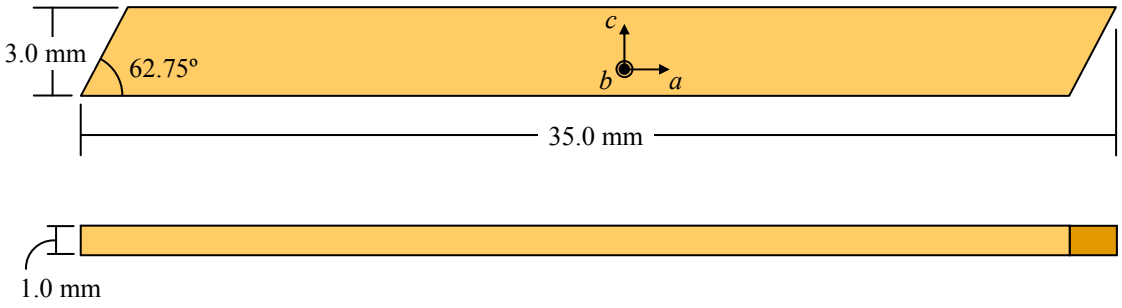

Figure 5.2: Tm:$YAlO_3$ slab geometry and crystal axes alignment.

5.2.2 Pumping geometry

Uniform pumping along the length of the slab is necessary to minimise unpumped, lossy regions as well as thermally-induced stress resulting from hot-spots. The long and thin design of the slab is ideal for pumping with diode stacks, which consist of a stack of fast-axis collimated diode bar emitters. Each bar emitter emits light in a long stripe, with near-uniform light along the long axis (slow axis) and good beam quality in the narrow axis (fast axis). A cylindrical lens can be used to combine the output from all emitters to form a single stripe of pump light at the focus to match the dimension of the slab. Multiple emitters also allow for very high powers in a compact package, with diode stacks capable of hundreds of watts of total output power, well in excess of the expected laser threshold of 100 W.

The pump source for the slab laser was a set of two diode stacks placed on opposite sides of the slab, with pump light incident on the side of the slab, i.e. the long thin faces. The diode stacks used were custom 720 W, fast-axis collimated diode stacks, made by Jenoptik (JOLD-720-CAFN-10A). The full specifications are discussed later in Section 5.3; however, the relevant parameters for modelling are shown in Table 5.1.

Mathematica, with the Optica toolbox, was used to model the pumping geometry using these diode parameters. Optica calculates beam propagation in the ray-tracing limit. The diode stacks were represented by an array of emitters, each of which emitted a fan of rays. A number of pump configurations were considered, including the use of lens ducts and double-pass pumping with a single diode stack. While the use of a lens duct improves the uniformity of the beam and prevents any stray beams from being incident on the indium, the complexity and cost involved with constructing and mounting the lens duct made it undesirable. Double passing the pump using a mirror at the other side of the slab resulted in non-uniform absorption of pump light across the width of the slab, with more pump light absorbed on the incident side. This would result in a thermal gradient across the slab and causing walk-off of the laser beam.

Axis	Width	Divergence
Horizontal (slow axis)	10 mm	6-7° FWHM
Vertical (fast axis)	17.75 mm (10 bars)	<0.5 mrad

Table 5.1: Relevant pump diode parameters.

Ultimately, primarily for simplicity, cylindrical lenses were used to couple the pump light into the slab.

A simulated cylindrical lens with variable focal length was placed in front of the emitters to determine the lens required to focus the pump light into the slab. Prioritising focal lengths that are commercially available, the final design, including simulated pump rays, is shown in Figure 5.3. A single cylindrical lens with $f = 60$ mm from Thorlabs was used to focus the beam in the vertical direction to <0.8 mm. The pump beam was allowed to diverge freely in the horizontal direction to fill the slab. This is applied to both diodes on the two sides of the slab.

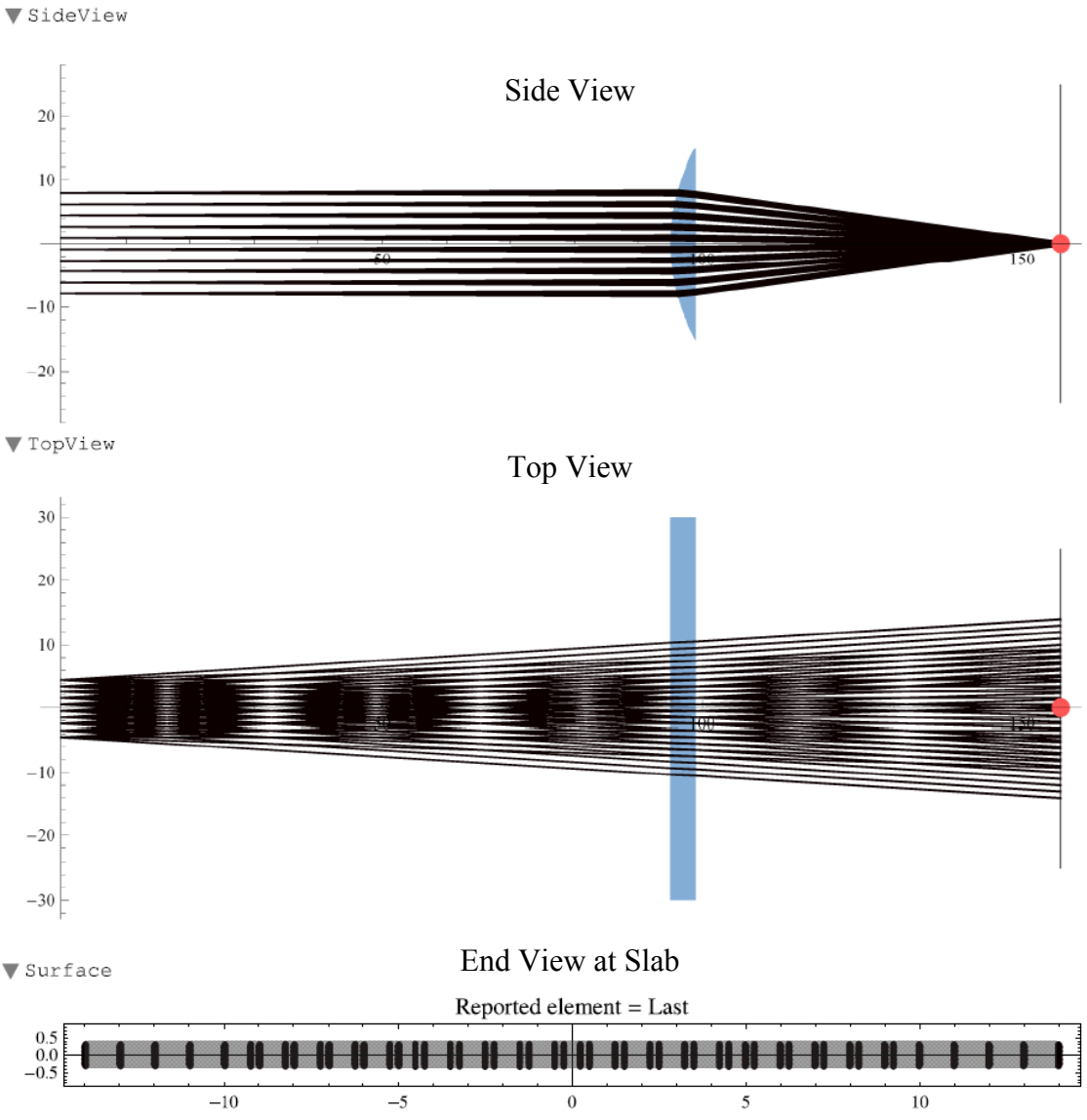

Figure 5.3: Pump geometry of the slab laser, showing the side view (top), top view (middle) and pump beam at the slab location (red dot). Unit is mm.

Note that, to minimise calculation time, only a 10 × 10 array of emitters and rays were used to represent the diode emission, resulting in discrete rays in the side and top views, and discrete points in the end view. However, in practice, this is a near-uniform rectangular region of illumination due to the emission region being continuous in the horizontal direction. Thus, a grey rectangle in the end view was used to fill in the region between the discrete points and illustrate the illuminated region.

5.2.3 Thermal modelling

The temperatures and thermal-induced stress in the slab due to pump absorption were modelled using the FEA package in COMSOL. The pump mode in the slab was approximated to be a collimated beam with a rectangular top-hat function, with a cross-sectional dimension of 31.5 mm × 0.8 mm, which is the length of the slab minus the Brewster ends. An exponentially decaying power density was used to simulate pump absorption as the pump beam passed through the slab. This was done for both sides of the slab to simulate balanced pumping from both sides. The absorption coefficient used was 3.5 cm^{-1}, calculated from the measured absorption of the pump light, which is described in Section 5.3.3. This gave a total heat deposition of 450 W from optical pumping. The cross-sections of the heat deposition within the slab from optical pumping are shown in Figure 5.4. Note that the artifacts above and below the simulated pump beam (between the red and blue regions in the cross-sectional slice) is due to the finite meshing conditions of the FEA modelling. Cooling is only through the top and bottom surfaces of the slab, which are fixed at a temperature of 288 K. All other surfaces are modelled as thermally insulated.

The resultant temperature distribution and thermal-induced stress are shown in Figure 5.5 and Figure 5.6 respectively. The hottest region is located in the plane at the centre of the slab parallel to the top and bottom cooled surfaces, as it is furthest away from the cooling. In this plane, the temperature becomes slightly hotter towards the pumped surfaces due to stronger absorption of the pump beam resulting in greater heat deposition. The hotter regions try to expand outwards as well as towards the cooling faces, resulting in high stress. At 450 W of heat deposition, the maximum stress of the slab is 142 MPa, which is just below the fracture limit for $YAlO_3$ of 160 MPa [145]. Heat deposition and stress scale linearly, and hence the slab is estimated to fracture at just over 500 W of deposited heat.

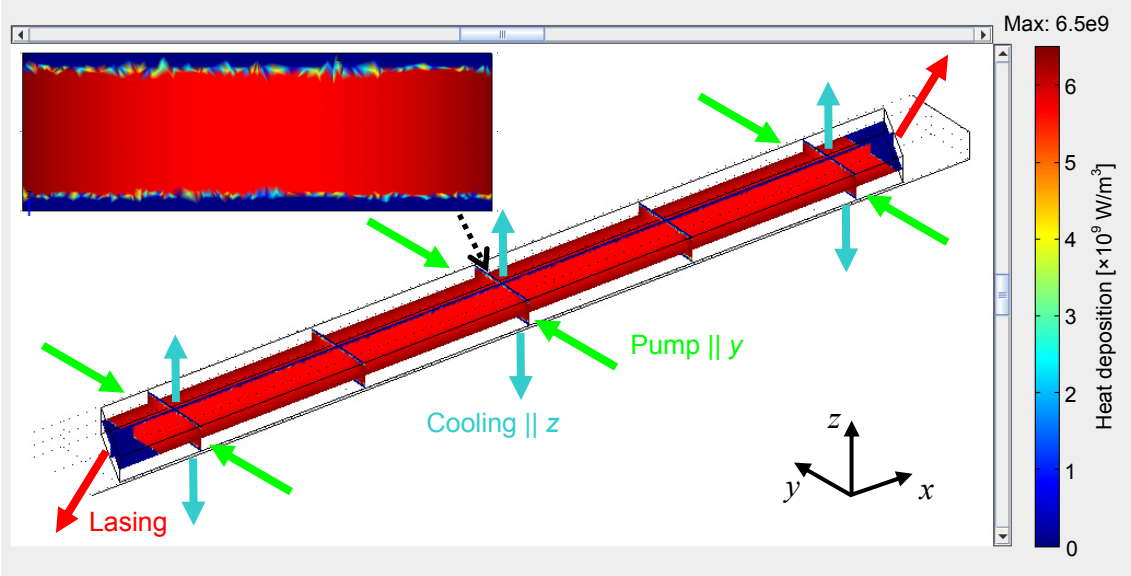

Figure 5.4: Cross-sections of the heat deposition within the slab, with a central cross-sectional slice shown in the inset.

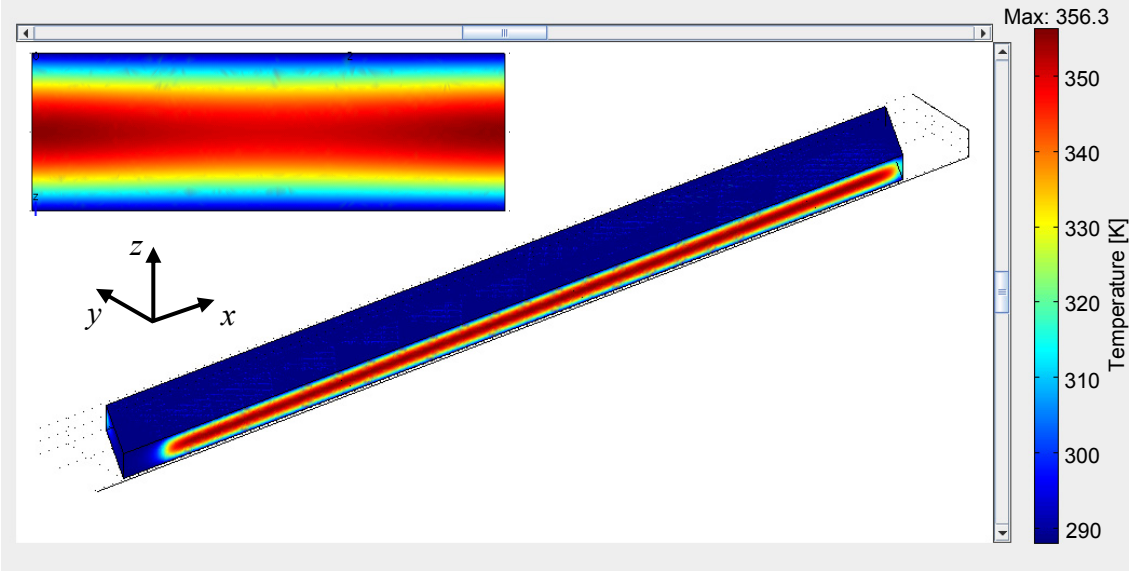

Figure 5.5: Modelled temperature distribution within the slab, with a central cross-sectional slice shown in the inset.

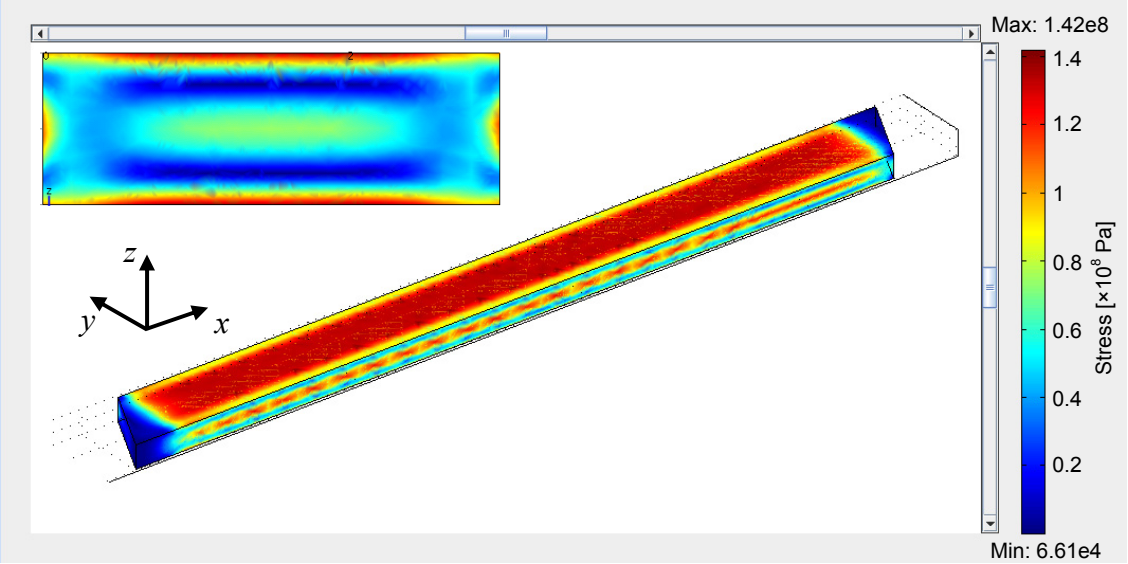

Figure 5.6: Modelled thermal-induced stress within the slab, with a central cross-sectional slice shown in the inset.

5.2.4 Resonator design

The laser mode is designed to be straight through the slab with no bounces. Consequently, no averaging of the thermal gradients occurs and the resonator mode is affected by thermal lensing as explained below. The heating of the crystal and hence the temperature gradients formed as a result of pumping is dependent on pump power. Thus, the thermal lens and hence the resonator mode is dependent on pump power.

The thermal lensing was estimated using the temperature differences along the *y*- and *z*-axis shown in Figure 5.5. The thermal lens assumes a parabolic profile under uniform pumping [64]. The temperature profile can therefore be approximated using a quadratic that is symmetric about the middle of the slab, with the maximum and minimum values defined by the temperatures in the middle of the slab and at the edges. In the vertical (*z*-axis) direction, a very strong positive lens is formed due to the centre being hotter than the edge, while a slight negative lens is formed in the horizontal (*y*-axis) direction. To estimate the thermal lens near initial operation conditions, the total heat deposition was scaled proportionally to 200 W. At this heat deposition, the vertical and horizontal temperature difference from the centre of the slab to the edges are ΔT_{vert} = 30.22 K and ΔT_{horiz} = -2.667 K respectively. Assuming an approximately quadratic temperature [64] and hence refractive index profile in the form

$n(r) = n_0 - \frac{n_2}{2} r^2$, these values of ΔT correspond to an n_2 in the vertical and horizontal direction of 3506 and -34.37 respectively.

The thermal lensing was modelled as a GRIN lens with these n_2 values for the two axes, using a modified version of the Matlab code from Section 2.3.1.2. The slight negative lens in the horizontal direction means that at least one of the resonator mirrors must be concave to maintain stability. The final resonator design is shown in Figure 5.7, with the $1/e^2$ beam width plotted against the length along the beam path.

The resonator mirror on the left-hand side in the figure is a curved mirror with a radius of curvature of 200 mm, while the other resonator mirror is a flat mirror. The mirrors are placed 5 mm from the end of the slab. The resonator mode in the vertical direction (blue) is significantly smaller than the horizontal direction (purple), due to the significantly greater thermal lens. The discontinuity at the interfaces for the horizontal direction is due to the crystal end-faces being at Brewster's angle.

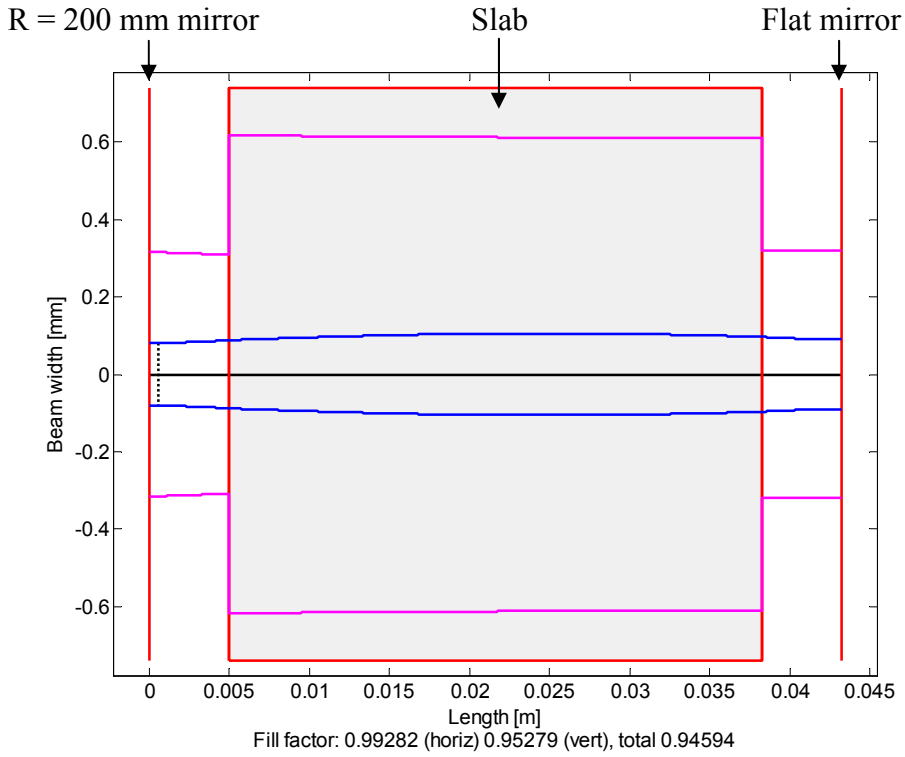

Figure 5.7: Fundamental resonator mode for 200 W heat deposition in the vertical direction (blue) and horizontal direction (purple).

Any pump light that is absorbed in regions not intersected by the laser mode is wasted. The maximum amount of extractable power is estimated using the fill factor, which is a measure of the overlap between the resonator mode and a rectangular prism, representing the rectangular aperture formed by the edges of the slab. The widths of higher-order modes are proportional to that of the fundamental mode [146], and hence the resonator beam shape is maintained throughout the resonator. The modelling estimates that approximately 94.6% of the pumped region can be accessed by the resonator mode; however, the exact amount extractable is likely less as it is dependent on the overlap of the laser and pump profiles.

5.2.5 Laser threshold

Lasing occurs when the round-trip gain of the laser system exceeds the losses, and is encompassed by the inequality [64]:

$$\exp[2(g - L_{distr})\, l] > \frac{1}{R_1 R_2 (1 - L_{pt})}, \tag{5.1}$$

where g is the gain coefficient, L_{distr} is the coefficient for any distributed loss in the gain medium, l is the gain length, R_1 and R_2 are the reflectivities of the two resonator mirrors, and L_{pt} is the point losses in the resonator, such as scattering from intra-cavity surfaces. The factor of two arises from two passes through the gain medium per round trip. In an initial simplified estimate of the threshold, the distributed losses are assumed to be negligible, while the point losses can are taken into account by a reduction in the reflectivity of the HR mirror (R_1).

Gain occurs when the probability of photon emission at the lasing wavelength exceeds that of photon absorption. For a quasi-three-level gain medium such as Tm:YAlO$_3$, the gain is given by:

$$g = \sigma(f_u N_2 - f_l[N - N_2]), \tag{5.2}$$

where σ is the emission cross-section, f_u and f_l are the thermal occupation factors for the upper and lower lasing manifolds respectively, and N_2 is the population density of the upper lasing manifold, and N is the total ion density. The thermal occupation factors

arise from the Stark splitting of the upper and lower lasing manifolds in quasi-three-level lasers, and will be discussed in the next section.

The number of excited ions required for laser threshold can be obtained by substituting Equation 5.2 into Equation 5.1:

$$f_u N_2 - f_l (N - N_2) > \frac{1}{2\sigma l} \ln\left(\frac{1}{R_1 R_2}\right),$$

$$\therefore N_2 > \frac{f_l N}{f_u + f_l} + \frac{1}{2\sigma l (f_u + f_l)} \ln\left(\frac{1}{R_1 R_2}\right). \tag{5.3}$$

The first term in the right-hand side of the inequality corresponds to the number of ions required for inversion, i.e. the number of ions required to make the gain medium transparent to the laser photons. The second term corresponds to the number of ions required to overcome the round-trip losses of the system.

Finally, the total absorbed pump power required to achieve threshold can be obtained by multiplying N_2 by $E_{pump} V / \tau \eta_q$, where E_{pump} is the pump photon energy, η_q is the quantum efficiency, and τ is the lifetime of the upper state. The quantum efficiency term includes cross-relaxation, which nearly doubles the number of upper-state ions per pump photon. Thus, the absorbed pump power required for transparency P_{trans} and to overcome losses P_{losses} are given by:

$$P_{trans} = \left(\frac{f_l N}{f_u + f_l}\right) \frac{E_{pump} V}{\tau \eta_q}, \tag{5.4}$$

$$P_{losses} = \frac{1}{2\sigma l (f_u + f_l)} \ln\left(\frac{1}{R_1 R_2}\right) \cdot \frac{E_{pump} V}{\tau \eta_q}. \tag{5.5}$$

5.2.5.1 Stark splitting and the Boltzmann distribution

To calculate the threshold pump power, the thermal occupation factors must be calculated. As mentioned previously, the thermal occupation factors arise from the Stark splitting of the upper and lower lasing manifolds. The Stark splitting observed in dopants arises from the distortion caused by the electrostatic crystal field of the lattice [147]. This results in the energy levels splitting into multiple sub-levels with different energies. The population density of each sub-level is determined by the Boltzmann

distribution, which gives the probability of which ions occupy a series of possible states (Stark levels) of an energy level. The Boltzmann distribution has the form:

$$P(state) \propto \exp\left(-\frac{E}{kT}\right), \tag{5.6}$$

where E is the energy of the Stark level relative to the lowest energy sub-level of that energy level, and kT is the product of the Boltzmann's constant and the temperature.

The Boltzmann distributions for ions in the Stark sub-levels for the upper and lower lasing manifolds for Tm:$YAlO_3$ [63] at 330 K are shown in Figure 5.8. Only the transitions between Stark sub-levels with energy difference corresponding to the laser photon energy are relevant to the lasing process. The laser emission wavelength is typically between 1940 – 1945 μm, which corresponds to photon energies of 5140 – 5155 cm^{-1}. Of the Stark-split levels for these two energy levels, the only transitions that correspond to this energy range are those between two of the Stark levels in the upper lasing manifold and the second from the top in the lower manifold. These are shown in

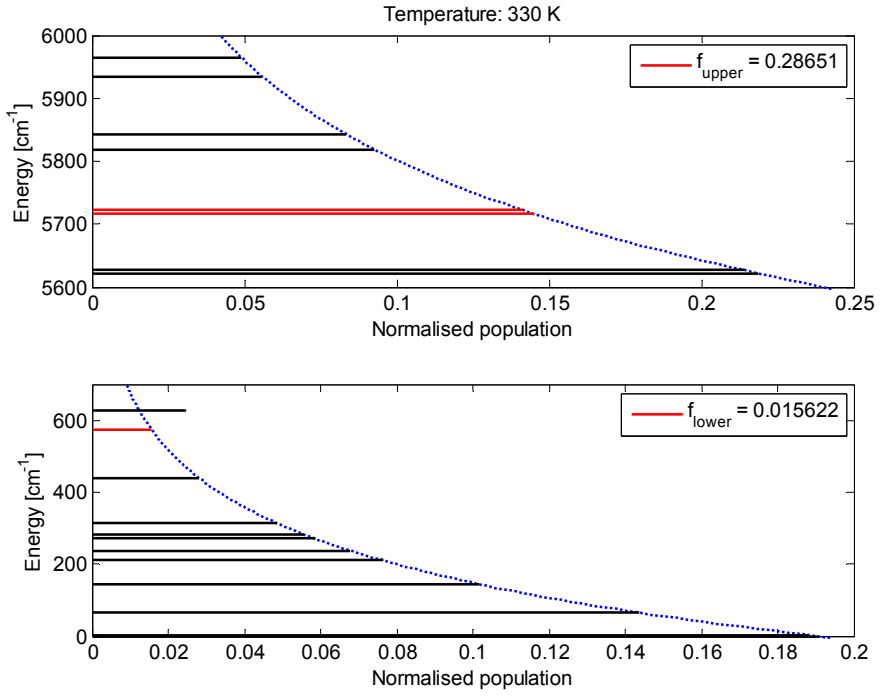

Figure 5.8: Boltzmann distribution for the Stark split levels in the upper and lower lasing manifolds for Tm:$YAlO_3$. Red denotes Stark levels involved in lasing at 1.94 μm. Note the two closely-spaced lines in the upper lasing manifold result in an effective Boltzmann factor of double the individual f_{upper} value.

red. Transitions between other Stark levels correspond to wavelengths shorter than 1930 nm or longer than 1960 nm, which are not observed.

The total normalised Boltzmann thermal occupation factors for these Stark levels at 330 K are f_u = 0.287 and f_l = 0.0156 respectively. This corresponds to inversion fraction of 5.17% of total ions N to reach transparency, which is consistent with the emission/absorption cross-section ratio in the literature [63]. Using Equation 5.4 for our slab laser, this corresponds to 91 W of absorbed pump power required to reach transparency.

The Boltzmann distribution and hence the inversion fraction required for transparency is dependent on temperature. A plot of the temperature dependence is shown in Figure 5.9, showing a near-linear dependence over the expected slab temperature range. The transparency power is directly proportional to the required inversion fraction, and hence also increases approximately linearly with temperature. Note that the dependence is not actually linear, but rolls off gradually at higher temperatures.

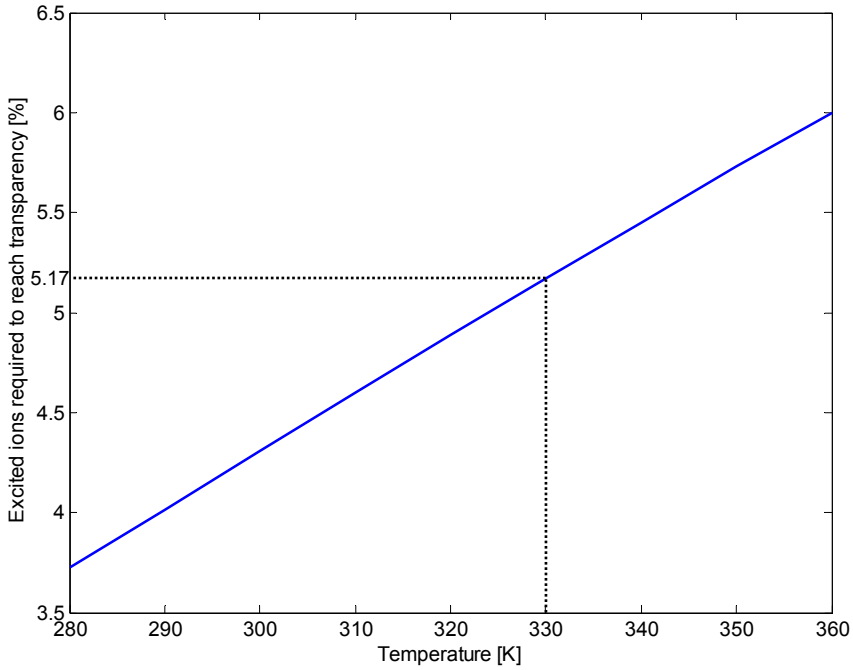

Figure 5.9: Dependence of required inversion fraction for transparency on temperature.

5.2.5.2 Estimated threshold pump power

In addition to the 91 W of absorbed pump power required for transparency, more pump power is required to overcome the round-trip losses for the laser to reach threshold. The additional pump power required was calculated using Equation 5.5 for the available output coupler reflectivities, i.e. R_1 = 1 and R_2 = 0.65, 0.75 and 0.88. The additional pump power required for the different output couplers, and the subsequent laser threshold power, is summarised in Table 5.2.

OC Reflectivity	Transparency	Gain > round-trip loss	Estimated laser threshold
65%	91 W	30.4 W	121.4 W
75%	91 W	20.3 W	111.3 W
88%	91 W	9.0 W	100 W

Table 5.2: Estimated laser threshold pump powers for different output coupling fraction.

5.2.6 Laser head design and assembly

The top and bottom surfaces of the slab must be cooled without obstructing the pump light entering from the sides and laser path from the ends of the slab. It was designed in the 3-dimensional computer-aided design (CAD) program, Solidworks, and manufactured by WB Tooling Pty Ltd. The final design of the laser head is shown in Figure 5.10 and Figure 5.11. The drawings of each component can be found in Appendix B.1.

The laser head consisted of three parts: a base aluminium block used to secure the slab at the correct height and bottom and top cooling blocks, both made of copper. Aside from the mounting holes, the two cooling blocks are identical. Each of the copper cooling blocks had a U-shaped water channel connected to an external water chiller for removing heat from the cooling surfaces of the slab. The two cooling blocks were secured together via four extended struts, which allowed access to all four remaining sides of the slab. Four spacers were used for support and to limit the compression on the slab. The ends of the struts were coplanar with the cooling surface to ensure flatness and uniform contact with the slab.

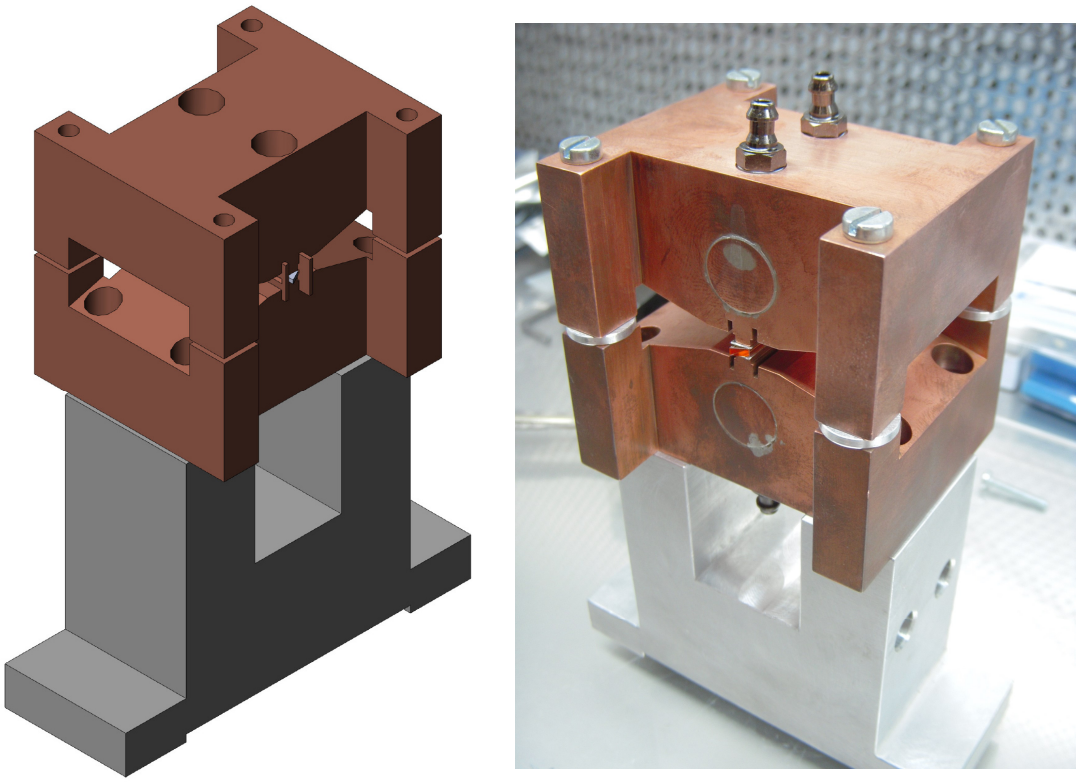

Figure 5.10: Full assembly of the final laser head design.

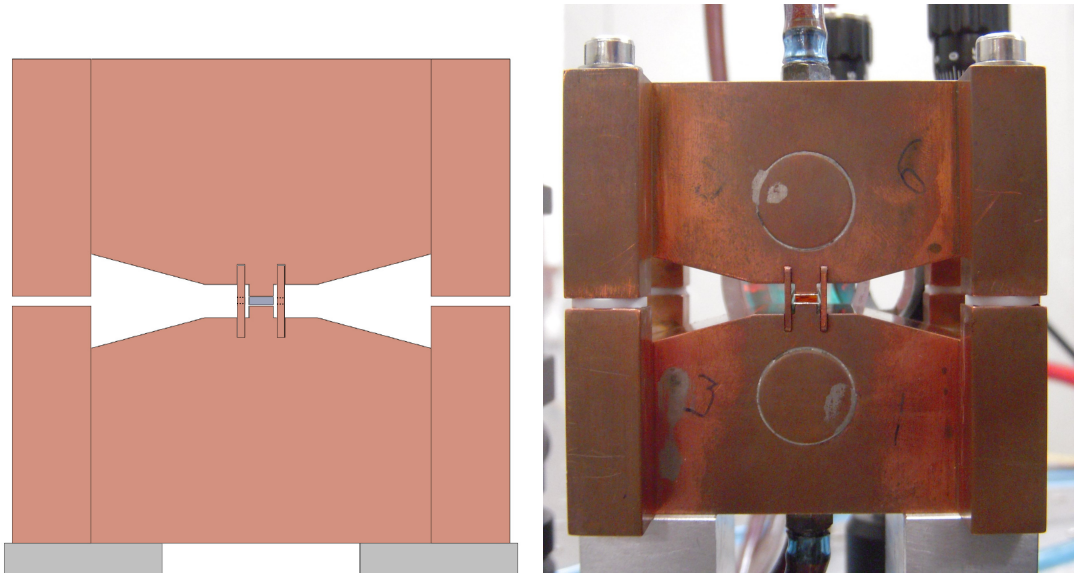

Figure 5.11: End-on view of the laser head, showing the two copper cooling blocks, the slab (grey) and the copper apertures.

Sheets of 125-μm thick pure indium was placed between the slab and copper cooling surfaces to improve the thermal contact due to the malleability of indium. By controlling the thickness of the spacers, a small amount of crush in the order of 5% of the thickness can be applied to the indium without significant stress on the slab. This was achieved by measuring both the indium sheets and slab thickness to an accuracy of ±1 μm using a micrometer, and machining the spacers to the exact thickness required. Due to the low melting point of indium, any stray light from the pump diode incident on the indium could melt it and cause catastrophic failure of the laser. Thus, copper apertures were manufactured and placed in the slots in the copper cooling blocks.

5.3 Pump diode characterisation

5.3.1 Pump diode specifications

Two 720 W diode stacks (Jenoptik JOLD-720-CAFN-10A) were used as the pump source for the Tm:$YAlO_3$ slab laser. These were custom-made to operate at 793 nm instead of the typical 808 nm. A photograph of the mounted diode stack is shown in Figure 5.12. Each diode stack consists of ten bar emitters, which stacked vertically. Each bar is 10 mm in width, giving a total emission area of 10 mm × 17.75 mm. Each bar emitter is collimated individually in the vertical direction (fast axis) via a Doric lens, such that the divergence in the vertical direction is <0.5 mrad. There is no collimation in the horizontal direction and the beam freely diverges, with the maximum divergence between 6-7° FWHM. The diode specifications are summarised in Table 5.3.

Parameter	JOLD-720-CAFN-10A
Centre wavelength	793 nm
Maximum output power	720 W
Spectral width	< 5 nm
Operating temperature	25°C
Threshold current	19 A
Operating current	100 A
Operating voltage	< 20 V

Table 5.3: Specifications of the 720 W pump diode stacks.

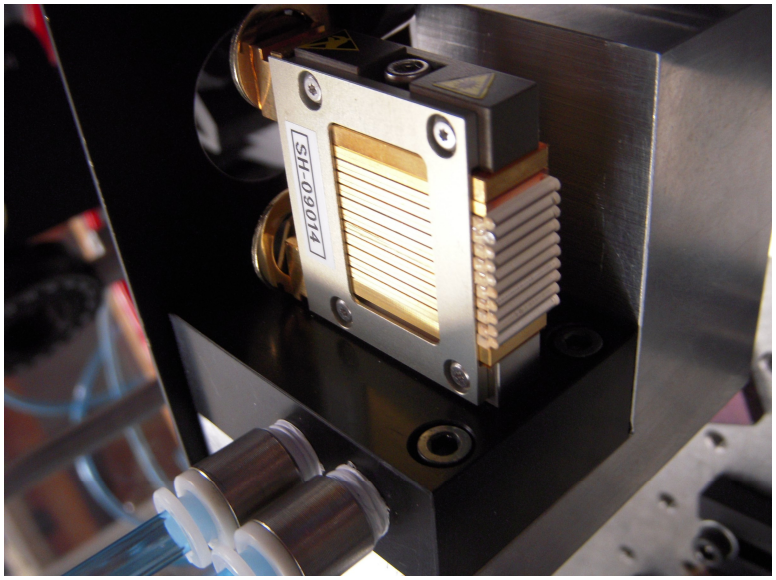

Figure 5.12: The 720 W pump diode stack, mounted on a Delrin block. The emitter bar width is 10 mm, with a total stack height of 18 mm.

5.3.2 Water cooling

The diode stacks were water-cooled with water passing inside the diode. To avoid corrosion, deionised (DI) water with conductivity of 2-6 $\mu S \cdot cm^{-1}$ was required.

A DI water chiller (Termotek P208-16676) was used to supply the required DI water to both diode stacks via a water manifold. The diode stacks were connected in parallel to the water manifold. Independent valves with flow meters were used to control the flow rate into each diode to ensure each received the required flow rate of 3.7 L/min. A flow switch for each diode stack, interlocked with the diode driver, was incorporated into the water manifold to guard against failure of the cooling water. A photograph of the water manifold is shown in Figure 5.13.

The diode stacks were each mounted on a Delrin block, a nonconductive plastic material, as shown in Figure 5.12. This block was used both to secure and to supply the DI water to the diode stacks. O-rings were used to seal the water connections between the diode stack and the Delrin block. The drawings for the Delrin blocks can be found in Appendix B.2.

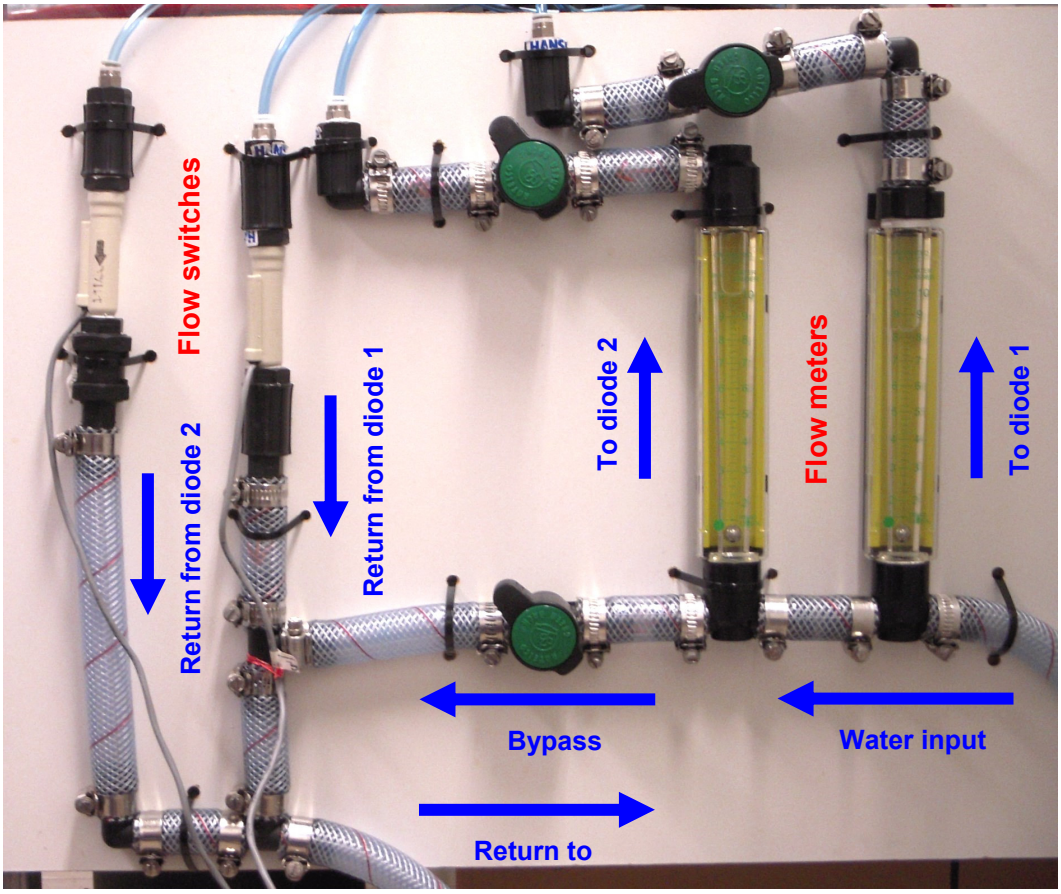

Figure 5.13: In-house DI water manifold for supplying DI water to the diodes.

5.3.3 Emission wavelength and pump absorption

The slab laser threshold was calculated to be approximately 100 W of total absorbed pump power and at this power the diode stacks will operate well below the maximum operating power. This results in the diodes emitting at wavelengths much shorter than the specified 793 nm at 25°C operating temperature, due to the corresponding lower temperature of the diode stacks. The peak absorption of Tm:$YAlO_3$ along the *b*-axis occurs at 793 nm and 795 nm, as seen in Figure 2.2, and hence a shorter wavelength than 793 nm will result in lower absorption. The shift in wavelength can be compensated for by increasing the operating temperature of the diode stacks, controlled by the cooling water. The emission wavelength was measured using a CCD spectrometer (CCS175) at an output power of 200 W at various cooling water temperatures, as shown in Figure 5.14. The absorption coefficient of the *b*-axis of Tm:$YAlO_3$ is also included for comparison.

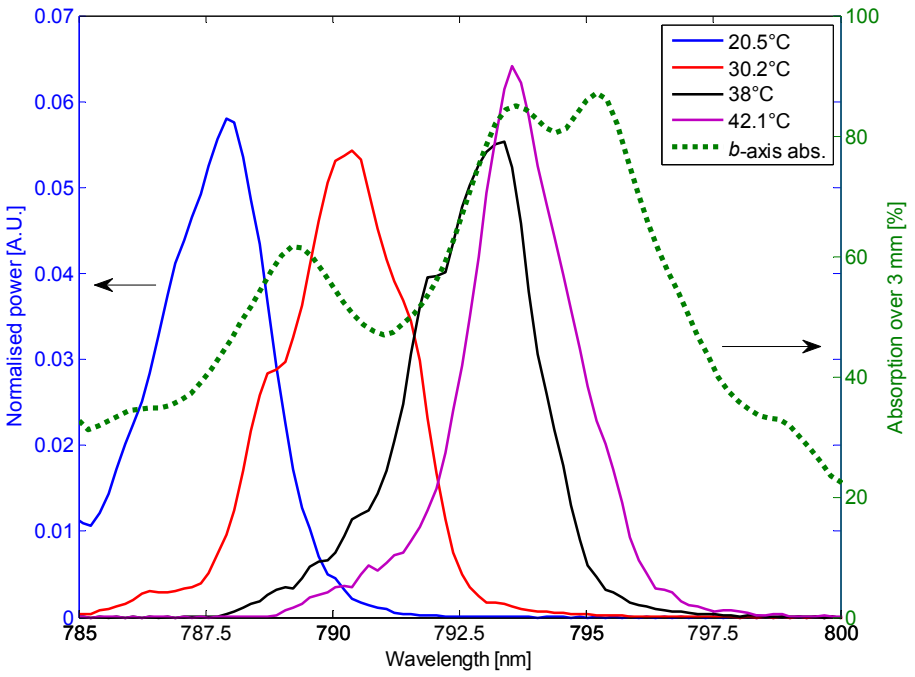

Figure 5.14: Diode stack emission wavelengths at different cooling water temperatures, at an output power of 200 W. The *b*-axis absorption of Tm:$YAlO_3$ (green) is for reference.

The cooling water temperature was set to 40°C in order for sufficient absorption of the pump light. However, due to a large temperature difference between the DI water and industrial water used to cool the DI chiller, the temperature of the DI water oscillated, with gradual heating to 42°C and rapid cooling to 38°C over approximately one minute.

The absorption of the pump light through the slab was measured at different operating currents by comparing the incident pump power with the transmitted pump power. At the operating temperature of 40°C, pump absorption for the diode stacks ranged between 60-62% for one diode stack and 69-72% for the other, with absorption increasing slightly at higher pump powers. The difference in absorption between the diode stacks was attributed to slightly different emission wavelengths.

5.4 Laser operation

5.4.1 Output power

The laser configuration described in Section 5.2.4 as well as several variations were constructed to maximise the output power. These variations included different radii of curvature of the HR mirror and changing the separation between resonator mirrors and the slab. Each configuration was tested with three different output coupler reflectivities (R = 65%, 75% and 88%). The laser configuration described in Section 5.2.4 resulted in the highest slope efficiency with the R = 65% output coupler. Fine adjustment of the pump lens location was performed to maximise output power.

The output power of this slab laser was measured at different pump powers, and is shown in Figure 5.15. The incident power and the measured absorption of each diode stack were used to obtain the absorbed power in the plot. The laser had a threshold of 114.2 W, similar to that predicted in Section 5.2.5. The slope efficiency was 33.4%, and the maximum power achieved was 32.2 W.

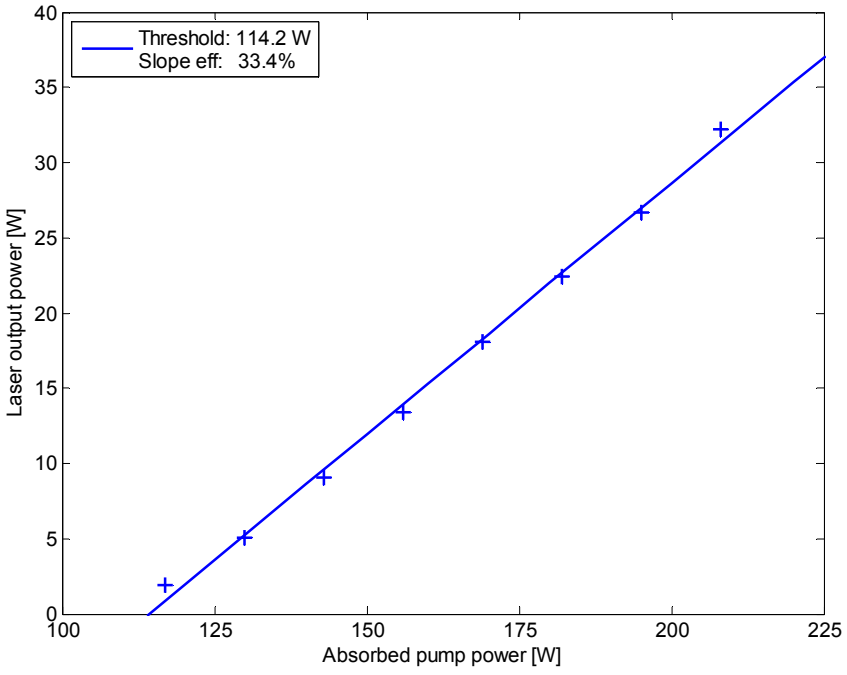

Figure 5.15: Laser output power versus absorbed pump power, with an R = 65% output coupler.

5.4.2 Output spectrum

The output spectrum of the laser was measured using an OSA (Yokogawa AQ6375). Light from the laser was coupled into a standard single-transverse-mode SMF-28 optical fibre, which is connected to the input of the OSA. An initial broad scan over the typical emission range of Tm:$YAlO_3$ lasers from 1.85 to 2 μm showed emission only around 1.94 μm. A higher-resolution sample of the output spectrum centred at 1.94 μm was obtained and is shown in Figure 5.16. The slab laser was operating at 20 W output power. The resolution of the OSA was set to 0.05 nm, and a 50-point average was used.

The cause of the spikes observed in the spectrum is unclear. The separation between peaks is approximately 0.12 nm. This would correspond to an etalon of 8 mm separation, of which none are present in the laser resonator. A measurement of the spectrum at a laser output power of 11 W showed a greater separation between the peaks of approximately 0.25 nm. It is possible that the spiking is an artifact resulting from the laser output oscillations. However, further investigation was not conducted due to time constraints and the shifting of focus to the ThOR slab described in the following chapter.

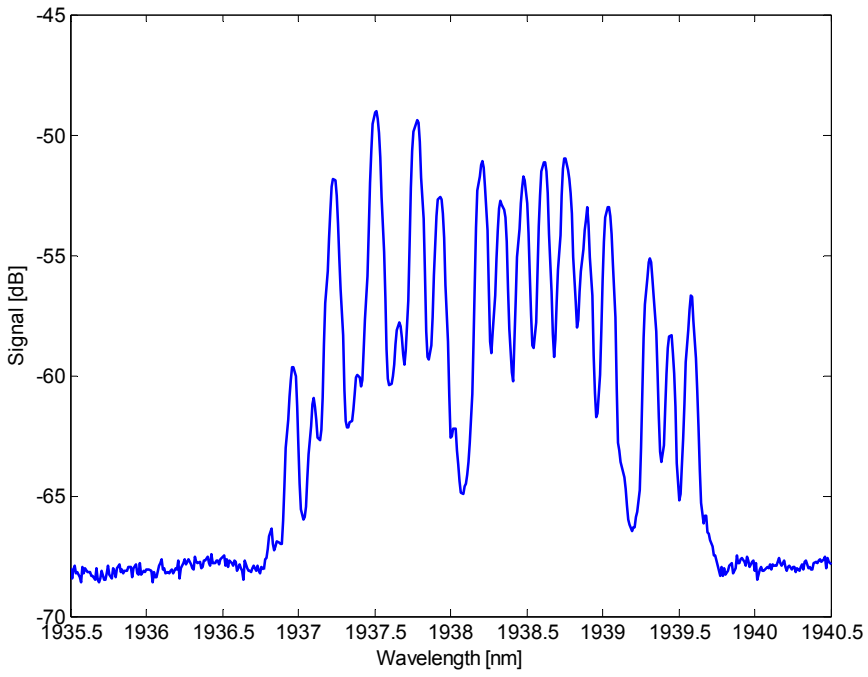

Figure 5.16: A sample output spectrum of the Tm:$YAlO_3$ slab laser.

5.5 Temporal properties

The temporal output of the Tm:$YAlO_3$ slab laser at different output powers was measured using an extended InGaAs photodetector (Thorlabs DET10D). At powers below 10 W, the laser exhibits strong self-pulsing behaviour similar to that of the cuboid laser. However, the laser output became more stable with increasing average output powers. This is shown in Figure 5.17, where the laser output traces at different output powers were normalised to the average power.

To visualise the relative oscillation amplitude temporal behaviour better, the instantaneous powers were placed into bins and plotted as histograms. The powers were normalised to a unity mean and used to show the power deviations from the mean. These histograms, as shown in Figure 5.18, show very similar spreads for average output powers below 10 W, with significant peak powers. The spread of the instantaneous powers reduced with increasing average output power, with the deviation reducing to 50% of the average output power at 28 W output.

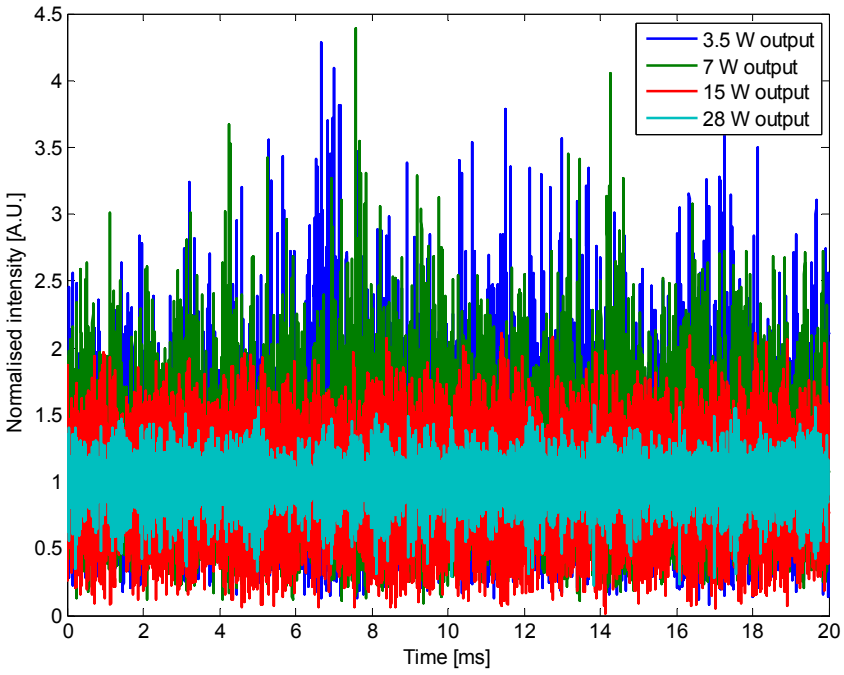

Figure 5.17: Normalised intensities at different laser output powers such that the average power is scaled to unity.

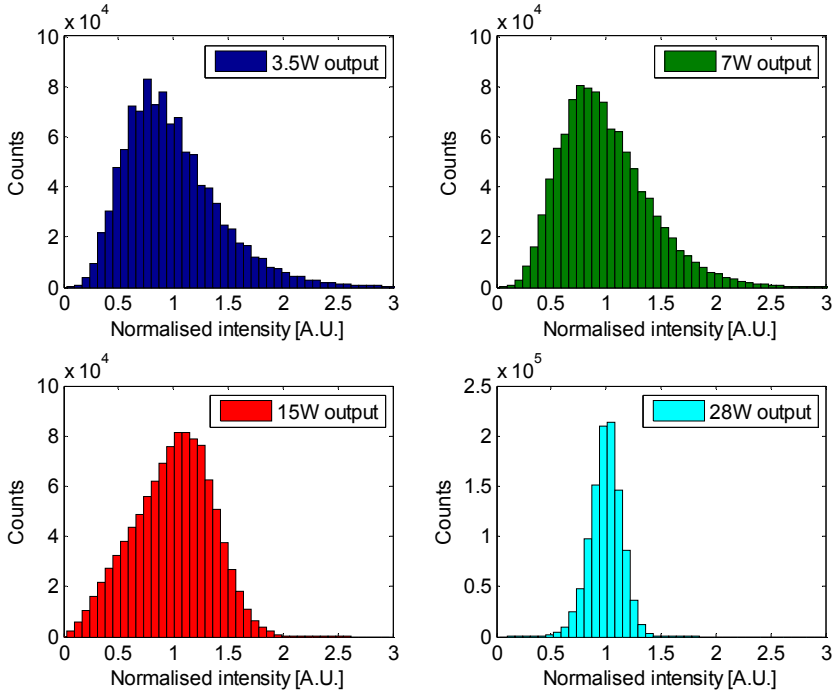

Figure 5.18: Histograms of the normalised powers at different output powers

The oscillation frequencies were obtained by taking the FFT of the output traces, and are shown in Figure 5.19. The central oscillation frequency increased with average output power with a linear dependence on the square root of output power, as shown in Figure 5.20. The central frequency was determined using the mid-point of a cumulative sum of the frequencies, and the error bars correspond to the 50% points of the cumulative sum. This is consistent with of the trend of the cuboid laser, which was discussed in Section 2.4.4. The FFT spectra were normalised to the average power, i.e. the DC (zero frequency) value, showing reducing relative oscillation power with increasing average power.

The output of the Tm:$YAlO_3$ laser is expected to stabilise with higher average power if the trends observed continue. A possible explanation may be that the laser "stability" may be related to the number of laser modes operating. The beam that was emitted from the slab laser was far from Gaussian and greater competition between more modes may have resulted in less temporal fluctuations in the output power on average. A Tm:$YAlO_3$ laser with higher power and better beam quality is required to test this hypothesis.

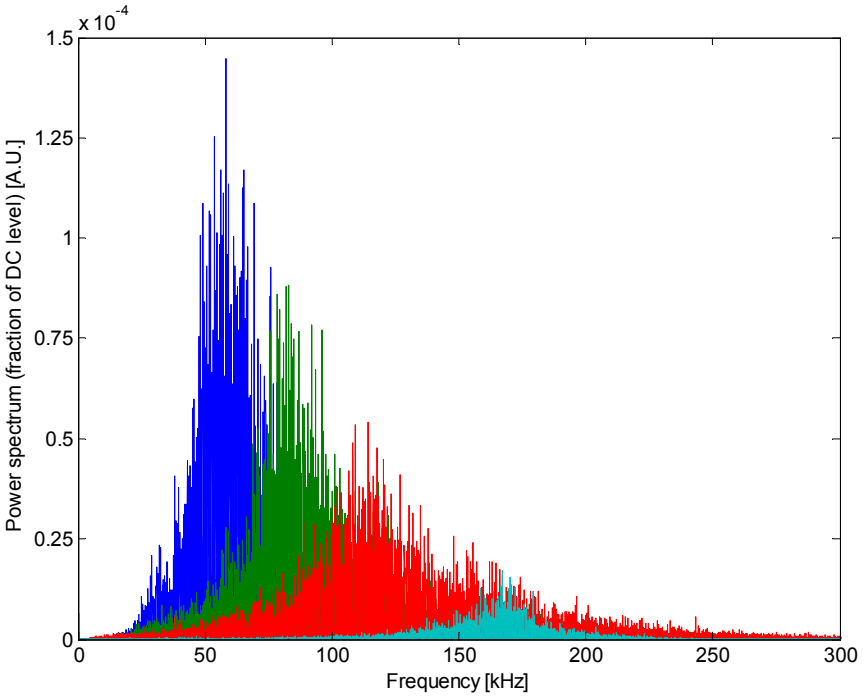

Figure 5.19: Normalised spectral density (oscillation frequency) at different output powers.

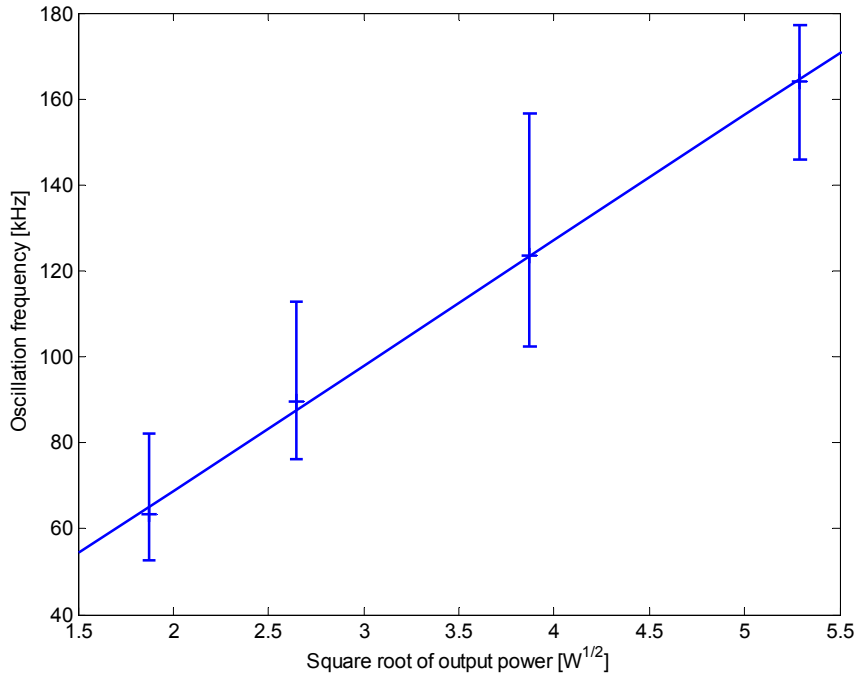

Figure 5.20: Dependence of oscillation frequency on output power.

5.6 Chaos analysis of the slab laser

An alternative explanation may be that the conditions required for the chaotic behaviour are no longer satisfied, and the laser output is dominated by noise and mode competition at higher output powers. The oscillations observed in this slab laser do not exhibit the same exponentially growing behaviour as observed in the cuboid laser, shown in Figure 2.19 and Figure 4.20. Instead, the output appears dominated by noise.

Time delay embedding, as described in Section 4.8.5, was performed on the slab laser output data. A subset of the time series at each power level, containing 32,000 data points, was used for time delay embedding.

The results of the chaos analysis for the laser operating at 15 W is shown below, with the average mutual information, false nearest neighbours and the data points in the reconstructed phase space shown in Figure 5.21, Figure 5.22, and Figure 5.23 respectively. The reconstructed phase space structures for each of the data sets at different powers were very similar, with each essentially showing a cloud of scattered points with little structure.

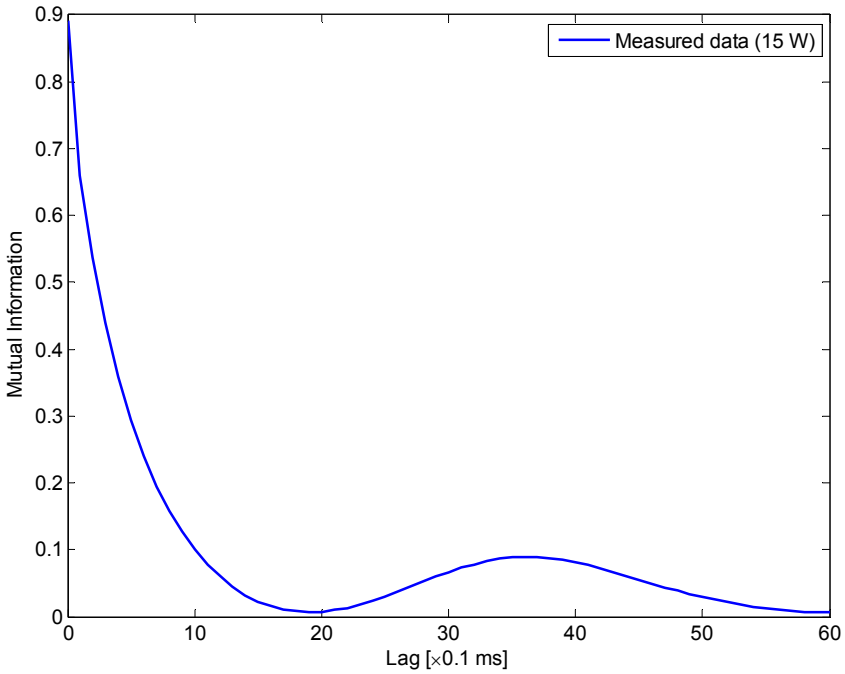

Figure 5.21: Average mutual information for the laser when operating at 15 W.

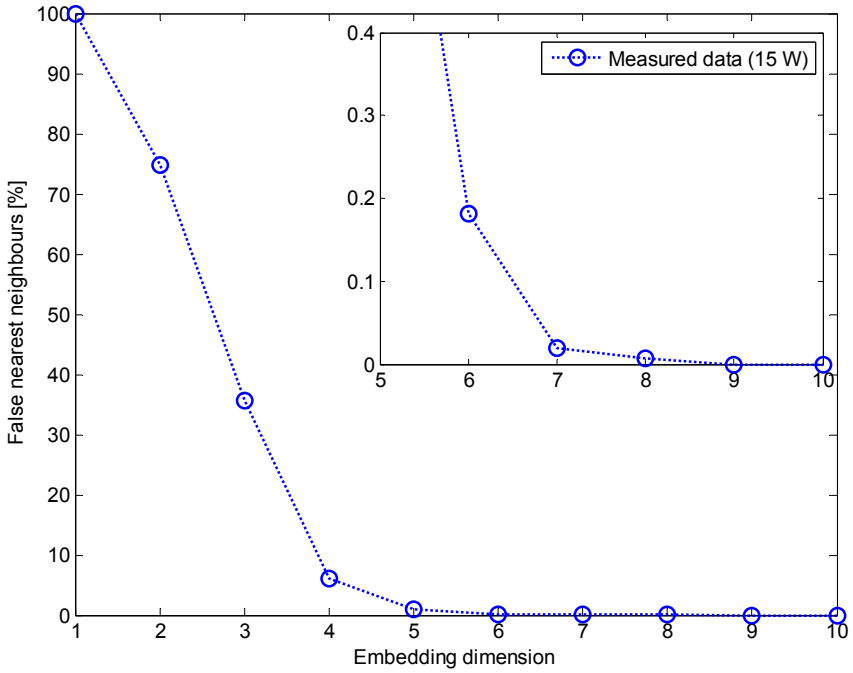

Figure 5.22: False nearest neighbours for the laser when operating at 15 W.

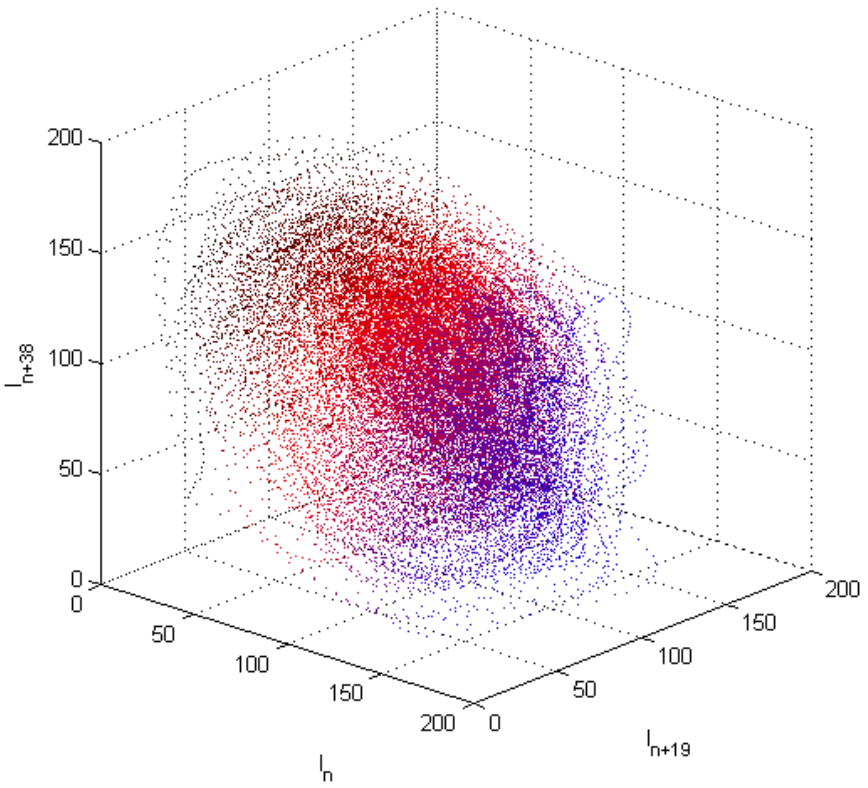

Figure 5.23: Phase space structure of the laser time series when operating at 15 W. The colour variations are for ease of viewing purposes only.

The average mutual information, false nearest neighbours and reconstructed phase space plots are all very similar to that of the linear stochastic case, which was described in Section 4.8.5. This indicates that the output of the slab laser is dominated by frequency-dependent noise and not in a chaotic regime. As suggested in the previous section, this may be the result of multiple competing modes. This can be verified using a high power laser with few modes, which is described in the following chapter.

5.7 Thermal distortions – optical wedging

The Tm:$YAlO_3$ slab laser had poorer performance than expected, based on the quantum efficiency of Tm:$YAlO_3$ and the theoretical maximum fill factor calculated in Section 5.2.4. Also, the slope efficiency of the slab laser is lower than that of similar lasers in literature [99], [101]. A lower slope efficiency not only results in less useful output from the laser, but also greater heat deposition into the crystal. This reduces the amount of pump power that can be absorbed before the crystal fractures, ultimately limiting the amount of output power attainable. To investigate the cause of the lower slope efficiency, a helium-neon (HeNe) laser was used to examine possible loss induced by thermal distortions in the slab during pumping. Under uniform pumping, a slab acts as a lens due to heating through pump absorption. Thus, light that propagates through the slab will be focused, with the focusing power increasing with pump power.

The beam from the HeNe laser was expanded and collimated such that the beam filled the slab. The beam was then aligned to propagate along the lasing path through the slab and then incident on a screen. When unpumped, the light transmitted through the slab without any noticeable distortions. As the pump power increased, the transmitted light split into two stripes of equal intensity, as shown in Figure 5.24, with the separation between the two stripes increasing with pump power.

The splitting of the HeNe beam is likely to be the result of thermal distortions in the form of a "double wedge". This occurs when heating through pump absorption is localised to a fraction of the height of the slab at the centre of the slab [109]. The top and bottom surfaces are conduction cooled, and are fixed at a constant temperature, set by the cooling blocks. A linear (to the first order) temperature gradient is formed in the unpumped regions, resulting in a "double wedge" as illustrated in Figure 5.25.

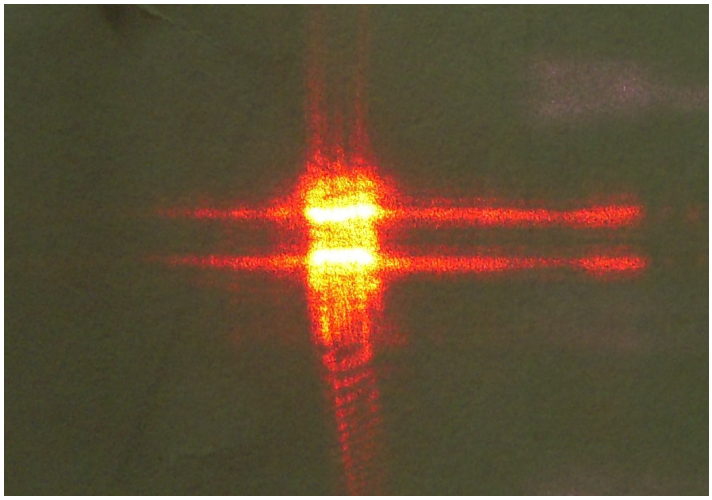

Figure 5.24: Splitting of the HeNe laser beam through the slab during pumping, the result of thermal distortions.

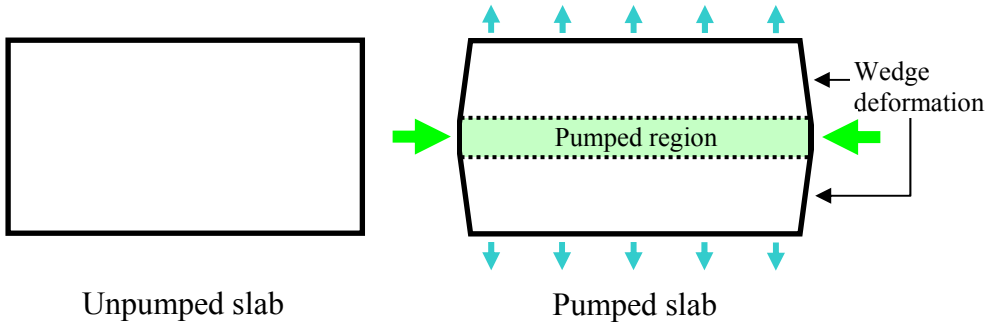

Figure 5.25: "Double wedge" thermal distortions induced due to localised heating through pump absorption. Green arrows denote the pump beams, and blue arrows denote cooling.

A thermal "double wedge" results in walk-off of the intra-cavity beam. This is detrimental to the laser efficiency, as there is lower intensity at the centre of the pumped region with highest gain. The beam also propagates through unpumped regions, which has a higher loss due to reabsorption.

The presence of a thermal double wedge was verified experimentally using a Mach Zehnder interferometer. An expanded HeNe laser beam was collimated and split into two beams using a beam splitter. One of the beams was used as the reference wavefront, while the other was passed through the lasing path of the slab. The two beams were recombined and imaged onto a screen. The interference patterns of the Mach Zehnder interferometer for no pump light and 100 W of absorbed power is

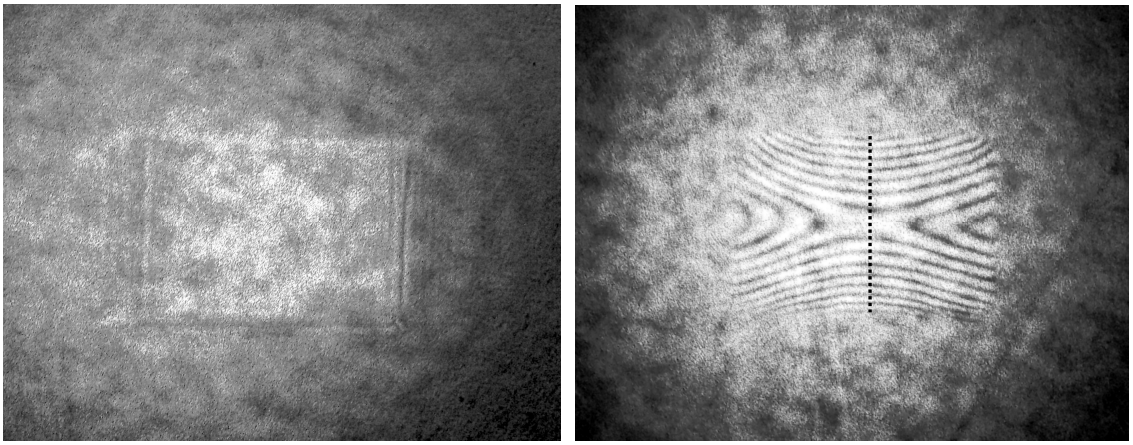

Figure 5.26: Mach Zehnder interference patterns of the slab under no pumping (left) and 100 of absorbed pump light (right).

shown in Figure 5.26. Note that the slab was not lasing, and hence the majority of the absorbed pump power was converted to heat.

Zero fringes was observed when the slab was not pumped, indicating minimal clamping stress. A number of fringes were observed when the slab was pumped. The fringes correspond to differences in refractive index as a result of the temperature gradient from the optical pumping and active cooling. The temperature is lowest at the top and bottom surfaces due to the cooling, and is hotter towards the centre of the slab. The temperature is highest at the centre left and centre right due to higher pump intensities from the side pumping.

The fringe pattern along the vertical axis in the middle of the slab was used to estimate the temperature profile along the slab, using the location of the fringe maximas and minimas. A plot of the profile is shown in Figure 5.27. A quadratic fit was made to the central region of the profile, clearly showing large discrepancies towards the edges of the slab. The optical double wedge effect is highlighted using linear fits to the profile towards edges of the slab. A fringe count of 7.1 corresponds to an optical path difference of 4.5 μm from the edge to the centre. This in turn corresponds to a dn of 1.35×10^{-4}, or a temperature difference of 10 K.

Defocusing the beam can result in better distribution of power over the slab volume. However, this reduces the margin of error for alignment, and gives a non-uniform beam as the pump diode is a diode stack that emits in discrete bars. An optical waveguide mounted directly next to the slab can be used to ensure the pump beam is

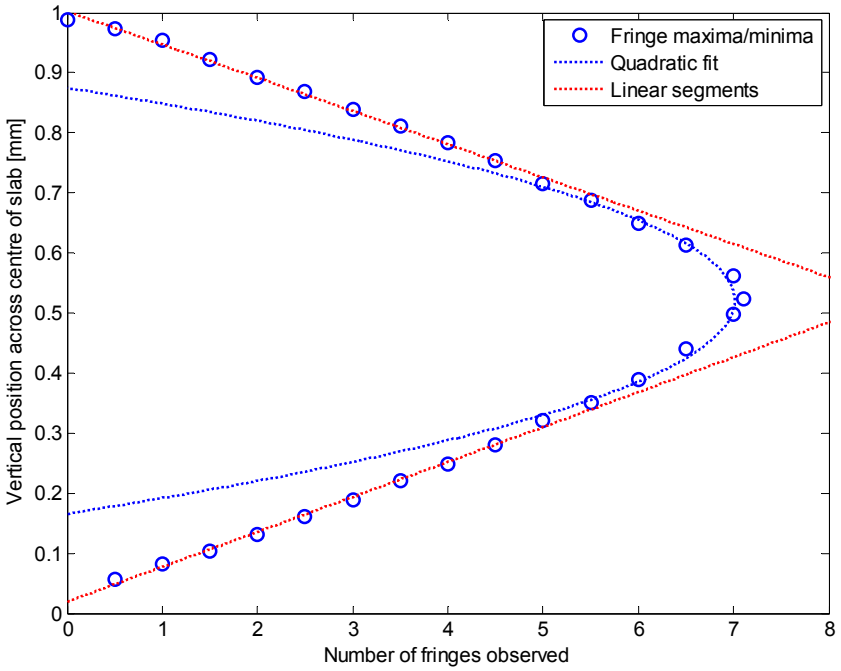

Figure 5.27: Fringe pattern along the vertical axis at the centre of the slab (dotted line in previous figure), with a quadratic fit to the central region and linear fits to the sides.

well mixed and uniform by the use of multiple reflections. The waveguide also allows the pump light to fill the slab completely, as the exiting pump beam is highly divergent. Subsequently, the pump light would be incident on the top and bottom surfaces of the slab and SiO_2 coatings are required on these surfaces to ensure the pump beam is total internal reflected and not incident on the indium.

This improvement was not attempted on the Tm:$YAlO_3$ slab laser as suitable waveguide were not available. In addition, the focus of the work had shifted to the ThOR geometry described in the next chapter due to time constraints, as it was expected to have a higher damage threshold and hence produce greater powers.

5.8 Chapter summary

A side-pumped, straight-through Tm:$YAlO_3$ slab laser was designed, modelled and constructed. The laser operated with a threshold of 114.2 W and an absorbed slope efficiency of 33.4%, up to a maximum output power of 32.2 W. The slab laser suffered from lower-than-expected slope efficiency, which limited the output power. This was due to thermal distortions in the Tm:$YAlO_3$ slab in the form of an optical "double

wedge. An optical waveguide to guide the pump light is expected to yield a more uniform pump, resulting in only the standard thermal lensing and therefore improve the slope efficiency. However, due to time constraints the focus of the work had shifted to the ThOR geometry described in the next chapter, which was expected to produce greater powers.

For output powers below 10 W, the laser output showed significant self-pulsing. However, the output became more stable with increasing output power, with the oscillation amplitude below 50% of the average power at 28 W output. If this trend continues for higher powers, then feedback may only be necessary to quieten intensity noise rather than suppress oscillations with 100% modulation. This is significantly less demanding on the feedback electronics. The cause of this lower modulation amplitude is currently unknown. Chaos analysis of the output did not show any evidence of chaotic behaviour in the laser. A possible explanation is competition between multiple modes, and a high power laser with few modes is required to verify this.

6 High-power Tm:$YAlO_3$ ThOR slab laser

6.1 Introduction

In order to attain very high powers, thermal management of the laser gain medium is of the utmost importance. The slab geometry offers ease of pumping and long gain length, but is generally limited to moderate powers by thermal issues. The disk geometry offers excellent thermal management, but is difficult to pump uniformly due to the shallow absorption length. This chapter describes the design of the **Th**in **O**uter-**R**egion-doped slab (ThOR slab) laser, a hybrid slab geometry that aims to combine the ease of pumping of slab lasers with the thermal management of disk lasers. A slab based on this geometry was manufactured; however high losses due to inclusions and ultimately a major error during manufacturing rendered the slab unusable. The design and modelling of the potential performance of this slab is described in this chapter.

An overview of the ThOR slab design and its expected benefits over conventional laser geometries are described in Section 6.2. The design specifics are described in Section 6.3, including slab geometry, pumping scheme and the cavity mode. Section 6.4 describes a comprehensive model of the ThOR laser design, including the pump absorption and a Rigrod analysis to predict the maximum attainable power. Section 6.5 describes the laser head design and outlines the assembly procedure. Issues with our manufactured ThOR slab, such as internal scatterers and pump absorption, are explained in Section 6.6 and Section 6.7. The chapter is concluded in Section 6.8.

6.2 ThOR slab design

The ThOR slab design is a hybrid of the standard slab and disk laser geometries. The pumping geometry and the laser mode path are like that of a standard end-pumped folded zigzag slab laser, but with the thermal capabilities of a disk laser [112]–[114].

The ThOR slab consists of a large undoped region in the centre of the slab and two thin, highly doped layers on the outer regions of the slab, as shown in Figure 6.1. The two doped layers act as gain regions of the slab. These are in direct contact with heat sinks, similar to that of disk lasers, for excellent heat dissipation. The undoped region provide a large aperture for the pump light, allowing it to be end-pumped similar to a standard slab. A typical folded zigzag laser mode sweeps out the entire gain region.

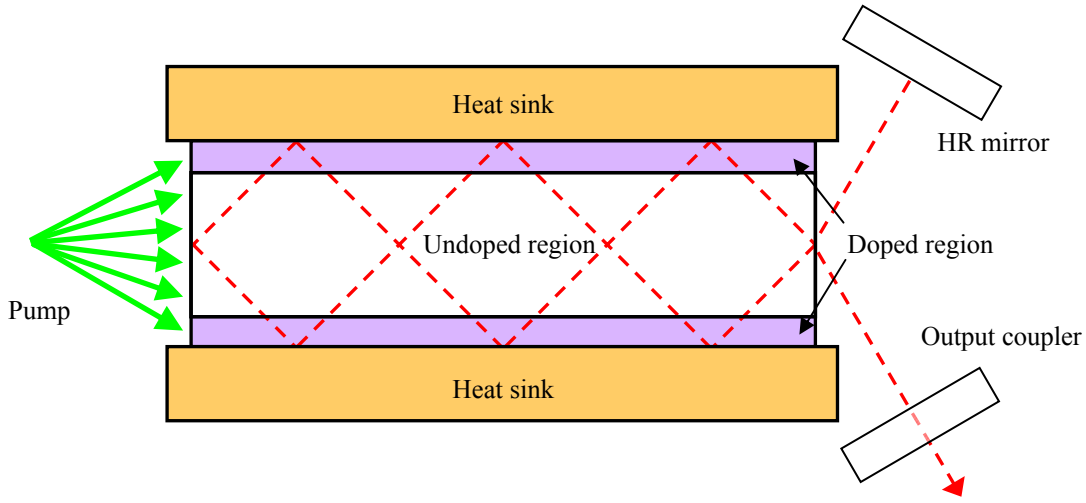

Figure 6.1: Illustration of the ThOR slab design – thin doped regions directly next to heat sinks, with an undoped region in between doped regions.

6.2.1 Comparison with a standard slab

To highlight the enhanced thermal handling of the proposed ThOR slab, the temperatures and thermal-induced stress due to pump absorption in both the ThOR slab and a standard slab were modelled in a simple case using FEA in COMSOL. The ThOR slab was modelled as a crystal of dimensions 40 × 5 × 3.2 mm, consisting of two 200-µm thick doped regions and a 2.8-mm thick undoped region (see Figure 6.2 (top)). A standard slab of dimensions 40 × 3 × 1.5 was used for the comparison. 300 W of uniform heat was distributed in the doped regions of both slabs. The results of the thermal modelling are shown in Figure 6.2, with the values obtained for the maximum

stress and temperature difference summarised in Table 6.1. The maximum heat deposition allowed is calculated based on a fracture limit of 160 MPa and a proportional relationship between stress and heat deposition [110]. The pump absorption for the ThOR slab was estimated using the ray tracing method, which is explained in Section 6.4.1.

The maximum heat deposition allowed in a slab is a key indicator for the maximum laser output power attainable. The total efficiency of a laser is below unity and the majority of the unextracted power is deposited in the crystal as heat. A greater maximum heat deposition allows for higher pump powers as well as output power,

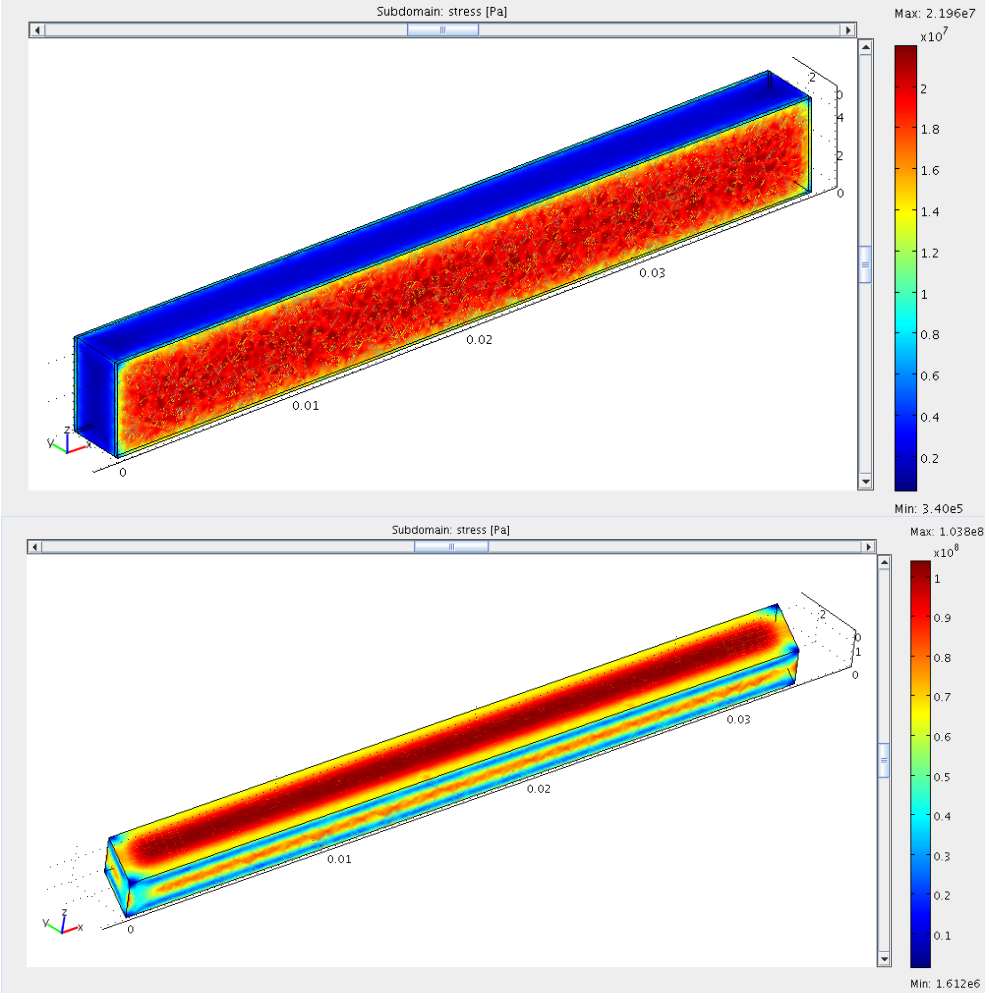

Figure 6.2: Modelled thermal-induced stress within the ThOR slab (top) and a standard slab (bottom) for 300 W of deposited heat.

	ThOR slab	**Standard slab**
Full dimensions	40 × 5 × 3.2 mm (2× 200-μm doped)	40 × 3 × 1.5 mm
Doped volume	80 mm^3	160 mm^3
Pump absorption	85% (end pumped)	80% (side pumped)
Maximum stress	22 MPa	104 MPa
ΔT (edge to centre)	7 K	49 K
Maximum heat deposition	> 2 kW	400 W

Table 6.1: Thermal handling comparison between the ThOR slab and a standard slab for 300 W heat deposition in the doped region from optical pumping.

assuming comparable slope efficiencies and thresholds. It is therefore expected that the ThOR slab has a much greater potential for high power operation, and potentially an order of magnitude greater output power attainable.

6.3 Thin-film-coated laser design

A zigzag laser mode is required to extract the gain from the Tm:$YAlO_3$ slab because the dopant only exists as a very thin layer on the sides of the slab. $YAlO_3$ is biaxial, and hence it is important to maintain the same laser polarisation throughout the slab. This maximises gain extraction, as the peak gain for each of the crystal axes are separated by 50 nm in wavelength in Tm:$YAlO_3$ [72]. For *p*-polarised light, the direction of the electric field vector changes on reflection; the direction remains constant for *s*-polarised light. Thus, the laser mode must be *s*-polarised at each reflection, i.e. aligned perpendicular to the zigzag plane, as shown in Figure 6.3. However, operating using *s*-polarisation makes it difficult to use Brewster end faces to minimise Fresnel losses, because the beam must exit the slab out-of-plane, as shown in Figure 6.3. The slab must therefore have end faces angled along an oblique plane, which is difficult to manufacture. The angles required for such a slab is described in Appendix F. For the initial design, thin-film coatings on the entrance and exit faces were used to simplify the slab geometry.

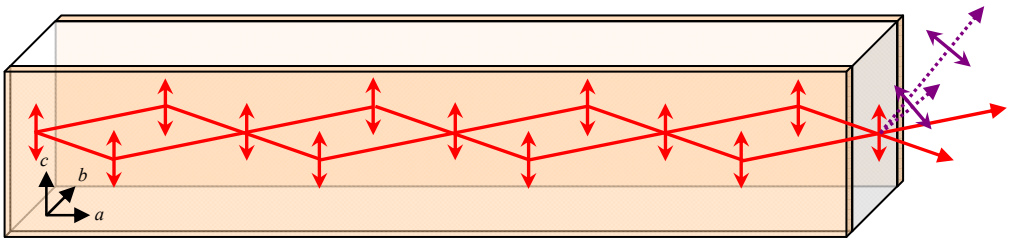

Figure 6.3: Polarisations required within the slab. The use of Brewster's angle for entry and exit requires different end faces angled along specific planes.

6.3.1 Laser design summary

The summary of the laser design is shown in Figure 6.4. Pump light from two diode stacks (green) are coupled into the ThOR slab via cylindrical lenses. Any unabsorbed pump light is retro-reflected back into the slab via a concave lens, in this case with a radius of curvature of 30 mm. The laser mode (red) zigzags through the slab and is incident on the resonator mirrors, 50 mm from the end of the slab. The details for the slab geometry, pumping geometry and laser mode are described in the following sections.

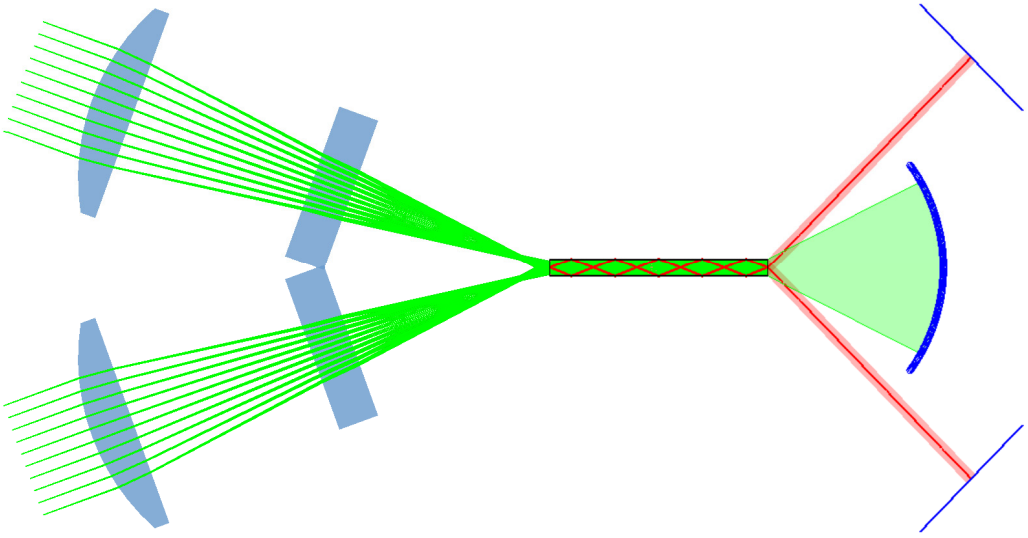

Figure 6.4: Summary of the laser design (top view), incorporating the pump light (green) and laser mode (red).

6.3.2 Slab geometry

A schematic of the ThOR slab is shown in Figure 6.5. The length of the slab was chosen to be 37 mm, the maximum allowed by the crystal boule from which the slab will be cut. The height of the slab was chosen arbitrarily to be 5 mm. The total width of the slab, including both doped and undoped layers, was chosen to be 3.2 mm based on pump absorption, described later, and aperture size. The thickness of the doped layers controls thermal handling of the slab, while the ratio of the doped and undoped layer thicknesses determines the pump absorption and the gain length of the laser path. Modelling of a dopant thickness of 200 μm showed a pump absorption of 87.5% and a thermal fracture limit of 1.4 kW, which is an excellent compromise between the two parameters. The pump absorption modelling is described later in Section 6.4.1.

The laser mode must be *s*-polarised at each reflection in order to maintain the same polarisation throughout the slab as mentioned previously. This is made to correspond to the crystalline *c*-axis, the desired lasing axis. The crystalline *b*-axis has the broadest absorption peak, as shown in Figure 2.2, and hence is aligned perpendicular to the doped/undoped interface for maximum pump absorption.

The ends of the slab are thin-film coated. The pumped end of the slab is coated to be HR at the lasing wavelength, with an internal angle of incidence (AoI) of 22° corresponding to the laser mode. This coating is also made to be highly transmissive (HT) at the pump wavelength. The end of the slab in which the lasing mode enters and exits the slab (the lasing end) is coated to be AR at the lasing wavelength at an internal AoI of 22°. The outer surfaces of the doped layers are coated with a layer of SiO_2 to ensure total internal reflection of the laser mode and pump beam.

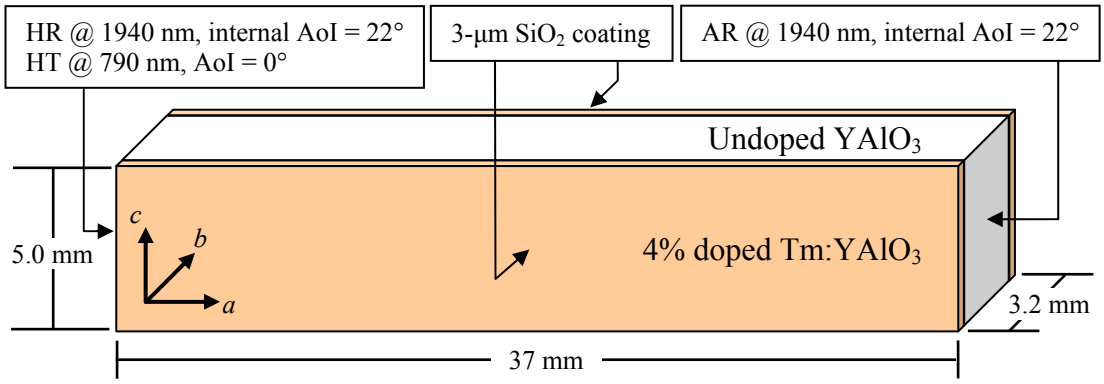

Figure 6.5: Schematic of the laser slab geometry.

The thickness of the SiO_2 layer must be sufficiently thick to ensure negligible power loss via evanescent fields, but also thin enough to minimise impedance to the heat flow. The intensity of the evanescent field into the SiO_2 layer is given by [148]:

$$I(z) = I(0)e^{-z/\delta}, \tag{6.1}$$

with the $1/e$ penetration depth given by:

$$\delta = \frac{\lambda}{4\pi}(n_1^{\,2}\sin^2\theta_{inc} - n_2^{\,2})^{-1/2}, \tag{6.2}$$

where λ is the wavelength, n_1 and n_2 are the refractive indices of $YAlO_3$ and the SiO_2 respectively and θ_{inc} is the angle of incidence. The value for δ was calculated to be 1.65×10^{-7} m for the laser wavelength and 8.61×10^{-8} m for the pump wavelength. The intensity of the evanescent field with depth is shown in Figure 6.6. The thickness of the SiO_2 layer was made to be 3 μm to ensure negligible power from the pump light and laser penetrates through onto the indium. Finally, to minimise the risk of parasitic lasing, a 2° wedge was applied to the top surface and the output end of the slab.

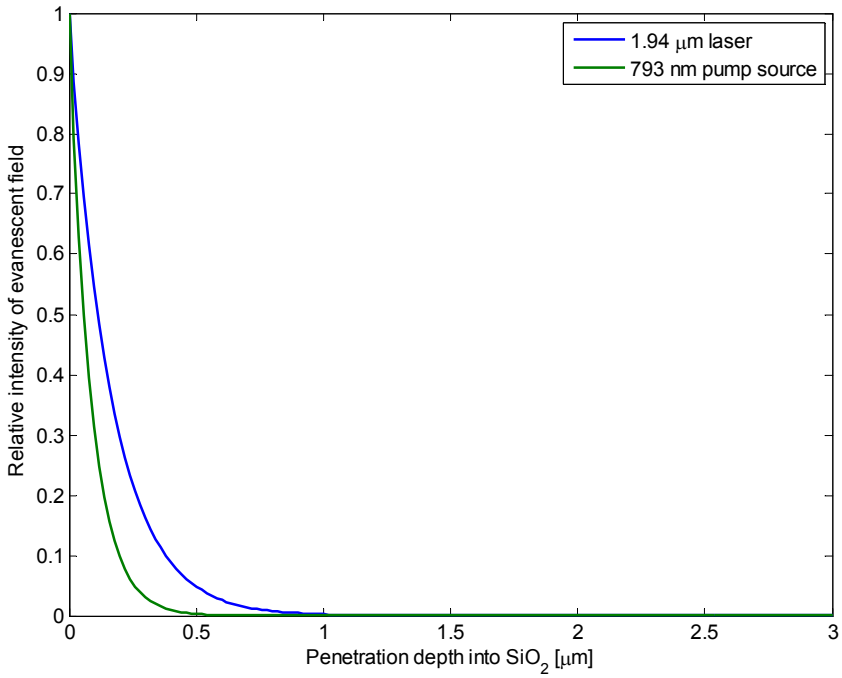

Figure 6.6: Relative intensity of the evanescent field for the laser and pump beams.

6.3.2.1 Crystal growth striations

An important but rarely mentioned consideration in zigzag slabs is the effect of crystal growth striations on the laser performance. Many crystals, such as the Tm:$YAlO_3$ crystals produced by Scientific Materials Corp., are grown using the Czochralski method. The Czochralski method is a common process used to grow large single-crystal boules of semiconductors and oxide crystals [149]. A high-purity melt of the crystal is prepared in a crucible. A seed crystal, used to define the crystal orientation, is dipped into the melt. The melt slowly crystallises onto the seed crystal, which is gradually pulled at a tightly controlled rate from the melt to form a single crystal. The shape of the resultant crystal can be controlled by controlling the temperature of the melt and the rate of pull [150]. By rotating the seed crystal while pulling, the crystal is isolated from the effect of spatial variations in thermal convections and dopant distributions in the melt [150], [151].

$YAlO_3$ crystals, like other crystals grown using this method, suffer from growth striations [152]–[154]. Growth striations result from variations in growth parameters with time, such as growth rate and rotation rate. As the crystal grows, a discontinuity exists between the solid crystal and the melt. Temporal variations in growth parameters lead to slight differences in the density of the melt at this solid-melt interface compared to the grown crystal. This variation is retained when the melt crystallises onto the crystal and leads to a slightly different refractive index. Due to the rotation while being pulled and the conic shape of the boule, the final result is conic layers of varying refractive indices.

A slab that is cut from the boule will have diagonal layers of varying refractive index along the length of the slab. Light that propagates near-parallel to the striation plane will suffer from significant diffraction [118], due to different regions of the beam propagating through different refractive indices. The effect can be profound in zigzag slabs as the light propagates at a diagonal angle to the surface of the slab. It is therefore important to ensure the slab is cut such that the zigzag plane is not perpendicular to the striation planes. The refractive index variations are averaged out as the beam propagates, minimising the impact of the striations.

6.3.3 Pumping geometry

As the doped regions are located only on the sides of the slab, the pump beams need to be incident on the end face at an angle to maximise the absorption of the pump light. The optimum angle of incidence is the minimum angle at which all parts of the pump beam passes through the doped region at least once. This ensures none of the beam passes straight through the slab, while distributing pump light along the length of the slab and minimising the beam divergence of the unabsorbed light for double-passing by retro-reflection by a curved mirror at the other end of the slab. The pump beam should also be made to fill the doped region of the slab as uniformly as possible for even heat distribution. Maintaining total internal reflection is also important for larger divergences, in order to prevent pump light from escaping the slab and hitting the indium directly.

Two pump configurations were designed in Mathematica using the Optica toolbox. The existing 720 W diode stacks (Jenoptik JOLD-720-CAFN-10A), which were characterised in Section 5.3, were used as the pump source. These diode stacks are fast-axis collimated only, resulting in significantly lower divergence along the fast axis. To achieve the minimum divergence for efficient retro-reflection, the diode stacks were mounted horizontally. The Mathematica code can be found in Appendix C.2.1.

6.3.3.1 Two-diode configuration

The initial configuration incorporates two diode stacks for a total pump power of 1.4 kW, and is shown in Figure 6.7. Two cylindrical lenses with $f = 60$ mm and $f = 30$ mm are used to focus the pump beam in the horizontal and vertical direction respectively. This configuration is mirrored for the second pump diode. The average angle of incidence used, taken as the minimum angle in which none of the pump light passes straight through the undoped part of the slab, was modelled to be 20°.

The pump beam at the focus of the lenses is smaller than that of the end face of the slab. This allows for a large margin of error when aligning the pump beam. The incident beam can be expanded to fill the slab by shifting the focus back from the slab end face, as shown in Figure 6.7, where the slab end face is located at the red circle.

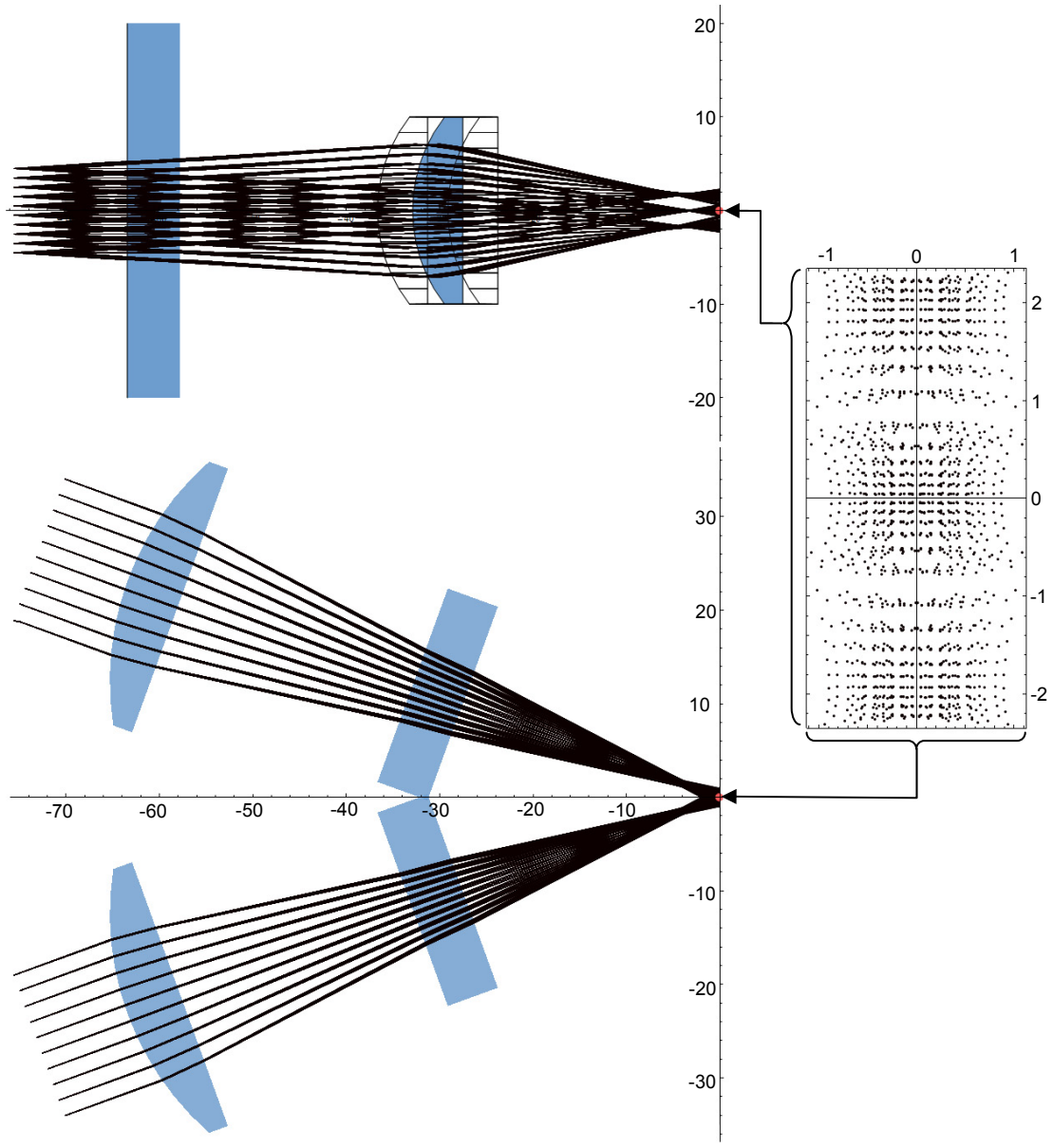

Figure 6.7: Optica output of the initial configuration with two pump diodes in the side view (top left) and top view (bottom left), and the rays incident on the slab.

6.3.3.2 Four-diode configuration

The final configuration incorporates four diode stacks for a total pump power of 2.8 kW, and is shown in Figure 6.8. Each diode stack in the initial configuration is replaced with two diode stacks mounted as close as possible along the same horizontal plane. A large cylindrical lens with $f = 150$ mm is used to focus the pump beam from

one set of the diodes in the horizontal direction. A set of two cylindrical lens, both with f = 70 mm placed 10 mm apart, are used to collimate then focus the pump beam in the vertical direction. This configuration is mirrored for the second pump diode. The same average angle of incidence of 20° was used.

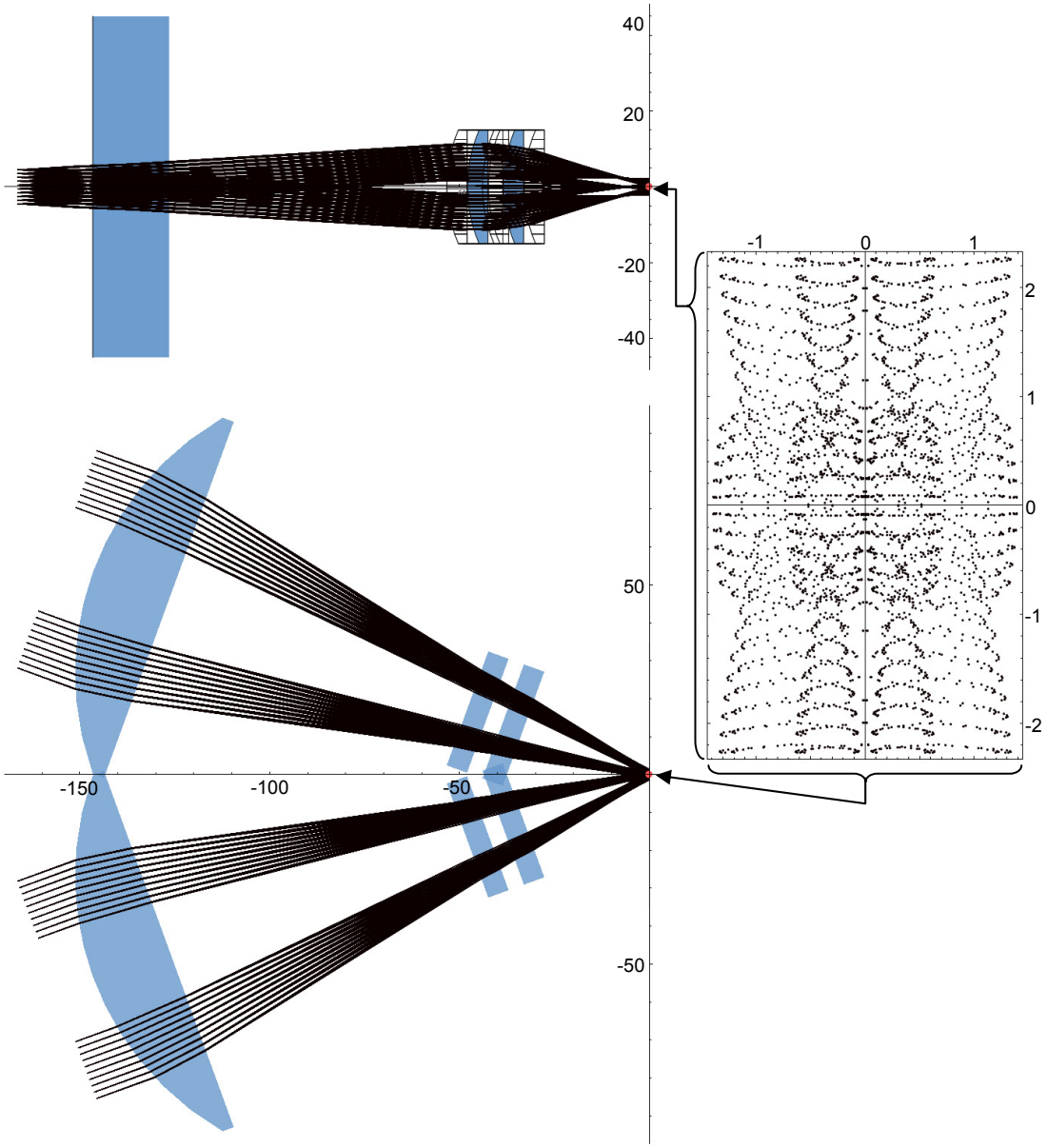

Figure 6.8: Optica output of the final configuration with four pump diodes in the side view (top left) and top view (bottom left), and the rays incident on the slab.

6.3.4 Resonator design

The ThOR slab laser is designed to operate with a folded zigzag laser mode, as shown in Figure 6.9. Near-uniform pumping along the slab is assumed; however this is not critical as the zigzag mode ensures that the majority of the gain region is swept out. The laser mode enters and exits the slab at one end, the opposite end at which the pump light enters the slab. A curved HR mirror at the lasing wavelength and a curved partially reflective mirror make up the laser resonator. The optimum reflectivity of the partially reflective mirror is discussed later in Section 6.4.5.

The thermal effects in the gain medium on the resonator mode are expected to be minimal. In the horizontal zigzag plane, the zigzag mode averages the thermal gradient in the doped regions [109], [118]. Negligible thermal gradients are expected in the vertical direction, as the entire surface of the slab is in uniform contact with the cooling block. Thus, the resonator mode should be determined by the resonator mirrors only.

The resonator design for the initial laser consists of two curved mirrors with a radius of curvature of 2 m, placed 50 mm from the end of the slab as shown in Figure 6.10. The resonator mode sweeps out almost the entire slab, as the beam is relatively collimated through the slab with a Rayleigh range of 0.37 m.

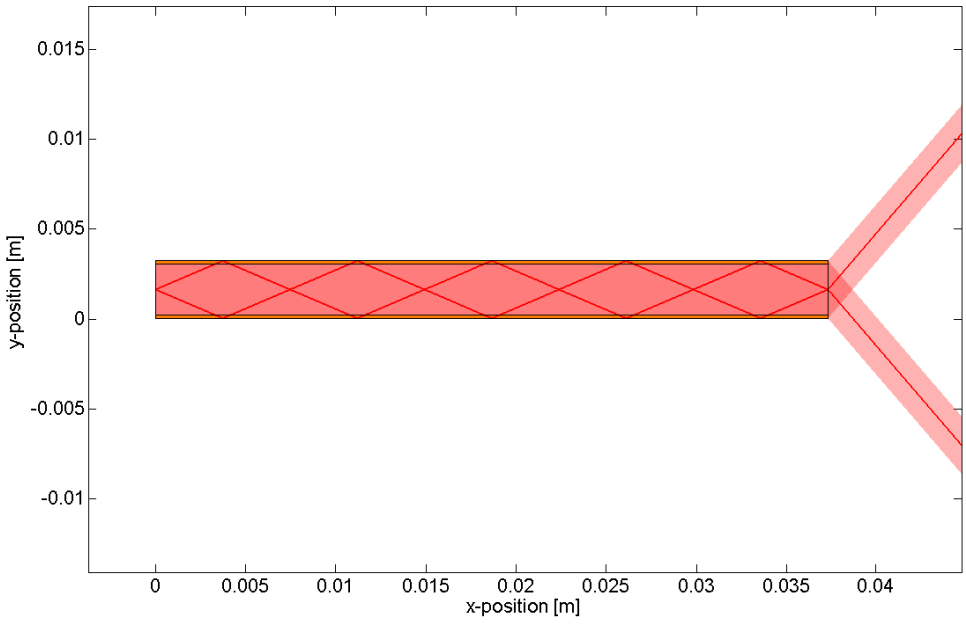

Figure 6.9: Top view of the folded zigzag laser mode through the ThOR slab.

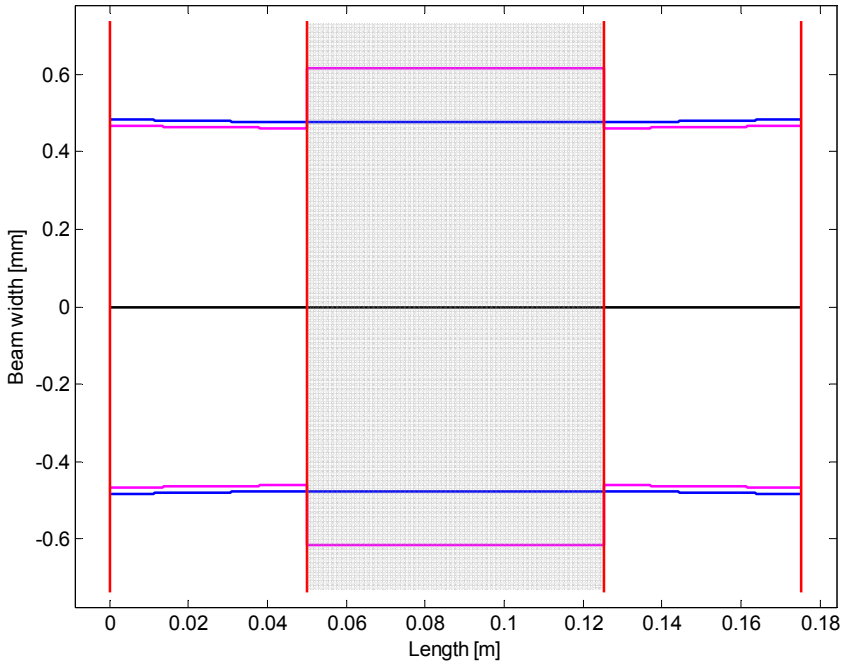

Figure 6.10: Modelled laser resonator mode ($^1/e^2$) in the vertical (blue) and horizontal directions (red). Note the grey area represents the slab with the zigzag path unfolded.

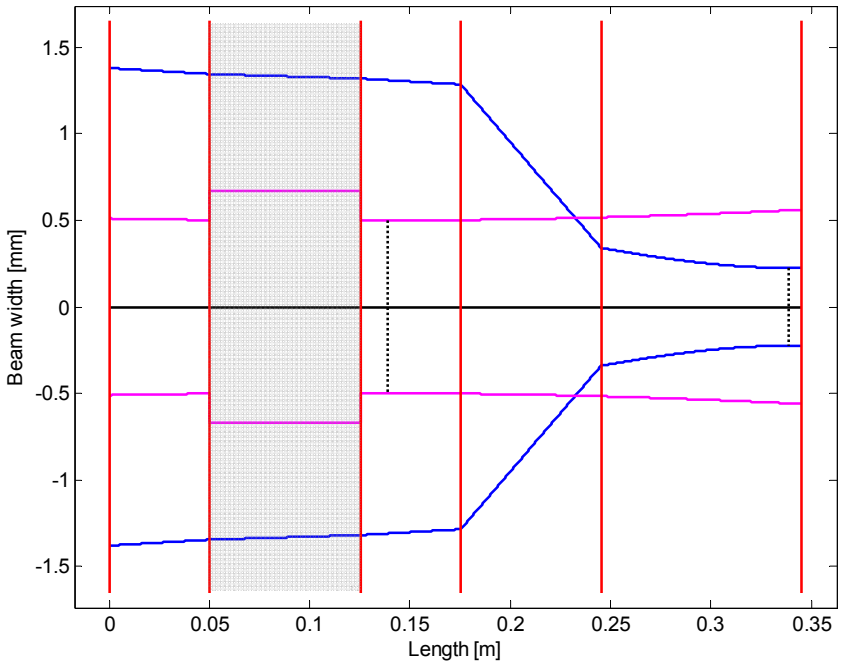

Figure 6.11: Modelled laser resonator mode in the vertical (blue) and horizontal directions (red), with an intra-cavity telescope in the vertical direction. Note the grey area represents the slab with the zigzag path unfolded

The ratio of the resonator mode to the slab dimension in the vertical direction is significantly lower than that of the horizontal zigzagging direction. This would result in a poorer beam quality in the vertical direction, as more higher-order modes are able to operate. This can be resolved using an intra-cavity telescope in the vertical direction, using cylindrical lenses, as shown in Figure 6.11. A possible telescope configuration would consist of an f = 100 mm convex cylindrical lens and an f = -30 mm concave cylindrical lens, placed 70 mm apart. The telescope would be placed 50 mm from the end of the slab, and end mirror is placed 100 mm from the end of the telescope. Due to the longer resonator length, the beam would expand in the horizontal direction. The radius of curvature of the mirror after the telescope would be reduced to 1 m to limit the beam size in the horizontal direction.

6.4 Modelling of the laser performance

A slab based on this geometry was manufactured. The Tm:$YAlO_3$ and undoped $YAlO_3$ crystals were purchased from Scientific Materials Inc. Initial polishing and diffusion bonding was carried out by Synoptics on a best effort basis, as they had never previously diffusion bonded $YAlO_3$. Final cut, polish and optical coatings were done by BAE Systems Australia. After one of the bonds was made, Synoptics reported that large amounts of scatterers were observed in both the bulk material and in the diffusion bond. As a result of the high losses, it was decided to perform only one of the bonds, with the slab treated as a proof-of-principle. The round-trip loss resulting from the scatterers was measured, and the details can be found later in Section 6.6.

A comprehensive model was written in MATLAB to predict various parameters associated with the manufactured Tm:$YAlO_3$ ThOR slab with dopant on one side only. These include, pump absorption, losses due to the interface between doped and undoped regions, the laser cavity mode, and threshold and maximum slope efficiency. The model has been written to also accommodate the original design with doped layers on both sides.

6.4.1 Pump absorption

The Tm:$YAlO_3$ ThOR slab is designed to be end-pumped by either two or four high-power diode stacks, as discussed previously in Section 6.3.3. To model the absorption

of pump light by the doped regions of the slab, the pump beam from each diode was modelled as an array of emitters located at the pump end of the slab, with each emitting a fan of rays. The emitters were spaced out evenly across the predicted width of the pump beam when focused at the end of the slab to emulate a top-hat profile. The fans of rays spanned the internal (within the crystal) FWHM divergence of the beam, and were offset to account for the tilt angle of the pump beam and refraction. This is illustrated in Figure 6.12.

Each ray was made to propagate along the slab, reflecting each time the ray was incident on the outer surfaces. The total distance each ray travelled through the doped region was calculated. The total absorption for each ray was determined using the absorption coefficient. Although this does not take into account any ground-state depletion from pumping, the pump saturation intensity was calculated to be several times the laser threshold (described later in Section 6.4.5), and thus is valid as an estimate. The pump absorption for each diode was taken to be the average absorption over all rays and emitters for that diode. A graphical representation of this process for pumping by a single diode (diode 1) is shown in Figure 6.12. This process was repeated for pumping by two diodes, the second of which (diode 2) is tilted away from the doped side due to space constraints. The overall total absorption is the average absorption over both diodes. Note that the angular components into/out of the page are not considered. As these components would lead to longer path lengths, this method gives an underestimate of the pump absorption.

While the Matlab code accommodates for dopants on both sides of the slab as per the original design, only a single 200-μm thick doped layer is shown here to reflect the manufactured slab.

Double-passing of the pump via a pump reflector was also considered. This was done by reversing the direction of each ray once it reached the end of the slab to emulate retro-reflection, then reapplying the process described above. The calculated pump absorption in both cases are summarised in Table 6.2.

	Diode 1	**Diode 2**	**Average**
Single pass	69.60%	53.01%	61.31%
Double pass	90.14%	75.16%	82.65%

Table 6.2: Pump absorption for single and double passing.

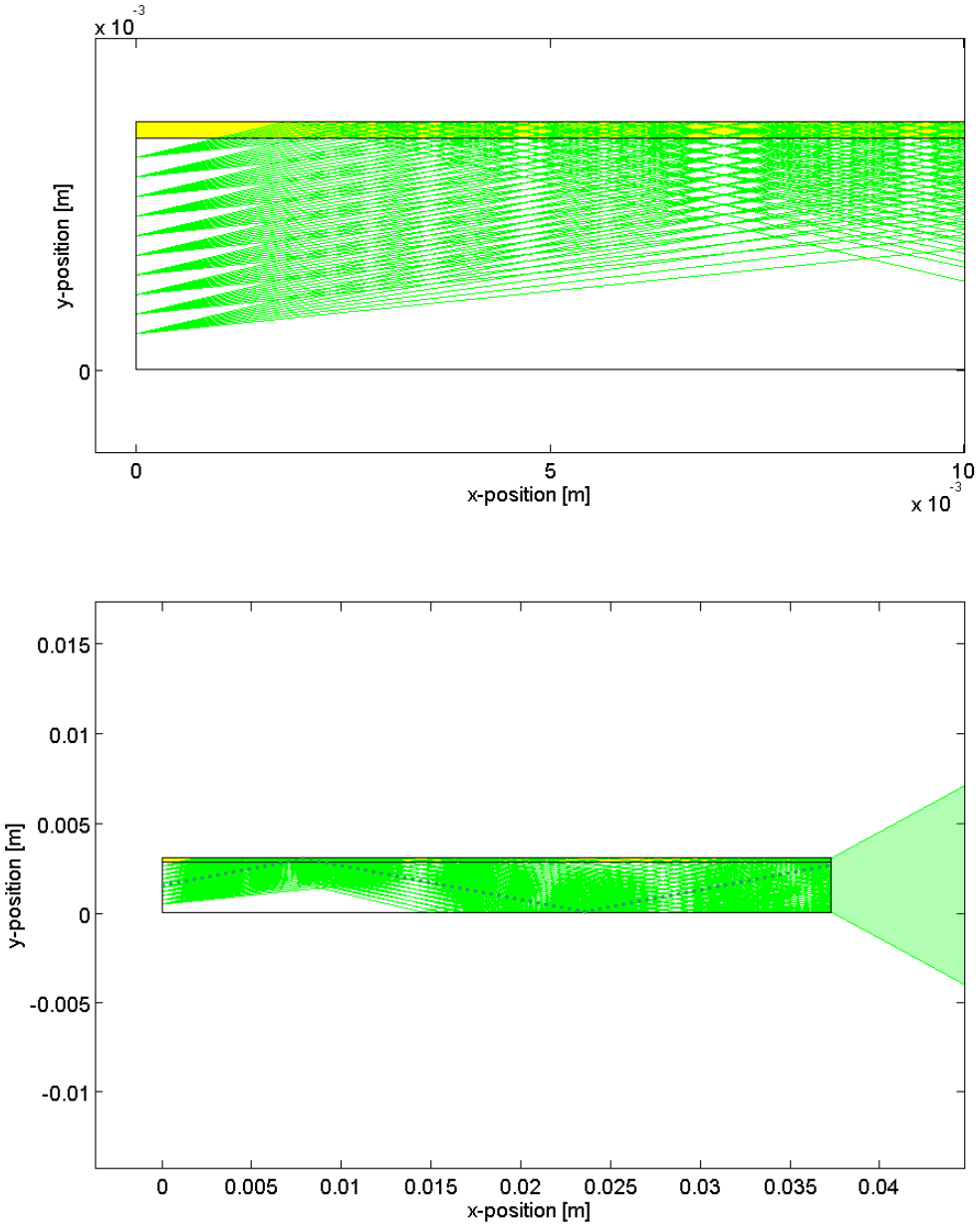

Figure 6.12: Graphical representation of the method used to estimate the pump absorption, showing the emitters and rays for pump diode 1 (top) and the rays' propagation along the slab (bottom).

6.4.2 Dopant thickness

A major consequence of the ThOR slab having only a single doped layer instead of two is a reduction in pump absorption. The feasibility of compensating for the pump absorption reduction by increasing the thickness of the doped layer was investigated, in terms of pump absorption improvement and increase in stress.

Two thicknesses for the single doped layer were investigated – the original 200 μm thickness, and doubling of the thickness to 400 μm. The undoped thickness was set to 2.8 mm for both cases. Pump absorption using one diode was estimated using the ray tracing method explained in the previous section, with 20º angle of incidence. FEA in COMSOL was used to determine the stress, using a nominal 500 W of total heat deposition from optical pumping. Uniform distribution was assumed over the doped volume for simplicity. The results are tabulated in Table 6.3.

Although the pump absorption increases by approximately 20%, the stress on and temperature gradient almost doubles due to a doubling of the maximum distance the heat must travel to the heat sink. This leads to a much lower fracture limit and thus a reduced maximum output power from the laser. As the aim is for higher power, based on these results, increasing the thickness of the doped layer to 400 μm is not a feasible option.

For sufficiently low incident angle and divergence for the pump beam, a concave mirror can be used to reflect the unabsorbed light back into the slab for double-passing. In this case, pump absorption for a single 200-μm-thick doped layer increases to 90.14%, which would greatly reduce any benefit of having a 400-μm thick doped layer.

	200 μm thickness	**400 μm thickness**
Pump absorption	69.6%	87.5%
Stress	57.38 MPa	106.3 MPa
ΔT (edge to interface)	26.5 K	49.9 K
Fracture point (heat deposition)	1394.3 W	752.6 W

Table 6.3: Thermal handling comparison between two dopant layer thicknesses.

6.4.3 Zigzag laser mode

The laser mode must be totally internally reflected when incident on the sides of the slab. This is satisfied for angle of incidence greater than the critical angle for the $YAlO_3$-SiO_2 interface, which is 51.4°, calculated from the Sellmeier equation for both materials at 1.94 μm.

The chosen number of bounces depends on several factors. Large number of bounces results in a higher round-trip loss, as there is Fresnel losses associated with each bounce. These occur at both the doped-undoped interface, due to the refractive index mismatch described in the next section, and the $YAlO_3$-SiO_2 interface. Conversely, a shallow exit angle makes double-passing of the pump very difficult or impossible, as the unabsorbed pump beam and the laser mode overlap considerably.

The number of bounces chosen was the lowest number of laser bounces such that the exiting laser mode has sufficient clearance from the unabsorbed pump beam. This was achieved by having 5 bounces per side, as shown in Figure 6.13.

When 5 bounces are used, the angles of incidence are 68.1° on the sides of the slab and 21.9° at the two ends of the slab. The exit angle and the slab aperture were calculated using Snell's Law to be 45.95° and 2.09 mm respectively.

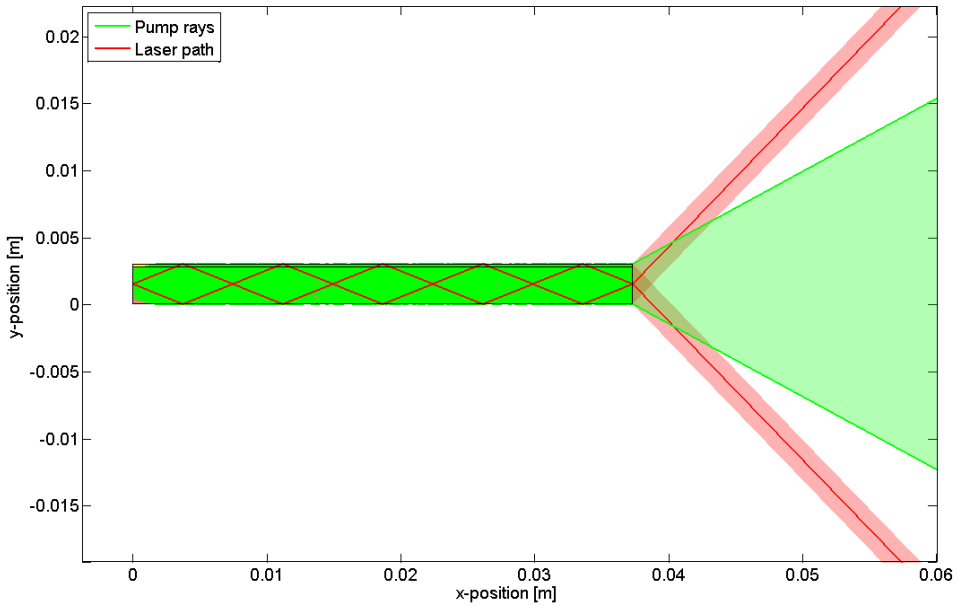

Figure 6.13: Modelled laser path with 5 bounces per side with the unabsorbed pump beam, showing sufficient clearance between the two.

6.4.4 Refractive index mismatch due to dopant

The density, and subsequently the refractive index, changes when impurities such as dopants are introduced into a crystal. The crystal lattice also distorts to accommodate the dopant. In the case of Thulium-doped $YAlO_3$, the Tm^{3+} ions displace Yttrium in the $YAlO_3$ lattice. The Tm^{3+} ion is of similar size to that of Yttrium [155] and therefore does not distort the lattice significantly. However, Thulium is almost twice as heavy as Yttrium, resulting in a higher density and refractive index for Tm:$YAlO_3$ compared to undoped $YAlO_3$.

The refractive index mismatch at the interface between Tm:$YAlO_3$ and undoped $YAlO_3$ causes a Fresnel loss per bounce of the laser mode through the slab of 0.23%, with the calculation show below.

The molar masses of each constituent atom and the mean of the lattice constants, shown in Table 6.4, were used calculate the refractive indices of 4% at. Tm:$YAlO_3$ and undoped $YAlO_3$.

The densities ρ of Tm:$YAlO_3$ and undoped $YAlO_3$ are given by:

$$\rho = \frac{4M}{N_{Av}V}, \tag{6.3}$$

where M is the average molar mass of the material, N_{Av} is Avagadro's number, and V is the volume of the unit cell of the material from Table 6.4. The factor of four arises from the number of $YAlO_3$ molecules in the unit cell.

Material	***a* [Å]**	***b* [Å]**	***c* [Å]**	***V* [Å^3]**	**Ref**
Tm:$YAlO_3$	5.17688(8)	5.32768(7)	7.3675(1)	203.202(9)	[156]
Tm:$YAlO_3$	5.17673(7)	5.32767(6)	7.3675(1)	203.195(8)	[156]
$YAlO_3$	5.179	5.329	7.370	203.4	[157]
$YAlO_3$	5.180	5.328	7.370	203.4	[158]
$YAlO_3$	5.180(2)	5.330(2)	7.375(2)	203.64	[70]

Table 6.4: Lattice constants and volumes for Tm:$YAlO_3$ and undoped $YAlO_3$.

	undoped $YAlO_3$	4% at. Tm:$YAlO_3$
Density [g·cm^{-3}]	5.3517	5.4637
Refractive index (*c*-axis)	1.9269	1.9463

Table 6.5: Calculated densities and refractive index for undoped and 4% at. Tm:$YAlO_3$.

The density of undoped $YAlO_3$ and 4% at. Thulium-doped $YAlO_3$ were calculated and given in Table 6.5. The refractive index for the *c*-axis (the lasing axis) of undoped $YAlO_3$ was calculated using the Sellmeier equation [77] for a wavelength of 1.94 μm. As $n-1 \propto \rho$ where n is the refractive index, the fractional increase in density translates to the same fractional increase in refractive index. This gives the predicted refractive index of 4% at. Tm:$YAlO_3$.

The reflection coefficient due to the interface between doped and undoped $YAlO_3$ was calculated using the Fresnel reflection equation:

$$r_s = \frac{n_1 \cos\theta_1 - n_2 \cos\theta_2}{n_1 \cos\theta_1 + n_2 \cos\theta_2}, \tag{6.4}$$

where r_s is the reflection coefficient for an incident *s*-polarisation beam, n_1, n_2 and θ_1, θ_2 are the refractive indices and angle of incidences for the two sides of the interface respectively.

The reflectivity per bounce is given by $2(r_s)^2$, with the factor of 2 due to the beam passing through the interface twice per bounce. At the design angle of incidence of θ_1 = 68.1º, the loss per bounce due to the reflectivity is 0.23%. Note that this loss can be reduced or eliminated by matching the refractive indices. This can be achieved by doping the central region with a non-absorbing dopant for both pump and laser wavelengths to increase the refractive index. Potential dopants include Yb^{3+}, Ce^{3+}, and Gd^{3+} [63].

6.4.5 Threshold and maximum output power

The laser thresholds and slope efficiencies were calculated for different output coupler reflectivities to obtain the theoretical maximum output power based on the Rigrod analysis [146]. From this, the optimum output coupler reflectivities can be obtained.

The theoretical threshold of the Tm:$YAlO_3$ ThOR slab was calculated using the method described in Section 5.2.5. The pump power required for transparency of the doped layer was calculated based on the inversion fraction, given by Equation 5.4. This is added to the pump power required to overcome round-trip losses, given by Equation 5.5, to yield the laser threshold P_{th}.

The maximum slope efficiency is given by [64]:

$$\eta_{slope} = \eta \frac{-\ln(R_2)}{L_{RT} - \ln(R_2)}, \tag{6.5}$$

where $L_{RT} = 1-(1-L_{Interface})(1-L_{Scatter})$ is the total round-trip loss, which includes the contributions from the interface $L_{Interface}$ and scattering $L_{Scatter}$, and η encompasses the efficiency factors, such as the quantum defect, quantum efficiency and pump absorption.

The maximum output power $P_{\max}$ for 1.4 kW of incident pump power is given by:

$$P_{\max} = \eta_{slope}(1400 - P_{th}). \tag{6.6}$$

The calculated thresholds and slope efficiencies for total round-trip loss between 10% to 20% are plotted in Figure 6.14 for different output coupler reflectivities. High levels of round-trip loss were assumed in the calculations due to significant scatter losses in both the doped and undoped laser crystals, as well as the diffusion bond. The maximum attainable output power for each case is plotted in Figure 6.15. Based on the modelled Rigrod analysis, the output coupler reflectivity was chosen to be R_2 = 50%.

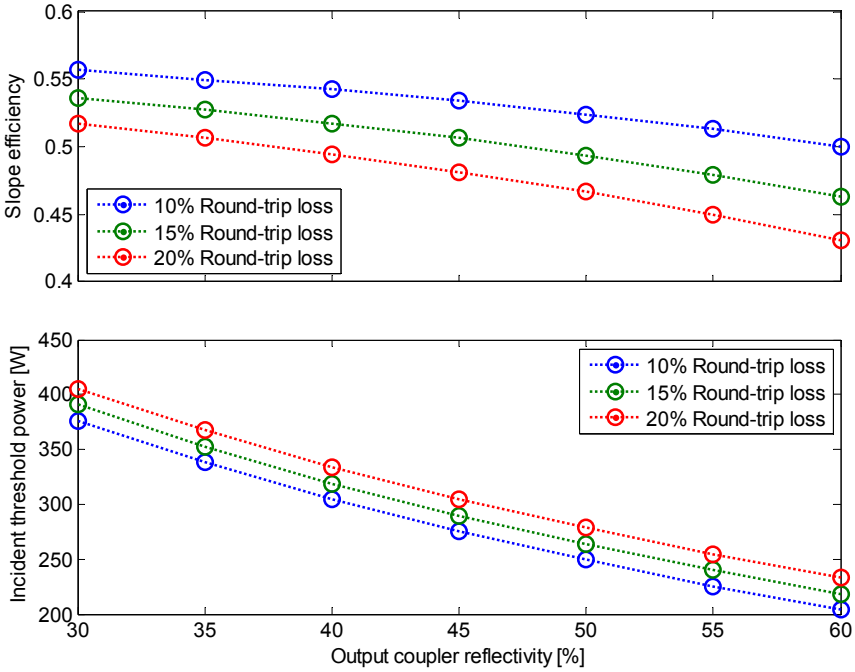

Figure 6.14: Maximum theoretical slope efficiency (top) and incident threshold (bottom) for different round-trip loss and output coupler reflectivity.

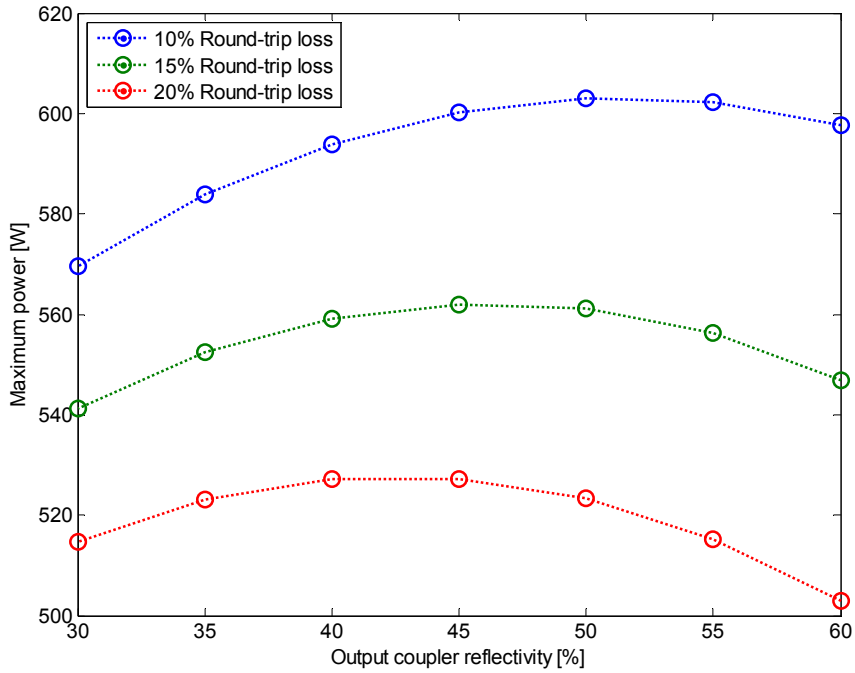

Figure 6.15: Maximum theoretically attainable power based on the Rigrod analysis for different round-trip loss and output coupler reflectivity.

6.5 Laser head design

The laser head assembly, shown in Figure 6.16, consisted of two rectangular copper blocks, which secured and cooled the ThOR slab, and an aluminium base block that elevated the slab to the correct height.

The copper block in contact with the doped layer, the copper cooling block, contained an 8-mm diameter U-shaped channel for water cooling, which ran along the length of the slab. Silver-soldered copper disks were used to seal the ends at the base of the "U". The other copper block, the securing block, was used to secure the slab. Note that for the original design of two doped layers, this copper block would be similarly water cooled. Two 125-μm thick indium sheets were placed between the slab and the blocks to improve thermal contact. Steel spacers were used to control the separation between the two blocks, ensuring a uniform crush of 5 μm on both sheets of indium. Aluminium knife edges were used to protect the sheets of indium from stray pump and laser light. This assembly was then bolted onto the aluminium base block. The drawings for each of these blocks can be found in Appendix B.

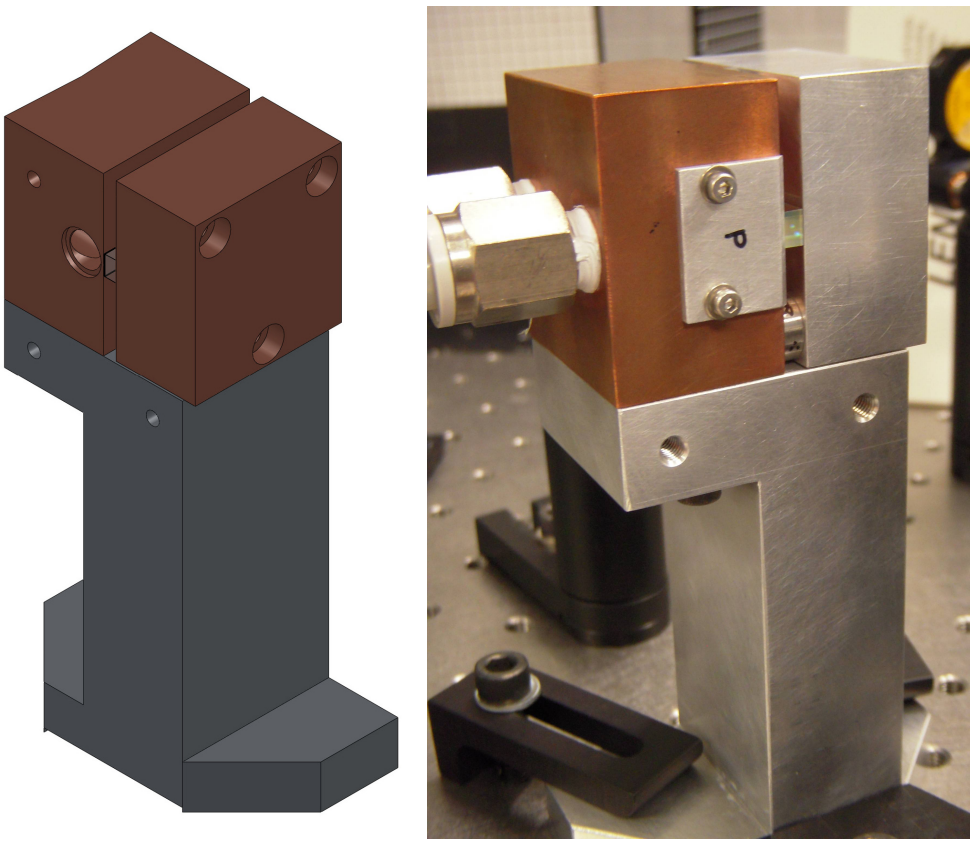

Figure 6.16: Laser head assembly for the Tm:$YAlO_3$ ThOR slab.

6.5.1 Flatness of the cooling blocks

During assembly of the laser head, the crush on the indium was found to be non-uniform, with significant crush in the central region and no crush at the ends as shown in Figure 6.17 (left). Uniform crush is critical, as it is an indication of the uniformity of the thermal contact and thus affects beam quality.

It was suspected that the copper blocks were not sufficiently stiff, and bent slightly due to the mounting. Thus, the copper securing block was replaced with a thick aluminium block. The slab is undoped on this side, and hence this replacement should not affect the performance of the laser. However, this did not improve the uniformity of the crush.

An interferometric surface profiler was used to examine the surfaces of the mounting blocks. The surface was shown to be slightly convex with the height difference from the centre to the edge on the order of 20 μm. The surfaces of both cooling and securing blocks were remachined and polished extremely carefully, with the surface flatness measured regularly using the surface profiler. The result was surfaces with flatness of within 2 μm for > 95% of the length of the slab. Significant improvement in the uniformity of the indium crush was observed, as shown in Figure 6.17 (right).

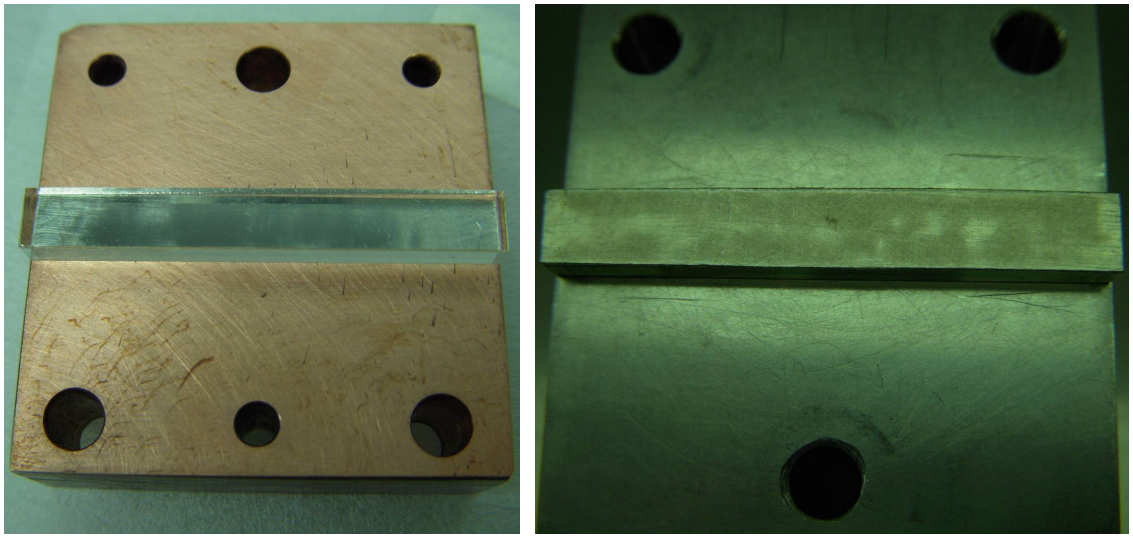

Figure 6.17: Photographs of the securing copper block after assembly before (left) and after (right) remachining of the surfaces, showing significant improvement in uniformity of the crush on the indium after machining.

6.6 Internal scatter loss

The ThOR slab that was delivered contained substantial amounts of scattering impurities, both in the bulk 4% at. Tm:$YAlO_3$ and undoped $YAlO_3$ crystals and the diffusion bond. Photographs of the pre-cut laser crystal after diffusion bonding can be seen in Figure 6.18.

To verify the large rectangular hazy region was introduced by the diffusion bonding, a microscope was used to examine the diffusion bond through the crystal. The sharpness of the image at the diffusion bond, as shown in Figure 6.19, indicates the scatterers are contained to a thin layer within the crystal, and therefore a result of the diffusion bond. Consequently, only one diffusion bond was performed to limit the scattering loss. The cause of the scatterers in the bond was not discovered.

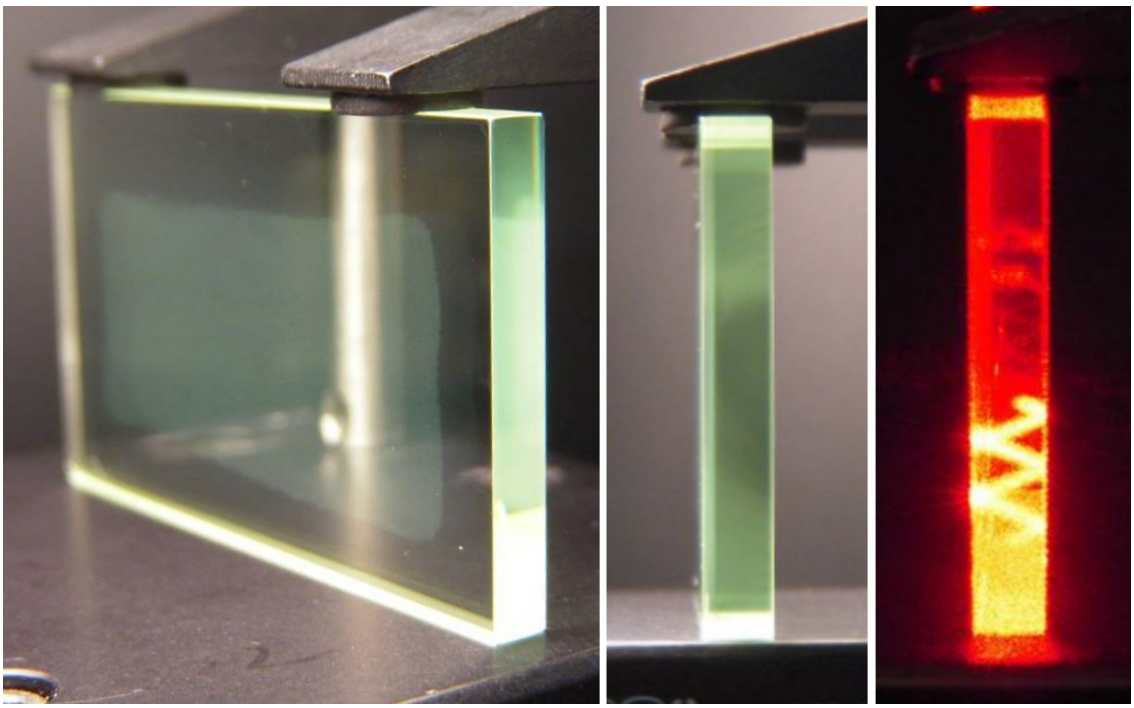

Figure 6.18: Photographs of the pre-cut laser crystal, with visible scatterers in the diffusion bond (left) and bulk crystal (centre). A HeNe laser beam is used to highlight the severity of the scatter loss through the crystal (right).

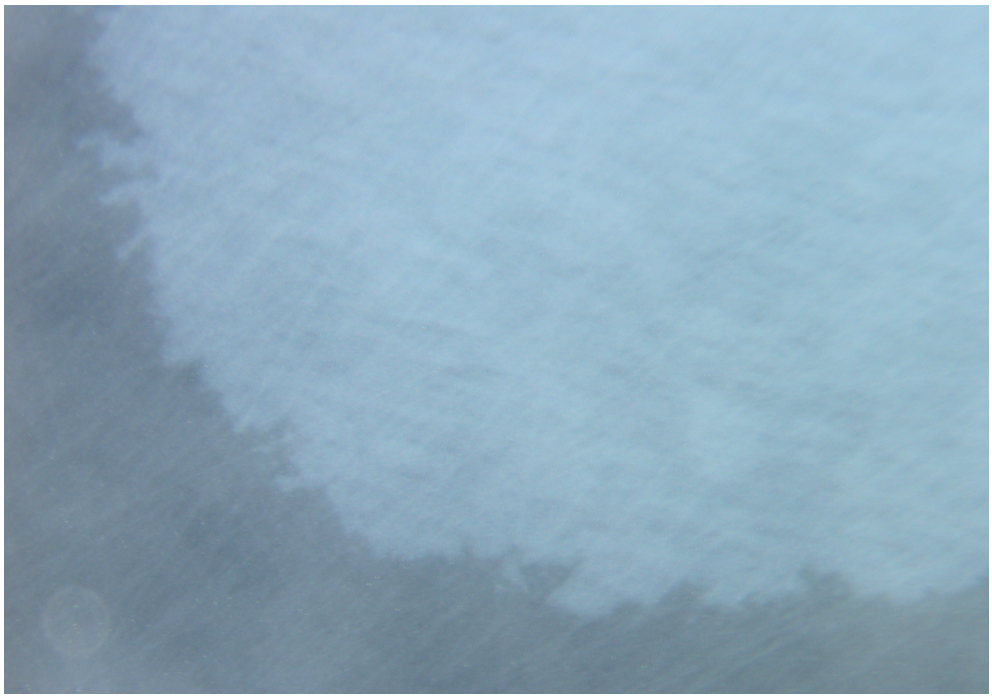

Figure 6.19: Microscope image of the hazy region in the diffusion bond.

6.6.1 Measurement of internal scatter loss

To determine if the lasing was still feasible using this laser slab, the resultant internal loss due to the scatterers was quantified. A collimated probe beam was made to trace a single pass of the laser path through the ThOR slab, i.e. with a total of five bounces. The incident and transmitted power was measured by an InGaAs photodetector to obtain the transmission loss through the slab. The two ends of the slab were not yet thin-film coated and thus entry and exit losses were accounted for using the standard Fresnel reflection calculations.

Scatter loss at the lasing wavelength cannot be measured directly because this wavelength is absorbed by the doped region. Scattering loss is strongly dependent on the relative size of the scatterers compared to the wavelength, and hence, a non-absorbing wavelength that is close to the lasing wavelength was used. The closest available wavelength was 1470 nm, the suitability of which is demonstrated by the broadband absorption spectra of Tm:$YAlO_3$ shown in Figure 6.20. A polarised 1470 nm laser diode (Princeton Lightwave HP-S-1480-PM) was used as the light source, with the polarisation aligned to the *c*-axis of the slab.

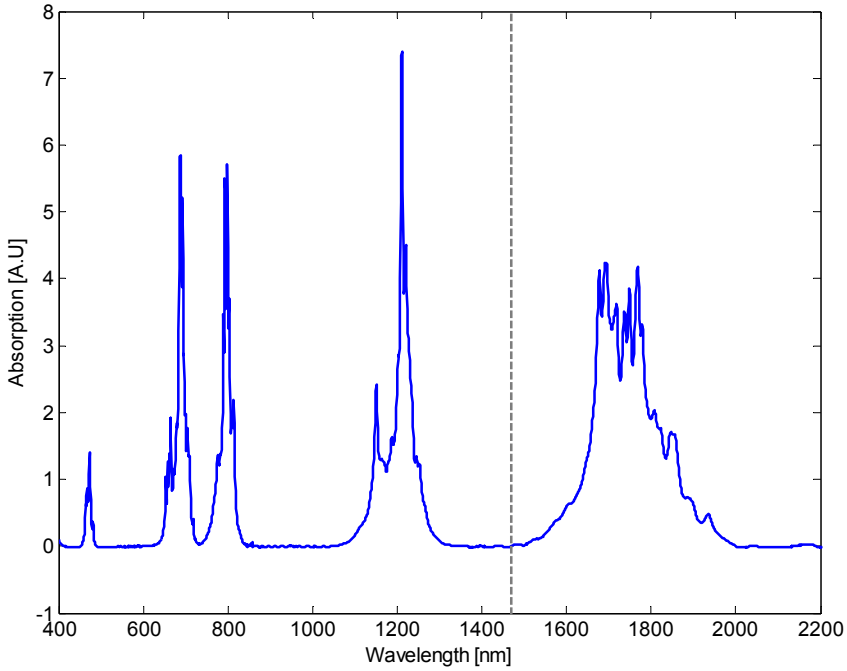

Figure 6.20: Broadband absorption spectra along the *c*-axis of the Tm:$YAlO_3$ in the ThOR slab; the dashed line denotes 1470 nm.

Repeated measurements were taken at different heights along the slab, with greater loss on the order of 1–2% was observed through the hazy region. The single pass loss at 1470 nm over the whole slab was measured to be $6.0\% \pm 1.5\%$, corresponding to a total four-pass round-trip loss of $20\% \pm 4\%$.

The relative size of the scatterers compared to the wavelengths is important in order to extrapolate the loss measurement at 1470 nm to the laser wavelength of 1.94 μm. If the wavelength is much larger than the scatterer size, then Rayleigh scattering occurs, and the scatter loss scales as the inverse of the 4th power of the wavelength ($1/\lambda^4$) [159]. For scatterers with sizes of the same order as the wavelength, Mie scattering occurs. While the scatter loss strongly depends on the scatter shape, it is generally inversely related to wavelength [160]. A direct measurement of the scatter size was not possible due to the presence of different scatterers in the bulk crystal and diffusion bond. Nevertheless, the measurement at 1470 nm puts an upper limit on the scatter loss. In the ideal case of Rayleigh scattering, the total round-trip losses at 1.94 μm is approximately $8\% \pm 2\%$. Lasing is still feasible for a total round-trip loss of between 8% and 20% based on the Rigrod analysis in Section 6.4.5.

6.7 Diode pumping of ThOR slab

The cut and coated Tm:$YAlO_3$ ThOR slab was mounted according to the assembly procedure summarised in Appendix E.2. For the initial demonstration, only the diode stack facing the doped layer was used to pump the slab. To monitor any potential stress in the slab, a collimated HeNe laser was used to construct a Mach-Zehnder interferometer around the slab. The HeNe beam was made to pass straight through the slab. As this region should be undoped, the stress in the slab is expected to be minimal. A photograph of the slab under low-power pumping is shown in Figure 6.21, with the scattered 790-nm rays visible to the digital camera. To aid in alignment, the pump spot was initially focused at the end of the slab instead of the filling the slab.

The Mach-Zehnder interferometer showed significant thermal distortions in the slab under low power pumping, as shown in Figure 6.22. Strong interference rings, concentric with the pump spot, were visible even under very low power pumping of 10 W. With such strong thermal distortions, it would be impossible for the laser to reach the predicted laser threshold of between 250 W and 300 W.

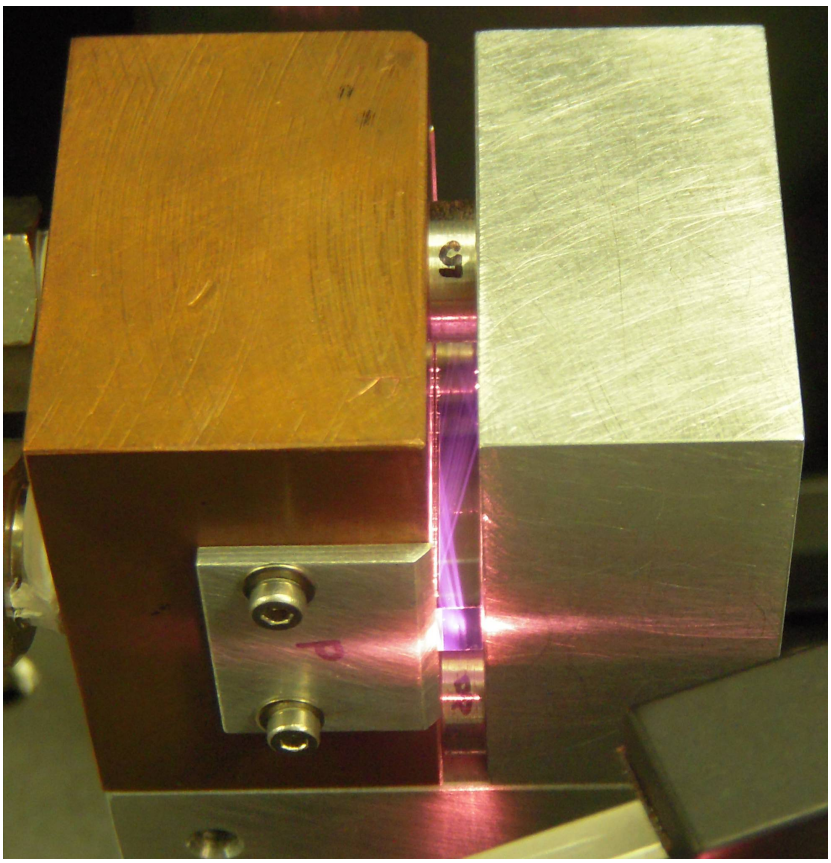

Figure 6.21: Photograph of the ThOR slab under 790 nm pumping.

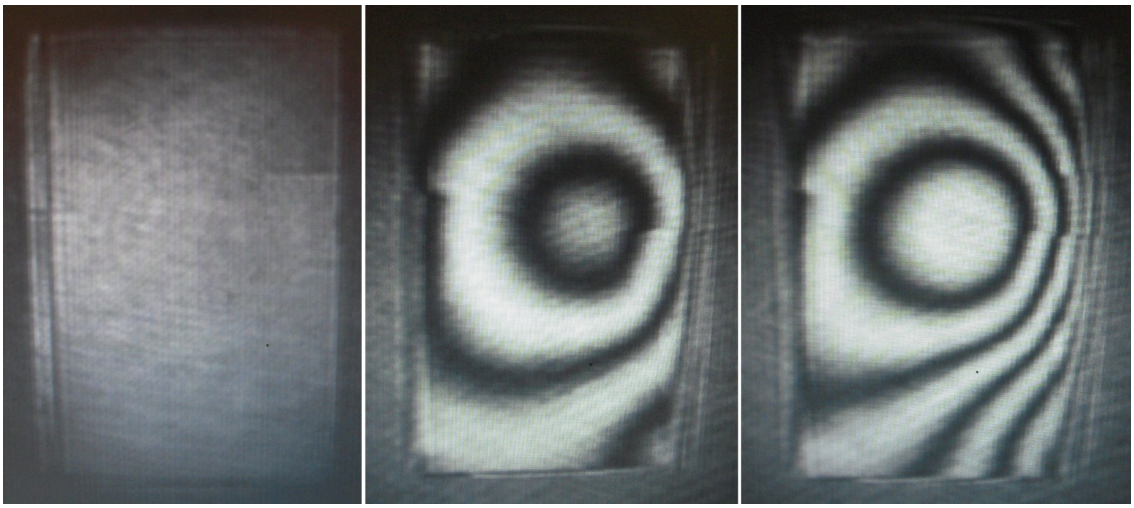

Figure 6.22: Output from the Mach-Zehnder interferometer for an incident pump power of 0 W (left), 10 W (centre) and 20 W (right), showing significant thermal distortions under pumping.

The primary explanation for the thermal distortions observed is significant absorption in the undoped region. A transmission spectrum through the undoped region was obtained using a super-continuum laser source and an OSA. The spectrum showed an absorption peak centred around 795 nm, the absorption peak of Tm:$YAlO_3$. The light from the super-continuum laser source was then focused to below 200 μm and made to pass through the thin doped layer. In contrast to the previous spectrum, the transmission through the doped layer was relatively flat. The two spectra are plotted in Figure 6.23.

From the transmission spectra, it was concluded that the two regions were interchanged during the manufacturing process, resulting in a slab with a thick Tm-doped region diffusion bonded to a thin undoped region. This results in a laser slab that is inferior to that of the standard slab geometry due to its thickness. The thin undoped layer also acts as a thermal buffer, reducing the cooling efficiency of the slab. Unfortunately, this was a fatal fault which could not be rectified and due to financial and time constraints, a new slab could not be manufactured. As a consequence, no further experimental work on the ThOR slab was possible. Exactly how the major error occurred has not been determined, with none of the parties involved in the design and manufacture of the slab admitting responsibility.

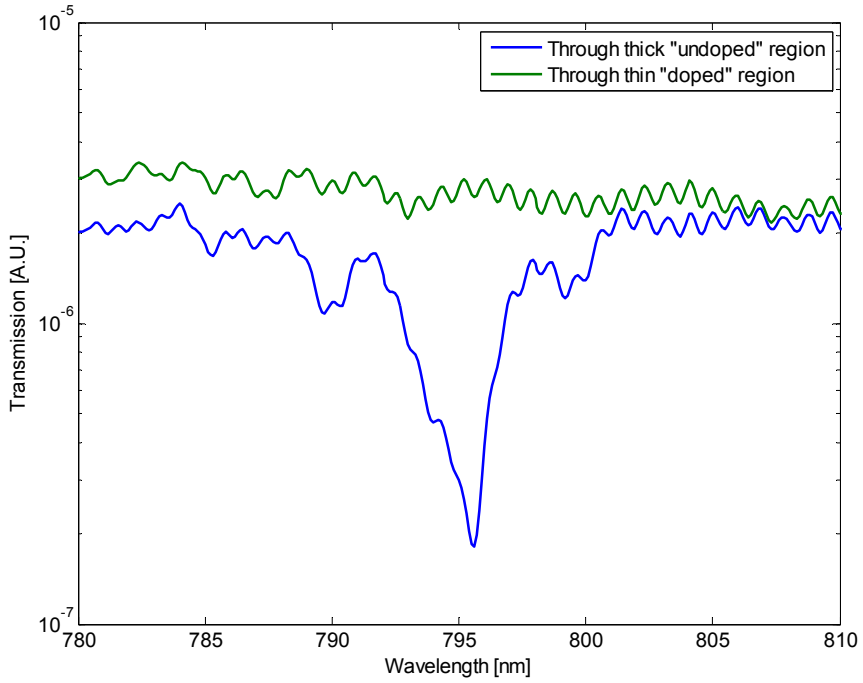

Figure 6.23: Transmission spectra through the two regions of the ThOR slab.

6.8 Chapter summary

A novel laser slab geometry for high power, the ThOR slab geometry, was proposed and analysed. The laser geometry is designed to incorporate the superior thermal management of disk lasers, using thin doped regions directly next to heat sinks, with the ease of pumping of slab lasers using a large undoped region in between. An end-pumped, folded zigzag slab laser was designed based the ThOR slab and manufactured. Significant scatter loss due to internal scattering from the bulk material and the bond was observed, and hence the slab had dopant only on one side. The operation of the laser with this slab was modelled, including pump absorption, threshold and maximum slope efficiency. For an incident pump power of 1.4 kW, the predicted output power was over 500 W.

Unfortunately, the experimental development of the ThOR slab was marred by a number of issues, including critical manufacturing faults:

- Scatter loss in the bulk crystal

  The crystals for the ThOR slab were procured without fine polishing, as they would be polished during the bonding phase. Prior to the crystals procured for the ThOR slab, crystals from the manufacturer have been of high quality with

minimal scatter, including the Tm:$YAlO_3$ crystals used in the cuboid and slab lasers. Thus, close inspection of the procured crystals was considered unnecessary at the time.

- Diffusion bonding issues

  The bonding company had no prior experience with bonding $YAlO_3$ crystals, and therefore the bond was performed on a best-effort basis. The resultant diffusion bond contained an unknown hazy region. In addition to contribution to the scatter loss, it was unclear whether this region would affect the mechanical or thermal properties of the crystal. The second bond was not performed to minimise risk.

- Interchange of doped and undoped crystals

  It is unclear during which stage of the manufacturing process the two regions were interchanged. Previous Tm:$YAlO_3$ crystals had a brown tinge and thus were easily distinguishable from undoped $YAlO_3$. However, it was discovered after the diffusion bonding process that the Tm:$YAlO_3$ for the ThOR slab was untinged. The side that the manufacturers believed to be the doped side was polished down, which ultimately was incorrect. Due to time constraints, a spectroscopic analysis on the crystal was not performed. This, or a physical marking throughout the manufacturing process such as a small chamfer, could have precluded the issue.

- Manufacturing time

  The time taken between the initial procurement of the Tm:$YAlO_3$ and undoped $YAlO_3$ crystals to a polished and coated crystal was in excess of three years. The delays included extensive paperwork and delays in import/export of the crystals between Australia and the United States, critical malfunction of the thin-film coating machine resulting in multiple recoatings, and extensive loss measurements to determine the scatter loss within the crystal.

Closer communication with the companies and thorough inspection of the crystals between each stage would hopefully prevent such incidents from occurring in future procurements of complex components.

Based on the modelling, we believe that the ThOR slab geometry has great potential for high power operation. However, further work is required to demonstrate the ThOR slab geometry in practice, and to develop it for high power operation.

7 Conclusion

7.1 Thesis summary

This thesis has described the investigation and development of Tm:$YAlO_3$ lasers for use as high power brightness converters and pump source for holmium silica fibre lasers.

The major drawback of Tm:$YAlO_3$ lasers for use as pump sources, namely the self-pulsing behaviour that occurs even under CW pumping, was analysed in detail. Experimental observations of a 6.5 W Tm:$YAlO_3$ laser showed the self-pulsing had the characteristics of an unstable relaxation oscillation in the gain medium. The laser dynamics was modelled based on an existing published model that assumes strong ESA at the lasing wavelength. The modelled result matched well with experiments in both the temporal and frequency domains. An experiment to measure the ESA cross-section in Tm:$YAlO_3$ was performed, and yielded a cross-section that was an order of magnitude lower than that required by the model to reproduce the observed laser dynamics. Thus, ESA at the lasing wavelength was found to be insufficient to explain the self-pulsing of Tm:$YAlO_3$ lasers. The Tm:$YAlO_3$ laser output intensity was analysed for chaotic dynamics. A chaotic attractor was identified in the reconstructed phase space of the laser system. Additionally, the output intensity was analysed using 0–1 test for chaos, which also gave a strong indication for the presence of chaotic dynamics. Thus, the self-pulsing in Tm:$YAlO_3$ lasers is likely to be the result of nonlinear dynamical chaos within the laser system.

A method of suppressing the self-pulsing that is applicable to high power operation was demonstrated, which involved current feedback to the pump diode. This

method was successfully demonstrated on a 6.5 W Tm:$YAlO_3$ laser, resulting in an oscillation-free CW output. These results, including the measurement of the optical transfer function, have been published in ref. [117] (Appendix A.1.1).

The self-pulsing behaviour of Tm:$YAlO_3$ at higher powers was investigated, with the design, modelling and construction of a side-pumped, straight-through Tm:$YAlO_3$ slab laser. The laser operated with a threshold of 114.2 W and an absorbed slope efficiency of 33.4%, up to a maximum output power of 32.2 W. Self-pulsing in the slab laser was observed to weaken with increasing output power, with the output oscillation amplitude below 50% of the average power observed at 28 W output. The output power of this laser was limited by thermal effects.

A novel laser slab geometry for high power operation, the ThOR slab geometry, was designed and analysed. This geometry combines the superior thermal handling of disk lasers with the ease of pumping and laser design of the slab laser. The predicted output power from a Tm:$YAlO_3$ laser with a gain medium based on this geometry was over 500 W for an incident pump power of 1.4 kW. However, multiple significant fabrication faults with the manufactured slabs rendered them unusable, and hence the design was not investigated experimentally.

7.2 Future directions

7.2.1 Self-pulsing of Tm:$YAlO_3$ lasers

The self-pulsing in Tm:$YAlO_3$ lasers was identified in this thesis to be consistent with nonlinear dynamical chaos within the laser system. However, the physical parameters responsible are currently unknown. Naturally chaotic class C lasers require three coupled nonlinear equations with parameters of similar time constants. These parameters are typically the relaxation oscillation for the field (cavity lifetime), polarisation of the gain medium, and the population inversion (upper-state lifetime). However, the time constant for the upper-state and the relaxation oscillation for the field in Tm:$YAlO_3$ are different by several orders of magnitude. Thus, a different parameter must be responsible for the chaotic behaviour. Additionally, the polarisation time constant has yet to be reported. In order to understand the self-pulsing behaviour

of Tm:$YAlO_3$ lasers, additional parameters that affect the lasing operation must be identified and the corresponding time constants measured.

7.2.2 Development of the Tm:$YAlO_3$ ThOR slab

The experimental development and investigation of the Tm:$YAlO_3$ ThOR slab design was marred by manufacturing faults. Nevertheless, the modelling of the ThOR slab geometry has shown great potential for high power laser operation. It is a design that can be applied to other dopants and hosts, such as Yb:YAG. An obvious further work is to demonstrate the ThOR slab geometry and develop it for high power operation.

A Publications

This appendix contains publications both associated with and arising as a result of this work.

A.1 Publications associated with this work

A.1.1 Self-pulsing in Tm-doped $YAlO_3$ lasers: Excited-state absorption and chaos

K. S. Wu, O. Henderson-Sapir, P. J. Veitch, J. Munch, M. Hamilton and D. J. Ottaway, *Phys. Rev. A*, vol. 91, pp. 043819, Apr. 2015. Ref. [129]

PHYSICAL REVIEW A **91**, 043819 (2015)

Self-pulsing in Tm-doped $YAlO_3$ lasers: Excited-state absorption and chaos

Ka S. Wu, Ori Henderson-Sapir, Peter J. Veitch, Murray Hamilton, Jesper Munch, and David J. Ottaway
School of Physical Sciences and Institute for Photonics & Advanced Sensing (IPAS), The University of Adelaide, Adelaide 5005, Australia
(Received 29 July 2014; published 13 April 2015)

Tm:$YAlO_3$ lasers suffer from self-pulsing. A four-level rate equation analysis suggested that the self-pulsing could be due to excited-state absorption. We report a measurement of the cross section for this absorption and show that it is too small to be the sole cause of the self-pulsing. We propose nonlinear dynamical chaos as an alternative explanation and present a chaos analysis of the output of a cw-pumped Tm:$YAlO_3$ laser, including experimental evidence of chaos.

DOI: 10.1103/PhysRevA.91.043819 PACS number(s): 42.60.Mi, 42.70.Hj, 78.20.Ci

I. INTRODUCTION

The development of lasers operating at wavelengths near 2 μm is of importance to many fields, such as medicine, remote sensing, and fundamental research. Tm:$YAlO_3$ (or Tm:YAP) lasers are of particular interest due to their high efficiency [1], excellent thermomechanical properties, and natural birefringence of the crystal. A major drawback of Tm:$YAlO_3$ lasers is their tendency to self-pulse, even under continuous-wave (cw) pumping [2–4], as shown in Fig. 1. This instability, along with the high peak powers associated with the self-pulsing, limits the usefulness of Tm:$YAlO_3$ lasers.

The origin of the self-pulsing is not well understood, although it has been suppressed using various types of feedback, including using intracavity acousto-optic modulators [2,3] and pump diode current actuation [4]. A number of mechanisms have been proposed to explain the self-pulsing in Tm:$YAlO_3$ lasers, such as pump power fluctuations [5], mechanical instabilities, and saturable absorption by water in the air of the laser resonator [6]. However, these explanations do not explain the observation of self-pulsing in all cases. For example, while Šulc *et al.* [6] observed that the output of their monolithic Tm:$YAlO_3$ laser was stable over a broad range of pump powers, Razdobreev and Shestakov [7] observed that the output of their monolithic laser pulsed regularly at higher pump powers.

Razdobreev and Shestakov [7] presented a rate equation model that showed the pulsing could be explained by including excited-state absorption (ESA) of photons at the lasing wavelength by the transition $^3H_5 \rightarrow {}^3H_4$. This model assumed an ESA to emission cross-section ratio of $\gamma = \sigma_{\mathrm{ESA}}/\sigma \approx 0.65$. They also pointed out that the measurement of the ESA cross section had not yet been performed and was required to verify the model.

Self-pulsing behavior in a laser may also be explained by nonlinear dynamics with chaotic solutions [8–12]. Of particular interest is the NH_3 laser [13,14], which can be made to exhibit self-pulsing without any external perturbations. The self-pulsing of our Tm:$YAlO_3$ laser [4] is remarkably similar to that of chaotic NH_3 lasers [8,13]. Additionally, the observation of two distinct dynamical regimes by Razdobreev and Shestakov [7], namely, a stable cw output at low pump power and robust self-pulsing beyond a certain threshold, is consistent with an explanation in terms of nonlinear dynamic systems.

We report here an investigation of the self-pulsing. We first describe measurement of the cross section for the ESA transition $^3H_5 \rightarrow {}^3H_4$ and show that it is too small to account solely for the self-pulsing in Tm:$YAlO_3$ lasers. We then show that the self-pulsing is consistent with nonlinear dynamical chaos. Here chaos has been observed in a simple solid-state crystal laser without any external perturbations or other nonlinear optical elements.

II. EXCITED-STATE ABSORPTION

The energy-level diagram of Tm:$YAlO_3$ is shown in Fig. 2. The ESA can be observed by using a short pump pulse to excite Tm^{3+} ions to the $^3H_5$ level and a cw probe beam at the lasing wavelength to observe the resulting change in the upper $^3F_4$ lasing manifold, as explained below.

The equilibrium transmittance of the probe beam through the Tm:$YAlO_3$ crystal prior to the pump pulse is given by

$$T_{eq} = \exp(\sigma[f_u N_2 - f_l(N - N_2)]l) \tag{1a}$$

$$\approx \exp(-\sigma f_l N l) \quad \text{for} \quad N_2 \ll N, \tag{1b}$$

where σ is the cross section for transitions at the probe wavelength between the ground state and the $^3F_4$ manifold, f_u and f_l are the Boltzmann factors for the $^3F_4$ manifold and ground state, respectively, N is the total Tm^{3+} ion density, N_2 is the equilibrium density in the $^3F_4$ manifold, and l is the length of the crystal.

During the pump pulse, ΔN ground-state ions are excited to the $^3H_5$ level. The absorption at the probe wavelength changes due to this excitation, as the excited ions no longer contribute to the ground-state absorption (GSA) but can instead contribute to ESA. The transmittance of the probe beam immediately after the pump pulse is given by

$$T_{ns} = T_{eq} \exp([\sigma f_l - \sigma_{\mathrm{ESA}}]\Delta N l), \tag{2}$$

where σ_{ESA} is the effective cross section for absorption of a probe photon by an ion in the $^3H_5$ level. If $\sigma_{\mathrm{ESA}} > \sigma f l$ as expected, then the pump pulse will result in a sudden decrease in probe transmittance, as illustrated in Fig. 3.

Ions in the $^3H_5$ level will readily decay nonradiatively to the $^3F_4$ manifold as the energy gap between the $^3H_5$ and $^3F_4$ levels is readily bridged by phonons, resulting in a predicted lifetime of the $^3H_5$ level on the microsecond scale [15]. However, some of the ions will absorb a probe photon and be excited to the $^3H_4$ level via ESA. The majority of these ions will then cross-relax to the $^3F_4$ level [16].

This cross relaxation results in additional ions being excited to the $^3F_4$ manifold from the ground state, which is undesirable

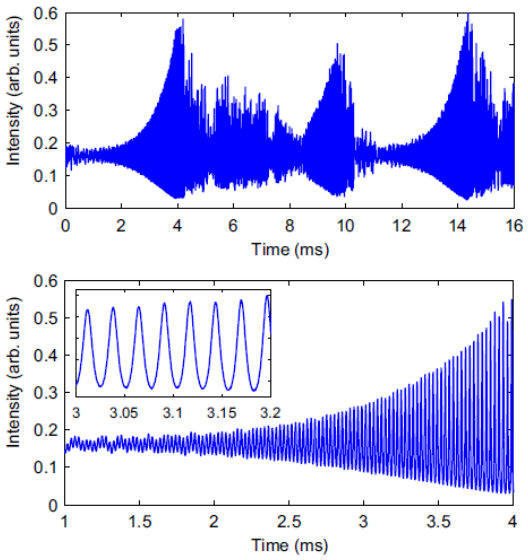

FIG. 1. (Color online) Typical output of a Tm:$YAlO_3$ laser (top), with a plot of a single "burst" with improved temporal resolution (bottom) and the underlying oscillations (inset).

in this experiment as it introduces uncertainty in the population density of the $^3F_4$ manifold. To ensure nonradiative decay is the dominant process, the probe beam needs to be sufficiently weak to minimize the number of ions that undergo ESA, but still strong enough to provide an adequate signal. The transmittance of the probe beam after the decay of the $^3H_5$ population is given by

$$T_{\mu s} \approx T_{eq} \exp(\sigma[f_u + f_l]\Delta N l). \tag{3}$$

The ions in the $^3H_4$ manifold then gradually decay back to the ground state and the system relaxes back to its equilibrium

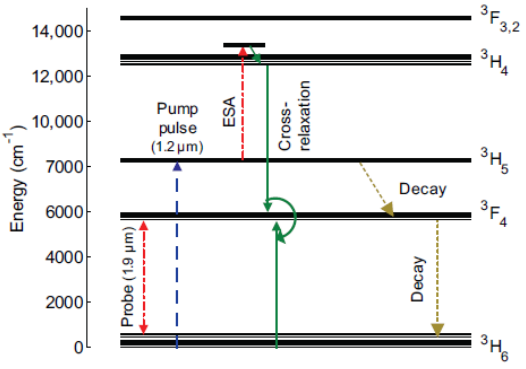

FIG. 2. (Color online) Energy-level diagram of Tm:$YAlO_3$, with the two main avenues for ions in $^3H_5$ to de-excite: ESA followed by cross relaxation, or nonradiative decay $^3H_5 \rightarrow {}^3F_4$.

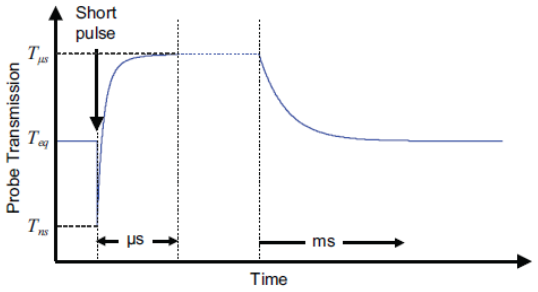

FIG. 3. (Color online) Expected probe transmittance trace during and after the short pump pulse.

state. Since the transitions of the Tm^{3+} ions occur at different time scales, they can be distinguished.

The ratio between the ESA and laser emission cross sections can be determined from the measurement of the changes in probe transmittance. If $\Delta N \ll |(\sigma[f_u + f_l]l)^{-1}|$ and $\Delta N \ll |([\sigma f_l - \sigma_{\mathrm{ESA}}]l)^{-1}|$, then the approximation $e^x \approx 1 + x$ can be applied to Eq. (3) and Eq. (2), giving

$$\Delta N = \frac{1}{\sigma(f_u + f_l)l}\left(\frac{T_{\mu s} - T_{eq}}{T_{eq}}\right), \tag{4}$$

and

$$\gamma = \frac{\sigma_{\mathrm{ESA}}}{\sigma} \approx f_l - \frac{1}{\sigma \Delta N l}\left(\frac{T_{ns} - T_{eq}}{T_{eq}}\right) \tag{5a}$$

$$= f_l - (f_u + f_l)\left(\frac{T_{ns} - T_{eq}}{T_{\mu s} - T_{eq}}\right). \tag{5b}$$

Assuming linearity of the detector, the ratio of the transmittance change is given by the ratio of the voltage change, further simplifying Eq. (5b):

$$\gamma = f_l - (f_u + f_l)\left(\frac{\Delta V_{ns}}{\Delta V_{\mu s}}\right), \tag{6}$$

where $\Delta V_{ns} = D(T_{ns} - T_{eq})P$ and $\Delta V_{\mu s} = D(T_{\mu s} - T_{eq})P$. Here, D is the detector constant and P is the probe power incident on the crystal. Equation (1b) can be used to determine the cross section σ and hence the ESA cross section σ_{ESA}.

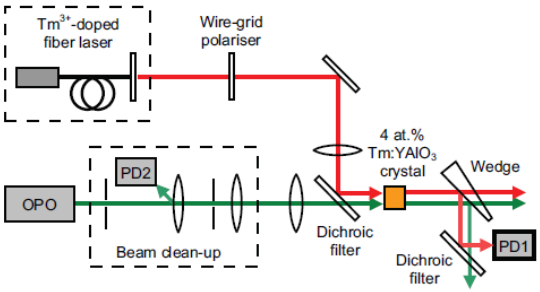

FIG. 4. (Color online) Schematic of the measurement system.

A schematic of the measurement system is shown in Fig. 4. An a-cut Tm:$YAlO_3$ crystal (4 at%) with dimensions 4.55 $\times$ 5.02 $\times$ 5.54 mm along the crystalline a, b, and c axes, respectively, was used. The end faces were antireflective coated for the pump and probe wavelengths.

The probe beam was generated by a Tm^{3+}-doped fiber laser at 1.944 μm that was stabilized by a fiber Bragg grating. Although this fiber laser operated at a slightly longer wavelength than the Tm:$YAlO_3$ peak emission wavelength of 1.940 μm, the energy difference of 10.6 cm^{-1} is negligible compared to the spread in energy of the Stark sublevels of the $^3H_4$ level and the phonon energies in $YAlO_3$, which are both of the order of 100 cm^{-1} [17,18]. A wire-grid polarizer with an extinction ratio of >1500 was used to ensure that the probe light incident on the Tm:$YAlO_3$ was polarized along the c axis, as observed during lasing [1]. The fiber laser was operated at an output power of 300 mW, which resulted in ~0.1% of ions in the $^3F_4$ level at steady state, satisfying the requirement for the approximation for Eq. (1b). Furthermore, it was calculated that negligible amounts of ions in the $^3H_5$ level after the pump pulse would undergo ESA due to the low intensities.

An optical parametric oscillator (OPO) was used to generate pump pulses with a duration of less than 10 ns at 1.21 μm for excitation of the $^3H_6 \rightarrow {}^3H_5$ transition. A spatial filter was used to improve the beam quality. The pulse energy incident on the crystal was 0.8 mJ. Approximately 2.2×10^{19} cm^{-3} or 2.8% of the total ions are excited by the OPO pulse. This satisfies the approximation condition for Eq. (4), as it is 2 orders of magnitude less than the term on the right-hand side.

The two beams were combined using a dichroic mirror, which was highly reflective (HR) at 1.94 μm and antireflective (AR) at 1.2 μm. The two beams were focused independently into the Tm:$YAlO_3$ crystal, and both had a beam diameter of 250 μm at the focus as measured by a pyroelectric camera. The camera was also used to align the two beams by overlapping the beam profiles.

The transmitted probe beam power was measured using an extended-InGaAs photodetector (PD1) with a rise time <250 ns. A wedge was used to reduce the power. The pump pulse was further attenuated using a dichroic mirror and long-pass filters (wavelength cutoff at 1500 nm). An InGaAs photodetector (PD2) with a rise time of less than 10 ns (Thorlabs DET10C) was used to detect the pulse from the OPO from scattered light and trigger the oscilloscope.

The time dependence of the transmitted probe beam for the microsecond and millisecond time scales is shown in Figs. 5 and 6, respectively. To increase the signal to noise of the measurement, the traces shown were averaged over 128 pulses. As expected, the transmittance increases exponentially with a microsecond time constant after the pump pulse, followed by an exponential decrease.

The increase in the probe transmittance on the microsecond time scale (shown in Fig. 5) corresponds to the decay $^3H_5 \rightarrow {}^3F_4$, which has a fitted time constant of 440 $\pm$ 5 ns. Note that the data earlier than 0.25 μs was not included in the fit due to electronic ringing, which is responsible for the sudden increase in transmittance near $t = 0$. The measurement of this time constant is approximately consistent with the calculated value from literature [15].

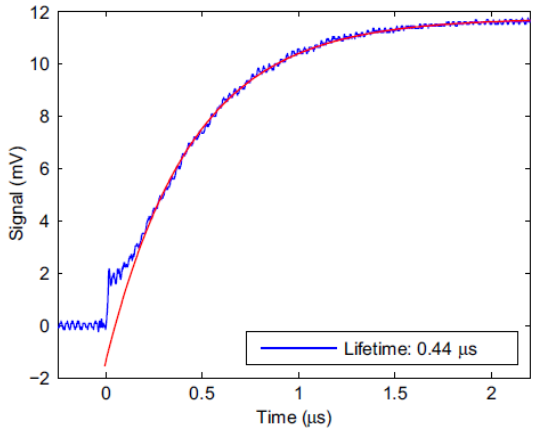

FIG. 5. (Color online) Probe beam signal from the ac-coupled detector PD1 in the microsecond range, with an exponential fit.

The decrease of transmittance in the millisecond time scale (shown in Fig. 6) corresponds to the transition $^3F_4 \rightarrow {}^3H_6$, which has a fitted time constant of $\tau = 3.35 \pm 0.05$ ms. This time constant is shorter than the spontaneous lifetime from literature [19], and this is due to stimulated emission induced by the incident probe beam. When the stimulated emission rate was subtracted from the total decay rate (determined from the fitted time constant), the spontaneous decay rate was consistent with that in the literature.

The expected instantaneous decrease in transmitted probe power following the pump pulse was obscured by some electronic ringing of the photodetector following the pump pulse. However, the instantaneous decrease can be estimated by extrapolating the exponential fit of the decay curve to $t = 0$. This result was checked by subtracting from the measured curve the temporal profile of the pump leakage measured with

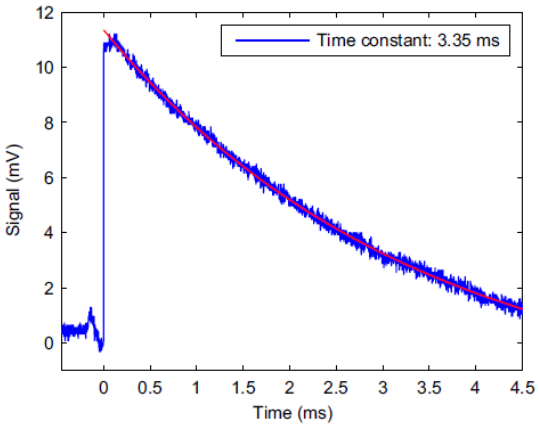

FIG. 6. (Color online) Probe beam signal from the ac-coupled detector PD1 in the millisecond range, with an exponential fit.

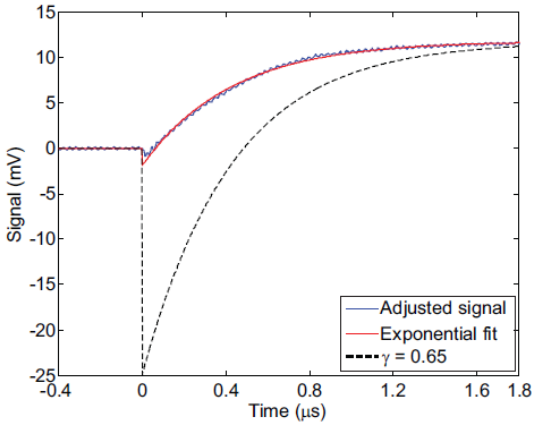

FIG. 7. (Color online) Corrected experimental trace (blue) and exponential fit (red), compared to the theoretical decay curve for a voltage drop of 25 mV corresponding to $\gamma = 0.65$ (black).

no probe. The resulting corrected signal is shown in Fig. 7, showing a small drop in the instantaneous transmittance.

The voltage changes from the steady state were estimated as shown in Fig. 5, giving $\Delta V_{ns} = 2 \pm 0.25$ mV and $\Delta V_{\mu s} = 11.75 \pm 0.25$ mV. The value of ΔN was calculated from $\Delta V_{\mu s}$ and the equilibrium dc voltage of 460 mV to be $3.1 \pm 0.3\%$ of the total number of ions. This is consistent with that calculated from the pump-pulse absorption, confirming good overlap of the two beams. Using the Boltzmann factors $f_u = 0.263$ and $f_l = 0.03$ [7], the ratio of ESA to GSA cross sections $\gamma = 0.08 \pm 0.01$.

The cross section σ for the absorption of the probe beam was calculated from the steady-state GSA of the probe beam using Eq. (1a), assuming $N_2 \ll N$. For a measured $T_{eq} = 0.920 \pm 0.005$, and $N = 7.8 \times 10^{20}$ cm^{-3} and $l = 0.455 \pm 0.001$ cm, the cross section $\sigma = (7.8 \pm 0.5) \times 10^{-21}$ cm^2. The ESA cross section is therefore $\sigma_{\mathrm{ESA}} = \gamma\sigma = (6.3 \pm 0.7) \times 10^{-22}$ cm^2.

Our measured value of γ is much less than that used in the model of Razdobreev and Shestakov [7]. To confirm that it would result in a stable cw output, we reproduced their model and used parameters for the laser in our previous work [4]. cw output was observed in the model even when various parameters were changed by a factor of 2, including the cross section, cross relaxation, and decay rates, pump rate, and cavity time constant. To further emphasize the robustness of our measurement, we compare the measured pump-probe temporal response with that predicted for $\gamma = 0.65$, as shown in Fig. 7.

It is thus clear that the rate equation model of Razdobreev and Shestakov would yield a stable cw output and is not by itself an explanation of the pulsing in Tm:$YAlO_3$.

III. CHAOTIC LASER DYNAMICS

The Tm:$YAlO_3$ laser described in our previous work [4] was reassembled to obtain the data for the analysis presented here. The laser was a simple crystal laser, pumped by a 790-nm fiber-coupled diode. The crystal from the ESA measurement was used as the gain medium. The resonator consisted of a flat, high-reflectivity mirror, the laser crystal, an intracavity lens to compensate for thermal lensing, and a flat output coupler with a reflectivity of 95% at 1.94 μm. The laser exhibited similar, exponentially growing bursts of oscillations, as presented in our previous work [4].

The output was measured using an extended-range InGaAs photodetector with a 25-ns rise/fall time, and digitized using a 2-MS/s oscilloscope, giving 32,000 points. The full data set is shown in Fig. 1. We describe below analyses of this data using two standard tests for chaotic dynamics: phase-space reconstruction [20,21], and the 0–1 test for chaos [22,23].

Time delay embedding [20] was used to reconstruct the phase-space trajectories to determine the nature of the system dynamics. This method uses the data set I_n and its time-delayed versions to construct vectors in a d-dimensional Euclidean space:

$$y(k) = [I_k, I_{k+\Delta n}, \ldots I_{k+(d-1)\Delta n}]. \tag{7}$$

These vectors define a trajectory that is topologically equivalent to the trajectory in the space of the actual physical variables. For sufficiently large d, the properties of the dynamic system are preserved and the trajectory is fully contained, or embedded, in this reconstruction of the phase space.

The delay Δn that would expand the trajectory maximally in the embedding space was determined using the average mutual information of the data set, which is given by

$$I_M(\Delta n) = \sum_k p(I_k, I_{k+\Delta n}) \log \left[\frac{p(I_k, I_{k+\Delta n})}{p(I_k) p(I_{k+\Delta n})} \right], \tag{8}$$

where $p(I_k, I_{k+\Delta n})$ is the joint probability distribution function and $p(I_k)$ and $p(I_{k+\Delta n})$ are the marginal probability distribution functions [21].

A minimum of I_M means that points in the time series, spaced by the corresponding delay, are as statistically independent as possible. When data spaced by this delay are used as coordinate values in the phase-space reconstruction, the coordinate axes are as close to orthogonal as possible. The optimum delay is chosen as the first minimum of I_M [21]. A plot of the average mutual information for different values of Δn is shown in Fig. 8, with the first minimum of I_M corresponding to $\Delta n = 13$.

The minimum number of dimensions required to embed the trajectory, without crossings, was obtained by calculating the fraction of false nearest neighbors for increasing dimensions [21]. The process is summarized in Appendix A. The trajectory is fully unfolded when the number of false neighbors reaches zero. The percentage of false neighbors in our data set, plotted in Fig. 9, reduces to 0.4% for embedding dimensions of 5, and remains approximately 0.2% for higher dimensions due to noise.

The three-dimensional (3D) projection of the reconstructed trajectory with an embedding dimension of 5 is shown in Fig. 10. The points of the reconstructed trajectory lie in a manifold of limited dimensionality, as shown in Fig. 10. A limited dimensionality implies dynamics with a limited number of physical variables, or degrees of freedom, and

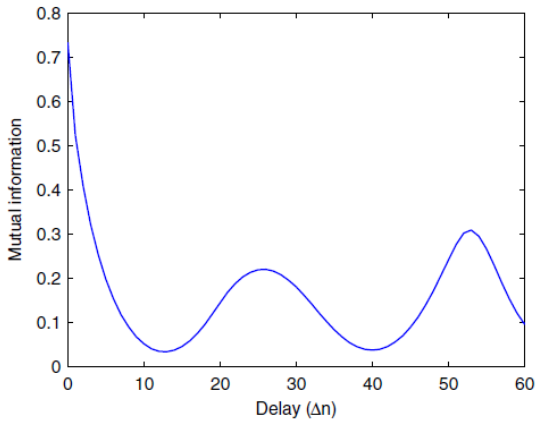

FIG. 8. (Color online) Average mutual information for different delays.

because the trajectory appears nonperiodic and is dense in the manifold, chaos is implied.

The dynamics of the time series were also investigated using the "0–1" test for chaos developed by Gottwald and Melbourne [22,23], which is summarized in Appendix B. This is a binary test that can distinguish between regular and chaotic dynamics in deterministic dynamical systems, even in the presence of moderate levels of noise [22]. The 0–1 test does not require the choice of parameters such as the delay and embedding dimension. The output of the test is a value $0 \leqslant K \leqslant 1$, corresponding to a linear correlation coefficient. For a sufficiently large number of samples $\mathcal{N}$ in the data set, $K = 0$ corresponds to regular dynamics and $K = 1$ corresponds to chaotic dynamics.

The 0–1 test was applied to the laser output data set and yielded $K = 0.99$, indicating that the pulsing is due to chaotic

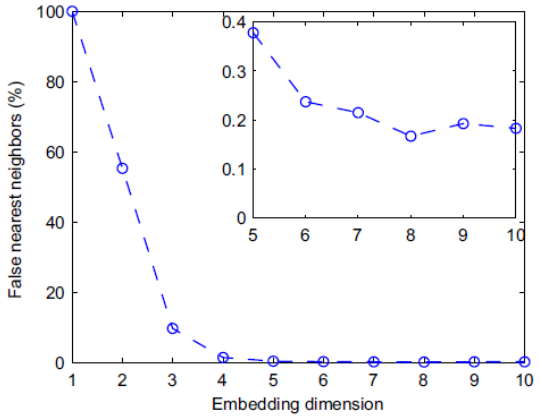

FIG. 9. (Color online) False nearest neighbors for increasing embedding dimensions.

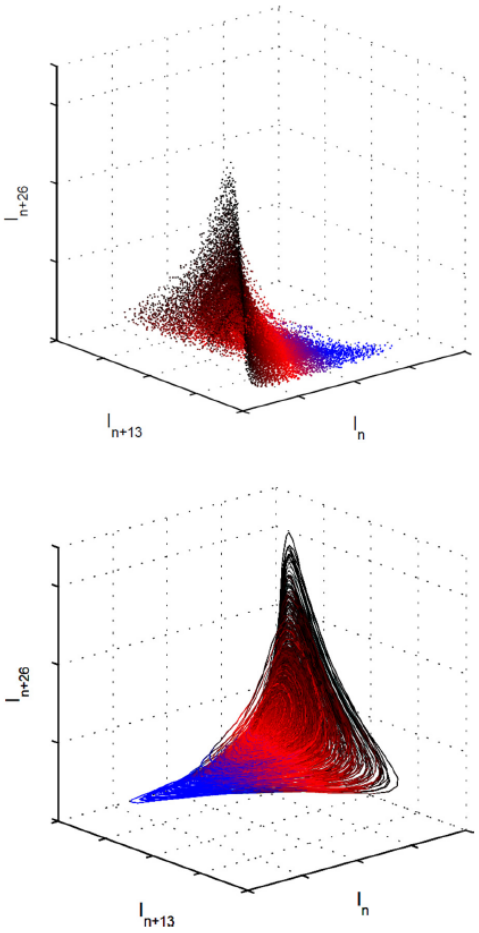

FIG. 10. (Color online) 3D projection of the phase-space structure from opposing angles, showing a trajectory of bound dimensionality (top) with dense, nonperiodic orbits (bottom). The color variations along I_n are for ease of viewing purposes only.

dynamics. This is consistent with the results from the phase-space reconstruction.

IV. CONCLUSIONS

We have shown that the self-pulsing in cw-pumped Tm:$YAlO_3$ lasers cannot be explained solely by the $^3H_5 \rightarrow {}^3H_4$ excited-state absorption suggested by Razdobreev and Shestakov [7], and is the result of chaotic dynamics in the laser. While chaotic behavior has been observed in more complex solid-state lasers involving known perturbations or intracavity nonlinearities [10–12], this is an example of chaos in a simple solid-state crystal laser without any external perturbations or other nonlinear optical elements.

The absence of any external perturbations for unstable pulsing in the Tm:$YAlO_3$ laser makes it comparable to a

chaotic class-C laser, with three or more coupled variables that have similar relaxation time constants [24]. Chaotic class-C lasers naturally have a second threshold for the onset of chaos above the lasing threshold [9]. This is consistent with the presence of two distinct dynamical regimes, as observed by Razdobreev and Shestakov [7]. However, the physical parameters responsible for the chaotic behavior are currently unknown. Typically, chaotic class-C lasers require the lifetimes of the polarization, inversion, and cavity field to be of the same order of magnitude. However in Tm:$YAlO_3$ lasers, the inversion lifetime is of the order of milliseconds, while the cavity field lifetime is of the order of nanoseconds; the polarization lifetime in $YAlO_3$ has not been measured to the best of our knowledge. Thus, there are likely additional parameters involved, and further investigation is necessary to identify them. Despite the parameters being unknown, we have demonstrated in our previous work that the chaotic behavior can be suppressed to a steady, cw state by controlling the inversion via proportional feedback to the pump diode laser [4].

ACKNOWLEDGMENTS

The authors would like to acknowledge Alexandre Francois for his assistance with the OPO. This work was supported by the South Australian Government through the Premier's Science and Research Fund.

APPENDIX A: CALCULATION OF FALSE NEAREST NEIGHBORS

The percentage of false nearest neighbors in dimension d is determined using the following process [21]:

(i) In dimension d, for each vector

$$y(k) = [I_k, I_{k+\Delta n}, \ldots I_{k+(d-1)\Delta n}], \tag{A1}$$

calculate the Euclidean distance R_d to every other vector in dimension d, given by

$$R_d(k,k')^2 = \sum_{l=0}^{d-1} [I_{k+l\Delta n} - I_{k'+l\Delta n}]^2. \tag{A2}$$

(ii) Identify the nearest neighbor $y(k_N)$ with the smallest R_d, and calculate the Euclidean distance between $y(k)$ and $y(k_N)$ in dimension $d+1$:

$$R_{d+1}(k,k_N)^2 = R_d(k,k_N)^2 + [I_{k+d\Delta n} - I_{k_N+d\Delta n}]^2. \tag{A3}$$

(iii) Determine whether $y(k)$ and $y(k_N)$ are true or false nearest neighbors; if

$$\frac{|I_{k+d\Delta n} - I_{k_N+d\Delta n}|}{R_d(k,k_N)} > R_T, \tag{A4}$$

where $R_T \in [10,50]$ is some fixed threshold value ($R_T = 15$ was used in our analysis), then $y(k)$ and $y(k_N)$ are considered false neighbors.

(iv) Repeat (i)–(iii) for all vectors in dimension d.

APPENDIX B: CALCULATION OF K IN THE "0–1" TEST

The value of K in the 0–1 test was determined using the following process [22,23]:

(i) For the data set I of size $\mathcal{N}$, define

$$p_c(n) = \sum_{k=1}^{n} I_k \cos(kc), \quad q_c(n) = \sum_{k=1}^{n} I_k \sin(kc), \tag{B1}$$

where $n = 1,2,\ldots\mathcal{N}$ and $c \in (\pi/5, 4\pi/5)$ is a randomly generated phase.

(ii) Define the modified mean-square displacement:

$$D_c(n) = M_c(n) - V_{\text{osc}}(c,n), \tag{B2}$$

where $M_c(n)$ is the mean-square displacement, given by

$$M_c(n) = \frac{1}{\mathcal{N}} \sum_{l=1}^{\mathcal{N}} [p_c(n+l) - p_c(l)]^2 + [q_c(n+l) - q_c(l)]^2, \tag{B3}$$

and

$$V_{\text{osc}}(c,n) = \left[\frac{1}{\mathcal{N}} \sum_{k=1}^{\mathcal{N}} I_k\right]^2 \frac{1-\cos nc}{1-\cos c}. \tag{B4}$$

(iii) Calculate the linear correlation coefficient K_c of $D_c(n)$:

$$K_c = \text{corr}(n, D(n)) \quad \text{for} \quad n = 1,2,\ldots\mathcal{N}/10. \tag{B5}$$

(iv) Repeat (i)–(iii) for 100 randomly generated values of c to prevent resonance phenomena when $\mathcal{N}$ is small. K is then defined as the median value of $\{K_c\}$.

[1] R. C. Stoneman and L. Esterowitz, Efficient 1.94-μm Tm:YALO laser, IEEE J. Sel. Top. Quantum Electron. **1**, 78 (1995).

[2] P. Černý, G. J. Valentine, and D. Burns, Actively stabilised diode pumped Tm:YAlO laser, Electron. Lett. **40**, 1061 (2004).

[3] A. C. Sullivan, A. Zakel, G. J. Wagner, D. Gwin, B. Tiemann, R. C. Stoneman, and A. I. R. Malm, High power Q-switched Tm: YALO lasers, OSA Proc. Adv. Solid-State Photonics **19**, 329 (2004).

[4] K. S. Wu, P. J. Veitch, J. Munch, and D. J. Ottaway, Suppression of self-pulsing in Tm:$YAlO_3$ lasers via current feedback, Appl. Phys. B **114**, 415 (2013).

[5] I. F. Elder and M. J. P. Payne, Lasing in diode-pumped Tm:YAP, Tm, Ho:YAP and Tm, Ho:YLF, Opt. Commun. **145**, 329 (1998).

[6] J. Šulc, H. Jelínková, K. Nejezchleb, and V. Škoda, Fluctuation-free CW Tm:YAP laser with monolithic resonator, in *European Conference on Lasers and Electro-Optics 2009 and the European Quantum Electronics Conference, CLEO Europe - EQEC 2009, Munich*, Vol. 269 (IEEE, Piscataway, NJ, 2009), p. 1.

[7] I. Razdobreev and A. Shestakov, Self-pulsing of a monolithic Tm-doped $YAlO_3$ microlaser, Phys. Rev. A **73**, 053815 (2006).

[8] C. Weiss, Chaotic laser dynamics, Opt. Quantum Electron. **20**, 1 (1988).
[9] J. Ohtsubo, *Semiconductor Lasers - Stability, Instability and Chaos*, 3rd ed. (Springer-Verlag, Berlin, 2013).
[10] E. A. Viktorov and P. Mandel, Low frequency fluctuations in a multimode semiconductor laser with optical feedback, Phys. Rev. Lett. **85**, 3157 (2000).
[11] P. Mandel and X.-G. Wu, Second-harmonic generation in a laser cavity, J. Opt. Soc. Am. **3**, 940 (1986).
[12] E. M. Pessina, G. Bonfrate, F. Fontana, and L. A. Lugiato, Experimental observation of the Risken-Nummedal-Graham-Haken multimode laser instability, Phys. Rev. A **56**, 4086 (1997).
[13] C. O. Weiss and J. Brock, Evidence for Lorenz-type chaos in a laser, Phys. Rev. Lett. **57**, 2804 (1986).
[14] C. O. Weiss, U. Hübner, N. B. Abraham, and D. Tang, Lorenz-like chaos in NH_3-FIR lasers, Infrared Phys. Technol. **36**, 489 (1995).
[15] J. A. Caird, L. G. DeShazer, and J. Nella, Characteristics of room-temperature 2.3-μm laser emission from Tm^{3+} in YAG and $YAlO_3$, IEEE J. Quantum Electron. **11**, 874 (1975).
[16] N. Borodin, P. Kryukov, and A. Popov, Diode-pumped cw Tm^{3+} : $YAlO_3$ laser, Quantum Electron. **35**, 511 (2005).
[17] M. J. Weber, Multiphonon relaxation of rare-earth ions in yttrium orthoaluminate, Phys. Rev. B **8**, 54 (1973).
[18] M. Eichhorn, Quasi-three-level solid-state lasers in the near and mid infrared based on trivalent rare earth ions, Appl. Phys. B **93**, 269 (2008).
[19] I. F. Elder and M. J. P. Payne, Comparison of diode-pumped Tm:YAP with Tm:YAG, OSA Proc. Adv. Solid-State Lasers **19**, ML6 (1998).
[20] F. Takens, in *Dynamical Systems and Turbulence*, edited by D. Rand and L.-S. Young, Lecture Notes in Mathematics, Vol. 898 (Springer, Berlin, 1981), pp. 366–381.
[21] H. D. Abarbanel, R. Brown, J. J. Sidorowich, and L. S. Tsimring, The analysis of observed chaotic data in physical systems, Rev. Mod. Phys. **65**, 1331 (1993).
[22] G. A. Gottwald and I. Melbourne, Testing for chaos in deterministic systems with noise, Phys. D (Amsterdam, Neth.) **212**, 100 (2005).
[23] G. A. Gottwald and I. Melbourne, On the implementation of the 0-1 test for chaos, SIAM J. Appl. Dynamical Systems **8**, 129 (2009).
[24] F. T. Arecchi, G. L. Lippi, G. P. Puccioni, and J. R. Tredicce, Deterministic chaos in laser with injected signal, Opt. Commun. **51**, 308 (1984).

Wu, K.S., Veitch, P.J., Munch, J. & Ottaway, D.J. (2013). Suppression of self-pulsing in Tm:$YAlO_3$ lasers via current feedback.
Applied Physics B: Lasers and Optics, 114(3), 415–419.

A.1.3 Self-pulsing and excited-state absorption in Tm:$YAlO_3$

K. S. Wu, O. Henderson-Sapir, P. J. Veitch, J. Munch, and D. J. Ottaway, *Australian Institute of Physics Congress 2014* (Canberra 2014)

Self-pulsing and excited-state absorption in Tm:$YAlO_3$

K. S. Wu[1], O. Henderson-Sapir[1], P. J. Veitch[1], J. Munch[1] and D. J. Ottaway[1]

[1]*Department of Physics, and Institute for Photonics & Advanced Sensing (IPAS), The University of Adelaide, Adelaide 5005, Australia*

Tm:$YAlO_3$ (or Tm:YAP) lasers operating at 2 μm are of particular interest due to their high efficiency [1], excellent thermo-mechanical properties and natural birefringence. A major drawback of Tm:$YAlO_3$ lasers is their tendency to self-pulse, even under continuous-wave (CW) pumping [2, 3]. This instability, along with the high peak powers associated with the self-pulsing, limit the usefulness of Tm:$YAlO_3$ lasers.

A Tm:$YAlO_3$ laser was constructed to investigate the self-pulsing. The output of the laser consisted of an exponentially growing burst of an oscillation that has a frequency of about 100 kHz, as shown in Fig. 1. The self-pulsing was suppressed via feedback to the pump diode laser [3]. The transfer function of the laser was measured, and was characteristic of an unstable oscillator, which has a negative damping coefficient.

However, this does not explain the cause of this self-pulsing. Razdobreev and Shestakov [4] showed that the pulsing could be explained by including phonon-assisted excited-state absorption (ESA) at the lasing wavelength in the rate equations. However their model required a ratio between the ESA and emission cross-section of $\gamma = \sigma_{ESA} / \sigma \approx 0.65$. They also pointed out that the measurement of the ESA cross-section has not yet been performed and was necessary to verify the model.

ESA at the lasing wavelength can be observed by using a short pump pulse to excite Tm^{3+} ions to the excited state while probing the crystal with a weak CW probe beam at the lasing wavelength.

An optical parametric oscillator (OPO) was used to generate pump pulses with a duration of less than 10 ns at 1.21 μm for populating the excited state. The probe beam was generated by a Tm^{3+}-doped fibre laser that lased at 1.944 μm.

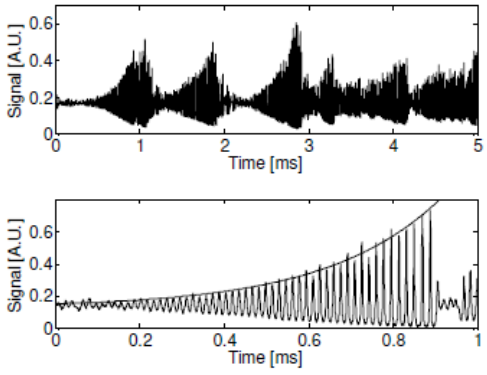

Figure 1: Top: A plot of the self-pulsing of the laser output. Bottom: A plot of a single 'burst' with improved temporal resolution, showing the high frequency oscillation within the pulse envelope, and an exponential fit to the envelope.

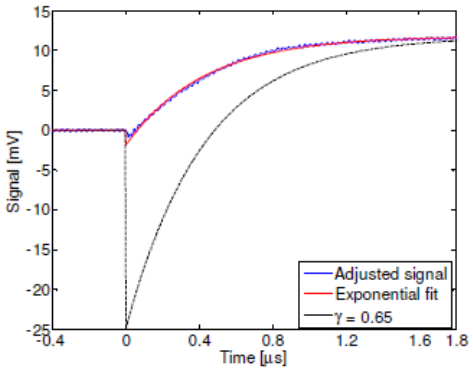

Figure 1: Experimental trace (blue) and exponential fit (red), compared to the theoretical decay curve for a voltage drop of 25 mV corresponding to $\gamma = 0.65$ (black).

The time dependence of the transmitted probe beam is shown in Fig. 1. As expected, the pump pulse produces a decrease in probe transmission. This is due to ions in the excited state contributing to ESA instead of ground-state absorption (GSA). The dip is followed by an exponential increase corresponding to non-radiative decay to the upper lasing level.

From this voltage drop, the ratio of ESA to GSA cross-sections was calculated to be $\gamma = 0.08 \pm 0.01$, with the ESA cross-section being $\sigma_{ESA} = (6.3 \pm 0.7) \times 10^{-22}$ cm^2.

The value of γ is almost an order of magnitude lower than that suggested by Razdobreev and Shestakov [4]. Their required value would result in a much larger decrease in transmission, as shown in Fig. 2. As illustrated by Razdobreev and Shestakov in their modelling results [4], $\gamma = 0.08$ would result in CW operation of their Tm:$YAlO_3$ laser for all pump rates.

Thus, the observed ESA cross-section σ_{ESA} does not result in self pulsing. We shall present the latest results with further details of our Tm:$YAlO_3$ laser as well as the measurement techniques and analysis. We shall also identify and discuss alternative mechanisms.

References

[1] R. Stoneman and L. Esterowitz, IEEE J. Sel. Topics Quantum Electron. 1, **40** (1995)
[2] A. Sullivan et al., ASSL (TOPS) **94**, 5 (2004).
[3] K. Wu *et al.*, Appl. Phys. B **114**, 415 (2014).
[4] I. Razdobreev and A. Shestakov, Phys. Rev. A **73**, 53815 (2006).

K. S. Wu, J. Munch, P. J. Veitch and D. J. Ottaway, (2011). Suppression of self-pulsing behaviour in Tm:$YAlO_3$ lasers via pump diode-current feedback. *2011 International Quantum Electronics Conference (IQEC) and Conference on Lasers and Electro-Optics (CLEO) Pacific Rim incorporating the Australasian Conference on Optics, Lasers and Spectroscopy and the Australian Conference on Optical Fibre Technology*, Sydney, NSW, 992-994.

B Mechanical drawings

This appendix contains the mechanical drawings associated with the lasers and mounts in this work.

B.1 Slab laser

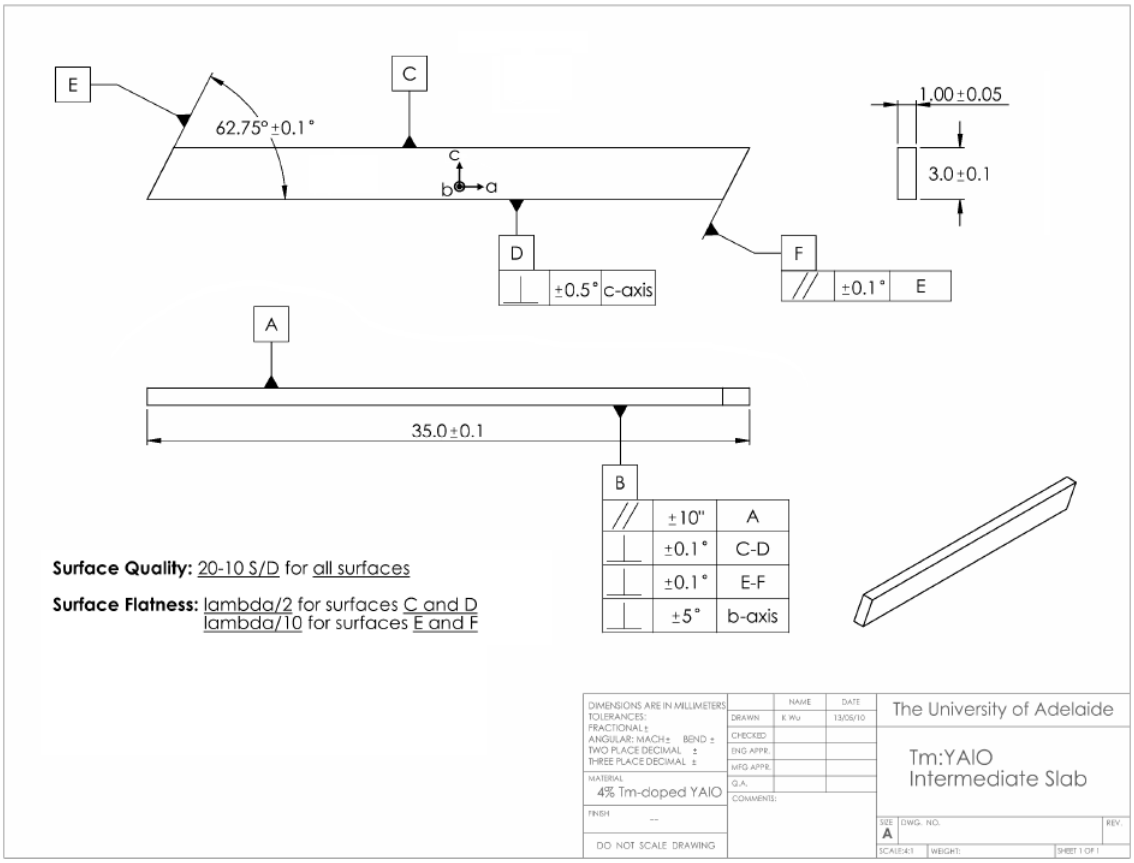

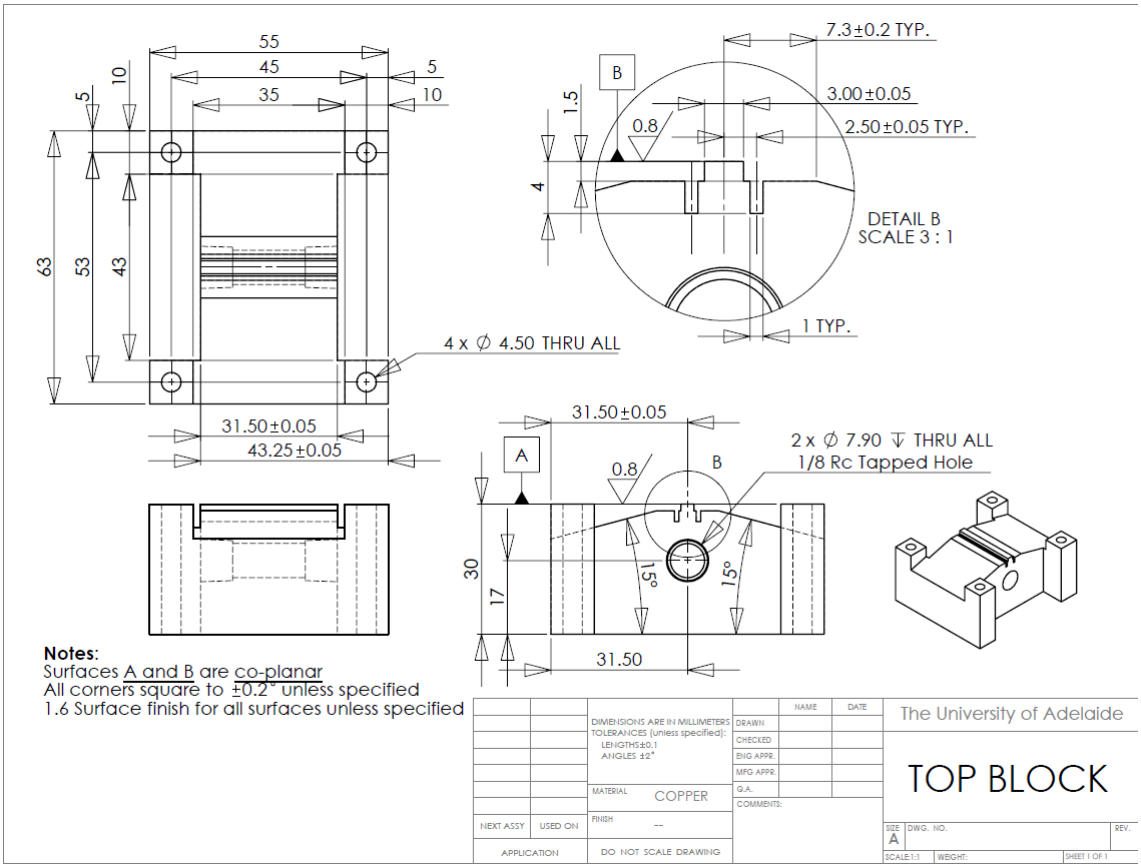

Notes:
Surfaces A and B are co-planar
All corners square to ±0.2° unless specified
1.6 Surface finish for all surfaces unless specified

		DIMENSIONS ARE IN MILLIMETERS TOLERANCES (unless specified): LENGTHS±0.1 ANGLES ±2°		NAME	DATE
			DRAWN		
			CHECKED		
			ENG APPR.		
			MFG APPR.		
			Q.A.		
			COMMENTS:		
		MATERIAL COPPER			
NEXT ASSY	USED ON	FINISH --			
APPLICATION		DO NOT SCALE DRAWING			

The University of Adelaide

TOP BLOCK

SIZE A | DWG. NO. | REV.
SCALE:1:1 | WEIGHT: | SHEET 1 OF 1

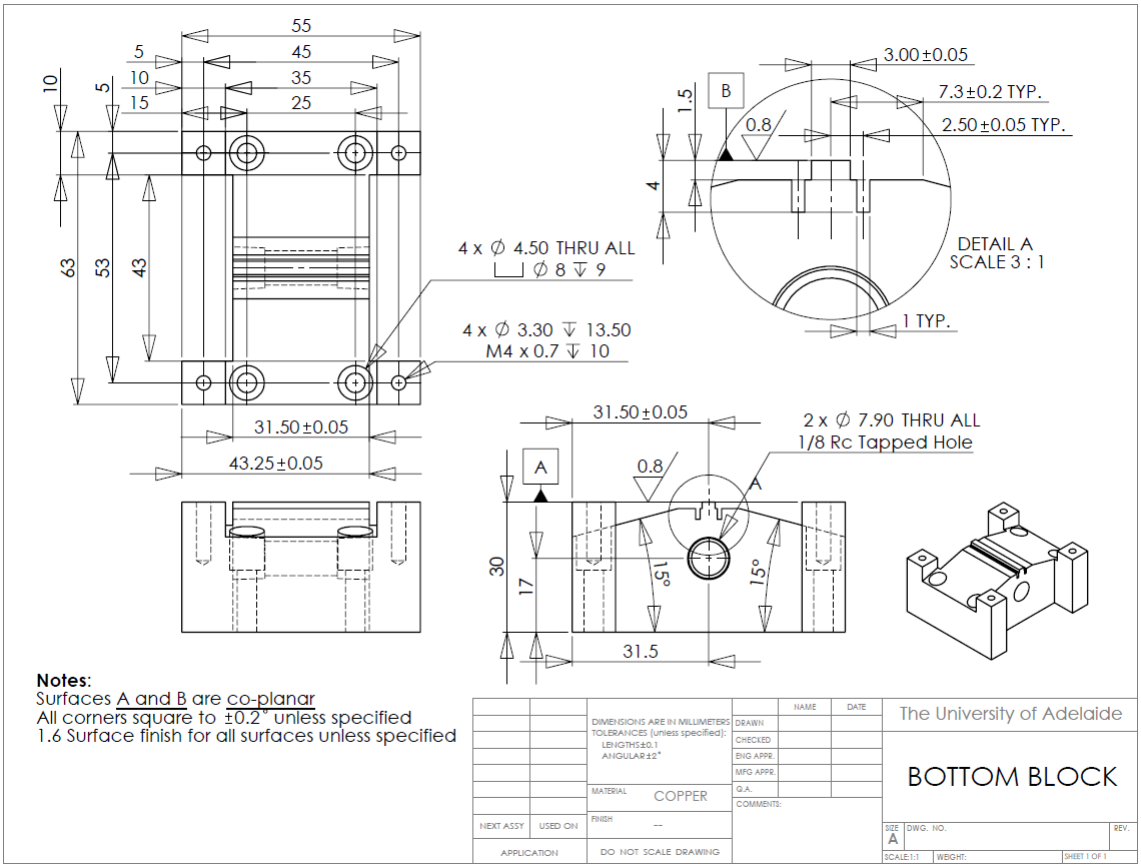

Notes:
Surfaces A and B are co-planar
All corners square to ±0.2° unless specified
1.6 Surface finish for all surfaces unless specified

		DIMENSIONS ARE IN MILLIMETERS TOLERANCES (unless specified): LENGTHS±0.1 ANGULAR±2°		NAME	DATE
			DRAWN		
			CHECKED		
			ENG APPR.		
			MFG APPR.		
			Q.A.		
			COMMENTS:		
		MATERIAL COPPER			
NEXT ASSY	USED ON	FINISH --			
APPLICATION		DO NOT SCALE DRAWING			

The University of Adelaide

BOTTOM BLOCK

SIZE A | DWG. NO. | REV.
SCALE:1:1 | WEIGHT: | SHEET 1 OF 1

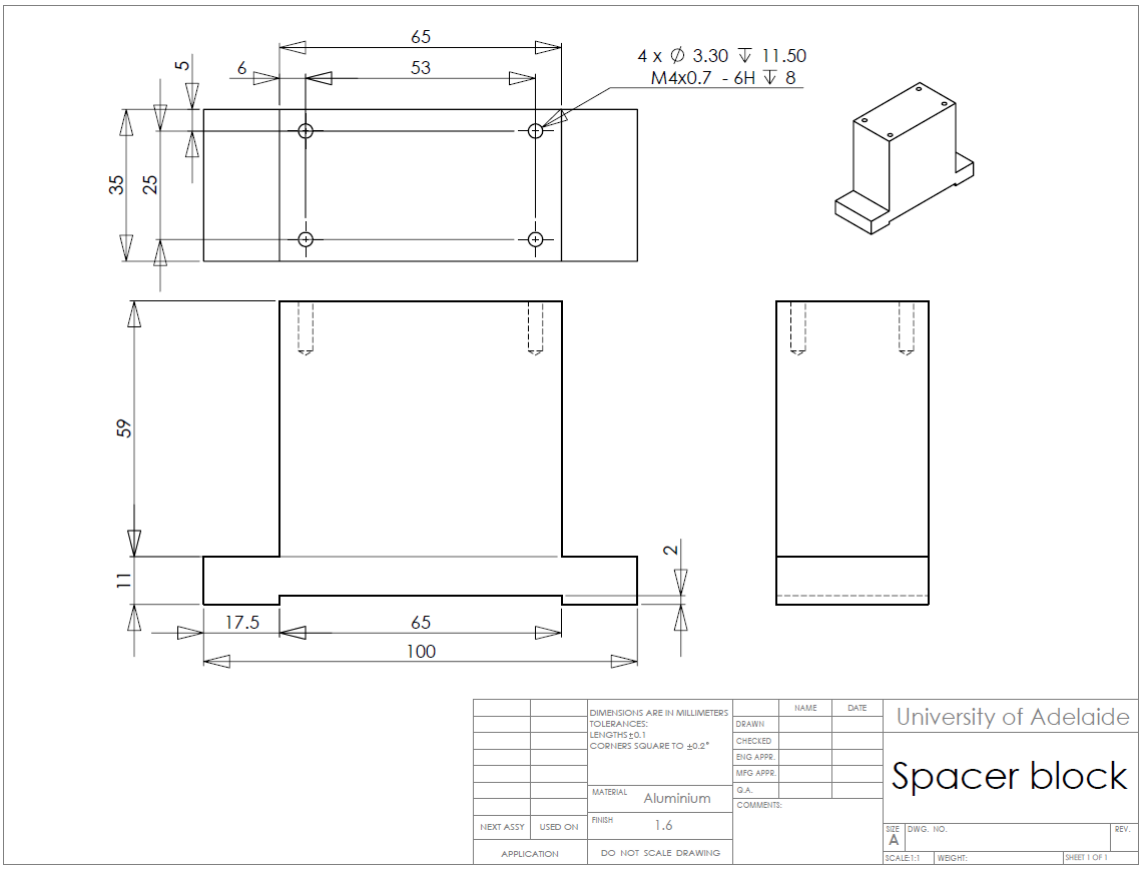
65
53
6
5
35
25
4 x ∅ 3.30 ↧ 11.50
M4x0.7 - 6H ↧ 8
59
11
2
17.5
65
100
DIMENSIONS ARE IN MILLIMETERS
TOLERANCES:
LENGTHS ±0.1
CORNERS SQUARE TO ±0.2°
MATERIAL Aluminium
FINISH 1.6
NEXT ASSY
USED ON
APPLICATION
DO NOT SCALE DRAWING
NAME
DATE
DRAWN
CHECKED
ENG APPR.
MFG APPR.
Q.A.
COMMENTS:
University of Adelaide
Spacer block
SIZE A
DWG. NO.
REV.
SCALE:1:1
WEIGHT:
SHEET 1 OF 1

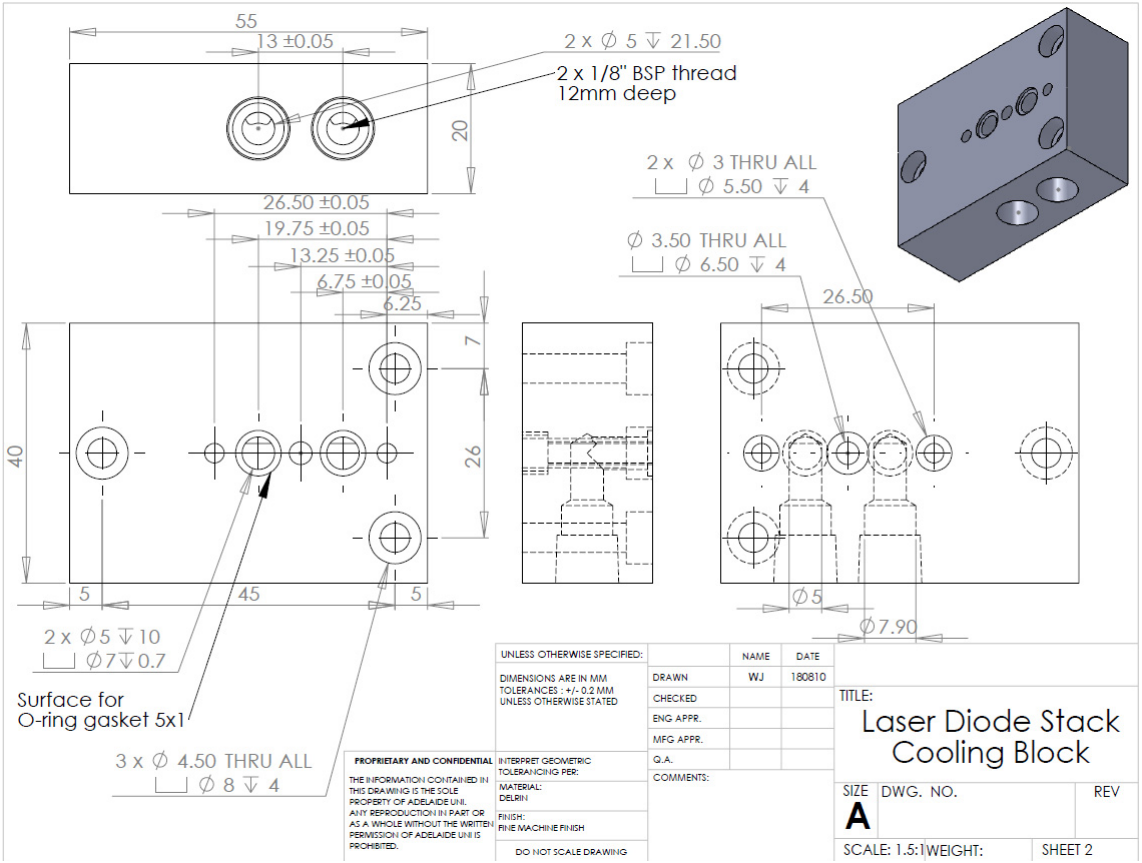
55
13 ±0.05
2 x ∅ 5 ↧ 21.50
2 x 1/8" BSP thread
12mm deep
20
2 x ∅ 3 THRU ALL
⌴ ∅ 5.50 ↧ 4
∅ 3.50 THRU ALL
⌴ ∅ 6.50 ↧ 4
26.50 ±0.05
19.75 ±0.05
13.25 ±0.05
6.75 ±0.05
6.25
26.50
7
26
40
5
45
5
∅5
∅7.90
2 x ∅5 ↧ 10
⌴ ∅7↧0.7
Surface for
O-ring gasket 5x1
3 x ∅ 4.50 THRU ALL
⌴ ∅ 8 ↧ 4
UNLESS OTHERWISE SPECIFIED:
DIMENSIONS ARE IN MM
TOLERANCES : +/- 0.2 MM
UNLESS OTHERWISE STATED
PROPRIETARY AND CONFIDENTIAL
THE INFORMATION CONTAINED IN THIS DRAWING IS THE SOLE PROPERTY OF ADELAIDE UNI. ANY REPRODUCTION IN PART OR AS A WHOLE WITHOUT THE WRITTEN PERMISSION OF ADELAIDE UNI IS PROHIBITED.
INTERPRET GEOMETRIC TOLERANCING PER:
MATERIAL: DELRIN
FINISH: FINE MACHINE FINISH
DO NOT SCALE DRAWING
NAME
DATE
DRAWN
WJ
180810
CHECKED
ENG APPR.
MFG APPR.
Q.A.
COMMENTS:
TITLE:
Laser Diode Stack
Cooling Block
SIZE A
DWG. NO.
REV
SCALE: 1.5:1
WEIGHT:
SHEET 2

B.2 ThOR slab laser

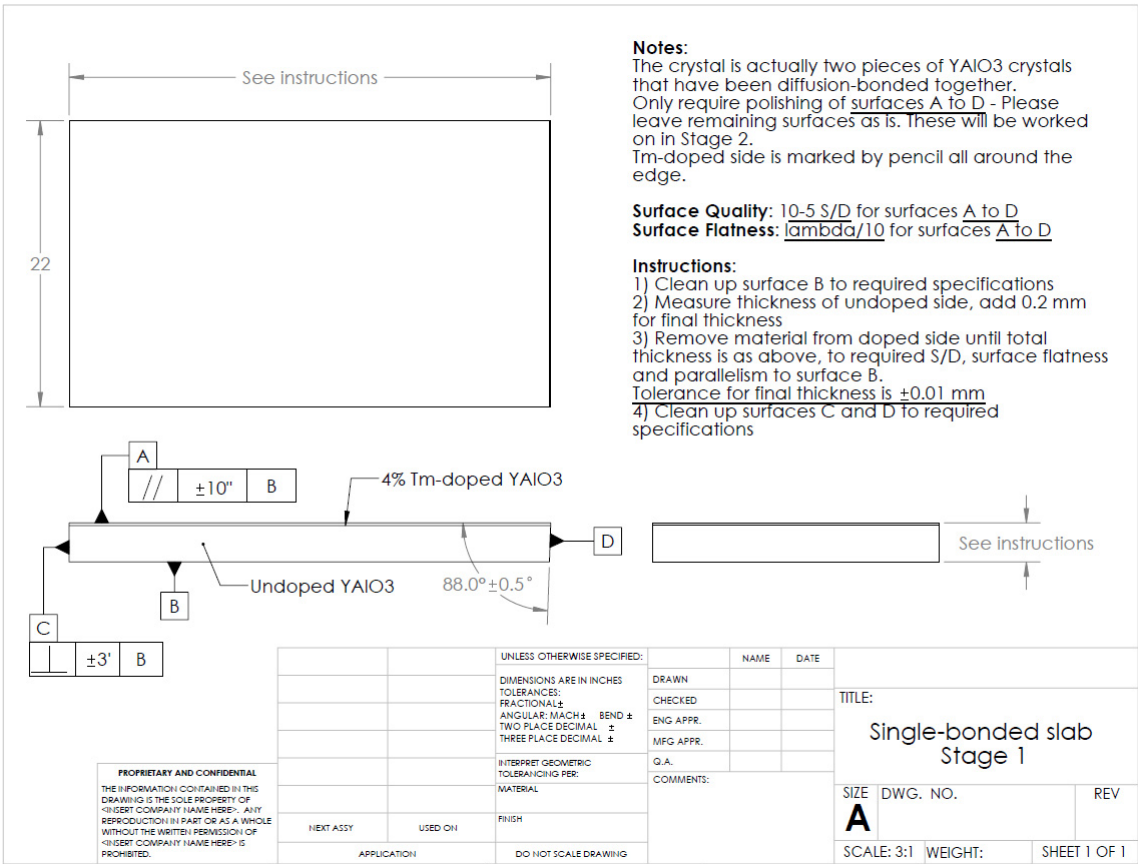

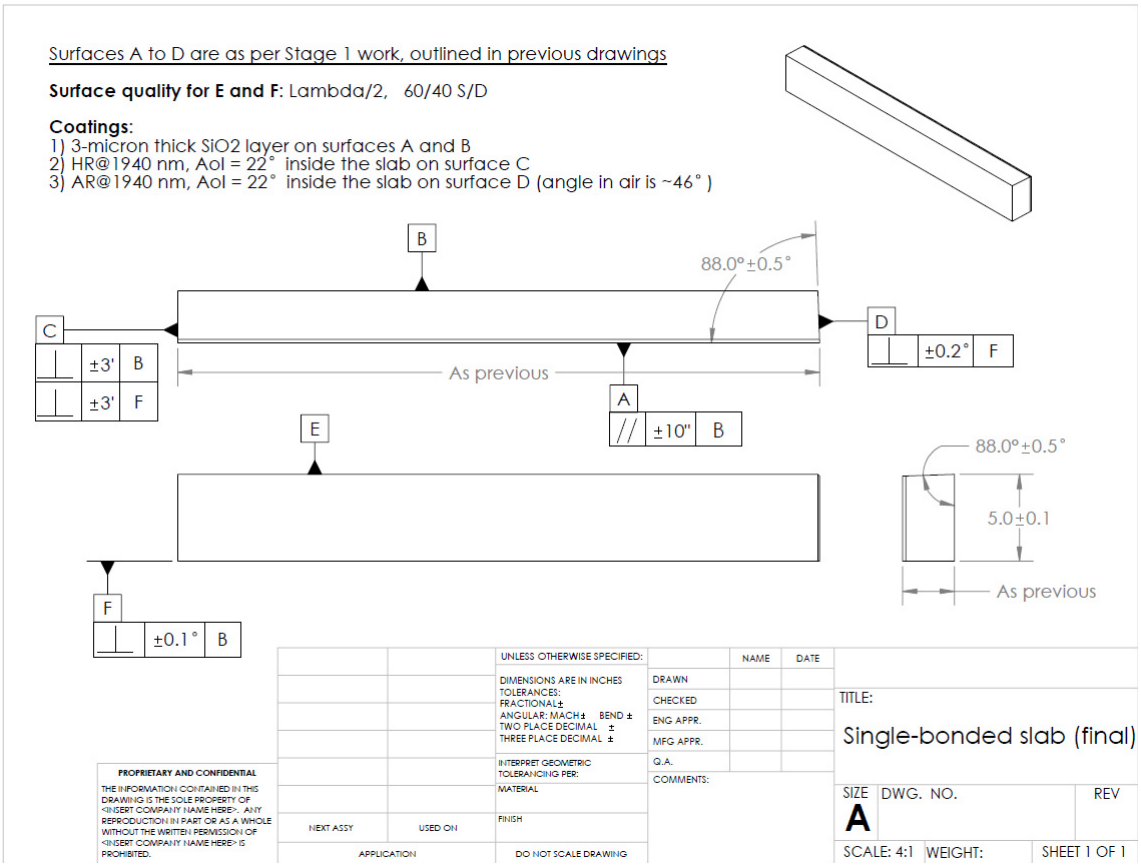

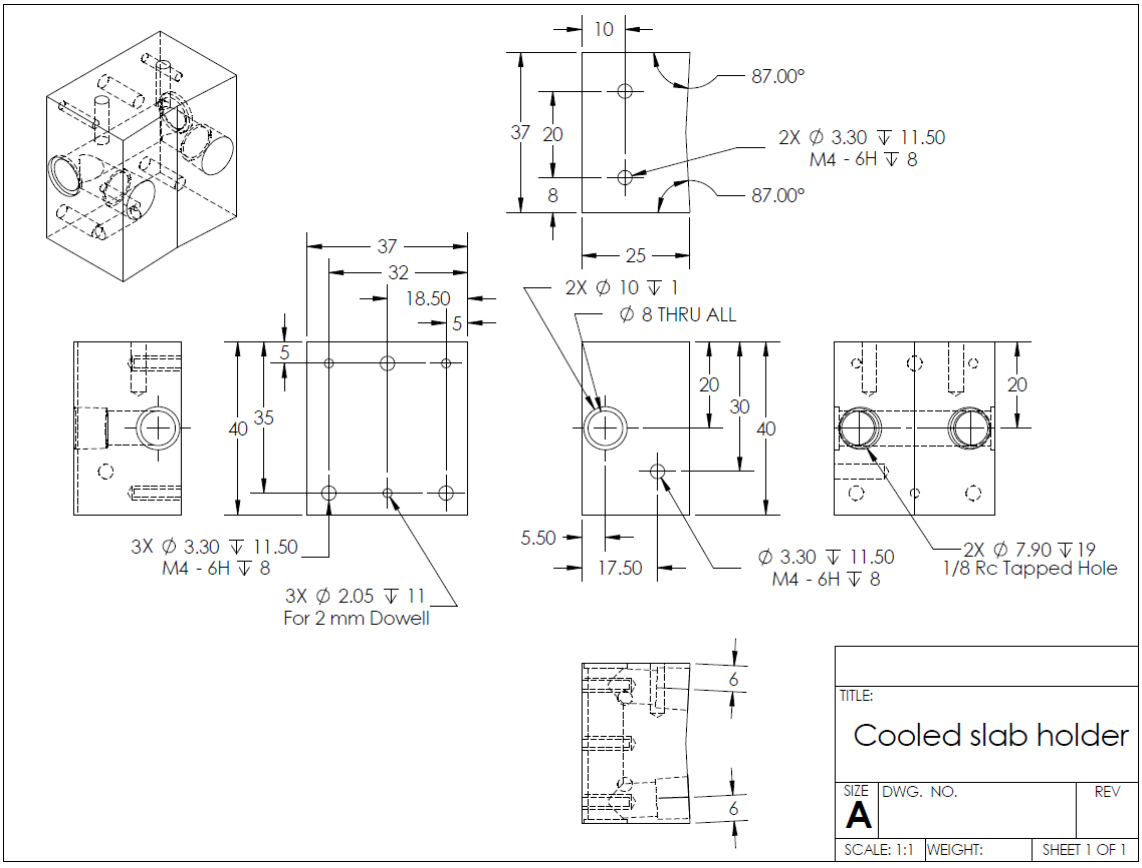
10
87.00°
37
20
8
2X Ø 3.30 ↧ 11.50
M4 - 6H ↧ 8
87.00°
25
37
32
18.50
5
2X Ø 10 ↧ 1
Ø 8 THRU ALL
5
40
35
20
30
40
20
3X Ø 3.30 ↧ 11.50
M4 - 6H ↧ 8
3X Ø 2.05 ↧ 11
For 2 mm Dowell
5.50
17.50
Ø 3.30 ↧ 11.50
M4 - 6H ↧ 8
2X Ø 7.90 ↧ 19
1/8 Rc Tapped Hole
6
6
TITLE:
Cooled slab holder
SIZE
A
DWG. NO.
REV
SCALE: 1:1
WEIGHT:
SHEET 1 OF 1

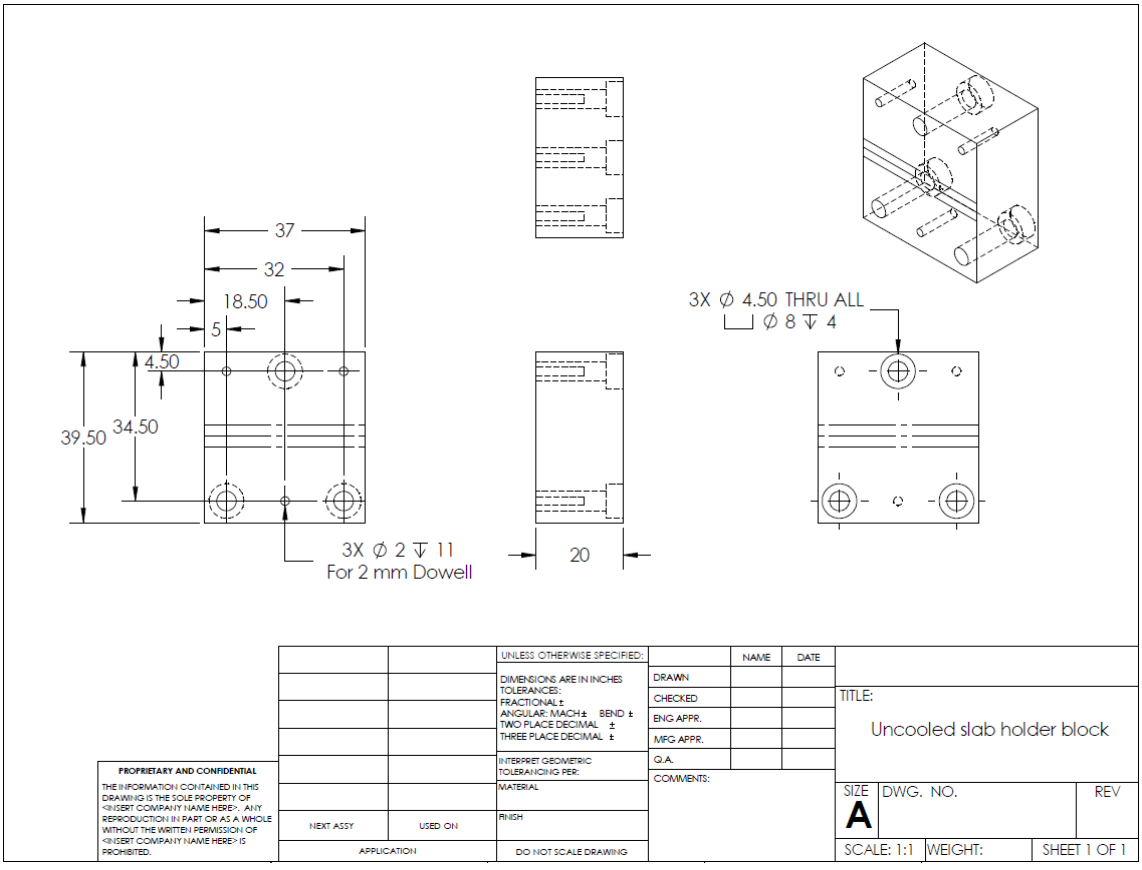
37
32
18.50
5
4.50
39.50
34.50
3X Ø 2 ↧ 11
For 2 mm Dowell
20
3X Ø 4.50 THRU ALL
⌴ Ø 8 ↧ 4
UNLESS OTHERWISE SPECIFIED:
DIMENSIONS ARE IN INCHES
TOLERANCES:
FRACTIONAL ±
ANGULAR: MACH ± BEND ±
TWO PLACE DECIMAL ±
THREE PLACE DECIMAL ±
INTERPRET GEOMETRIC TOLERANCING PER:
MATERIAL
FINISH
NEXT ASSY
USED ON
APPLICATION
DO NOT SCALE DRAWING
NAME
DATE
DRAWN
CHECKED
ENG APPR.
MFG APPR.
Q.A.
COMMENTS:
PROPRIETARY AND CONFIDENTIAL
THE INFORMATION CONTAINED IN THIS DRAWING IS THE SOLE PROPERTY OF <INSERT COMPANY NAME HERE>. ANY REPRODUCTION IN PART OR AS A WHOLE WITHOUT THE WRITTEN PERMISSION OF <INSERT COMPANY NAME HERE> IS PROHIBITED.
TITLE:
Uncooled slab holder block
SIZE
A
DWG. NO.
REV
SCALE: 1:1
WEIGHT:
SHEET 1 OF 1

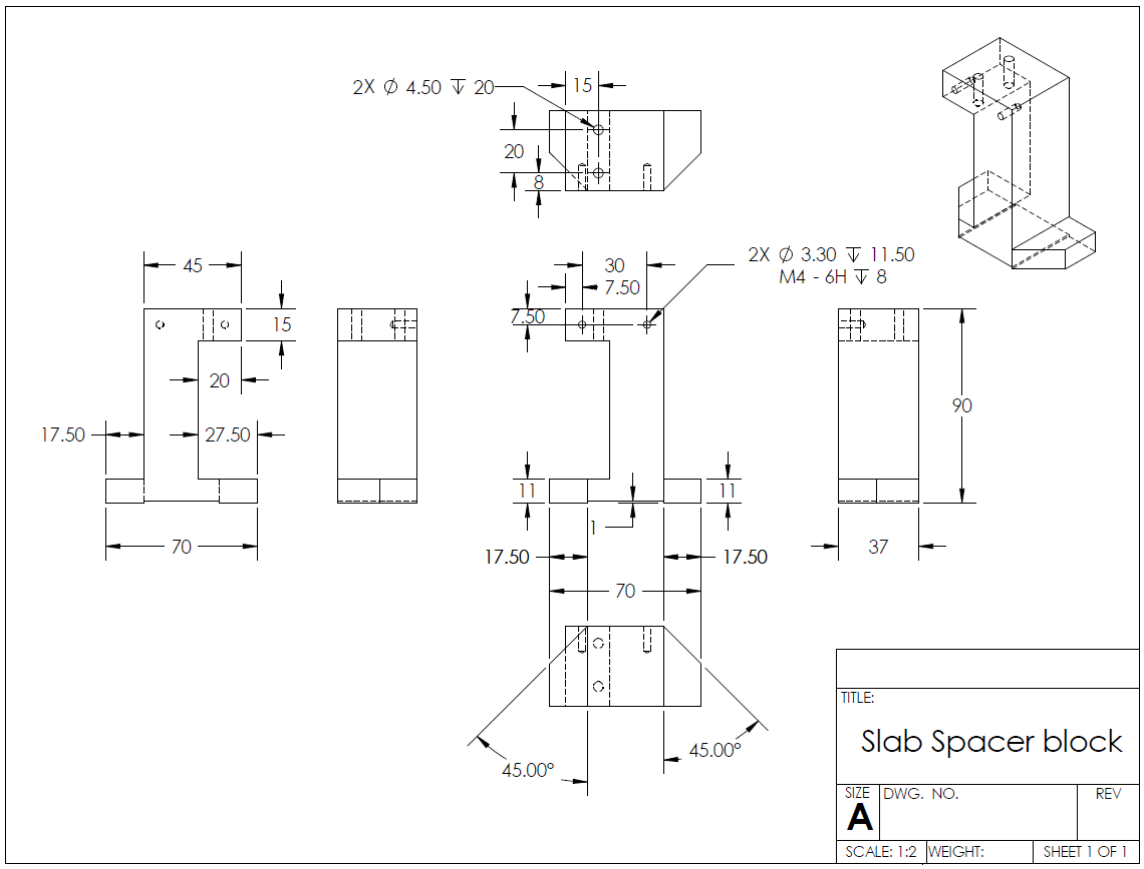
2X ∅ 4.50 ↧ 20
15
20
8
45
15
20
17.50
27.50
70
30
7.50
7.50
2X ∅ 3.30 ↧ 11.50
M4 - 6H ↧ 8
11
11
1
17.50
17.50
70
45.00°
45.00°
90
37
TITLE:
Slab Spacer block
SIZE
A
DWG. NO.
REV
SCALE: 1:2
WEIGHT:
SHEET 1 OF 1

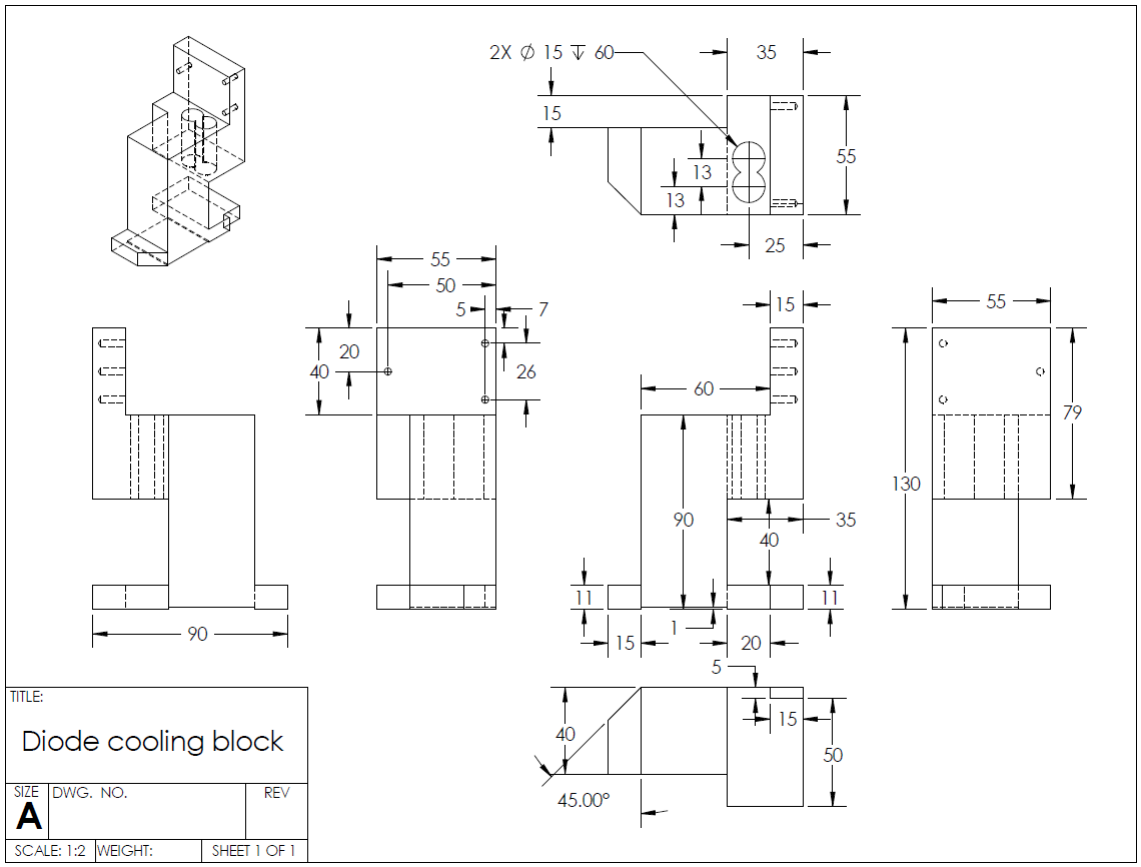
2X ∅ 15 ↧ 60
35
15
55
13
13
25
55
50
5
7
20
40
26
90
15
60
90
35
40
11
11
15
1
20
5
40
45.00°
15
50
55
130
79
TITLE:
Diode cooling block
SIZE
A
DWG. NO.
REV
SCALE: 1:2
WEIGHT:
SHEET 1 OF 1

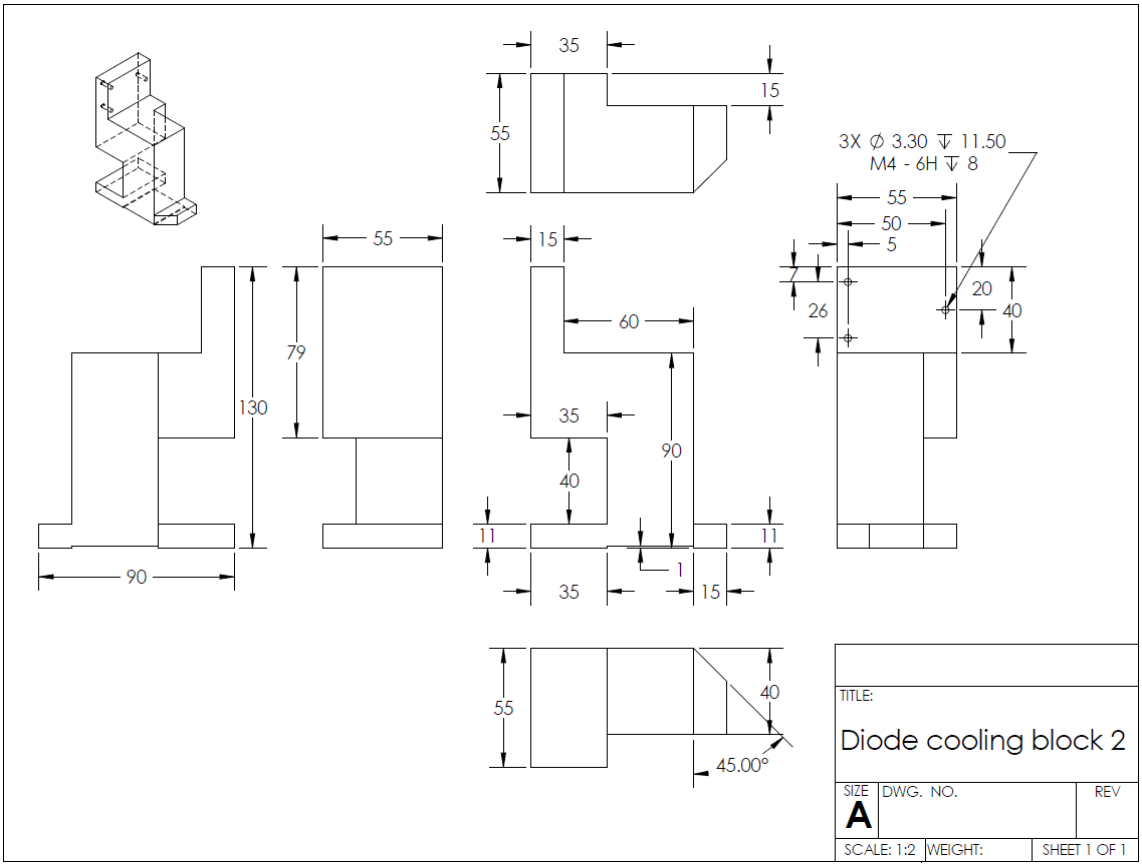

Note that the Diode cooling blocks are designed for diode stacks already mounted to the Laser Diode Stack Cooling Block, and hence are assembled together.

C Programming code

This appendix contains the major programming codes that were written for this work.

C.1 Matlab code

C.1.1 Tm:$YAlO_3$ laser dynamics

C.1.1.1 TmYAlO_model.m

```
% Model of the temporal dynamics of the Tm:YAlO3 cuboid laser, including
% cross-relaxation, bleaching and ESA at the lasing wavelength. Also
% includes a feedback loop for pulse suppression.

close all
clear all

tspan = 100e-5;      % Time span to solve ODEs
Servo.OnOff = 0;     % 1 = servo on, 0 = servo off
laser_param;         % Load laser parameters

% Find initial population densities when gain exceeds unity
P0 = [find_onset(a);0;0;0];
dP_0 = [0;0;0;0;0;0];

% Solve expanded rate equations, with Ni -> (Ni_av + dNi)
Rate_Eq_r = @(t,Pin) Rate_Equations(Pin,t,a,P0);
[t,P] = ode45(Rate_Eq_r,[0,tspan],dP_0);

% Solve alternative rate equations, equivalent to above
% Rate_Eq = @(t,Pin) Rate_Equations(Pin,t,a);
% [t,P] = ode45(Rate_Eq,[0,tspan],P0);

% Define the population densities
N2 = P(:,1) + P0(1);
N3 = P(:,2) + P0(2);
N4 = P(:,3) + P0(3);
phi = P(:,4) + P0(4);

% Estimate the pulse repetition frequency
```

```
[pks,locs] = findpeaks(phi,'minpeakdistance',10);
locs = t(locs);
av_freq = 1/(mean(diff(locs)));

%%% Default Graphic Settings %%%%
set(0,'DefaultAxesFontSize',12);
set(0,'DefaultAxesFontWeight','normal');
set(0,'DefaultTextFontSize',12);
set(0,'DefaultTextFontWeight','normal');
set(0,'DefaultUicontrolFontSize',12);
set(0,'DefaultUicontrolFontWeight','normal');
set(0,'DefaultAxesTickLength',[0.025 0.015]);
set(0,'DefaultLineLineWidth', 1.5);

% Plot results
subplot(2,1,1)
plot(t,phi/max(phi))
ylabel('Power [A.U.]')
legend(['Estimated PRF: ' num2str(av_freq/1000) ' kHz'])
subplot(2,1,2)
plot(t,N2)
ylabel('Density [cm^{-3}]')
xlabel('Time [s]')
legend('N2')
figure
subplot(2,1,1)
plot(t,N3)
ylabel('Density [cm^{-3}]')
legend('N3')
subplot(2,1,2)
plot(t,N4)
ylabel('Density [cm^{-3}]')
legend('N4')
xlabel('Time [s]')

% Estimate the average population densities after reaching equilibrium
P_av(1) = mean(N2(round(size(N2)/2):size(N2),:));
P_av(2) = mean(N3(round(size(N3)/2):size(N3),:));
P_av(3) = mean(N4(round(size(N4)/2):size(N4),:));
P_av(4) = mean(phi(round(size(phi)/2):size(phi),:));

TmYAlO_model_linear;    % Call linear model to obtain transfer functions
```

C.1.1.2 laser_param.m

```
% Parameters from Tm:YAlO3 cuboid laser
% NOTE: centimetres used as base length unit!

% Physical parameters
pump.wave = 793e-9;             % Pump wavelength [m]
laser.wave = 1.945e-6;          % Laser wavelength [m]
pump.power = 4;                 % Incident pump power [W]
pump.abs_alpha = 3;             % Absorption coefficient [/cm]

pump.rad = 1e-2;                % Pump beam radius [cm]
laser.rad = pump.rad*0.75;      % Laser beam radius [cm]
pump.area = pi*pump.rad^2;      % Laser mode area [cm^2]
laser.area = pi*laser.rad^2;    % Pump mode area [cm^2]
l_crys = 0.4545;                % Length of crystal [cm]
l_air = 20.5;                   % Length of air in cavity [cm]
T_OC = 0.1;                     % Transmission of output coupler

% Tm:YAlO3 parameters
a.conc = 7.87e20;               % Ion concentration [/cm^3] (Ka)
[~, ~, n_c] = n_YAlO(laser.wave);   %Ref ind of YAlO at laser wavelength
a.n_YAlO = n_c; clear n_a n_b n_c
a.sigma_e = 7.8e-21;            % Stim. emission cross-section N2->N1 [cm^2]
```

```
gamma = 0.65;
a.sigma_a = gamma*a.sigma_e;     % Stim. absorption cross-section N3->N4 [cm^2]
a.fu = 0.263;                    % Upper state ion fraction
a.fl = 0.03;                     % Lower state ion fraction
solid_angle = 1e-6;              % Solid angle in which radiative decay
                                 % contributes to photon count

% Ion transfer rates
% Cross relaxation
a.a4212 = 1.5e-14;       % N4 -> N2 and N1 -> N2
a.a3212 = 0;             % N3 -> N2 and N1 -> N2
a.a2123 = 2.8e-18;       % N2 -> N1 and N1 -> N3
a.a2124 = 8e-19;         % N2 -> N1 and N2 -> N4

% Spontaneous decay
a.r42 = 1.3e2;
a.r43 = 1.46e3;
a.r32 = 1.8e5;
a.r4 = a.r42+ a.r43;
a.r3 = a.r32;
a.r2 = 2.1e2;

% Servo Parameters
% Servo.OnOff = 0;           % Servo controlled in main program
Servo.input_frac = 0.001;    % Fraction of laser power onto detector
Servo.G_preamp = 10;         % Gain of pre-amp [V/V]
Servo.G_VtoA = 1;            % Gain of V-to-A converter [A/V]
Servo.pump_resp = 1;         % Response of the pump diode [W/A]
Servo.Rt = 100;              % Transimpedance gain

Servo.f_lp = 1e6;            % Corner freq of servo flat -> 1/f (low-pass) [Hz]
Servo.f_hp = 1e4;            % Corner freq of AC part f -> flat (high-pass)
[Hz]
a.Satfrac = 1;            % Limit on the servo as fraction of driver current
% _in = hp, _out = lp

% Global Constants
a.c = 3e10;                  % Speed of light [cm/s]
c_m = 3e8;                   % Speed of light [m/s]
h = 6.63e-34;                % Planck's Constant

% Calculated Parameters
a.density_red = 2*(a.n_YAlO*l_crys)/(a.n_YAlO*l_crys+l_air);  % Relative ion
    % density in cavity compared to ion density. 2 due to standing wave
laser.E = h*c_m/laser.wave;              % Energy of the pump photons
pump.E = h*c_m/pump.wave;                % Energy of the pump photons
sigma_p = pump.abs_alpha/a.conc;         % Pump cross section
% pump.decaying_abs = (1-exp(-pump.abs_alpha*l_crys))/pump.abs_alpha/l_crys;
    % Value that accounts for exponential decay of intensity along crystal
a.Rp = pump.power/pump.E*sigma_p/pump.area*laser.area/pump.area;
    % Pump rate (N1 -> N4)

time_rt = 2*(l_air+a.n_YAlO*l_crys)/a.c;     % Cavity round-trip time [s]
a.rc = -log(1-T_OC)/time_rt;                 % Cavity photon decay rate [/s]

Servo.V_in = T_OC*Servo.input_frac*Servo.OnOff; % Voltage induced on Servo
Servo.A_to_diode = Servo.V_in*Servo.G_preamp*Servo.G_VtoA*Servo.Rt;
    % Current sent to the pump diode
a.Gservo = Servo.A_to_diode*Servo.pump_resp*sigma_p/pump.E/pump.area;
    % Overall servo gain to pump diode

a.tau_lp = 1/(2*pi*Servo.f_lp);          % Low-pass filter time constant
a.tau_hp = 1/(2*pi*Servo.f_hp);          % High-pass filter time constant

a.rsp = a.r2*solid_angle;        % Radiative decay rate (N2 -> N1)
```

C.1.1.3 Rate_Equations.m

```
function dP = Rate_Equations (P,t,a,P_av)
%Function containing the ODEs relating to the ion transitions for Tm:YAlO3.
%P(i) for i = 1:3 is the values of N_(i-1). P(4) is the photon population.
%P(5) and P(6) relate to the servo loop

% Allow for switching on and off feedback loop
% u = 1;
% if (t >= a.t0)&&(t <= a.t1)
%     % u = 1-(2*abs(t-((a.t1+a.t0)/2))/(a.t1-a.t0))^1000;
%     u = 1;
% end

% vib = 0;

% The ODEs set
N1 = a.conc - P_av(1)-P_av(2)-P_av(3);
N2 = P_av(1);
N3 = P_av(2);
N4 = P_av(3);
phi = P_av(4);

dN1 = -(P(1)+P(2)+P(3));   %Ground-state population
dN2 = P(1);                      %Upper lasing level
dN3 = P(2);                      %Intermediate level
dN4 = P(3);                      %Pump level
dphi = P(4);                     %Photon population in cavity
resp = P(5);                    %Servo response after amplifier stage
dRp = P(6);                     %Pump rate change due to servo

% Allow servo saturation
if abs(dRp) > a.Satfrac*a.Rp;
    dRp = sign(dRp)*a.Satfrac*a.Rp;
end

%Rate equations
% dN2N1 = 2*a.a4212*N4 + 2*a.a3212*N3 + 2*a.sigma_e*a.c*a.fl*phi;
dN2N2 = -2*a.a4212*N4 - 2*a.a3212*N3 - 4*(a.a2124 + a.a2123)*N2...
    - 2*a.sigma_e*a.c*(a.fl+a.fu)*phi - a.r2 - a.rsp;
dN2N3 = -2*a.a4212*N4 - 2*a.a3212*N3 - 2*a.sigma_e*a.c*a.fl*phi...
    + 2*a.a3212*N1 + a.r32;
dN2N4 = -2*a.a4212*(N4-N1) - 2*a.a3212*N3 - 2*a.sigma_e*a.c*a.fl*phi...
    + a.r42;
dN2phi = -2*a.sigma_e*a.c*(a.fu*N2 - a.fl*N1);
dN2X = 2*a.a4212*dN1*dN4 - 2*(a.a2124 + a.a2123)*dN2^2 + 2*a.a3212*dN1*dN3...
 - 2*a.sigma_e*a.c*a.fu*dN2*dphi + 2*a.sigma_e*a.c*a.fl*dN1*dphi;
dN2const = 2*a.a4212*N1*N4 - 2*(a.a2124 + a.a2123)*N2^2 + 2*a.a3212*N1*N3...
    - 2*a.sigma_e*a.c*a.fu*N2*phi + 2*a.sigma_e*a.c*a.fl*N1*phi...
    + a.r42*N4 + a.r32*N3 - (a.r2 + a.rsp)*N2;

% dN3N1 = -a.a3212*N3;
dN3N2 = a.a3212*N3 + 2*a.a2123*N2;
dN3N3 = a.a3212*(N3-N1) - 2*a.sigma_a*a.c*phi - a.r3;
dN3N4 = a.a3212*N3 + 2*a.sigma_a*a.c*phi + a.r43;
dN3phi = 2*a.sigma_a*a.c*(N4-N3);
dN3X = a.a2123*dN2^2 - a.a3212*dN1*dN3 + 2*a.sigma_a*a.c*(dN4-dN3)*dphi;
dN3const = a.a2123*N2^2 - a.a3212*N1*N3 + 2*a.sigma_a*a.c*(N4-N3)*phi...
    + a.r43*N4 - a.r3*N3;

% dN4N1 = a.Rp - a.a4212*N4;
dN4N2 = -a.Rp + a.a4212*N4 + 2*a.a2124*N2;
dN4N3 = -a.Rp + a.a4212*N4 + 2*a.sigma_a*a.c*phi;
dN4N4 = -2*a.Rp + a.a4212*(N4-N1) - 2*a.sigma_a*a.c*phi - a.r4;
dN4phi = -2*a.sigma_a*a.c*N4 + 2*a.sigma_a*a.c*N3;
dN4Rp = N1 - N4;
dN4X = -dRp*(dN4-dN1) + a.a2124*dN2^2 - 2*a.sigma_a*a.c*(dN4-dN3)*dphi...
```

```
    - a.a4212*dN1*dN4;
dN4const = a.Rp*N1 - a.Rp*N4 + a.a2124*N2^2 - 2*a.sigma_a*a.c*(N4-N3)*phi...
    - a.a4212*N1*N4 - a.r4*N4;

% dphiN1 = -a.c*a.density_red*a.sigma_e*a.fl*phi;
dphiN2 = a.c*a.density_red*a.sigma_e*(a.fl + a.fu)*phi + a.rsp;
dphiN3 = a.c*a.density_red*(a.sigma_e*a.fl - a.sigma_a)*phi;
dphiN4 = a.c*a.density_red*(a.sigma_e*a.fl + a.sigma_a)*phi;
dphiphi = a.c*a.density_red*(a.sigma_e*(a.fu*N2 - a.fl*N1)...
    + a.sigma_a*(N4-N3)) - a.rc;
dphiX = a.c*a.density_red*(a.sigma_e*(a.fu*dN2 - a.fl*dN1)...
    + a.sigma_a*(dN4-dN3))*dphi;
dphiconst = a.c*a.density_red*(a.sigma_e*(a.fu*N2 - a.fl*N1)...
    + a.sigma_a*(N4-N3))*phi - a.rc*phi + a.rsp*N2;

% dN2X = 0;
% dN3X = 0;
% dN4X = 0;
% dphiX = 0;

dN2dt = dN2N2*dN2 + dN2N3*dN3 + dN2N4*dN4 + dN2phi*dphi...
    + dN2X + dN2const;
dN3dt = dN3N2*dN2 + dN3N3*dN3 + dN3N4*dN4 + dN3phi*dphi...
    + dN3X + dN3const;
dN4dt = dN4N2*dN2 + dN4N3*dN3 + dN4N4*dN4 + dN4phi*dphi...
    + dN4Rp*dRp + dN4X + dN4const;
dphidt = dphiN2*dN2 + dphiN3*dN3 + dphiN4*dN4 + dphiphi*dphi...
    + dphiX + dphiconst;

drespdt = a.Gservo*dphidt - resp/a.tau_hp;
ddRpdt = (resp - dRp)/a.tau_lp;

dP = [dN2dt; dN3dt; dN4dt; dphidt; drespdt; ddRpdt];
end
```

C.1.1.4 find_onset.m

```
function res = find_onset(a)
% Function to find the population densities when gain exceeds unity. a is
% the initial parameters. Returns population densities at the onset.

sigma_e = a.sigma_e;    % Emission cross-section
% Turn off all photon interactions for model
a.sigma_e = 0;
a.sigma_a = 0;
a.rsp = 0;
tau2 = 1/a.r2;          % Unity gain should be reached within N2 lifetime
P0 = [0;0;0;0;0;0];     % All ions in N1 state

% Solve rate equations (ignoring photon interactions)
Rate_Eq = @(t,Pin) Rate_Equations(Pin,t,a);
[t,P] = ode45(Rate_Eq,[0,tau2],P0);

% Define population densities
N2 = P(:,1);
N3 = P(:,2);
N4 = P(:,3);
N1 = a.conc - (N2 + N3 + N4);

% Find the gain coefficient based on population densities
gain_coeff = (sigma_e*a.c*(a.fu*N2 - a.fl*N1) + a.sigma_a*a.c*(N4 - N3))...
    *a.density_red - a.rc;

% Find the time and population densities when gain exceeds unity
nn = find(gain_coeff > 0,1);
t_zero = interp1(gain_coeff((nn-5):(nn+5)),t((nn-5):(nn+5)),0);
```

```
N2_onset =  interp1(t((nn-5):(nn+5)),N2((nn-5):(nn+5)), t_zero);
N3_onset =  interp1(t((nn-5):(nn+5)),N3((nn-5):(nn+5)), t_zero);
N4_onset =  interp1(t((nn-5):(nn+5)),N4((nn-5):(nn+5)), t_zero);

res = [N2_onset;N3_onset;N4_onset];
end
```

C.1.1.5 TmYAlO_model_linear.m

```
% Model of the transfer function of the Tm:YAlO3 cuboid laser, including
% cross-relaxation, bleaching and ESA at the lasing wavelength. Uses
% linearised rate equations.

% Use existing average population density if it exists, else use the onset
% values as the average population density
if exist('P_av','var') == 0
    close all
    clear all
    Servo.OnOff = 0;    % 1 = servo on, 0 = servo off
    laser_param;        % Load laser parameters
    disp('Using onset values as mean populations')
    P_av = [find_onset(a);7.8e13];  % Initial photon value from other model
end

freq_v = logspace(2,6,1e3);     % Define the frequency space

% Solve for the transfer functions for each of the population densities
P_TF = zeros([length(freq_v),4]);
for ii = 1:length(freq_v)
    P_TF(ii,:) = Rate_Equations_linear(a,2*pi*freq_v(ii),P_av);
end

% Define the transfer functions
N2_TF = P_TF(:,1);
N3_TF = P_TF(:,2);
N4_TF = P_TF(:,3);
phi_TF = P_TF(:,4);

% Obtain the oscillation frequency (peak of the gain)
osc_freq = freq_v(abs(phi_TF) == max(abs(phi_TF)));

% Plot normalised results
figure
subplot(2,1,1)
loglog(freq_v,abs(phi_TF)/abs(phi_TF(1)))
legend(['Osc. freq = ' num2str(osc_freq/1000) ' kHz'],...
    'Location','NorthWest')
ylabel('Amplitude')
axis([1e2 1e6 1e-4 1e4])
grid on
subplot(2,1,2)
semilogx(freq_v,180/pi*unwrap(angle(phi_TF)))
grid on
set(gca,'YTick',[-270 -180 -90 0 90 180 270])
ylabel('Phase [degrees]')
xlabel('Frequency [Hz]')
figure
subplot(2,1,1)
loglog(freq_v,abs(N2_TF)/abs(N2_TF(1)),...
    freq_v,abs(N3_TF)/abs(N3_TF(1)),...
    freq_v,abs(N4_TF)/abs(N4_TF(1)))
legend('N2','N3','N4','Location','NorthWest')
ylabel('Amplitude')
axis([1e2 1e6 1e-4 1e4])
grid on
subplot(2,1,2)
semilogx(freq_v,180/pi*unwrap(angle(N2_TF)),...
```

```
    freq_v,180/pi*unwrap(angle(N3_TF)),...
    freq_v,180/pi*unwrap(angle(N4_TF)))
grid on
set(gca,'YTick',[-360 -180 0 180 360])
ylabel('Phase [degrees]')
xlabel('Frequency [Hz]')
```

C.1.1.6 Rate_Equations_linear.m

```
function P_TF = Rate_Equations_linear(a,w,P_av)
% Function containing the linearised ODEs relating to the ion transitions
% for Tm:YAlO3. a is the initial parameters; w is the angular frequency
% to solve for. P_av(i) for i = 1:3 is the average population density of
% N_(i-1). % P(4) is the average photon population.
% Returns the transfer function.

% Defining average populations
N1 = a.conc - P_av(1)-P_av(2)-P_av(3);
N2 = P_av(1);
N3 = P_av(2);
N4 = P_av(3);
phi = P_av(4);

s = 1i*w;   % Define the s parameter

% Linearised rate equations
% Dependence of ddN2/dt on dN2, dN3, dN4 and dphi respectively
M(1,1) = -2*a.a4212*N4 - 4*(a.a2124+a.a2123)*N2 - 2*a.a3212*N3...
    - 2*a.sigma_e*a.c*(a.fu+a.fl)*phi - a.r2 - a.rsp;
M(1,2) = -2*a.a4212*N4 - 2*a.a3212*N3 + 2*a.a3212*N1...
    - 2*a.sigma_e*a.c*a.fl*phi + a.r32;
M(1,3) = -2*a.a4212*(N4-N1)- 2*a.a3212*N3 - 2*a.sigma_e*a.c*a.fl*phi + a.r42;
M(1,4) = -2*a.sigma_e*a.c*(a.fu*N2-a.fl*N1);

% Dependence of ddN3/dt on dN2, dN3, dN4 and dphi respectively
M(2,1) = 2*a.a2123*N2+a.a3212*N3;
M(2,2) = a.a3212*(N3-N1) - 2*a.sigma_a*a.c*phi - a.r3;
M(2,3) = a.a3212*N3 + 2*a.sigma_a*a.c*phi + a.r43;
M(2,4) = 2*a.sigma_a*a.c*(N4-N3);

% Dependence of ddN4/dt on dN2, dN3, dN4 and dphi respectively
M(3,1) = -a.Rp + 2*a.a2124*N2 + a.a4212*N4;
M(3,2) = -a.Rp + 2*a.sigma_a*a.c*phi + a.a4212*N4;
M(3,3) = -2*a.Rp - 2*a.sigma_a*a.c*phi + a.a4212*(N4-N1) - a.r4;
M(3,4) = -2*a.sigma_a*a.c*(N4-N3);   %Ka Correction first term

% Dependence of ddphi/dt on dN2, dN3, dN4 and dphi respectively
M(4,1) = a.sigma_e*a.c*(a.fu+a.fl)*phi*a.density_red;
M(4,2) = (a.sigma_e*a.c*a.fl - a.sigma_a*a.c)*phi*a.density_red;
M(4,3) = (a.sigma_e*a.c*a.fl + a.sigma_a*a.c)*phi*a.density_red;
M(4,4) = 0;

% Constant terms for each population density
C(1) = 2*a.a4212*N1*N4 - 2*(a.a2124 + a.a2123)*N2^2 + 2*a.a3212*N1*N3...
    - 2*a.sigma_e*a.c*a.fu*N2*phi + 2*a.sigma_e*a.c*a.fl*N1*phi...
    + a.r42*N4 + a.r32*N3 - (a.r2 + a.rsp)*N2;
C(2) = a.a2123*N2^2 - a.a3212*N1*N3 + 2*a.sigma_a*a.c*(N4-N3)*phi...
    + a.r43*N4 - a.r3*N3;
C(3) = a.Rp*N1 - a.Rp*N4 + a.a2124*N2^2 - 2*a.sigma_a*a.c*(N4-N3)*phi...
    - a.a4212*N1*N4 - a.r4*N4;
C(4) = a.c*a.density_red*(a.sigma_e*(a.fu*N2 - a.fl*N1)...
    + a.sigma_a*(N4-N3))*phi - a.rc*phi + a.rsp*N2;
C = C'/s;

% Solve for the transfer functions
P_TF = (s*eye(4)- M)\([0;0;(N1-N4);0] + C);
```

C.1.1.7 n_YAlO.m

```
function [n_a, n_b, n_c] = n_YAlO(wavelength)
%returns the refractive index of YAlO3 at one or more wavelength(s) in [m]

lambda = wavelength * 1e6; %coefficients in microns
% equations from
% http://www.mennerat.fr/gab/References/DatabaseLasers/tables/sellout.htm

B_a = 2.6196;
B_b = 2.67171;
B_c = 2.70381;
C_a = 0.012338;
C_b = 0.012605;
C_c = 0.012903;

n_a = sqrt(1 + (B_a*lambda.^2)./(lambda.^2 - C_a));
n_b = sqrt(1 + (B_b*lambda.^2)./(lambda.^2 - C_b));
n_c = sqrt(1 + (B_c*lambda.^2)./(lambda.^2 - C_c));

% plot(lambda/1e6,n_a,lambda/1e6,n_b,lambda/1e6,n_c)
% legend('n_a','n_b','n_c')
```

C.1.2 Tm:$YAlO_3$ ThOR slab modelling

C.1.2.1 ThOR_modelling.m

```
clear all
close all

% Slab properties
slab.width_undoped = 2.8e-3;    % Undoped width [m]
slab.width_doped1 = 0.2e-3;     % Doped width (top) [m]
slab.width_doped2 = 0.0e-3;     % Doped width (bottom) [m]
slab.length = 37.2e-3;            % Slab length ("diamonds" only; no nose) [m]
slab.height = 5e-3;             % Slab height [m]
slab.temperature = 300;         % Slab temperature [K]
Tm.conc = 0.04;                 % Doping concentration [atom%]
scatt_loss = 0.15;             % Scatter loss fraction (per round trip)

slab.width_full = slab.width_doped1+slab.width_doped2+slab.width_undoped;
show_plot = [0,0];      % Whether to plot [pump, laser] (1 or 0)

% Cavity properties
mirrors.R1 = 1;                 % Back mirror reflectivity
mirrors.R2 = 0.50;              % Output coupler reflectivity

% Pump properties
wave_p = 793e-9;                              % pump wavelength [m]
pump_power = 1400;                             % Pump power [W]
% NOTE: Parameters are for the beam as it is incident on the slab
beam_p.spot_size = 2e-3;%slab.width_full*0.50;    % Pump spot size [m]
beam_p.tilt = 20;                              % Emitter angle offsets [deg]
%beam_p.FWHM_div = 16.3;                         % FWHM divergence [deg]
% Alternatively, calculate FWHM based on focal length of lens
lens_f = 60e-3;
diode_height = 18e-3;
beam_p.FWHM_div = 2*atand(diode_height/(2*lens_f));

% Laser properties
wave_l = 1.94e-6;       % laser wavelength [m]
bounces = 5;            % number of bounces off of sides

% Physical properties
```

```
Tm.sigma_a_p = 5.00e-21;     % Absorption cross-section (pump) [cm^2]
Tm.sigma_e_l = 5.00e-21;     % Emission cross-section (laser) [cm^2]
Tm.lifetime_upper = 5e-3;    % Upper state lifetime [s]
Tm.CR_eff = 0.80;            % cross-relaxation efficiency

% Physical constants
n_air = 1.0003;               % Refractive index of air
av_num = 6.02e23;            % Avagadro's Number
c = 3e8;                     % Speed of Light
h = 6.63e-34;                % Planck's constant

% Calculated parameters
[a,b,n_YAlO3_l] = n_YAlO(wave_l);   %Refractive index of YAlO for laser
wavelength
[a,b,n_YAlO3_p] = n_YAlO(wave_p);   %Refractive index of YAlO for laser
wavelength
quantum_eff = 1 + Tm.CR_eff;
quantum_defect = wave_p/wave_l;
fract_limit = 2000*1.6e8/2.295e8;   %Fracture limit (heat dep) from COMSOL [W]

% Pump beam properties within the slab
beam_p.in_FWHM_max =
asind(n_air/n_YAlO3_p*sind(beam_p.tilt+beam_p.FWHM_div/2));
beam_p.in_FWHM_min = asind(n_air/n_YAlO3_p*sind(beam_p.tilt-
beam_p.FWHM_div/2));
beam_p.in_spot_size = beam_p.spot_size/cosd(beam_p.tilt);

%%%%%%%%%%%%%%%%%%%%%%%%%%%%%%%%%%%%%%%%%%%%%%%%%%%%%%%%%%%%
%%% Aperturing due to end face
AoI_back = atand(bounces*slab.width_full/slab.length);
    % Angle of incidence on back surface [deg]

% Aperturing due to end face
beam_l.bounce_loc = (0.5:bounces-0.5)/bounces*slab.length;
beam_l.edge_diff = slab.width_full/2;
beam_l.side_diff = beam_l.edge_diff/tand(AoI_back);
beam_l.edge_l = beam_l.bounce_loc - beam_l.side_diff;
beam_l.edge_r = beam_l.bounce_loc + beam_l.side_diff;

% Impact due to refractive index difference between doped/undoped YAlO3
[AoI_doped,loss_pp,YAlO,n_doped] =
doped_undoped_interface(AoI_back,Tm,wave_l);
total_trans = (1-loss_pp)^(2*bounces*...
    ((slab.width_doped1 ~= 0) + (slab.width_doped2 ~= 0)));
interf_loss = 1 - total_trans;
length_corr = (2*slab.width_doped1*(tand(AoI_doped)-tand(90-AoI_back))+...
    2*slab.width_doped2*(tand(AoI_doped)-tand(90-AoI_back)))*bounces;

%%%%%%%%%%%%%%%%%%%%%%%%%%%%%%%%%%%%%%%%%%%%%%%%%%%%%%%%%%%%
%%% Pump absorption
Tm.density = YAlO.TmYAlO_density/YAlO.TmYAlO_molar_mass*av_num*Tm.conc;
    %Ion density [cm^-3]
Tm.alpha_p = Tm.density*Tm.sigma_a_p;   %Absorption coefficient [cm^-1]
% Total pump absorption
pump_abs = ThOR_pump_abs(slab,beam_p,wave_p,Tm.alpha_p,show_plot(1));

% Applying second beam, at the negative angle
beam_p.tilt = -beam_p.tilt;
beam_p.in_FWHM_max =
asind(n_air/n_YAlO3_p*sind(beam_p.tilt+beam_p.FWHM_div/2));
beam_p.in_FWHM_min = asind(n_air/n_YAlO3_p*sind(beam_p.tilt-
beam_p.FWHM_div/2));
% Total pump absorption
pump_abs2 = ThOR_pump_abs(slab,beam_p,wave_p,Tm.alpha_p,show_plot(1));
pump_abs = (pump_abs + pump_abs2)/2;
```

```
%%%%%%%%%%%%%%%%%%%%%%%%%%%%%%%%%%%%%%%%%%%%%%%%%%%%%%%%%%%%%%%%%%%%%%%%
%%% Threshold calculation
% Transparency
slab.dopant_vol = (slab.width_doped1 + slab.width_doped2) ...
    * slab.length*slab.height;   % dopant volume [m^3]
slab.Tm_ions = (slab.dopant_vol*1e6)*Tm.density;    % Total number of ions
inversion = Tm_YAlO_Boltzmann(slab.temperature);
    % Fraction of excited ions required for inversion
excitation = inversion * slab.Tm_ions;  % Number of ions required for
inversion
E_photon_p = h*c/wave_p;    % Photon energy (pump)
% Power required to achieve transparency
transp_power = excitation*E_photon_p/Tm.lifetime_upper /(quantum_eff);

% Mirror/losses power
total_loss = 1-(mirrors.R1*mirrors.R2*(1-interf_loss)*(1-scatt_loss));
beam_l.pathlength_gain = 2*bounces*(slab.width_doped1/cosd(AoI_doped) + ...
    slab.width_doped2/cosd(AoI_doped));
gain_req = -1/(2*beam_l.pathlength_gain*100)*log(1-total_loss);  % [cm^-1]
RTloss_power = slab.dopant_vol*1e6*gain_req*E_photon_p /...
    (Tm.sigma_e_l*(quantum_eff)*Tm.lifetime_upper);

threshold_power_abs = transp_power + RTloss_power; % threshold absorbed [W]
threshold_power_inc = threshold_power_abs/pump_abs; % threshold incident [W]

beam_l.pathlength = 2*bounces*slab.width_undoped/sind(AoI_back)...
    + beam_l.pathlength_gain;

%%%%%%%%%%%%%%%%%%%%%%%%%%%%%%%%%%%%%%%%%%%%%%%%%%%%%%%%%%%%%%%%%%%%%%%%
%%% Area of unextracted region (ray analysis)
jj = beam_l.edge_l(2)-beam_l.edge_r(1);  % length along side that is
unextracted
intersect = jj/2*tand(AoI_back);
if intersect > slab.width_doped1    % makes a trapezoid
    unextr.doped1 = (jj - slab.width_doped1/tand(AoI_back))*slab.width_doped1;
else
    unextr.doped1 = intersect*jj/2;
end
if intersect > slab.width_doped2    % makes a trapezoid
    unextr.doped2 = (jj - slab.width_doped2/tand(AoI_back))*slab.width_doped2;
else
    unextr.doped2 = intersect*jj/2;
end
unextr.tot = (unextr.doped1+unextr.doped2)*bounces; % total unextracted area
[m^2]
unextr.fract = unextr.tot/(slab.dopant_vol/slab.height); %fraction of doped
unextracted

%%%%%%%%%%%%%%%%%%%%%%%%%%%%%%%%%%%%%%%%%%%%%%%%%%%%%%%%%%%%%%%%%%%%%%%%
%%% Pump power available for lasing
avail_pump_power = ...
    (pump_power-threshold_power_inc)... % incident power after transparency
    *pump_abs...    % ...that is absorbed
    *(1-unextr.fract);  % ...that lies within the laser beam path

% Theoretical maximum slope efficiency
power_conv_eff = quantum_defect*quantum_eff;
eff_factors = power_conv_eff*(1-unextr.fract)*pump_abs;
internal_loss = 1-((1-interf_loss)*(1-scatt_loss));
max_slope_eff_inc = eff_factors*-log(mirrors.R2)/...
    (internal_loss-log(mirrors.R2));

% Laser output power estimate
eff_pump = 0:pump_power;
eff_laser = max_slope_eff_inc*(eff_pump-threshold_power_inc);
eff_laser(eff_laser < 0) = 0;
```

```
eff_pump2 = linspace(0,pump_power,20);
eff_laser2 = max_slope_eff_inc*(eff_pump2-threshold_power_inc);
eff_laser2(eff_laser2 < 0) = 0;
figure
plot(eff_pump,eff_laser,'k',0,0,'k',0,0,'k',...
    eff_pump2,eff_laser2,'ok','markersize',8')
xlabel('Pump power (incident) [W]')
ylabel('Output power [W]')
legend(['Threshold: ' num2str(threshold_power_inc) ' W'],...
    ['Slope efficiency: ' num2str(max_slope_eff_inc*100) '%'],...
    ['Max output power: ' num2str(max(eff_laser)) ' W'],...
    'Location','nw')
heat_dep = pump_power*pump_abs - max(eff_laser);

%%%%%%%%%%%%%%%%%%%%%%%%%%%%%%%%%%%%%%%%%%%%%%%%%%%%%%%%%%%%
%%% Laser zigzag path
figure(1)
beam_1.path = 0;

n_clad_1 = n_silica(wave_1); %Refractive index of cladding outside doped
crit_angle = asind(n_silica(wave_1)/n_doped);
crit_angle2 = asind(n_air/n_YAlO3_1);

% Plot the paths over the pump beams
for kk = -1:2:1
    beam_1.exit_angle = asind(n_YAlO3_1/n_air*sind(AoI_back));
    beam_1.exit_width = slab.width_full*cosd(beam_1.exit_angle);
    if (show_plot(2) == 0); break; end
    if AoI_back >= (90-crit_angle)  % if beam loses TIR on sides
        x = linspace(0.7*slab.length,2*slab.length,500);
        beam_1.path = kk*tand(AoI_back)*(x-slab.length)+slab.width_full/2;
        plot(x,beam_1.path,'--b')
        REPORT = 'Laser invalid: Breaks TIR on sides';
    elseif AoI_back > crit_angle2  % if beam is TIR on end faces
        x = linspace(0,slab.length,2000);
        beam_1.path_orig = slab.width_full/2 + tand(kk*AoI_back)*x;
        beam_1.path = beam_guiding(x,beam_1.path_orig,slab.width_full,...
            [0 slab.length],bounces);
        plot(x,beam_1.path,'--b')
        REPORT = 'Laser invalid: Beam trapped inside slab';
    else
        x = linspace(0,slab.length,2000);
        beam_1.path_orig = slab.width_full/2 + tand(kk*AoI_back)*x;
        beam_1.path = beam_guiding(x,beam_1.path_orig,slab.width_full,...
            [0 slab.length],bounces);

        x2 = linspace(slab.length,2*slab.length,100);
        exit_path = slab.width_full/2 + tand(kk*beam_1.exit_angle)*(x2-x2(1));

        x = [x,x2];
        beam_1.path = [beam_1.path,exit_path];
        plot(x,beam_1.path,'r','LineWidth',2)

        % Show aperturing due to end face - Rays - shading
        % Beams on left input
        patch([0,beam_1.edge_1(1),beam_1.edge_r(1),0],...
            [slab.width_full/2+kk*beam_1.edge_diff,(kk+1)/2*slab.width_full,...
            (kk+1)/2*slab.width_full,slab.width_full/2-kk*beam_1.edge_diff],...
            'r','EdgeColor','none','FaceAlpha',0.3);
        % Beams along the slab
        for jj = 2:bounces
            patch([beam_1.edge_1(jj-1),beam_1.edge_1(jj),...
                beam_1.edge_r(jj),beam_1.edge_r(jj-1)],...
                slab.width_full*[(-kk+1)/2,(kk+1)/2,(kk+1)/2,(-kk+1)/2],...
                'r','EdgeColor','none','FaceAlpha',0.3);
        end
        % Output beams
```

```
        patch(slab.length-[0,beam_l.edge_l(1),beam_l.edge_r(1),0],...
            [slab.width_full/2+kk*beam_l.edge_diff,(kk+1)/2*slab.width_full,...
            (kk+1)/2*slab.width_full,slab.width_full/2-kk*beam_l.edge_diff],...
            'r','EdgeColor','none','FaceAlpha',0.3);

        if (min(beam_l.path) < 0)
            beam_l.path = slab.width_full-beam_l.path;
        end
        patch([slab.length,max(x),max(x),slab.length],...
            [(kk+1)/2*slab.width_full,...
            (-
kk+1)/2*slab.width_full+kk*(max(beam_l.path)+beam_l.edge_diff),...
            (-kk+1)/2*slab.width_full+kk*(max(beam_l.path)-
beam_l.edge_diff),...
            (-kk+1)/2*slab.width_full],...
            'r','EdgeColor','none','FaceAlpha',0.3);
    end
end

% Drawing slab around beams
legend('Pump rays','Laser path','location','NW')
%'Pump ray (breaks TIR)','Invalid laser path (breaks TIR)'

rectangle('Position',[0,0,slab.length,slab.width_full]);
rectangle('Position',[0,slab.width_full-slab.width_doped1,...
    slab.length,slab.width_doped1+1e-20],'FaceColor','y');
rectangle('Position',[0,0,slab.length,slab.width_doped2+1e-20],...
    'FaceColor','y');
xlim([-0.1*slab.length 1.2*slab.length])
daspect([1 1 1])
pbaspect([1 0.65 1])
xlabel('x-position [m]')
ylabel('y-position [m]')

%%%%%%%%%%%%%%%%%%%%%%%%%%%%%%%%%%%%%%%%%%%%%%%%%%%%%%%%%%%%%%%%%%%%%%%
%%% Exiting pump beam
figure(1)

% Assuming well-mixed pump, out angle = max(in angle)
beam_p.out_FWHM_max = abs(beam_p.tilt) + beam_p.FWHM_div/2;
beam_p.out_FWHM_min = -beam_p.out_FWHM_max;
x = linspace(slab.length,slab.length+30e-3,1000);
% % x-location of intersect point between inner edge of laser beam and outer
% % edge of pump beam
% out_beams.intersect = slab.length + slab.width_full/...
%     (tand(beam_l.exit_angle)-tand(beam_p.out_FWHM_max));
%
% out_beams.sep_dist = tand(beam_l.exit_angle-beam_p.out_FWHM_max)/...
%     cosd(beam_l.exit_angle)*(x-out_beams.intersect);
% figure
% plot(x-slab.length,out_beams.sep_dist,'k')
% xlabel('Distance from end of slab [m]')
% ylabel('Clearance between laser and pump beam [m]')
% grid on

if (show_plot(1) == 1)
    figure(1)
    beam_p.path1 = slab.width_full+(x-slab.length)*tand(beam_p.out_FWHM_max);
    beam_p.path2 = (x-slab.length)*tand(beam_p.out_FWHM_min);
    plot(x,beam_p.path1,'g',x,beam_p.path2,'g','LineWidth',1)
    patch([slab.length,max(x),max(x),slab.length],...
            [slab.width_full,max(beam_p.path1),...
            min(beam_p.path2),0],...
            'g','EdgeColor','none','FaceAlpha',0.3);
end
```

```
%%%%%%%%%%%%%%%%%%%%%%%%%%%%%%%%%%%%%%%%%%%%%%%%%%%%%%%%%%%%%%%%
%%% Pump reflector mirror location
p_refl_height = 35e-3;  % Height of pump reflector
p_refl_R = 30e-3;       % Radius of curvature
% start_x = slab.length-p_refl_R;
% start_y = slab.width_full/2-p_refl_R;
% rectangle('Position',[start_x,start_y,2*p_refl_R,2*p_refl_R],...
%     'Curvature',[1,1]); % Guide circle
theta = asind(p_refl_height/(2*p_refl_R))*(-1:0.01:1);
x_arc = p_refl_R*cosd(theta)+slab.length;
y_arc = p_refl_R*sind(theta)+slab.width_full/2;
plot(x_arc,y_arc,'o');  % Arc representing mirror surface

mirrors.size = 25.4e-3; % Mirrors size
mirrors.dist = 50e-3;   % Mirrors distance to slab
xx = mirrors.size/2*cosd(beam_1.exit_angle);
yy = mirrors.size/2*sind(beam_1.exit_angle);
x_loc = slab.length + mirrors.dist*cosd(beam_1.exit_angle);
y_loc = slab.width_full/2 + mirrors.dist*sind(beam_1.exit_angle);
line([x_loc-xx x_loc+xx],[y_loc+yy,y_loc-yy],'linewidth',2);
line([x_loc-xx x_loc+xx],[slab.width_full-(y_loc+yy),...
    slab.width_full-(y_loc-yy)],'linewidth',2);

%%%%%%%%%%%%%%%%%%%%%%%%%%%%%%%%%%%%%%%%%%%%%%%%%%%%%%%%%%%%%%%%
%%% Run report (put all important data into one variable array)
if (exist('REPORT','var') == 0)
    REPORT.slab_dimensions = 1e3*[slab.length+length_corr,...
        slab.width_full,slab.height];
    REPORT.exit_angle = beam_1.exit_angle;
    REPORT.exit_beam_width = 1e3*beam_1.exit_width;
    REPORT.inversion_fraction = inversion;
    REPORT.pump_absorption = pump_abs;
    REPORT.total_RT_losses = total_loss;
    REPORT.AoI_end__crit_angle = [AoI_back,crit_angle2];
    REPORT.AoI_side__crit_angle = [AoI_doped,crit_angle];
    REPORT.unextracted_gain_vol_fraction = unextr.fract;
    REPORT.threshold_incident = threshold_power_inc;
    REPORT.available_pump_power = avail_pump_power;
    REPORT.slope_efficiency = max_slope_eff_inc;
    REPORT.theoretical_max_laser_power = max(eff_laser);
    REPORT.heat_deposited__fracture_limit = [heat_dep, fract_limit];
end
clear a b x x2 exit_path show_plot jj kk eff_laser2 eff_pump2 intersect
clear start_x start_y theta x_arc y_arc

REPORT
```

C.1.2.2 ThOR_pump_abs.m

```
%%%%%%%%%%%%%%%%%%%%%%%%%%%%%%%%
% Pump absorption of ThOR slab %
%%%%%%%%%%%%%%%%%%%%%%%%%%%%%%%%

% Used in Disk_Slab_modelling.m for calculating the total pump absorption
% when end-pumped. Uses ray-propagation method, where the pump beam is
% split into a series of emitters, each with rays. Propagates each ray down
% the slab, and calculates the total distance each ray has travelled
% through the doped region. Calculates the absorption of each ray, then
% averages the final intensities to give the total absorption.

% Input:
%     slab = Slab properties (uses slab dimensions)
%     wave_p = Pump wavelength [m]
%     alpha = Absorption coefficient [cm^-1]
%     plot_onoff = Whether to plot ray paths
% Output:
%     absorbed = Total pump absorption
```

```
function absorbed = ThOR_pump_abs(slab,beam,wave_p,alpha,plot_onoff)

% ThOR slab parameters
width_doped1 = slab.width_doped1;    % Width of top doped region [m]
width_doped2 = slab.width_doped2;    % Width of bottom doped region [m]
width_undoped = slab.width_undoped; % Width of undoped region [m]
length = slab.length;                % Length of slab [m]
width_full = width_doped1 + width_doped2 + width_undoped; % Full width of slab
[m]

% Beam parameters
FWHM_max = beam.in_FWHM_max;        % FWHM divergence max angle [deg]
FWHM_min = beam.in_FWHM_min;        % FWHM divergence min angle [deg]
spot_size = beam.in_spot_size;      % Pump spot size [m]

[a,n_b,b] = n_YAlO(wave_p);
n_YAlO3 = n_b;                    %Refractive index of YAlO
n_clad = n_silica(wave_p);    %Refractive index of cladding outside doped

crit_angle = (asin(n_clad/n_YAlO3))*180/pi;

%Analysis parameters
num_rays = 9;           %Number of rays
num_emitters = 10;       %Number of emitters

beam_angles = linspace(FWHM_min,FWHM_max,num_emitters);

total_bounces = zeros(num_emitters,num_rays);
prop_doped_dist = zeros(num_emitters,num_rays);
beam_intensity = zeros(num_emitters,num_rays);
beam_angle_d = zeros(num_emitters,num_rays);
beam_loc = zeros(num_emitters,num_rays);

for i = 1:num_emitters
    for j = 1:num_rays
        %Beam angle from horizontal [deg], upwards = +ve
        beam_angle_d(i,j) = beam_angles(j);
        if (num_emitters > 1)
            beam_loc(i,j) = (width_full/2)+((i-1)/(num_emitters-1)-0.5)...
                *spot_size;          %Beam displacement from top edge [mm]
        else
            beam_loc(i,j) = width_full/2;
        end
        beam_intensity(i,j) = 1;       %Beam intensity
        total_bounces(i,j) = 0;
        prop_doped_dist(i,j) = 0;
    end
end
if max(max(beam_angle_d >= (90-crit_angle)))  %If any beams breaks TIR
    disp('!!! WARNING: Some of the pump rays will break TIR !!!')
    disp(['Max beam angle: ' num2str(max(max(beam_angle_d))) ' degrees;'])
    disp(['Critical angle: ' num2str(90-crit_angle) ' degrees;'])
end

%Creating plot for all beams
x = linspace(0,length,1000);
figure(1)
plot(0,0,'g',0,0,'r',0,0,'b',0,0,'--b')
hold on

%Individual ray analysis
for i = 1:num_emitters
    %If any rays are propagating at 90 degrees or greater from normal
    if (max(max(abs(beam_angle_d) >= 90)) == 1)
        disp(['ERROR: Some of the rays are propagating at >90 degrees'...
```

```
        'from surface. Calculation Aborted'])
    break
end
for j = 1:num_rays
    prop_doped = 0;     %distance propagated through doped region
    beam_exited = 0;    % = 1 if beam has left the slab
    bounces = 0;        %logging how many bounces the beam makes
    loc_y = beam_loc(i,j);
    angle = beam_angle_d(i,j)*pi/180;

    if (angle < 0)                  %invert if beam points downwards
        angle = -1*angle;
        loc_y = 2*width_full - loc_y;
    elseif (angle == 0)         %special case
        prop_doped = 0;
        if ((loc_y > width_doped2+width_undoped)||(loc_y < width_doped2))
            prop_doped = length;
        end
        beam_exited = 1;
    end
    total_y = length*tan(angle);

    %Beam propagation through ThOR slab
    while (beam_exited ~= 1)
        if (loc_y <= width_doped2)       % in lower doped region
            if (total_y < width_doped2-loc_y)
                %beam leaves while in this region
                prop_doped = prop_doped + total_y;
                beam_exited = 1;break
            else     %accumulate propagated distance through region
                total_y = total_y - (width_doped2-loc_y);
                prop_doped = prop_doped + width_doped2-loc_y;
                loc_y = width_doped2;
            end
        end
        if (loc_y <= width_doped2+width_undoped) % in undoped region
            if (total_y < width_doped2+width_undoped-loc_y)
                %beam leaves while in this region
                beam_exited = 1;break
            else
                total_y = total_y - (width_doped2+width_undoped-loc_y);
                loc_y = width_doped2+width_undoped;
            end
        end
        if (loc_y <= width_full+width_doped1)  % in upper doped region
            if (total_y < width_full-loc_y)
                %beam leaves while in this region
                prop_doped = prop_doped + total_y;
                beam_exited = 1;break
            elseif (total_y < width_full+width_doped1-loc_y)
                %beam leaves while in this region after bounce
                prop_doped = prop_doped + total_y;
                bounces = bounces + 1;
                beam_exited = 1;break
            else     %accumulate propagated distance through region
                total_y = total_y - (width_full+width_doped1-loc_y);
                prop_doped = prop_doped + width_full+width_doped1-loc_y;
                bounces = bounces + 1;
                loc_y = width_full+width_doped1;
            end
        end
        if (loc_y <= width_full+width_doped1+width_undoped)
            % back in undoped region
            if (total_y < width_full+width_doped1+width_undoped-loc_y)
                %beam leaves while in this region
                beam_exited = 1;break
            else
                total_y = total_y - ...
```

```
                        (width_full+width_doped1+width_undoped-loc_y);
                    loc_y = width_full+width_doped1+width_undoped;
                end
            end
            if (loc_y <= 2*width_full)       % back in lower doped region
                if (total_y < 2*width_full-loc_y)
                    %beam leaves while in this region
                    prop_doped = prop_doped + total_y;
                    beam_exited = 1;break
                else     %accumulate propagated distance through region
                    total_y = total_y - (2*width_full-loc_y);
                    prop_doped = prop_doped + 2*width_full-loc_y;
                    bounces = bounces + 1;
                    loc_y = 0;  %one round trip, so reset loc_y.
                end
            end
        end

        if (angle ~= 0)
            prop_doped = prop_doped / sin(angle);
        end
        total_bounces(i,j) = bounces;
        prop_doped_dist(i,j) = prop_doped;
        %calculate absorbed power (*100 due to cm -> m conversion)
        beam_intensity(i,j) = exp(-alpha*prop_doped*100);

        %formulate the beam path
        if (plot_onoff == 1)
            beam_path = beam_loc(i,j) + tand(beam_angle_d(i,j))*x;
            if abs(beam_angle_d(i,j)) >= (90-crit_angle)
                plot(x,beam_path,'b')
            else
                beam_path_orig = beam_loc(i,j) + tand(beam_angle_d(i,j))*x;
                beam_path = beam_guiding(x,beam_path_orig,width_full,...
                    [0 length],bounces);
                plot(x,beam_path,'g')
            end
        end
    end
end

% Final absorption calculation
beam_intensity = beam_intensity.^2;     %Assuming beams return by same path
transmitted = mean(mean(beam_intensity));
absorbed = 1 - transmitted;
```

C.1.2.3 Tm_YAlO_Boltzmann.m

```
%%%%%%%%%%%%%%%%%%%%%%%%%%%%%%%%%%%%%%%%%%%%%%%%%%%%%%%%%%%%%%%%
% Boltzmann distribution for transparency calculation %
%%%%%%%%%%%%%%%%%%%%%%%%%%%%%%%%%%%%%%%%%%%%%%%%%%%%%%%%%%%%%%%%

% Used in Disk_Slab_modelling.m for calculating the power required to reach
% transparency.

% Input:
%     Temp = Temperature [K]
% Output:
%     ions_req = Fraction of ions required to be excited for transparency

% Reference: M. Eichhorn, "Quasi-three-level solid-state lasers in the near
% and mid infrared based on trivalent rare earth ions," Applied Physics B
% 93 (2008)

function ions_req = Tm_YAlO_Boltzmann(Temp)
```

```
% The sub-levels of the three energy levels of Tm:YAlO3
E_levels2 = [0,3,65,144,210,237,271,282,313,440,574,628,628,... % 3H6
    5622,5627,5716,5722,5819,5843,5935,5965,...                 % 3H5
    12515,12574,12667,12742,12783,12872,12885,12910,12950];     % 3H4

suppr_plot = 1;     % Suppress plotting of boltzmann distribution

k = 1.38e-23;       % Boltzmann constant
T = Temp;           % Temperature

%Energy conversion from [cm^-1] to [J]
energies_upper = (E_levels2(14:21)-E_levels2(14))*1.9851e-23;
pop_upper = exp(-energies_upper/(k*T));  %Boltzmann distribution (upper state)
Zg_upper = sum(pop_upper);
pop_upper = pop_upper/Zg_upper;    %Normalisation

%Energy conversion from [cm^-1] to [J]
energies_lower = E_levels2(1:12)*1.9851e-23;
pop_lower = exp(-energies_lower/(k*T));  %Boltzmann distribution (ground
state)
pop_lower(12) = pop_lower(12)*2;         %Degeneracy
Zg_lower = sum(pop_lower);
pop_lower = pop_lower/Zg_lower;    %Normalisation

% sub-levels that contribute to ~1940nm emission/absorption
f_upper = sum(pop_upper(1:4));
f_lower = sum(pop_lower(10:11));

% fraction of ions required to be excited for transparency
ions_req = f_lower/(f_upper+f_lower);

% Graphics-related
temp_energy = -100:5:700;   % Energy plotting range
boltz = exp(-(temp_energy*1.9851e-23/(k*T)));   % Boltzmann (for plotting)
popn = @(energy,width,color) line([0,width],[energy,energy],...
    'Color',color,'LineWidth',3);

% Plot the graphs (if not suppressed)
if suppr_plot == 0
    figure
    subplot(2,1,1)
    plot(1,1,'r','LineWidth',3)
    hold on
    % Plot sub-levels of upper level
    plot(boltz/Zg_upper,temp_energy+5622,':')
    for ii = 14:17
        popn(E_levels2(ii),pop_upper(ii-13),'r')
    end
    for ii = 18:21
        popn(E_levels2(ii),pop_upper(ii-13),'k')
    end
    legend(['f_{upper} = ' num2str(f_upper)])
    axis([0,0.25,5600,6000])
    ylabel('Energy [cm^{-1}]')
    xlabel('Normalised population')
    title(['Temperature: ' num2str(T) ' K'])

    subplot(2,1,2)
    plot(1,1,'r','LineWidth',3)
    hold on
    % Plot sub-levels of lower level
    plot(boltz/Zg_lower,temp_energy,':')
    for ii = [10,11]
        popn(E_levels2(ii),pop_lower(ii),'r')
    end
    for ii = [1:9,12]
```

```
        popn(E_levels2(ii),pop_lower(ii),'k')
    end
    legend(['f_{lower} = ' num2str(f_lower)])
    axis([0,0.2,0,700])
    ylabel('Energy [cm^{-1}]')
    xlabel('Normalised population')
end
```

C.1.2.4 doped_undoped_interface.m

```
%%%%%%%%%%%%%%%%%%%%%%%%%%%%%%%%%%%%%%%%%%%%%%%
% Refractive index change due to dopants %
%%%%%%%%%%%%%%%%%%%%%%%%%%%%%%%%%%%%%%%%%%%%%%%

% Used in Disk_Slab_modelling.m for calculating the refractive index
% increase caused by doping Tm ions into the YAlO3 crystal (Tm replaces Y).
% Calculates the reflection losses to the primary beam and angle of
% incidence change at the bond interface.

% Input:
%     AoI_back = Angle of incidence at the ends of the slab [deg]
%     Tm = Thulium properties (uses Tm.conc)
% Output:
%     AoI_doped = Angle of incidence at the doped side [deg]
%     R_s = Reflection coefficient of the interface
%     YAlO = YAlO properties (molar masses and densities)

% Reference: A.O. Matkovskii et al., "Growth and properties of YAlO3:Tm
% single crystals for 2-mm laser operation" Journal of Crystal Growth
% 241 (2002) 455-462

function [AoI_doped,R_s,YAlO,n2] = doped_undoped_interface(AoI_back,Tm,wave)

Av_num = 6.02e23;   % Avagadro's number
doping = Tm.conc;   % doping [atom%]

% Molar masses of each element [g/mol]
mm_Y = 88.90585;
mm_Al = 26.9815386;
mm_O = 15.9994;
mm_Tm = 168.93421;

% Molar mass of cell [g/mol]
YAlO.YAlO_molar_mass = mm_Y+mm_Al+3*mm_O;
YAlO.TmYAlO_molar_mass = doping*mm_Tm + (1-doping)*mm_Y+mm_Al+3*mm_O;

% Lattice constants [cm]
TmYAlO3.a = mean([5.17688 5.17673])*1e-8;
TmYAlO3.b = mean([5.32768 5.32767])*1e-8;
TmYAlO3.c = mean([7.3675 7.3675])*1e-8;
TmYAlO3.Vol = TmYAlO3.a*TmYAlO3.b*TmYAlO3.c;  % Cell volume [cm^3]

YAlO3.a = mean([5.179 5.180 5.180])*1e-8;
YAlO3.b = mean([5.329 5.328 5.330])*1e-8;
YAlO3.c = mean([7.370 7.370 7.375])*1e-8;
YAlO3.Vol = YAlO3.a*YAlO3.b*YAlO3.c;           % Cell volume [cm^3]

% Densities [g/cm^3]
% Factor of 4 is due to 4 x "Y+Al+O3" in each cell; obtained from
% trail-and-error match to density of YAlO3 in literature
YAlO.TmYAlO_density = 4*YAlO.TmYAlO_molar_mass/(Av_num*TmYAlO3.Vol);
YAlO.YAlO_density = 4*YAlO.YAlO_molar_mass/(Av_num*YAlO3.Vol);

increased_frac = (YAlO.TmYAlO_density - YAlO.YAlO_density)/YAlO.YAlO_density;
YAlO.n_doped_inc_frac = increased_frac; % fraction of increase in n due to
doping
```

```
[a,b,n1] = n_YAlO(wave);     % Refractive index of YAlO3 at laser wavelength
n2 = (1+increased_frac)*(n1-1) + 1; % Refractive index of Tm:YAlO3 at laser
wavelength

AoI = 90-AoI_back;   % Angle of incidence at undoped side [deg]
AoI_doped = asind(n1/n2*sind(AoI)); % Angle if incidence at doped side [deg]

% Reflection coefficient for s-polarised light
rs = (n1*cosd(AoI)-n2*sqrt(1-((n1/n2)*sind(AoI)).^2))./...
    (n1*cosd(AoI)+n2*sqrt(1-((n1/n2)*sind(AoI)).^2));
R_s = rs.^2;
```

C.1.2.5 beam_guiding.m

```
%%%%%%%%%%%%%%%%%%%%%%%%%%%%%%%%%%%%%%%%%%%%%%%%%%%%%%%%%%%%%%%%%%%%%%%%
% Total internal reflection of beam inside parallel waveguide %
%%%%%%%%%%%%%%%%%%%%%%%%%%%%%%%%%%%%%%%%%%%%%%%%%%%%%%%%%%%%%%%%%%%%%%%%

% Confines a beam to a parallel waveguide by inverting the direction of the
% beam when it is incident on the sides. Can define the length of the
% waveguide so that the beam is unaltered before and after the waveguide.
% Can be used for general functions of x.

% Input:
%     x = The position of the beam along the length of the waveguide
%     beam_path = original beam path that is to be altered
%     width = width of the waveguide
%     guide_region = region (along x) in which to alter the beam path
%     bounces = upper limit of the number of bounces [default: 10]

% Output:
%     beam_path = altered beam path

function beam_path = beam_guiding(x,beam_path,width,guide_region,bounces)

% defining guide_region and bounces are optional.
% Default: Full length of x and 10 bounces
if nargin == 3
    guide_region = [min(x) max(x)];
    bounces = 10;
elseif nargin == 4
    bounces = 10;
end
% Loop up to the maximum number of bounces
for ii = 1:bounces
    jj = find(beam_path > width);   % Find when the beam exceeding upper bound
    jj(x(jj) < guide_region(1)) = [];   % Ignore if before the guide region
    beam_mod = beam_path(jj);
    if (x(jj(find(beam_mod > width,1,'first'))) > guide_region(2))
        % If the first instance is after the guide region, exit loop
        break;
    end
    % Invert the direction of the beam
    for aa = jj
        beam_path(aa) = 2*width - beam_path(aa);
    end
    jj = find(beam_path < 0);   % Find when the beam exceeds the lower bound
    jj(x(jj) < guide_region(1)) = [];   % Ignore if before the guide region
    beam_mod = beam_path(jj);
    if (x(jj(find(beam_mod < 0,1,'first'))) > guide_region(2))
        % If the first instance is after the guide region, exit loop
        break;
    end
    % Invert the direction of the beam
    for aa = jj
        beam_path(aa) = -beam_path(aa);
    end
```

```
end
```

C.1.2.6 n_YAlO.m

```
%%%%%%%%%%%%%%%%%%%%%%%%%%%%%%
% Refractive index of YAlO3 %
%%%%%%%%%%%%%%%%%%%%%%%%%%%%%%

% Returns the refractive index of each axis of YAlO3 at one or more
% wavelength(s)

% Input:
%     wavelength = Wavelength(s) of incident light [m]
% Output:
%     n_a = Refractive index of the a-axis of YAlO3 at incident wavelength
%     n_b = Refractive index of the b-axis of YAlO3 at incident wavelength
%     n_c = Refractive index of the c-axis of YAlO3 at incident wavelength

% Reference:
% http://www.mennerat.fr/gab/References/DatabaseLasers/tables/sellout.htm

function [n_a, n_b, n_c] = n_YAlO(wavelength)

lambda = wavelength * 1e6; %coefficients in microns

% Sellmeier coefficients
B_a = 2.6196;
B_b = 2.67171;
B_c = 2.70381;
C_a = 0.012338;
C_b = 0.012605;
C_c = 0.012903;

% Refractive indices
n_a = sqrt(1 + (B_a*lambda.^2)./(lambda.^2 - C_a));
n_b = sqrt(1 + (B_b*lambda.^2)./(lambda.^2 - C_b));
n_c = sqrt(1 + (B_c*lambda.^2)./(lambda.^2 - C_c));
```

C.1.2.7 n_silica.m

```
%%%%%%%%%%%%%%%%%%%%%%%%%%%%%%%%%%%%%%
% Refractive index of Silica (SiO2) %
%%%%%%%%%%%%%%%%%%%%%%%%%%%%%%%%%%%%%%

% Returns the refractive index of silica at one or more wavelength(s)

% Input:
%     wavelength = Wavelength(s) of incident light [m]
% Output:
%     n = Refractive index of silica at incident wavelength

% Reference: http://refractiveindex.info/?group=CRYSTALS&material=SiO2

function [n] = n_silica(wavelength)

lambda = wavelength * 1e6; %coefficients in microns

% Sellmeier coefficients
A = 1.28604141;
B = 1.07044083;
C = 1.00585997e-2;
D = 1.10202242;

% Refractive index
n = sqrt(A + B*lambda.^2./(lambda.^2-C) + D*lambda.^2./(lambda.^2-100));
```

C.1.3 Gaussian beam propagation

C.1.3.1 Gaussian_beams.m

```
% Gaussian_beams.m version 1.3 (10/10/2012)
% Written by Ka Wu

% Driver program for Gaussian beam propagation. Define each component of
% the optic system, then propagates a Gaussian beam through the system.
% Finds waist locations and widths, and can calculate eigenmode (cavity
% mode) of the system.
% See readme.rtf file for details regarding how to use.
% Note: requires the following .m files to run properly:
    % eigenmode.m, propagate.m, gauss_addgraphics.m
    % Components:
    % curv_surf.m, free_space.m, GRIN_lens.m, mirror.m, thick_lens.m,
    % thin_lens.m, user_defined.m

clear all
close all

wavelength = 1.94e-6;   %wavelength of light [m]
%init_w0 = 0.5e-3;   %initial beam waist size [m] at d = 0
%init_w0_2 = 0.5e-3;   %initial beam waist size [m] in secondary axis
plot_units = 'um';  %Units for beam width. use 'm', 'cm', 'mm' or 'um'
fill_factor = 'on';    %Calculate fill-factor for slabs if 'on'

%defining each component (check readme.rtf or each .m file for details)
mirror1 = mirror(0.2);
space1 = free_space(10e-3);
in_face = curv_surf(1,1.93,Inf,0,63.73);
lens2 = GRIN_lens(0.03325,1.93,2000,-25);
out_face = curv_surf(1.93,1,Inf,0,27.27);
space2 = free_space(5e-3);
lens1 = thin_lens(0.1);
space3 = free_space(9e-3);
mirror2 = mirror;

%defining the system of components in sequence
system = {mirror1,space1,in_face,lens2,out_face,space2,...
    lens1,space3,mirror2};

%init_q = 1i*pi*init_w0^2/wavelength; %define initial q from initial waist
%init_q2 = 1i*pi*init_w0_2^2/wavelength; %initial q for secondary axis
[init_q,stab_v] = eigenmode(system); %look for eigenmodes of the system
[init_q2,stab_h] = eigenmode(system,2);  %look for eigenmodes of the system
                                %in secondary axis


%%%%%%%%%%%%%%%%%%%%%%%%%%%%%%%%%%%%%%%%%%%%%%%%%%%%%%%%%%%%%%%%%%%%%%%%%%%
scaling = 1;
if strcmp(plot_units,'cm'); scaling = 100;
elseif strcmp(plot_units,'mm'); scaling = 1000;
elseif strcmp(plot_units,'um'); scaling = 1e6;
end;

%call propagate.m for primary axis and calculate R and w
[q,d,waist_loc,waist_size,graphics] =...
    propagate(wavelength,init_q,system,1);
q_inv = 1./q;
R_system = 1./real(q_inv);  %radii of curvature of beam
w_system = sqrt(-wavelength./(pi*imag(q_inv)))*scaling; %beam widths

%call propagate.m for secondary axis and calculate R and w
[q2,d2,waist_loc2,waist_size2,graphics2] =...
```

```
    propagate(wavelength,init_q2,system,2);
q_inv2 = 1./q2;
R_system2 = 1./real(q_inv2);  %radii of curvature of beam
w_system2 = sqrt(-wavelength./(pi*imag(q_inv2)))*scaling;   %beam widths

ax_label = 'Length [m]';
if isequal(fill_factor, 'on')
    %Determine the fill factor within the GRIN lens (i.e. laser slab)
    startloc = graphics.startloc;
    endloc = graphics.endloc;
    stepsize = d(startloc+5)-d(startloc+4);
    %integrate to find total area swept out by beam
    areainbeam_vert = sum(real(w_system(startloc:endloc-1)))*stepsize;
    areainbeam_horiz = sum(real(w_system2(startloc:endloc-1)))*stepsize;
    %total pumped area, assuming rectangular pumped region
    pumped_area_vert = (d(endloc)-d(startloc))*...
        max(real(w_system(startloc:endloc)));
    pumped_area_horiz = (d(endloc)-d(startloc))*...
        max(real(w_system2(startloc:endloc)));
    %fill factor of the pumped region by laser beam (higher order modes have
    %widths proportional to that of fundamental Gaussian)
    eff_vert = areainbeam_vert/pumped_area_vert;
    eff_horiz = areainbeam_horiz/pumped_area_horiz;
    ax_label = {'Length [m]',...
        ['Fill factor: ' num2str(eff_horiz) ' (horiz) '...
    num2str(eff_vert) ' (vert), total '  num2str(eff_vert*eff_horiz)]};
end

%plot beam profile(s)
figure(1)
plot(d,w_system,d,-w_system,'color','b')    %vertical beam
hold on
plot(d2,w_system2,d2,-w_system2,'color','m')    %horizontal beam
title('Beam profile of system', 'FontWeight','bold')
xlabel(ax_label)
if strcmp(plot_units,'um'); plot_units = '\mum'; end;
ylabel(['Beam width [' plot_units ']'])

%axes limits
ax_max = max(max(real(w_system)),max(real(w_system2)))*1.2;
axis ([-max(d)*0.05 max(d)*1.05 -ax_max*1.05 ax_max*1.05])
%add component locations and waist locations to graph
gauss_addgraphics(ax_max,graphics,waist_loc,waist_size*scaling,...
    waist_loc2,waist_size2*scaling)
hold off
```

C.1.3.2 eigenmode.m

```
function [init_q,stability] = eigenmode(system,axis)
% For use in Gaussian_beams.m.
% Calculates the eigenmode (self-consistent mode) of the system, i.e.
% cavity modes. Multiplies the ABCD matrices of each component in system
% (both forward and backwards direction) and finds the self-consistent
% solution. Returns an initial q = 0 if no mode is found (unstable).
% For systems that differ in the two axes, define axis variable - 1 for
% primary (uses the .mat matrix of each component), 2 for secondary (uses
% the .mat2 matrix of each component if defined, else assumes the component
% is identical in both and uses .mat matrix).
% Also returns the 'g' parameter (stability of the cavity)

ABCD = [1,0;0,1];
if nargin == 1;axis = 1;end
for i = 1:length(system) %forward propagation through system
    if strcmp(system{i}.type,'thick lens')
        %special provisions required for thick lens due to asymetry.
        surf1 = curv_surf(1,system{i}.n_inner,system{i}.R1);
        inside_lens = free_space(system{i}.length,system{i}.n_inner);
```

```
        surf2 = curv_surf(system{i}.n_inner,1,system{i}.R2);
        ABCD = surf2.mat*inside_lens.mat*surf1.mat*ABCD;
    else
        %component ordering begins from the right
        if (axis == 2)&&(isfield(system{i}, 'mat2'))
            ABCD = system{i}.mat2*ABCD;
        else
            ABCD = system{i}.mat*ABCD;
        end
    end
end
for i = length(system):-1:1  %backward propagation through system
    if strcmp(system{i}.type,'thick lens')
        %special provisions required for thick lens due to asymetry.
        surf2 = curv_surf(1,system{i}.n_inner,-system{i}.R2);
        inside_lens = free_space(system{i}.length,system{i}.n_inner);
        surf1 = curv_surf(system{i}.n_inner,1,-system{i}.R1);
        ABCD = surf1.mat*inside_lens.mat*surf2.mat*ABCD;
    elseif strcmp(system{i}.type,'curved surface')
        %special provisions required for curved surfaces due to asymetry.
        R = -system{i}.RoC;
        n1 = system{i}.n_i;
        n0 = system{i}.n_f;
        AoI1 = system{i}.AoI1_deg;
        AoR1 = asind(n1/n0*sind(AoI1));
        AoI2 = system{i}.AoI2_deg;
        AoR2 = asind(n1/n0*sind(AoI2));
        surf = curv_surf(n0,n1,R,AoR1,AoR2);
        if (axis == 2)&&(isfield(system{i}, 'mat2'))
            ABCD = surf.mat2*ABCD;
        else
            ABCD = surf.mat*ABCD;
        end
    elseif strcmp(system{i}.type,'mirror')
        %only single "pass" through mirrors - skip for backward propagation
    else
        if (axis == 2)&&(isfield(system{i}, 'mat2'))
            ABCD = system{i}.mat2*ABCD;
        else
            ABCD = system{i}.mat*ABCD;
        end
    end
end

A = ABCD(1,1);
B = ABCD(1,2);
C = ABCD(2,1);
D = ABCD(2,2);
% finding real and imaginary part of initial q value
re_part = (D-A)/(2*B);
im_part = sqrt(4-(A+D)^2)/(2*B);
% stability parameter - cos(theta) (see Kogelnik and Li)
stability = 0.5*(A+D);

if isreal(im_part)
    if im_part > 0
        im_part = -im_part; %if the +ve solution is +ve, use -ve solution
    end
    init_q = 1/(re_part + 1i*im_part);
else %no solution (unstable resonator)
    init_q = 0;
end
```

C.1.3.3 propagate.m

```
function [q,d,waist_loc,waist_size,graphics] =...
    propagate(wavelength,init_q,system,axis)
% For use in Gaussian_beams.m.
```

```
% Analyses the system, going through the components one by one to calculate
% the value of q throughout the system, as well as the waist size and
% locations. Initial beam q defined by init_q. All components of non-zero
% length (free space, GRIN lenses, thick lenses) are divided into segments
% and q is obtained for each segment. Other components are assumed to have
% zero length. Waist locations are determined when inside free space only.
% Returns q, d, waist locations and size, and locations of components (used
% in gauss_addgraphics.m)

q = init_q; %initial beam q parameter. Elements are appended to the end of
            %q as the beam is propagated through the system.
d = 0;  %propagation distance vector. Elements are appended to the end of
        %d as the beam is propagated through the system.
graphics.stops = 0; %locations of each non-zero-length component
segm = 500;  %number of segments for free space and GRIN lenses.
                    %(divided by 5 for thick lens due to smaller lengths)
graphics.x_b = [0;0;0;0];   %location of any grey boxes (n > 1 regions)
waist_loc = [];
waist_size = [];
if nargin == 3;axis = 1;end %assumes primary axis if none defined

%propagate beam (calculate q and d) for each component in the system
for i = 1:length(system)
    %dividing components of non-zero length into segments
    if strcmp(system{i}.type,'free space')
        waist_dist = -real(q(length(q))); %distance to waist
        %if a waist lies in this section, record the location and size
        if ((waist_dist >= 0)&&...
                (system{i}.refInd*waist_dist < system{i}.length))
            waist_loc = [waist_loc,system{i}.refInd*waist_dist+...
                graphics.stops(length(graphics.stops))];
            w_size = sqrt(imag(q(length(q)))*wavelength/pi());
            waist_size = [waist_size,w_size];
        end
        for j = 1:segm
            %propagate beam through free space.
            q = [q,q(length(q))+system{i}.mat(1,2)/segm];
            d = [d,d(length(d))+system{i}.length/segm];
        end
        %graph-related - mark for greying if n > 1
        if system{i}.refInd > 1
            graphics.x_b = [graphics.x_b,...
                [graphics.stops(length(graphics.stops));...
                graphics.stops(length(graphics.stops));...
                graphics.stops(length(graphics.stops))+system{i}.length;...
                graphics.stops(length(graphics.stops))+system{i}.length]];
        end
        %graph-related - marks location of end of free space
        graphics.stops = [graphics.stops,system{i}.length+...
            graphics.stops(length(graphics.stops))];

    elseif strcmp(system{i}.type,'GRIN lens')
        %marks start of GRIN lens in array; used for determining fill
        %factor - applicable for laser crystals. Placed inside graphics
        %for convenience
        graphics.startloc = length(q);

        %dividing GRIN lens into segments and calculating individually
        l_segment = system{i}.length/segm;
        n0 = system{i}.n0;
        n2 = system{i}.n2(axis);
        if (axis == 2)&&(length(system{i}.n2) == 2) %for secondary axis
            n2 = system{i}.n2(2);
        end
        %recalculate lensing for each segment
        A = cos(l_segment*sqrt(n2/n0));
        B = sin(l_segment*sqrt(n2/n0))/sqrt(n0*n2);
        if n2 == 0; B = l_segment/n0;end    %for n2 = 0 case
        C = -sqrt(n0*n2)*sin(l_segment*sqrt(n2/n0));
        D = cos(l_segment*sqrt(n2/n0));
        for j = 1:segm
            %propagate beam through GRIN lens
            q = [q, (A*q(length(q)) + B)/(C*q(length(q)) + D)];
            d = [d,d(length(d))+l_segment];
        end
```

```
        %graph-related - marks GRIN lens for greying
        graphics.x_b = [graphics.x_b,...
            [graphics.stops(length(graphics.stops));...
            graphics.stops(length(graphics.stops));...
        graphics.stops(length(graphics.stops))+system{i}.length;...
        graphics.stops(length(graphics.stops))+system{i}.length]];
        graphics.endloc = length(q);  %marks end of GRIN lens in array
        %graph-related - marks location of end of GRIN lens
        graphics.stops = [graphics.stops,...
            graphics.stops(length(graphics.stops))+system{i}.length];

    elseif strcmp(system{i}.type,'thick lens')
        %separates thick lens into the 3 parts - curved interfaces and free
        %space propagation within the thick lens

        %beam passing through curved interface into thick lens
        surf1 = curv_surf(1,system{i}.n_inner,system{i}.R1);
        q = [q, (surf1.mat(1,1)*q(length(q)) + surf1.mat(1,2))/...
            (surf1.mat(2,1)*q(length(q)) + surf1.mat(2,2))];
        d = [d,d(length(d))];

        %beam propagating within the lens
        inside_lens = free_space(system{i}.length,system{i}.n_inner);
        for j = 1:segm/5 %divide into segments, 5x less than free space
            %propagate beam through thick lens
            q = [q,q(length(q))+inside_lens.mat(1,2)*5/segm];
            d = [d,d(length(d))+inside_lens.length*5/segm];
        end
        %beam passing through curved interface out of thick lens
        surf2 = curv_surf(system{i}.n_inner,1,system{i}.R2);
        q = [q, (surf2.mat(1,1)*q(length(q)) + surf2.mat(1,2))/...
            (surf2.mat(2,1)*q(length(q)) + surf2.mat(2,2))];
        d = [d,d(length(d))];

        %graph-related - marks thick lens for greying
        graphics.x_b = [graphics.x_b,...
            [graphics.stops(length(graphics.stops));...
            graphics.stops(length(graphics.stops));...
            graphics.stops(length(graphics.stops))+system{i}.length;...
            graphics.stops(length(graphics.stops))+system{i}.length]];
        %graph-related - marks location of end of thick lens
        graphics.stops = [graphics.stops,system{i}.length + ...
            graphics.stops(length(graphics.stops))];

    else    %components with zero length
        A = system{i}.mat(1,1);
        B = system{i}.mat(1,2);
        C = system{i}.mat(2,1);
        D = system{i}.mat(2,2);
        if (axis == 2)&&(isfield(system{i}, 'mat2'))
            %use matrix for secondary axis if it exists, else use primary
            A = system{i}.mat2(1,1);
            B = system{i}.mat2(1,2);
            C = system{i}.mat2(2,1);
            D = system{i}.mat2(2,2);
        end
        %calculate q change due to component
        q = [q, (A*q(length(q)) + B)/(C*q(length(q)) + D)];
        d = [d,d(length(d))];
    end
end
```

C.1.3.4 gauss_addgraphics.m

```
function gauss_addgraphics(ax_max,graphics,waist_loc,waist_size,...
    waist_loc2,waist_size2)
% For use in Gaussian_beams.m.
% Takes the "graphics" and beam waist data from propagate.m and applies to
% current plot. "Graphics" corresponds to thick red lines that represent
% component locations and greying of areas with n > 1.

%draw semi-transparent boxes around areas with n > 1
a = size(graphics.x_b);
```

```
y_box = [-ax_max;ax_max;ax_max;-ax_max];
y_b = [0;0;0;0];
for i = 1:a(2)-1
    y_b = [y_b,y_box];
end
patch(graphics.x_b,y_b,'k','LineStyle','none','FaceAlpha',0.1)

line([0,max(graphics.stops)],[0,0],'Color','k') %centre line

%draw thick red lines representing component locations at "stop" locations
for i = 1:length(graphics.stops)
    line([graphics.stops(i),graphics.stops(i)],[ax_max,...
        -ax_max],'Color','r','LineWidth',1.5);
end

%draw dotted lines at the beam waists (inside free space components only)
if nargin > 2
    for i = 1:length(waist_loc)
        line([waist_loc(i),waist_loc(i)],...
            [waist_size(i),-waist_size(i)],'LineStyle',':','Color','k');
    end
end
if nargin > 4
    for i = 1:length(waist_loc2)
        line([waist_loc2(i),waist_loc2(i)],...
            [waist_size2(i),-waist_size2(i)],'LineStyle',':','Color','k');
    end
end
```

C.1.3.5 Components

curv_surf.m

```
function cf = curv_surf(n0,n1,R,AoI1,AoI2)
% For use in Gaussian_beams.m.
% Defines an interface object, with the beam passing from n0 to n1, with
% radius of curvature R [m]. Defaults as normal incidence for both angles;
% define one or both angles [degrees] to override.
% Note: This is unnecessary for flat interfaces at normal incidence.

cf.type = 'curved surface';
cf.RoC = R;
cf.n_i = n0;
cf.n_f = n1;

if nargin == 3; AoI1 = 0; AoI2 = 0; end   %angle of incidence
if nargin == 4; AoI2 = 0; end
cf.AoI1_deg = AoI1;
cf.AoI2_deg = AoI2;
AoI1 = AoI1*pi()/180;   %degrees to radians
AoI2 = AoI2*pi()/180;
AoR1 = asin(n0/n1*sin(AoI1));  %angle of refraction
AoR2 = asin(n0/n1*sin(AoI2));

%The following matrix form is from Paraxia.
dn1 = (n1*cos(AoR1)-n0*cos(AoI1))/(cos(AoR1)*cos(AoI1));
dn2 = (n1*cos(AoR2)-n0*cos(AoI2))/(cos(AoR2)*cos(AoI2));

cf.mat = [cos(AoR1)/cos(AoI1),0;dn1/R,cos(AoI1)/cos(AoR1)];
if (AoI1 ~= AoI2)
    cf.mat2 = [cos(AoR2)/cos(AoI2),0;dn2/R,cos(AoI2)/cos(AoR2)];
end
```

free_space.m

```
function space = free_space(l,n)
% For use in Gaussian_beams.m.
% Defines a free space propagation object of length l [m] and refractive
% index n. Defaults to vacuum (n = 1) if no refractive index is passed.

space.type = 'free space';
space.length = l;
if nargin == 1;
    space.refInd = 1;
elseif nargin == 2;
    space.refInd = n;
end
space.mat = [1,l/space.refInd;0,1];
```

GRIN_lens.m

```
function quad = GRIN_lens(l,n0,n2,n2_2)
% For use in Gaussian_beams.m.
% Defines a gradient index (GRIN) lens object of length l [m], central
% refractive index n0, and quadratically reducing refractive index with
% radius with equation: n(r) = n0 - 0.5*n2*r^2. Define both n2 (primary
% axis) and n2_2 (secondary axis) for astigmatic lenses.

quad.type = 'GRIN lens';
quad.length = l;
quad.n0 = n0;
quad.n2 = n2;
if n2 == 0  %for n2 = 0, revert to free space.
    quad.mat = [1,l/n0;0,1];
else
    quad.mat = [cos(l*sqrt(n2/n0)),sin(l*sqrt(n2/n0))/sqrt(n0*n2);...
        -sqrt(n0*n2)*sin(l*sqrt(n2/n0)),cos(l*sqrt(n2/n0))];
end
if nargin == 4; %if the lens is astigmatic
    quad.n2(2) = n2_2;
    if n2_2 == 0    %for n2_2 = 0, revert to free space.
        quad.mat2 = [1,l/n0;0,1];
    else
        quad.mat2 = [cos(l*sqrt(n2_2/n0)),...
            sin(l*sqrt(n2_2/n0))/sqrt(n0*n2_2);...
            -sqrt(n0*n2_2)*sin(l*sqrt(n2_2/n0)),cos(l*sqrt(n2_2/n0))];
    end
end
```

mirror.m

```
function mirror = mirror(R)
% For use in Gaussian_beams.m.
% Defines a mirror object of radius of curvature R [m]. Defaults to a flat
% mirror when no arguments are passed.

mirror.type = 'mirror';
if nargin == 1;
    mirror.RoC = R;
else
    mirror.RoC = Inf;
end
mirror.mat = [1,0;-2/mirror.RoC,1];
```

thick_lens.m

```
function thick = thick_lens(l,n2,R1,R2)
% For use in Gaussian_beams.m.
% Defines a thick lens object with a thickness of l [m], a refractive
```

```
% index of n2, front radius of curvature R1 [m] and a back radius of
% curvature of R2 [m].
% Note: For a convex-convex lens, R1 < 0 and R2 > 0.

thick.type = 'thick lens';
thick.length = l;
n_outer = 1;    % Refractive index outside the lens
thick.n_inner = n2;
thick.R1 = R1;
thick.R2 = R2;

% Defines the thick lens as two curved surfaces with a medium inside
surf1 = curv_surf(n_outer,thick.n_inner,thick.R1);
inside_lens = free_space(l,thick.n_inner);
surf2 = curv_surf(thick.n_inner,n_outer,thick.R2);
thick.mat = surf2.mat*inside_lens.mat*surf1.mat;
```

thin_lens.m

```
function th_lens = thin_lens(f,f2)
% For use in Gaussian_beams.m.
% Defines a thin lens object of focal length f [m]. Define both f (primary
% axis) and f2 (secondary axis) for astigmatic lenses.

th_lens.type = 'thin lens';
th_lens.f = f;
th_lens.mat = [1,0;-1/f,1];
if nargin == 2; %if the lens is astigmatic
    th_lens.f2 = f2;
    th_lens.mat2 = [1,0;-1/f2,1];
end
```

user_defined.m

```
function user_def = user_defined(A,B,C,D)
% For use in Gaussian_beams.m.
% Defines a user-defined component object with user-defined ABCD matrix.
% Assumed to be of zero length. Can pass in either a 2x2 matrix or A, B, C
% and D individually.

user_def.type = 'user-defined';
if nargin == 1;
    user_def.mat = A;
else
    user_def.mat = [A,B;C,D];
end
```

C.1.4 M^2 estimation

C.1.4.1 M2_fit.m

```
% M2_fit.m version 1.0.5  (28/03/2012)
% Written by Ka Wu, The University of Adelaide
% Uses the method from Dave Lancaster's code, and incorporates some code
% written by Nick Chang.

% Code to estimate M^2 of a low-M^2 beam from a series of beam profiles.
% Opens .csv (or other comma-delimited) files containing the array of
% intensity data. Averages the array to find beam centre, then fits a
% Gaussian to the vertical and horizontal data set from the beam centre
% to find the approximate beam widths and height at different locations.
% Loops for all files, then fits a hyperbola to the beam widths to obtain
% w0 and theta.
```

```
% Requires M2_fitting.m for M^2 fitting; M^2 fitting can be disabled and
% the program used to just obtain beam width and height from profiles.

clear all
close all

profile_loc = 30:10:160; %distance of each profile from arb. point in [mm]
wavelength = 1.94e-6;  %wavelength of light in [m]
pixel_width = 100;%11.66; %camera's pixel width, in [microns]
pixel_height = 100;% 13.5; %camera's pixel width, in [microns]
blur_factor = 5;   %pixel averaging. Used to estimate beam centre.
back_av = 15;  %4 squares with dimension back_av are taken from each corner
               %to calibrate out the background for better Gaussian fit
suppress_plot = 1; % 1 = only plot beam propagation and final M^2.
do_M2_fit = 0; % 1 = do M^2 fit; 0 = just do Gaussian fit to profiles.
               % Also doesn't do M^2 fit for < 3 data points

%File name for exporting of beam width and height data
output_filename = 'beam_width_data.xls';

num_loop = length(profile_loc); %min 3 for an M^2 fit
x_width = zeros(num_loop, 1);
y_width = zeros(num_loop, 1);
distance = zeros(num_loop, 1);
num_fig = ceil(num_loop/6); %number of figures required

for a = 1:num_loop
    dist = profile_loc(a);
% Import comma-delimited raw data of beam profile. Adjust file names
% accordingly.
    filename = ['10mm2W\' num2str(dist) 'mm.csv'];
    RAW = csvread(filename);
    RAW = transpose(RAW);   %depends upon camera orientation

% remove background from 4 samples in blurred image by taking the average
% of 4 squares in the corners
    ii = size(RAW);
    back = mean(mean([RAW(1:back_av,1:back_av)...
        RAW(ii(1)-back_av+1:ii(1),1:back_av)...
        RAW(1:back_av,ii(2)-back_av+1:ii(2))...
        RAW(ii(1)-back_av+1:ii(1),ii(2)-back_av+1:ii(2))]));
    RAW = RAW - back;

% blurring image and finding max of profile (assumed to be beam centre)
% adjust blur_factor above if necessary. Larger number = more blur.
    window = (1:blur_factor)*0+1/blur_factor;
    blurred = convn(RAW,window,'same');
    blurred = transpose(convn(transpose(blurred),window,'same'));
    [colMax max_loc_y] = max(blurred);
    [peak max_loc_x] = max(colMax);
    max_loc_y = max_loc_y(max_loc_x);

% taking the row and column data centred at the beam centre
    x_mode = transpose(RAW(max_loc_y,:));
    width = transpose(1:length(x_mode))*pixel_width;
    y_mode = RAW(:,max_loc_x);
    height = transpose(1:length(y_mode))*pixel_height;

% Gaussian curve fitting and extracting the beam width and height
    f = fittype('gauss1');
    x_fit = fit(width,x_mode,f);
    y_fit = fit(height,y_mode,f);
    x_coeff = coeffvalues(x_fit);
    y_coeff = coeffvalues(y_fit);
    distance(a) = dist;
    x_width(a) = x_coeff(3)*sqrt(2);
```

```
    y_width(a) = y_coeff(3)*sqrt(2);

% Plotting each image with the centre line and centroid in an array
    if (suppress_plot == 0)
        rows = (num_loop>2)+1;
        cols = rows + (num_loop==2) + (num_loop>4);
        figure(ceil(a/6))
        subplot(rows,cols,(a-6*floor((a-1)/6)))
        image(RAW,'CDataMapping','scaled')
        line([max_loc_x,max_loc_x], [0,length(RAW)],'color','w')
        line([0,length(RAW)], [max_loc_y,max_loc_y],'color','w')
        rectangle('Position',[max_loc_x-(x_width(a)/pixel_width),...
            max_loc_y-(y_width(a)/pixel_height),2*(x_width(a)/pixel_width),...
            2*(y_width(a)/pixel_height)],'Curvature',[1,1],'EdgeColor','w')
        title(['Profile at ' num2str(dist) 'mm'],'FontWeight','bold')
        set(gca,'DataAspectRatio',[1 1 1],'xtick',[],'ytick',[])

    % Plotting each fit (x-axis and y-axis) in an array
        figure(ceil(a/6)+num_fig)
        subplot(rows,cols*2,(a*2-1)-12*floor((a*2-2)/12))
        plot(width,x_mode)
        hold on
        plot(x_fit,'m')
        legend off
        hold off
        title(['x-axis fit (' num2str(dist) 'mm)'],'FontWeight','bold')
        set(gca,'xtick',[],'ytick',[])
        axis ([min(width) max(width)...
            min(x_mode)-abs(min(x_mode)*1.2) max(x_mode)*1.2])
        subplot(rows,cols*2,(a*2)-12*floor((a*2-2)/12))
        plot(height,y_mode)
        hold on
        plot(y_fit,'m')
        legend off
        hold off
        title(['y-axis fit (' num2str(dist) 'mm)'],'FontWeight','bold')
        set(gca,'xtick',[],'ytick',[])
        axis ([min(height) max(height)...
            min(y_mode)-abs(min(y_mode)*1.2) max(y_mode)*1.2])
    end
end

%call M2_fitting to do the M2 fit
if (num_loop >= 3)&&(do_M2_fit == 1)
    [x_M2,x_M2_fit] = M2_fitting(distance,x_width/1000,wavelength);
    [y_M2,y_M2_fit] = M2_fitting(distance,y_width/1000,wavelength);
end

%write beam width and height data to file
fileID = fopen(output_filename,'w');
fprintf(fileID,'location [mm]\tbeam height [mm]\tbeam width [mm]\n');
for a = 1:num_loop
    fprintf(fileID,[num2str(distance(a)) '\t' num2str(y_width(a)/1000)...
        '\t' num2str(x_width(a)/1000) '\n']);
end
if (num_loop >= 3)&&(do_M2_fit == 1)
    fprintf(fileID,['\nEstimated M^2:\n\t' num2str(y_M2) '\t'...
        num2str(x_M2)]);
end
fclose(fileID);

%plotting profiles of the beam propagation
if (num_loop >= 3)
    b = str2double(num2str(max(x_width),0))*2;
    c = str2double(num2str(max(y_width),0))*2;
    xw_axis = linspace(-b,b,100);
    xh_axis = linspace(-c,c,100);
```

```
    func = zeros(num_loop,100);
    func2 = zeros(num_loop,100);
    peakx = 1./(x_width*sqrt(pi()));
    peaky = 1./(y_width*sqrt(pi()));
    [X1,Y1] = meshgrid(distance,xw_axis/1000);
    [X2,Y2] = meshgrid(distance,xh_axis/1000);
    for i = 1:num_loop
        func(i,:) = peakx(i)*exp(-(xw_axis./x_width(i)).^2);
        func2(i,:) = peaky(i)*exp(-(xh_axis./y_width(i)).^2);
    end
    func = transpose(func);
    func2 = transpose(func2);
    figure
    subplot(1,2,1)
    plot3(Y1,X1,func)
    hold on
    contour(Y1,X1,func)
    title('horizontal Gaussian fits','FontWeight','bold')
    xlabel('Width [mm]')
    ylabel('Beam propagation [mm]')
    zlabel('Intensity [A.U.]')
    grid on
    subplot(1,2,2)
    plot3(Y2,X2,func2)
    hold on
    contour(Y2,X2,func2)
    title('vertical Gaussian fits','FontWeight','bold')
    xlabel('Height [mm]')
    ylabel('Beam propagation [mm]')
    zlabel('Intensity [A.U.]')
    grid on
end

% plotting the M^2 fit to beam widths
if (num_loop >= 3)&&(do_M2_fit == 1)
    figure
    subplot(1,2,1)
    hold on
    plot(distance,x_width/1000,'o')
    plot(x_M2_fit)
    title(['horizontal M^2 fit: M^2 = ' num2str(x_M2)],'FontWeight','bold')
    xlabel('Beam propagation [mm]')
    ylabel('Beam width [mm]')
    subplot(1,2,2)
    hold on
    plot(distance,y_width/1000,'o')
    plot(y_M2_fit)
    title(['vertical M^2 fit: M^2 = ' num2str(y_M2)],'FontWeight','bold')
    xlabel('Beam propagation [mm]')
    ylabel('Beam height [mm]')
end
```

C.1.4.2 M2_fitting.m

```
function [M2,M2_fit] = M2_fitting(distance,width,wavelength)

% M^2 fitting function.
% Fits directly to {w^2 = w0^2 + th^2*(z-z0)^2} to obtain the waist size
% and far-field divergence angle, then calculates the M^2.
% Distance (from arb point) and beam width is in [mm]; wavelength in [m].
% Returns the M^2 and the fit parameters

wavelength = wavelength*1000; %converts wavelength to [mm]
%fitting directly to w^2 = w0^2 + th^2*(z-z0)^2
fo_ = fitoptions('method','NonlinearLeastSquares','Lower',...
    [0 0 min(distance)],'Upper',[max(width) Inf max(distance)]);
set(fo_,'Startpoint',[min(width) 0.02 mean(distance)]);
```

```
ft_ = fittype('(w0^2+theta^2*((x-c)^2))^0.5','dependent',{'y'},...
    'independent',{'x'},'coefficients',{'w0', 'theta', 'c'});

M2_fit = fit(distance,width,ft_,fo_);
w0_x=M2_fit.w0;
th_x=M2_fit.theta;
M2=(w0_x*th_x*pi)/(wavelength);
```

C.2 Mathematica (optica) code

C.2.1 Pumping of Tm:$YAlO_3$ ThOR slab

```
(* JenOptik Diode 19x10 emitters *)

ClearAll;
Needs["Optica`Optica`"];
flgDiode = 1; (*1 for full diode array, 0 for simplified version *)
(* Divergence in degree, Number of emitter, Separation in mm *)
horiz = 1;
divX = 7; divY = 0.5;
noX = 10; noY = 10;
sepX = 1; sepY = 1.775;

emitter = PointOfRays[{divX, divY}, NumberOfRays → 3, WaveLength → 0.79];
diode = 0;
If [flgDiode == 1,
  For[i = 0, i < noX, i++,
    For[j = 0, j < noY, j++,
      tmp    =    Translate[emitter,    {0,    (i-(noX-1)/2)*sepX,    (j-(noY-
        1)/2)*sepY}];
      diode = {diode, tmp};
  ]],

  diode = {emitter,
    Translate[emitter, {0, (-(noX-1)/2)*sepX, (-(noY-1)/2)*sepY}],
    Translate[emitter, {0, (-(noX-1)/2)*sepX, ((noY-1)/2)*sepY}],
    Translate[emitter, {0, ((noX-1)/2)*sepX, (-(noY-1)/2)*sepY}],
    Translate[emitter, {0, ((noX-1)/2)*sepX, ((noY-1)/2)*sepY}];
];
diode = Move[diode, 0, 0, 90];
diodes = diode;
If[horiz == 2,
  diodes  =  {Move[diodes,  {0,  22.5,  0},  0,  0],  Move[diodes,  {0,  -22.5,
    0}, 0, 0]}];

If[horiz == 1, (*Two-diode case*)
  pumping = {diodes,
    Move[PlanoConvexCylindricalLens[60, {30, 40}, 6,
      CurvatureDirection → Front], 10, 0, 0],
    Move[PlanoConvexCylindricalLens[30, {20, 22}, 5.7,
      CurvatureDirection → Front], 42.5, 0, 90]};
  pumping = Move[pumping, -77.5, 0, 0];

  system = {Move[pumping, {0, 0, 0}, -20, 0], Move[pumping, {0, 0, 0},
    20, 0],
    Move[Screen[70], {xscreen, 0}]};
  ManipulateSystem[system,
    {DynamicFrame[PlotType → SideView, Axes → True],
    DynamicFrame[PlotType → TopView, Axes → True],
    DynamicFrame[PlotType → Surface, Axes → True]}]
]
```

```
If[horiz == 2, (*Four-diode case*)
  pumping = {diodes,
    Move[PlanoConvexCylindricalLens[150, {100, 90}, 21.3,
      CurvatureDirection → Front], {10, 0, 0}, 0, 0]};
  pumping2 = {Move[PlanoConvexCylindricalLens[70, {30, 32}, 5.7,
    CurvatureDirection → Front], 115, 0, 90],
    Move[PlanoConvexCylindricalLens[70, {30, 32}, 5.7,
      CurvatureDirection → Front], 125, 0, 90]};
  pumping = Move[pumping, -166, 0, 0];
  pumping2 = Move[pumping2, -166, 0, 0];
  system = {Move[pumping, {0, 0, 0}, -20, 0], Move[pumping, {0, 0, 0},
    20, 0],
    Move[pumping2, {0, 0, 0}, -20, 0],Move[pumping2, {0, 0, 0}, 20, 0],
    Move[Screen[70], {xscreen, 0}]};
  ManipulateSystem[system,
    {DynamicFrame[PlotType → SideView, Axes → True],
    DynamicFrame[PlotType → TopView, Axes → True],
    DynamicFrame[PlotType → Surface, Axes → True]}]
]
```

D Circuit diagrams

This appendix contains the diagrams of the circuit used in this work.

D.1 Diode current feedback circuit

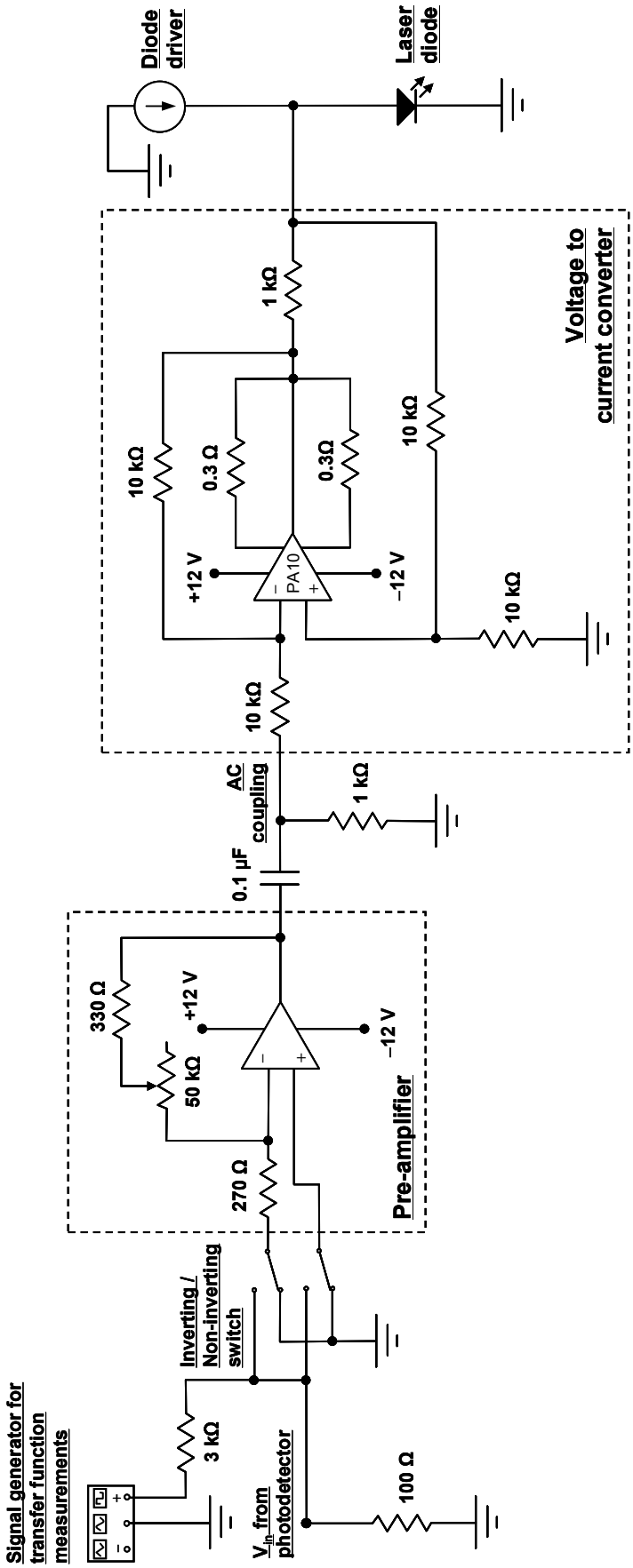
Diode driver
Laser diode
Voltage to current converter
1 kΩ
10 kΩ
0.3 Ω
0.3Ω
10 kΩ
+12 V
PA10
–12 V
10 kΩ
10 kΩ
AC coupling
1 kΩ
0.1 µF
330 Ω
+12 V
50 kΩ
–12 V
Pre-amplifier
270 Ω
Inverting / Non-inverting switch
Signal generator for transfer function measurements
3 kΩ
V_{in} from photodetector
100 Ω

E Assembly procedures

This appendix contains the procedures for the assembly of the lasers in this work.

E.1 Tm:$YAlO_3$ slab laser

The laser head for the Tm:$YAlO_3$ slab laser was assembled as follows:

1. A sheet of 125-μm-thick 99.999%-pure indium was first carefully cut using a razor blade to yield two strips that match the dimensions of the cooled surface of the slab. These sheets were cleaned using isopropanol to remove any surface dust and impurities
2. One strip of indium was set aside, while the other was placed on the cleaned bottom copper cooling block. The indium strip was carefully aligned such that it was centred on the cooling surface and parallel to the edges
3. The Tm:$YAlO_3$ slab was cleaned repeatedly using both isopropanol and acetone to ensure the surfaces were free of all dust and residue. Using soft-tip tweezers, the Tm:$YAlO_3$ slab was placed on top of the indium strip and centred on the cooling surface of the cooling block for full thermal contact
4. The second strip of indium was placed on top of the slab and similarly aligned
5. The spacers were placed on the four struts of the bottom cooling block. Two guide pins were used to align the top cooling block and to maintain parallelism while assembling. These guide pins were positioned where two of the bolts would be located, with the top block sliding smoothly onto the pins. The guide pins fitted tightly into the tapped holes in the bottom cooling block, but could be removed through the top cooling block.

6. The top cooling block was then gently lowered down to rest on the indium and slab stack.
7. Two bolts were inserted through the top cooling block in the holes opposite the guide pins, and used to just barely secure the top cooling block. The two guide pins were then carefully removed without shifting the top cooling block, and the remaining two bolts were placed through the holes and tightened to the same extent as the existing bolts.
8. The bolts were each tightened to secure the top cooling block and to compress the two strips of indium. To ensure even pressure when tightening, each bolt was only tightened slightly in a repeated figure eight sequence until all four bolts were equally and sufficiently tight. While subjective, this was found to be when wrist strength alone was used to tighten the bolts.
9. Finally, the apertures were slid into place in the slots on both sides of the slab.

E.2 Tm:$YAlO_3$ ThOR slab laser

The laser head for the ThOR slab laser was assembled as follows:

10. A sheet of 125-μm-thick 99.999%-pure indium was cut using a razor blade to yield two strips that match the dimensions of the cooled surface of the slab. These sheets were cleaned using isopropanol
11. With the copper cooling block placed with the cooling surface up, one of the indium strips was placed on the surface and aligned at the centre of the block
12. The knife edges were then located to shield the edge of the indium completely. This was done by using a large flat surface placed on top of the indium to define the top edge of the indium. The knife edges were then slid up such that the top edge made contact with the large surface. The knife edges were secured and the large surface removed. The top of the knife edges are now co-planar with the surface of the indium.
13. The Tm:$YAlO_3$ slab was cleaned repeatedly using both isopropanol and acetone to ensure the surfaces were free of all dust and residue. Using soft-tip tweezers, the ThOR slab was placed on top of the indium strip with the doped side down, and centred on the cooling surface of the cooling block for full thermal contact
14. The second strip of cut indium was placed on top of the slab and aligned

15. The spacers were placed on the three holes of the cooling block
16. The securing block was held just above the indium and the spacers, and the three bolts placed through the holes into the tapped hole of the cooling block. These bolts were gradually tightened until the block was almost in contact with the indium on top of the slab
17. The securing block was carefully aligned and then lowered gently onto the indium on the slab
18. The bolts were each tightened to secure the securing block and to compress the two strips of indium. Each bolt was only tightened slightly in a repeated sequence until all three bolts were equally and sufficiently tight. Again, while subjective, this was found to be when wrist strength alone was used to tighten the bolts
19. Finally, the assembled laser head was placed on top of the aluminium block and secured with two bolts from underneath.

F Brewster's angle ThOR slab

This appendix contains the design and crystal dimensions for an uncoated ThOR slab laser that uses Brewster's angle at the entrance and exit faces.

Brewster's angle requires incident light on an interface to be *p*-polarised; however, the laser mode must be *s*-polarised (vertical, perpendicular to the zigzag plane) inside the crystal to ensure the polarisation is always aligned to a single crystal axis. Thus, the laser beam must enter and exit out of the zigzag plane. The angle of incidence must be Brewster's angle in the vertical direction only, and 0° in the lateral direction. The crystal design is shown below, which results in 7 bounces on each side.

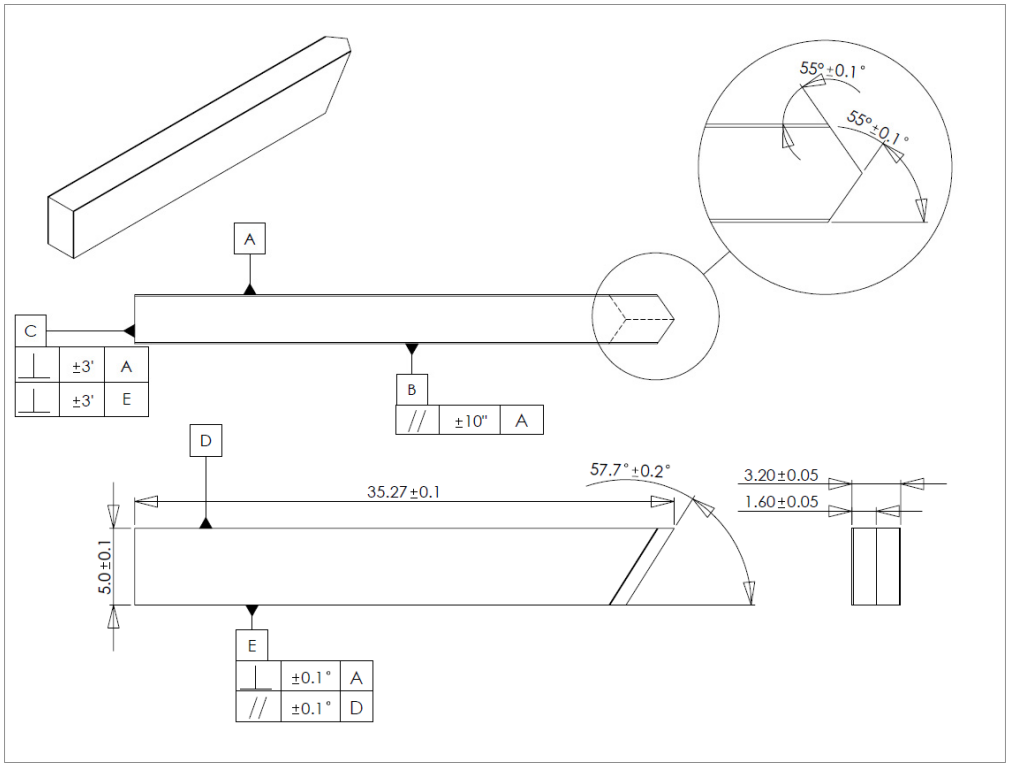

References

[1] T. H. Maiman, “Stimulated optical radiation in ruby,” *Nature*, vol. 187, no. 4736, pp. 493–494, Aug. 1960.

[2] F. Träger, *Springer Handbook of Lasers and Optics*. Springer Science & Business Media, 2012, p. 1726.

[3] J. H. Taylor and H. W. Yates, “Atmospheric Transmission in the Infrared,” *J. Opt. Soc. Am.*, vol. 47, no. 3, p. 223, Mar. 1957.

[4] S. D. Lord, “Transmission Spectra | Gemini Observatory,” *NASA Technical Memorandum 103957*, 1992. [Online]. Available: http://www.gemini.edu/node/196?q=node/10789. [Accessed: 26-Aug-2014].

[5] H. Jelínková, J. Pašta, M. Němec, J. Šulc, and P. Koranda, “Near-and mid-infrared laser radiation interaction with eye tissue,” *Appl. Phys. A*, vol. 92, pp. 975–980, 2008.

[6] K. Ota, Y. Mine, M. Doshida, G. Sugizaki, M. Makino, K. Kobayashi, M. Saga, Y. Takada, K. Komatsu, H. Saito, K. Tanikawa, and H. Shirahata, “A novel multi-function 2-micron imaging laser radar system,” in *EUROPTO Conference on Laser Radar Ranging and Atmospheric Lidar Techniques II*, 1999, vol. 3865, pp. 128–133.

[7] N. Sugimoto, N. Sims, K. Chan, and D. K. Killinger, “Eye-safe 2.1-μm Ho lidar for measuring atmospheric density profiles,” *Opt. Lett.*, vol. 15, no. 6, pp. 302–304, 1990.

[8] C. Weitkamp, *Lidar: Range-Resolved Optical Remote Sensing of the Atmosphere*. New York, NY, USA: Springer Science & Business Media, 2005.

[9] H. H. P. T. Bekman, J. C. van den Heuvel, F. J. M. van Putten, and H. M. A. Schleijpen, “Development of a Mid-Infrared Laser for Study of Infrared Countermeasures Techniques,” in *European Symposium on Optics and Photonics for Defence and Security*, 2004, pp. 27–38.

[10] A. Krier, *Mid-infrared semiconductor optoelectronics*. Springer London, 2006.

[11] A. Schliesser, N. Picqué, and T. W. Hänsch, "Mid-infrared frequency combs," *Nat. Photonics*, vol. 6, no. June, 2012.

[12] M. Seiter and M. W. Sigrist, "Trace-gas sensor based on mid-IR difference-frequency generation in PPLN with saturated output power," *Infrared Phys. Technol.*, vol. 41, no. 5, pp. 259–269, Oct. 2000.

[13] D. Richter, D. G. Lancaster, and F. K. Tittel, "Development of an automated diode-laser-based multicomponent gas sensor," *Appl. Opt.*, vol. 39, no. 24, pp. 4444–4450, Aug. 2000.

[14] N. Gayraud, Ł. W. Kornaszewski, J. M. Stone, J. C. Knight, D. T. Reid, D. P. Hand, and W. N. MacPherson, "Mid-infrared gas sensing using a photonic bandgap fiber," *Appl. Opt.*, vol. 47, no. 9, pp. 1269–1277, Mar. 2008.

[15] N. Menyuk and D. K. Killinger, "Atmospheric remote sensing of water vapor, HCl and CH4 using a continuously tunable Co:MgF2 laser," *Appl. Opt.*, vol. 26, no. 15, pp. 3061–3065, Aug. 1987.

[16] P. F. Ambrico, A. Amodeo, P. Di Girolamo, N. Spinelli, and P. Di Girolamo, "Sensitivity analysis of differential absorption lidar measurements in the mid-infrared region," *Appl. Opt.*, vol. 39, no. 36, pp. 6847–6865, Dec. 2000.

[17] T. J. Carrig, "Novel Pulsed Solid-State Sources for Laser Remote Sensing," in *Proc. SPIE 5620, Solid State Laser Technologies and Femtosecond Phenomena*, 2004, vol. 5620, pp. 187–198.

[18] J. A. Curcio and C. C. Petty, "The Near Infrared Absorption Spectrum of Liquid Water," *J. Opt. Soc. Am.*, vol. 41, no. 5, pp. 302–304, May 1951.

[19] R. Kaufmann, A. Hartmann, and R. Hibst, "Cutting and Skin-Ablative Properties of Pulsed Mid-Infrared Laser Surgery," *J. Dermatol. Surg. Oncol.*, vol. 20, no. 2, pp. 112–118, 1994.

[20] T. Bilici, S. Mutlu, H. Kalaycioglu, A. Kurt, A. Sennaroglu, and M. Gulsoy, "Development of a thulium (Tm:YAP) laser system for brain tissue ablation," *Lasers Med. Sci.*, vol. 26, no. 5, pp. 699–706, Sep. 2011.

[21] H. Jelínková, P. Koranda, J. Šulc, M. Nemec, P. Černý, and J. Pašta, "Diode-Pumped Tm:YAP Laser for Eye Microsurgery," in *Proc. SPIE 6871, Solid State Lasers XVII: Technology and Devices*, 2008, vol. 6871, p. 68712N.

[22] L. F. Johnson, G. D. Boyd, and K. Nassau, "Optical maser characteristics of Tm^{3+} in $CaWO_4$," *Proc. IRE*, vol. 50, p. 86, 1962.

[23] L. F. Johnson, G. D. Boyd, and K. Nassau, "Optical maser characteristics of Ho^{3+} in $CaWO_4$," *Proc. IRE*, vol. 50, p. 87, 1962.

[24] L. A. Pomeranz, P. A. Ketteridge, and P. A. Budni, “Tm: $YAlO_3$ laser pumped ZGP mid-IR source,” in *Advanced Solid-State Photonics (TOPS)*, 2003, pp. 2–6.

[25] P. A. Budni, L. A. Pomeranz, M. L. Lemons, P. G. Schunemann, T. M. Pollak, and E. P. Chicklis, “10W mid-IR holmium pumped $ZnGeP_2$ OPO,” in *Advanced Solid-State Lasers (TOPS) Vol. 19*, 1998, pp. 226–229.

[26] P. G. Schunemann, S. D. Setzler, L. Mohnkern, and T. M. Pollak, “2.05-μm-Laser-Pumped Orientation-Patterned Gallium Arsenide (OPGaAs) OPO,” in *Conference on Lasers and Electro-Optics (CLEO)*, 2005, pp. 1835–1837.

[27] C. Kieleck, M. Eichhorn, A. Hirth, D. Faye, and E. Lallier, “High-efficiency 20–50 kHz mid-infrared orientation-patterned GaAs optical parametric oscillator pumped by a 2 μm holmium laser,” *Opt. Lett.*, vol. 34, no. 3, pp. 262–264, 2009.

[28] K. S. Wu, D. J. Ottaway, J. Munch, D. G. Lancaster, S. Bennetts, and S. D. Jackson, “Gain-switched holmium-doped fibre laser,” *Opt. Express*, vol. 17, no. 23, pp. 20872–20877, Nov. 2009.

[29] M. A. Emanuel, N. W. Carlson, and J. A. Skidmore, “High-efficiency AlGaAs-based laser diode at 808 nm with large transverse spot size,” *IEEE Photonics Technol. Lett.*, vol. 8, no. October, pp. 1291–1293, 1996.

[30] M. Tao, Q. Huang, T. Yu, P. Yang, W. Chen, and X. Ye, “Cross relaxation in Tm-doped fiber lasers,” in *Proc. SPIE 8796, 2nd International Symposium on Laser Interaction with Matter (LIMIS 2012)*, 2013, p. 87961W.

[31] E. C. Honea, R. J. Beach, S. B. Sutton, J. A. Speth, S. C. Mitchell, J. A. Skidmore, M. A. Emanuel, and S. A. Payne, “115-W Tm:YAG diode-pumped solid-state laser,” *IEEE J. Quantum Electron.*, vol. 33, no. 9, pp. 1592–1600, 1997.

[32] N. G. Zakharov, O. L. Antipov, a P. Savikin, V. V Sharkov, O. N. Eremeikin, Y. N. Frolov, G. M. Mishchenko, and S. D. Velikanov, “Efficient emission at 1908 nm in a diode-pumped Tm:YLF laser,” *Quantum Electron.*, vol. 39, no. 5, pp. 410–414, May 2009.

[33] S. D. Jackson, “Cross relaxation and energy transfer upconversion processes relevant to the functioning of 2 μm Tm^{3+}-doped silica fibre lasers,” *Opt. Commun.*, vol. 230, pp. 197–203, Jan. 2004.

[34] B. M. Walsh and N. P. Barnes, “Comparison of Tm : ZBLAN and Tm : silica fiber lasers; Spectroscopy and tunable pulsed laser operation around 1.9 μm,” *Appl. Phys. B*, vol. 78, pp. 325–333, Feb. 2004.

[35] J. Wu, Z. Yao, J. Zong, and S. Jiang, “Highly efficient high-power thulium-doped germanate glass fiber laser,” *Opt. Lett.*, vol. 32, no. 6, pp. 638–640, Mar. 2007.

[36] K. van Dalfsen, S. Aravazhi, C. Grivas, S. M. García-Blanco, and M. Pollnau, "Thulium channel waveguide laser with 1.6 W of output power and ~80% slope efficiency.," *Opt. Lett.*, vol. 39, no. 15, pp. 4380–4383, Aug. 2014.

[37] D. Cao, Q. Peng, S. Du, J. Xu, Y. Guo, J. Yang, Y. Bo, J. Zhang, D. Cui, and Z. Xu, "A 200 W diode-side-pumped CW 2 μm Tm:YAG laser with water cooling at 8°C," *Appl. Phys. B*, vol. 103, no. 1, pp. 83–88, Nov. 2010.

[38] C. Wang, Y.-X. Niu, S.-F. Du, C. Zhang, Z.-C. Wang, F. Li, J. Xu, Y. Bo, Q.-J. Peng, D.-F. Cui, J.-Y. Zhang, and Z. Xu, "High-power diode-side-pumped rod Tm: YAG laser at 2.07 μm," *Appl. Opt.*, vol. 52, no. 31, pp. 7494–7497, 2013.

[39] T. Ehrenreich, R. Leveille, I. Majid, K. Tankala, G. Rines, and P. Moulton, "1 kW, all-glass Tm:fiber laser," in *SPIE Photonics West 2010: LASE, Fibre Lasers VII: Technology, Systems and Applications*, 2010.

[40] A. S. Kurkov, E. M. Sholokhov, O. I. Medvedkov, V. V Dvoyrin, Y. N. Pyrkov, V. B. Tsvetkov, A. V Marakulin, and L. A. Minashina, "Holmium fiber laser based on the heavily doped active fiber," *Laser Phys. Lett.*, vol. 6, no. 9, pp. 661–664, Sep. 2009.

[41] J. Kwiatkowski, J. K. Jabczynski, W. Zendzian, L. Gorajek, and M. Kaskow, "High repetition rate, Q-switched Ho:YAG laser resonantly pumped by a 20 W linearly polarized Tm: fiber laser," *Appl. Phys. B*, vol. 114, no. 3, pp. 395–399, Jun. 2013.

[42] E. Lippert, S. Nicolas, G. Arisholm, K. Stenersen, and G. Rustad, "Midinfrared laser source with high power and beam quality," *Appl. Opt.*, vol. 45, no. 16, pp. 3839–3845, Jun. 2006.

[43] M. Schellhorn, "Performance of a Ho:YAG thin-disc laser pumped by a diode-pumped 1.9 μm thulium laser," *Appl. Phys. B*, vol. 85, no. 4, pp. 549–552, Jul. 2006.

[44] B.-Q. Yao, X.-M. Duan, L.-L. Zheng, Y.-L. Ju, Y. Wang, G.-J. Zhao, and Q. Dong, "Continuous-wave and Q-switched operation of a resonantly pumped Ho:YAlO3 laser," *Opt. Express*, vol. 16, no. 19, p. 14668, Sep. 2008.

[45] X. T. Yang, X. Z. Ma, W. H. Li, and Y. Liu, "Q-switched Ho:$YAlO_3$ laser pumped by Tm:YLF laser at room temperature," *Laser Phys.*, vol. 21, no. 12, pp. 2064–2067, Oct. 2011.

[46] A. Hemming, S. Bennetts, N. Simakov, A. Davidson, J. Haub, and A. Carter, "Resonantly Pumped 2 μm Holmium Fibre Lasers," in *Specialty Optical Fibers*, 2011, no. 5194642, p. SOMB1.

[47] G. Armagan, A. M. Buoncristiani, W. C. Edwards, A. T. Inge, and B. DiBartolo, "Spectroscopic characterization of dynamical processes for Tm, Ho: YAG lasers," in *Advanced Solid-State Lasers*, 1990, pp. 144–149.

[48] C. Zhang, S.-F. Du, Y.-X. Niu, C.-L. Wang, Z.-C. Wang, J.-L. Xu, Y. Bo, Q.-J. Peng, D.-F. Cui, and Z.-Y. Xu, "A Compact High Power Laser-Diode Side-Pumped Tm,Ho:YAG Laser Nearly at Room Temperature with Intracavity Tm:YAG Laser," *Chinese Phys. Lett.*, vol. 31, no. 4, p. 044201, Apr. 2014.

[49] N. Simakov, A. Hemming, J. Haub, and A. Carter, "High Power Holmium Fiber Lasers," in *European Conference on Optical Communications (ECOC 2014)*, 2014, p. Tu.3.4.1.

[50] S. D. Jackson, A. Sabella, A. Hemming, S. Bennetts, and D. G. Lancaster, "High-power 83 W holmium-doped silica fiber laser operating with high beam quality," *Opt. Lett.*, vol. 32, no. 3, pp. 241–243, Feb. 2007.

[51] Y. Wang, C.-Q. Xu, and H. Po, "Thermal effects in kilowatt fiber lasers," *IEEE Photonics Technol. Lett.*, vol. 16, no. 1, pp. 63–65, 2004.

[52] M. C. Gupta and J. Ballato, *The Handbook of Photonics*, 2nd ed. CRC Press, 2007.

[53] D. Marcuse, "Curvature loss formula for optical fibers," *J. Opt. Soc. Am.*, vol. 66, no. 3, p. 216, Mar. 1976.

[54] A. Yariv and P. Yeh, *Photonics: Optical Electronics in Modern Communications*, 6th ed. Oxford University Press, USA, 2006.

[55] K. O. Hill, Y. Fujii, D. C. Johnson, and B. S. Kawasaki, "Photosensitivity in optical fiber waveguides: Application to reflection filter fabrication," *Appl. Phys. Lett.*, vol. 32, no. 10, pp. 647–649, 1978.

[56] E. Snitzer, H. Po, R. P. Tumminelli, and F. Hakimi, "Optical fiber lasers and amplifiers," *U.S. Pat. 4,815,079*, 1989.

[57] L. Zenteno, "High-power double-clad fiber lasers," *J. Light. Technol.*, vol. 11, no. 9, pp. 1435–1446, 1993.

[58] R. Paschotta, "Brightness Converters," *Encyclopedia of Laser Physics and Technology*, 2008. [Online]. Available: http://www.rp-photonics.com/brightness_converters.html. [Accessed: 03-Sep-2014].

[59] K. Yasui, "Efficient and stable operation of a high-brightness cw 500-W Nd:YAG rod laser," *Appl. Opt.*, vol. 35, no. 15, pp. 2566–2569, May 1996.

[60] R. Diehl, *High-power diode lasers: Fundamentals, Technology, Applications*. Springer-Verlag, 2000.

[61] G. Erbert, F. Bugge, A. Knauer, J. Sebastian, A. Thies, H. Wenzel, M. Weyers, and G. Tränkle, "High-power tensile-strained GaAsP-AlGaAs quantum-well lasers emitting between 715 and 790 nm," *IEEE J. Sel. Top. Quantum Electron.*, vol. 5, no. 3, pp. 780–784, 1999.

[62] S. L. Yellen, A. H. Shepard, R. J. Dalby, J. A. Baumann, H. B. Serreze, T. S. Guido, R. Soltz, K. J. Bystrom, C. M. Harding, and R. G. Waters, "Reliability of GaAs-based semiconductor diode lasers: 0.6-1.1 μm," *IEEE J. Quantum Electron.*, vol. 29, no. 6, pp. 2058–2067, 1993.

[63] M. Eichhorn, "Quasi-three-level solid-state lasers in the near and mid infrared based on trivalent rare earth ions," *Appl. Phys. B*, vol. 93, pp. 269–316, Sep. 2008.

[64] W. Koechner, *Solid State Laser Engineering*, 6th ed. Springer New York, 2006.

[65] Y. Tian, G. Li, B. Q. Yao, and Y. Z. Wang, "Time-dependent analytical model of thermal effects in continuous-wave end-pumped Tm:YAP lasers," *Appl. Phys. B*, vol. 103, no. 1, pp. 107–112, Sep. 2010.

[66] X. Peng, L. Xu, and A. Asundi, "High-power efficient continuous-wave TEM_{00} intracavity frequency-doubled diode-pumped Nd : YLF laser," *Appl. Opt.*, vol. 44, no. 5, pp. 801–807, 2005.

[67] E. P. Chicklis, J. Baer, M. Knights, and J. McCarthy, "XeF Pumped Tm:YLF Laser Scaling," *Contract N00014-80-C-0444, Sanders Assoc. Inc. Final Rep.*, 1981.

[68] I. F. Elder and M. J. P. Payne, "Comparison of diode-pumped Tm:YAP with Tm:YAG," in *Advanced Solid-State Lasers (TOPS) Vol. 19*, 1998, pp. 212–217.

[69] O. A. Buryy, D. Y. Sugak, S. B. Ubizskii, I. I. Izhnin, M. M. Vakiv, and I. M. Solskii, "The comparative analysis and optimization of the free-running Tm^{3+}:YAP and Tm^{3+}:YAG microlasers," *Appl. Phys. B*, vol. 88, no. 3, pp. 433–442, Jul. 2007.

[70] R. Diehl and G. Brandt, "Crystal structure refinement of $YAlO_3$, a promising laser material," *Mater. Res. Bull.*, vol. 10, no. 3, pp. 85–90, 1975.

[71] A. A. Kaminskii, *Crystalline Lasers: Physical Processes and Operating Schemes*. New York, NY, USA: CRC Press, 1996.

[72] R. C. Stoneman and L. Esterowitz, "Efficient 1.94-μm Tm: YALO laser," *IEEE J. Sel. Top. Quantum Electron.*, vol. 1, no. 1, pp. 1077–1080, 1995.

[73] Y. Kuwano, "Refractive indices of YAlO3 : Nd," *J. Appl. Phys.*, vol. 49, no. 7, pp. 4223–4224, 1978.

[74] D. Y. Sugak, Y. Zhydachevskii, O. A. Buryy, S. B. Ubizskii, A. Börger, M. Schrader, and K.-D. Becker, "Optical in situ study of reduction/oxidation processes in $YAlO_3$," *Acta Mater.*, vol. 56, no. 20, pp. 6310–6318, Dec. 2008.

[75] J. K. Jabczynski, L. Gorajek, W. Zendzian, J. Kwiatkowski, H. Jelínková, J. Šulc, and M. Nemec, "Actively Q-switched thulium lasers," in *Advances in Solid State*

Lasers: Development and Applications, no. February, M. Grishin, Ed. InTech, 2010, pp. 95–118.

[76] R. C. Liebermann, L. E. A. Jones, and A. E. Ringwood, "Elasticity of aluminate, titanate, stannate and germanate compounds with the perovskite structure," *Phys. Earth Planet. Inter.*, vol. 14, no. 2, pp. 165–178, 1977.

[77] P. L. Cross, "Sellmeier Coefficients for materials in Database Lasers," *NASA*, 2002. [Online]. Available: http://www.mennerat.fr/gab/References/DatabaseLasers/tables/sellout.htm. [Accessed: 10-Sep-2014].

[78] I. F. Elder and M. J. P. Payne, "Lasing in diode-pumped thulium and thulium, holmium YAP," in *Advanced Solid-State Lasers (TOPS) Vol. 1*, 1996, vol. 1, pp. 319–325.

[79] I. F. Elder and M. J. P. Payne, "Lasing in diode-pumped Tm:YAP, Tm,Ho:YAP and Tm,Ho:YLF," *Opt. Commun.*, vol. 145, pp. 329–339, 1998.

[80] A. C. Sullivan, A. Zakel, and G. J. Wagner, "High power Q-switched Tm: YALO lasers," in *Advanced Solid-State Lasers (TOPS) Vol. 94*, 2004, vol. 94, pp. 5–8.

[81] J. Šulc, H. Jelínková, K. Nejezchleb, and V. Škoda, "Fluctuation-free CW Tm:YAP laser with monolithic resonator," in *Lasers and Electro-Optics 2009 and the European Quantum Electronics Conference. CLEO Europe - EQEC 2009.*, 2009, vol. 269, no. 2003, p. 1.

[82] M. Ding and P. K. Cheo, "Analysis of Er-Doped Fiber Laser Stability by Suppressing Relaxation Oscillation," *IEEE Photonics Technol. Lett.*, vol. 21, no. 9, pp. 1151–1153, 1996.

[83] D. Marcuse, "Pulsing behavior of a three-level laser with saturable absorber," *IEEE J. Quantum Electron.*, vol. 29, no. 8, 1993.

[84] S. D. Jackson and T. A. King, "Dynamics of the output of heavily Tm-doped double-clad silica fiber lasers," *J. Opt. Soc. Am. B*, vol. 16, no. 12, pp. 2178–2188, 1999.

[85] I. Razdobreev and A. Shestakov, "Self-pulsing of a monolithic Tm-doped $YAlO_3$ microlaser," *Phys. Rev. A*, vol. 73, no. 5, p. 53815, May 2006.

[86] Y. Tang and J. Xu, "Model and Characteristics of Self-Pulsing in Tm^{3+}-doped Silica Fiber Lasers," *IEEE J. Quantum Electron.*, vol. 47, no. 2, pp. 165–171, 2011.

[87] C. O. Weiss and J. Brock, "Evidence for Lorenz-Type Chaos in a Laser," *Phys. Rev. Lett.*, vol. 57, no. 22, pp. 2804–2806, Dec. 1986.

[88] C. O. Weiss, “Chaotic laser dynamics,” *Opt. Quantum Electron.*, vol. 20, no. 1, pp. 1–22, 1988.

[89] C. O. Weiss, U. Hübner, N. B. Abraham, and D. Tang, “Lorenz-like chaos in NH_3-FIR lasers,” *Infrared Phys. Technol.*, vol. 36, no. 1, pp. 489–512, 1995.

[90] J. Ohtsubo, *Semiconductor Lasers - Stability, Instability and Chaos*, 3rd ed. Berlin: Springer-Verlag, 2013.

[91] P. Černý, G. J. Valentine, and D. Burns, “Actively stabilised diode pumped Tm: YAlO laser,” *Electron. Lett.*, vol. 40, no. 17, pp. 40–41, 2004.

[92] T. J. Kane, “Intensity noise in diode-pumped single-frequency Nd:YAG lasers and its control by electronic feedback,” *IEEE Photonics Technol. Lett.*, vol. 2, no. 4, pp. 244–245, Apr. 1990.

[93] G. De Geronimo, S. Taccheo, and P. Laporta, “Optoelectronic feedback control for intensity noise suppression in a codoped erbium-ytterbium glass laser,” *Electron. Lett.*, vol. 33, no. 15, p. 1336, 1997.

[94] C. Ishibashi, M. Notcutt, J. Ye, and J. Hall, “Suppression of intensity noise in a diode-pumped Yb:YAG laser,” in *Conference on Lasers and Electro-Optics (CLEO)*, 2004, no. 1, pp. 4–6.

[95] F. Seifert, P. Kwee, M. Heurs, B. Willke, and K. Danzmann, “Laser power stabilization for second-generation gravitational wave detectors.,” *Opt. Lett.*, vol. 31, no. 13, pp. 2000–2002, Jul. 2006.

[96] C. C. Harb, M. B. Gray, H.-A. Bachor, R. Shilling, P. Rottengatter, I. Freitag, and H. Welling, “Suppression of the intensity noise in a diode-pumped neodymium: YAG nonplanar ring laser,” *IEEE J. Quantum Electron.*, vol. 30, no. 12, pp. 2907–2913, 1994.

[97] P. Laporta, M. Marano, L. Pallaro, and S. Taccheo, “Amplitude and frequency stabilisation of a Tm–Ho: YAG laser for coherent lidar applications at 2.1 μm,” *Opt. Lasers Eng.*, vol. 37, no. 2002, pp. 447–457, 2002.

[98] S. Bielawski, M. Bouazaoui, D. Derozier, and P. Glorieux, “Stabilization and characterization of unstable steady states in a laser,” *Phys. Rev. A*, vol. 47, no. 4, pp. 3276–3280, 1993.

[99] X. Cheng, J. Xu, Y. Hang, G.-J. Zhao, and S. Zhang, “High-power diode-end-pumped Tm: YAP and Tm: YLF slab lasers,” *Chinese Opt. Lett.*, vol. 9, no. 9, p. 091406, 2011.

[100] L. Han, B. Yao, X.-M. Duan, S. Li, T. Dai, Y.-L. Ju, and Y. Wang, “High power slab Tm:YAP laser dual-end-pumped by fiber coupled laser diodes,” *Opt. Quantum Electron.*, pp. 1–7, Jun. 2014.

[101] X. Cheng, J. Xu, G. Zhao, Y. Pan, and B. Jiang, "Diode-end-pumped Tm3+-doped thin slab solid-state lasers," in *Conference on Lasers and Electro-Optics (CLEO)*, 2009, vol. 3, p. MD1_3.

[102] X. Cheng, F. Chen, G. Zhao, and J. Q. Xu, "High-efficiency, high-power, diode-pumped continuous-wave Tm:$YAlO_3$ slab lasers," *Appl. Phys. B*, vol. 97, no. 3, pp. 639–643, Oct. 2009.

[103] P. Černý, J. Šulc, and H. Jelínková, "Continuously tunable diode pumped Tm:YAP laser," in *Proc. SPIE 6190, Solid State Lasers and Amplifiers II*, 2006, p. 619008.

[104] W. Koechner, "Absorbed pump power, thermal profile and stresses in a cw pumped Nd: YAG crystal," *Appl. Opt.*, vol. 9, no. 6, pp. 1429–1434, 1970.

[105] T. Kimura and K. Otsuka, "Thermal effects of a continuously pumped Nd^{3+}:YAG laser," *IEEE J. Quantum Electron.*, vol. 7, no. 8, pp. 403–407, 1971.

[106] Y. Chen, B. Chen, M. K. R. Patel, and M. Bass, "Calculation of thermal-gradient-induced stress birefringence in slab lasers-I," *IEEE J. Quantum Electron.*, vol. 40, no. 7, pp. 909–916, 2004.

[107] B. Yao, Y. Tian, W. Wang, G. Li, and Y. Wang, "Analysis and compensation of thermal lens effects in Tm: YAP lasers," *Chinese Opt. Lett.*, vol. 8, no. 10, pp. 996–999, 2010.

[108] G. Li, B. Q. Yao, X.-M. Duan, C. H. Zhang, and Y.-Z. Wang, "Thermal analysis and laser performance modelling of a dual-end-pumped c-cut CW Tm:YAP laser," *J. Phys. B At. Mol. Opt. Phys.*, vol. 43, no. 20, p. 205401, Oct. 2010.

[109] A. McInnes and J. Richards, "Thermal effects in a coplanar-pumped folded-zigzag slab laser," *IEEE J. Quantum Electron.*, vol. 32, no. 7, pp. 1243–1252, 1996.

[110] J. M. Eggleston, T. J. Kane, K. Kuhn, J. Unternahrer, and R. L. Byer, "The slab geometry laser--Part I: theory," *IEEE J. Quantum Electron.*, vol. 20, no. 3, pp. 289–301, 1984.

[111] D. Mudge, M. Ostermeyer, P. J. Veitch, J. Munch, B. Middlemiss, D. J. Ottaway, and M. W. Hamilton, "Power Scalable TEM_{00} CW Nd:YAG Laser with Thermal Lens Compensation," *IEEE J. Sel. Top. Quantum Electron.*, vol. 6, no. 4, pp. 643–649, 2000.

[112] A. Giesen, H. Hiigep, A. Voss, K. Wittig, U. Brauch, and H. Opower, "Scalable concept for diode-pumped high-power solid-state lasers," *Appl. Phys. B*, vol. 58, pp. 365–372, 1994.

[113] J. A. Abate, L. Lund, D. Brown, S. Jacobs, S. Refermat, J. Kelly, M. Gavin, J. Waldbillig, and O. Lewis, "Active mirror: a large-aperture medium-repetition rate Nd:glass amplifier," *Appl. Opt.*, vol. 20, no. 2, pp. 351–361, Jan. 1981.

[114] K. Ueda and N. Uehara, “Laser-diode-pumped solid state lasers for gravitational wave antenna,” in *Proc. SPIE 1837*, 1992, pp. 336–345.

[115] N. Pavel, K. Lünstedt, K. Petermann, and G. Huber, “Multipass pumped Nd-based thin-disk lasers: continuous-wave laser operation at 1.06 and 0.9 μm with intracavity frequency doubling,” *Appl. Opt.*, vol. 46, no. 34, pp. 8256–8263, Dec. 2007.

[116] P. Peterson, A. Gavrielides, T. C. Newell, N. Vretenar, and W. P. Latham, “ASE in thin disk lasers: theory and experiment,” *Opt. Express*, vol. 19, no. 25, pp. 25672–25684, Dec. 2011.

[117] K. S. Wu, P. J. Veitch, J. Munch, and D. J. Ottaway, “Suppression of self-pulsing in Tm:$YAlO_3$ lasers via current feedback,” *Appl. Phys. B*, vol. 114, no. 3, pp. 415–419, Jun. 2013.

[118] M. Ostermeyer, D. Mudge, P. J. Veitch, and J. Munch, “Thermally induced birefringence in Nd:YAG slab lasers,” *Appl. Opt.*, vol. 45, no. 21, pp. 5368–5376, Jul. 2006.

[119] W. A. Clarkson, N. S. Felgate, and D. C. Hanna, “Simple method for reducing the depolarization loss resulting from thermally induced birefringence in solid-state lasers,” *Opt. Lett.*, vol. 24, no. 12, pp. 820–822, Jun. 1999.

[120] H. Kogelnik and T. Li, “Laser beams and resonators,” *Appl. Opt.*, vol. 5, no. 10, pp. 1550–1567, Oct. 1966.

[121] G. F. Franklin, J. D. Powell, and A. Emami-Naeini, *Feedback control of Dynamic Systems*, 3rd ed. Addison-Wesley, New York, 1994, pp. 111–112.

[122] T. Thevar and N. P. Barnes, “Diode-pumped, continuous-wave Tm:$YAlO_3$ laser,” *Appl. Opt.*, vol. 45, no. 14, pp. 3352–3355, May 2006.

[123] T. Corbitt, D. J. Ottaway, E. Innerhofer, J. Pelc, and N. Mavalvala, “Measurement of radiation-pressure-induced optomechanical dynamics in a suspended Fabry-Perot cavity,” *Phys. Rev. A*, vol. 74, no. 2, p. 021802, Aug. 2006.

[124] G. Rustad and K. Stenersen, “Modeling of laser-pumped Tm and Ho lasers accounting for upconversion and ground-state depletion,” *IEEE J. Quantum Electron.*, vol. 32, no. 9, pp. 1645–1656, 1996.

[125] F. Sanchez and A. Kellou, “Laser dynamics with excited-state absorption,” *J. Opt. Soc. Am. B*, vol. 14, no. 1, p. 209, Jan. 1997.

[126] M. J. Weber, “Multiphonon Relaxation of Rare-Earth Ions in Yttrium Orthoaluminate,” *Phys. Rev. B*, vol. 8, no. 1, pp. 54–64, Jul. 1973.

[127] S. A. Payne, L. L. Chase, L. K. Smith, W. L. Kway, and W. F. Krupke, "Infrared cross-section measurements for crystals doped with Er^{3+}, Tm^{3+}, and Ho^{3+}," *IEEE J. Quantum Electron.*, vol. 28, no. 11, pp. 2619–2630, 1992.

[128] J. A. Caird, L. G. DeShazer, and J. Nella, "Characteristics of room-temperature 2.3-μm laser emission from Tm^{3+} in YAG and $YAlO_3$," *IEEE J. Quantum Electron.*, vol. 11, no. 1, pp. 874–881, 1975.

[129] K. S. Wu, O. Henderson-Sapir, P. J. Veitch, M. Hamilton, J. Munch, and D. J. Ottaway, "Self-pulsing in Tm-doped $YAlO_3$ lasers: Excited-state absorption and chaos," *Phys. Rev. A*, vol. 91, no. 4, p. 43819, Apr. 2015.

[130] N. I. Borodin, P. V Kryukov, A. V Popov, S. N. Ushakov, and A. V Shestakov, "Diode-pumped cw Tm^{3+} : $YAlO_3$ laser," *Quantum Electron.*, vol. 35, no. 6, pp. 511–514, 2005.

[131] H. D. I. Abarbanel, *Analysis of Observed Chaotic Data*. New York, NY, USA: Springer-Verlag, 1996.

[132] N. H. Packard, J. P. Crutchfield, J. D. Farmer, and R. S. Shaw, "Geometry from a time series," *Phys. Rev. Lett.*, vol. 45, no. 9, pp. 712–716, 1980.

[133] F. Takens, "Detecting strange attractors in turbulence," in *Dynamical Systems and Turbulence, Lecture Notes in Mathematics, vol 898*, vol. 898, D. Rand and L.-S. Young, Eds. Springer Berlin Heidelberg, 1981, pp. 366–381.

[134] A. M. Fraser and H. L. Swinney, "Independent coordinates for strange attractors from mutual information," *Phys. Rev. A*, vol. 2, no. February, pp. 1134–1140, 1986.

[135] M. B. Kennel, R. Brown, and H. D. I. Abarbanel, "Determining embedding dimension for phase-space reconstruction using a geometrical construction," *Phys. Rev. A*, vol. 45, no. 6, pp. 3403–3411, 1992.

[136] S. M. Boker, "Linear and Nonlinear Dynamical Systems Data Analytic Techniques and an Application to Developmental Data," University of Virginia, 1996.

[137] M. B. Kennel and S. Isabelle, "Method to distinguish possible chaos from colored noise and to determine embedding parameters," *Phys. Rev. A*, vol. 46, no. 6, pp. 3111–3118, 1992.

[138] J. Theiler, S. Eubank, A. Longtin, B. Galdrikian, and J. D. Farmer, "Testing for nonlinearity in time series: the method of surrogate data," *Phys. D Nonlinear Phenom.*, vol. 58, pp. 77–94, 1992.

[139] D. Prichard and J. Theiler, "Generating surrogate data for time series with several simultaneously measured variables," *Phys. Rev. Lett.*, vol. 73, no. 7, pp. 951–954, 1994.

[140] T. Schreiber and A. Schmitz, “Improved surrogate data for nonlinearity tests,” *Phys. Rev. Lett.*, vol. 77, pp. 635–638, 1996.

[141] G. A. Gottwald and I. Melbourne, “A new test for chaos in deterministic systems,” *Proc. R. Soc. A Math. Phys. Eng. Sci.*, vol. 460, pp. 603–611, Feb. 2004.

[142] G. A. Gottwald and I. Melbourne, “Testing for chaos in deterministic systems with noise,” *Phys. D Nonlinear Phenom.*, vol. 212, no. 1–2, pp. 100–110, Dec. 2005.

[143] G. A. Gottwald and I. Melbourne, “On the implementation of the 0-1 test for chaos,” *SIAM J. Appl. Dyn. Syst.*, vol. 8, no. 1, pp. 129–145, 2009.

[144] F. T. Arecchi, G. L. Lippi, G. P. Puccioni, and J. R. Tredicce, “Deterministic chaos in laser with injected signal,” *Opt. Commun.*, vol. 51, no. 5, pp. 308–314, 1984.

[145] G. Li, H. Liu, F. Lu, X. Wen, Y. Gu, and Y.-Z. Wang, “Analysis on preferential free running laser wavelength and performance modeling of Tm3+-doped YAP and YLF,” *Appl. Opt.*, vol. 53, no. 22, pp. 4987–4996, Aug. 2014.

[146] A. E. Siegman, *Lasers*. California: University Science Books, 1986.

[147] C. E. Webb and J. D. C. Jones, *Handbook of Laser Technology and Applications: Laser design and laser systems*. CRC Press, 2004.

[148] D. Axelrod, T. P. Burghardt, N. L. Thompson, and S. Francisco, “Total Internal Reflection Fluorescence,” *Annu. Rev. Biophys. Bioeng.*, vol. 13, no. 17, pp. 247–268, Jan. 1984.

[149] C. D. Brandle, “Czochralski growth of oxides,” *J. Cryst. Growth*, vol. 264, no. 4, pp. 593–604, Mar. 2004.

[150] D. T. J. Hurle, “The evolution and modelling of the Czochralski growth technique,” *J. Cryst. Growth*, vol. 85, pp. 1–8, 1987.

[151] J. R. Carruthers, “Flow transitions and interface shapes in the Czochralski growth of oxide crystals,” *J. Cryst. Growth*, vol. 36, no. 2, pp. 212–214, Dec. 1976.

[152] T. I. Butaeva, A. A. Kaminskii, K. L. Ovanesyan, and A. G. Petrosyan, “Investigation of optical properties of YAlO3Pr3+ single crystals,” *Cryst. Res. Technol.*, vol. 21, no. 12, pp. 1577–1581, 1986.

[153] G.-J. Zhao, X. H. Zeng, S. M. Zhou, J. Q. Xu, Y. L. Tian, and W. X. Huang, “Growth defects in Czochralski-grown Ce:$YAlO_3$ scintillation crystals,” *Phys. Status Solidi*, vol. 199, no. 2, pp. 186–191, Sep. 2003.

[154] Y. Lu, J. Wang, Y. Yang, Y. Dai, B. Sun, and S. Li, “Czochralski growth of YAP crystal doped with high Tm concentration,” *J. Cryst. Growth*, vol. 292, no. 2, pp. 381–385, Jul. 2006.

[155] R. Shannon, “Revised effective ionic radii and systematic studies of interatomic distances in halides and chalcogenides,” *Acta Crystallogr. Sect. A*, vol. 32, no. 5, pp. 751–767, 1976.

[156] A. O. Matkovskii, D. I. Savytskii, and D. Y. Sugak, “Growth and properties of $YAlO_3$:Tm single crystals for 2-μm laser operation,” *J. Cryst. Growth*, vol. 241, pp. 455–462, 2002.

[157] S. Geller and E. A. Wood, “Crystallographic studies of perovskite-like compounds. I. Rare earth orthoferrites and $YFeO_3$, $YCrO_3$, $YAlO_3$,” *Acta Crystallogr.*, vol. 9, no. 7, pp. 563–568, Jul. 1956.

[158] T. Noguchi and M. Mizuno, “Liquidus Curve Measurements in the System Y_2O_3—Al_2O_3,” *Kogyo Kagaku Zasshi*, vol. 70, no. 6, pp. 834–839, 1967.

[159] J. W. Strutt, “On the transmission of light through an atmosphere containing small particles in suspension, and on the origin of the blue of the sky,” *Philos. Mag. Ser. 5*, vol. 47, no. 287, pp. 375–394, 1899.

[160] G. Mie, “Beiträge zur Optik trüber Medien, speziell kolloidaler Metallösungen,” *Ann. Phys.*, vol. 330, pp. 377–445, 1908.